2000

Metallic compounds of scandium-tellurium and related systems

Paul Anthony Maggard Jr.
Iowa State University

Recommended Citation

Maggard, Paul Anthony Jr., "Metallic compounds of scandium-tellurium and related systems " (2000). *Retrospective Theses and Dissertations*. 12702.
https://lib.dr.iastate.edu/rtd/12702

INFORMATION TO USERS

This manuscript has been reproduced from the microfilm master. UMI films the text directly from the original or copy submitted. Thus, some thesis and dissertation copies are in typewriter face, while others may be from any type of computer printer.

The quality of this reproduction is dependent upon the quality of the copy submitted. Broken or indistinct print, colored or poor quality illustrations and photographs, print bleedthrough, substandard margins, and improper alignment can adversely affect reproduction.

In the unlikely event that the author did not send UMI a complete manuscript and there are missing pages, these will be noted. Also, if unauthorized copyright material had to be removed, a note will indicate the deletion.

Oversize materials (e.g., maps, drawings, charts) are reproduced by sectioning the original, beginning at the upper left-hand corner and continuing from left to right in equal sections with small overlaps.

Photographs included in the original manuscript have been reproduced xerographically in this copy. Higher quality 6" x 9" black and white photographic prints are available for any photographs or illustrations appearing in this copy for an additional charge. Contact UMI directly to order.

Bell & Howell Information and Learning
300 North Zeeb Road, Ann Arbor, MI 48106-1346 USA
800-521-0600

UMI®

Metallic compounds of scandium–tellurium and related systems

by

Paul Anthony Maggard Jr.

A dissertation submitted to the graduate faculty
in partial fulfillment of the requirements for the degree of
DOCTOR OF PHILOSOPHY

Major: Inorganic Chemistry
Major Professor: John D. Corbett

Iowa State University
Ames, Iowa
2000

Bell & Howell Information and Learning Company
300 North Zeeb Road
P.O. Box 1346
Ann Arbor, MI 48106-1346

Graduate College

Iowa State University

This is to certify that the Doctoral dissertation of

Paul Anthony Maggard Jr.

has met the dissertation requirements of Iowa State University

Signature was redacted for privacy.

Major Professor

Signature was redacted for privacy.

For the Major Program

Signature was redacted for privacy.

For the Graduate College

TABLE OF CONTENTS

ABSTRACT[1]

Research contributions from our group have evinced significant progress in the solid-state chemistry of the rare-earth metal halides. This thesis presents results of the first extension of this progress into the scandium-tellurium and related ternary systems. The first evidence for the existence of metal-rich compounds in this system was the synthesis of Sc_2Te. The internal metal-bonded features of the structure are double quasi-infinite chains of trans-edge-sharing metal octahedra, further augmented on each end by square-pyramids down the chain. These scandium chains have a blade-like shape and are spaced apart by tellurium atoms and a scandium zigzag chain. A second metal-rich compound was uncovered in Sc_8Te_3. Chains of trans-edge-sharing octahedra are again featured in much of the metal framework, but condensed into 2D sheets. In the Y_8Te_3 analog there is apparent disorder on some of the internal metal positions within the chains. The metal-richest compound synthesized in the scandium-tellurium system was Sc_9Te_2. A higher degree of metal aggregation forms in four trans-edge-sharing metal octahedra chains condensed into 3 × 3 blocks, and linked together to form much thicker 2D sheets compared to Sc_8Te_3. Interesting distortions were analyzed with relationship to higher symmetry structures. The insertion of later transition metals into the earlier transition-metal framework results in the formation of the compounds $Sc_5Ni_2Te_2$, Sc_6MTe_2 (M = Mn, Fe, Co, Ni), $Y_5M_2Te_2$ (M = Fe, Co, Ni) and the corresponding hydride, $Y_5Ni_2Te_2H_{0.41(1)}$. These compounds contain diverse sheet and columnar metal frameworks. Structural interrelationships among the many known ternary compounds are analyzed. The reaction of small amounts of aluminum into the scandium–tellurium systems revealed new substitution chemistry. The systems $Sc_5B_xB'_{3-x}$ (B = Al or Ga; B' = Sn, Sb or Te) contained varied amounts of the triel elements (B) substituted on the same sites for either the tetrel, pnictide or chalcogenide (B'), respectively. Analysis of the synthesis and structure of these compounds was used to incrementally improve the continuously evolving scientific answers about recurring structural features and structure/property relationships in solids.

---

[1] This research was supported by the National Science Foundation (Solid State Chemistry grant DMR-9510278) and was carried out in the facilities of Ames Laboratory, U.S. Department of Energy

CHAPTER 1. GENERAL BACKGROUND MATERIAL

Introduction

To increase the knowledge of solid-state compounds is the goal of the experimentation and analysis described in this thesis. Since nature constructs a solid based upon the most efficient energetic gains and kinetic barriers, atomic structural and bonding features within one or several systems may be very similar. Chemical intuition is developed by recognizing the geometric and electronic interrelationships of atomic packing and extending them to the construction of new compounds. This approach is used in the analysis of the research results, which involved the synthesis of new compounds containing scandium and tellurium, and sometimes a late transition metal. Parallel reactions with yttrium were used to test chemical flexibility of a structure type, while metallic compounds containing metal clustering was the goal.

Previous investigations into the scandium-tellurium system were performed in 1959 and the early 1960's. The first compound reported to form from the combination of scandium and tellurium was Sc_2Te_3,[1] having a NaCl structure type, with vacancies randomly distributed on the scandium sites. The compound is valence balanced (Sc^{+3} and Te^{-2}), and there is no direct metal-metal bonding. A NiAs structure type was found in the next reported compound, ScTe,[2] while a polytype having both the NiAs and NaCl atomic packing was reported for $Sc_{2.3}Te_3$.[3] Even though these compounds are not valence balanced, neither structure contains metal-atom clustering. Beyond these initial results, no systematic explorations into the metal-rich chemistry of scandium and tellurium had been reported. This relatively simple binary system was prime for experimental exploration.

However, related research in other metallic systems has uncovered a great number of compounds with early transition metals in combination with the halides or chalcogenides.[4,5] Those examples with scandium and yttrium in combination with a halide are Sc_7Cl_{10},[6] and Y_2Cl_3.[7] A basic structural unit inherent in both of the compounds is the quasi-infinite trans-edge-sharing octahedral chain formed by the early transition metal. The chains are doubly condensed in the former, and singly in the latter. One can find more chemistry by incorporating a third element, such as a late-transition metal, which becomes inserted within the early-transition metal octahedra. Some of these compounds are $R_7I_{12}M$ (R= Sc, Y; M = Mn, Fe, Co),[8] $Y_6I_{10}Ru$,[9] Y_3I_3Ru,[10] $Sc_{19}Br_{28}Z_4$ (Z= Mn, Ru, Os),[11] and $Y_{16}X_{20}Ru_4$ (X= Br, I).[12] The basic structural unit within each compound is an octahedron again, either singular or condensed into chains, tetramers, or sheets of scandium or yttrium, that is centered by the late-transition metal. The discrete early transition-metal octahedra in the ternaries usually have the edge-capping halides in the well known M_6X_{12} configuration, as opposed to a face-capped M_6X_8 arrangement. Bonding for the M_6X_{12} cluster is optimized at 14 - 18 electrons (i.e. $Y_6I_{10}Ru$), while for M_6X_8 it is usually 21 - 24 electrons.[13] In the more condensed metal frameworks, such as in infinite chains and sheets, face capping is more often exhibited by the halides, and no discernible electron count preference. The relatively well-explored chemistry of the metal halides has revealed many cluster shapes and patterns preferred by reduced scandium or yttrium. The research described herein answers the question of how these cluster shapes and patterns are re-expressed when halogens are replaced with tellurium.

Related compounds may also be found in the metal-rich chemistry of titanium and zirconium chalcogenides, such as Ti_9Se_2,[14] $Ti_{11}Se_4$,[15] Ti_8Z_3[16,17] and Ti_2Z,[18,19] (Z = S, Se), Zr_3Te,[20] and Zr_2Te.[21] The metal framework in these compounds is 3D in connection, and also with no discernible preference for electron count or directional bonding. They are much condensed versions of the quasi-infinite trans-edge-sharing metal-octahedral chains apparent in the scandium and yttrium halides described above, and as described in a review.[22] The research results here includes many relationships to this electron- richer chalcogenide chemistry.

In solid-state chemistry, valence electron concentrations (VEC), and the metal-to-nonmetal proportions play key roles in the determination of structural features and types. The structural and electronic relationships of new metal-bonded compounds comprising scandium and tellurium are compared with the known chemistries of the halides and of the electron-richer transition-metal chalcogenides. Highlights of this research include an appreciation of cooperative matrix and bonding effects (Ch. 2, 3, and 5), distortions in low-dimensional metals (Ch. 4), new structural interrelationships (Ch. 5, 6), and the amazing flexibility of some structure types (Ch. 7, 8), all within the Sc–Te and related systems.

Experimental Techniques

Starting Materials

All compounds were synthesized from an appropriate mixture of the elements with either Sc_2Te_3 or Y_2Te_3, which were used instead of the relatively volatile and active tellurium. The elements were used as received, with the manufacturer and purity levels of the starting materials reported in the respective chapters.

To synthesize Sc_2Te_3 and Y_2Te_3, the elements were loaded in a 2:3 stoichiometry into a fused-silica container. The fused silica container was evacuated, sealed off, and heated to 450°C for 12 h and then to 900°C for 72 h. The sample was allowed to radiatively cool to room temperature. Guinier film data confirmed the products were the R_2Te_3 ($\geq$95%), NaCl-type phases.

In some instances, the scandium and yttrium metals were powderized according to the method as reported by S.-J. Hwu.[23] The method consists of the preparation of the brittle ScH_2 or YH_2, which is ground into small pieces, thermally decomposed back to the metal under dynamic vacuum at 700 - 750°C, and stored inside a He-filled dry box with the other starting materials.

Inert Atmospheres

The air-sensitive character of many of the products and starting materials required the use of oxygen and moisture free environments. All reactions were loaded inside a helium-filled dry box from Vacuum Atmospheres Co., model DLX-001-S-P, equipped with a Vacuum Atmospheres DRI-TRAIN regeneration system, model HE-493. The helium atmosphere was continuously circulated through an activated Cu/molecular sieve catalyst to minimize moisture and oxygen levels. The moisture level of the helium environment was continuously monitored using a Panametrics System 3A hygrometer.

A nitrogen-filled Blickman glovebox, equipped with a microscope, was used to handle all product materials. The glovebox was outfitted with an identical gas purification system by Vacuum Atmospheres, model HE-493. The moisture level of the nitrogen environment was continuously monitored using a Panametrics model 700 hygrometer.

During customary work usage, the water levels in the dry box or glovebox never exceeded 1 - 2 ppm.

Reaction Containers

The highly reactive nature of the materials required the use of tantalum tubing as a container material during the reactions. Prior to use, the 3/8" tubing was cut to size, usually to 1½" pieces, and cleansed with an acid mixture of 55% sulfuric, 25% nitric, and 20% hydrofluoric acid by volume. After thorough rinsing and drying, each tube was crimped on one end and welded together under an argon atmosphere in an arc welder. The tubes, with one open end, were then transferred to the dry box for use.

Inside the dry box, starting materials for each reaction were weighed out on metal trays and carefully poured into the tantalum tubing. The tubes were crimped shut and placed inside a glass jar for transportation to the arc-welder for final sealing. Total time outside an inert atmosphere was usually less than 1 - 2 minutes for a crimped tantalum tube. The sealed tubes were cleansed again in the acid solution, washed thoroughly, and sometimes further sealed inside a evacuated silica jacket. The silica jacket is used to protect the tantalum tubing from oxidation and breakdown at high temperatures in the tube furnaces. During the sealing procedure of the fused-silica jacket, a Welch Duoseal vacuum pump and mercury diffusion pump were used in linear combination to evacuate the container. Additionally, the fused-silica jacket was heated under vacuum with a natural gas torch to remove any moisture from the walls of the container before sealing.

Not all chemical reactions required the full procedure here, and cogent details are found in the experimental section of each chapter.

Synthetic Equipment

Three types of synthetic equipment were employed for chemical reaction of the starting materials: tube furnaces, a vacuum furnace and arc-melting.

A majority of the reactions were performed in simple tube furnaces with a maximum operating temperature of 1200°C. All reactions carried out in these furnaces were sealed in tantalum and fused-silica tubing. Programmable temperature controllers from Eurotherm and J-type thermocouples were used to control and monitor the temperature cycles. Heating cycles were varied and depended on the system under study, but most reactions required temperatures >800°C to initiate product formation in an acceptable amount of time. Heating to within ±50°C of the melting point of a compound and cooling at a rate of 1 - 5°C/hr for several hours was usually sufficient to achieve desired crystal growth.

A vacuum furnace from Thermal Technology Inc., Model # 1000-2560-FP20, was used on occasions that required temperatures >1200°C and a dynamic vacuum. Reactions performed in this furnace were sealed only in tantalum tubing. A Eurotherm programmable temperature controller and Aeropak T/C thermocouple were used to control and monitor the temperature cycles, as before.

A Miller Maxstar 91 arc-melter, connected to the glovebox through a port, was used on a few occasions for extreme temperatures and for those reactions that habitually reacted with tantalum tubing at high temperatures. Inside the glovebox, the reactions were first pressed (~1–2 tons) into 10mm pellets, containing about 300mg of starting materials, and then transferred to the arc-melter. A water-cooled copper hearth with three depressions was used to hold a zirconium getter pellet and two reaction pellets. The arc-melter was loaded with the copper hearth and then evacuated and re-filled with argon three times before use. Under a flowing argon atmosphere, the zirconium getter was melted/activated, and the reaction pellets were arc-melted for approximately 20 seconds per side at about 50 - 70A. The zirconium getter was repeatedly re-melted during the procedure. After cooling, the reactions were then moved back to the dry box.

Pressed pellets of the starting materials were made with a SPECAC manual hydraulic press, P/N 15011, and dies. 5mm and 10mm dies were used for reactions in tantalum tubing or for arc-melting, respectively.

Product Identification

The product was initially prepared for analysis inside the nitrogen-filled glovebox with an optical microscope mounted on the plexiglass top. The tantalum tubing was opened inside the glovebox by cutting off one of the welded ends with a metal tube cutter. Products were then poured out of the tube, or scraped from the tubing walls with a scalpel, into a mortar. The sample was visually inspected for crystal morphology and crystallinity. Crystal morphologies helped to preliminarily identify the character and number of phases present, and to streamline the process of crystal picking. If crystals of unknown morphology and suitable crystallinity were present, they were loaded into 0.3mm diameter capillary tubes with grease and sealed with a gas microtorch outside the glovebox. Otherwise, the entire product was then ground into chunks and powder using a mortar and pestle inside the glovebox. The majority of the ground sample was later sealed off in evacuated Pyrex tubing using a natural gas/oxygen torch, while a small portion was separated from the bulk and mixed with NIST (NBS) standard silicon.

The sample, mixed with standard silicon, was fixed between two pieces of cellophane tape to reduce exposure to air, transferred to a rotating sample holder, and placed inside a Guinier X-ray powder diffraction unit. The Guinier cameras, Enraf-Nonius model FR552, gave filtered monochromated Cu Kα_1 radiation ($\lambda = 1.540562$ Å), with the samples under continuous vacuum by Welch Duoseal vacuum pumps. The X-ray powder diffraction patterns were recorded with Kodak BIOMAX MR Scientific Imaging Film.

The observed X-ray diffraction powder patterns were compared with theoretical powder patterns of known compounds to assist in product identification. The theoretical powder patterns were calculated and output using the program POWDER.[24] In multi component samples the percentage of each of the known products was estimated from the visual inspection of powder line intensities. An LS20 Line Scanner from KEJ Instruments allowed a more precise measurement of line positions and intensities using the Si standardization to account for the individual camera and film variations. Final lattice parameters of the compounds were calculated using these line positions in the least squares program LATT.[25]

Single Crystal X-ray Diffraction

After identification of an unknown in the powder-diffraction patterns, the quality of single crystals obtained therefrom were evaluated from Laue photographs taken with Weissenberg cameras. The best single crystals were taken for data set collection on one of three single crystal X-ray diffractometers, a Rigaku AFC6R with a rotating anode, an Enraf-Nonius CAD4 with a sealed tube, or a Bruker CCD equipped with an area detector and a sealed tube. Each diffractometer output monochromatic Mo Kα_1 radiation (λ = 0.71069 Å). Single-crystal data sets were collected and analyzed using associated software analysis packages. Some separate packages used for refinement and data manipulation included the TEXSAN[26] and SHELXTL[27] software programs. Details of the data collection and analysis may be found in the experimental sections of each of the chapters.

Energy-Dispersive X-ray Spectroscopy Measurements

Elemental compositions of the crystals and powdered samples were occasionally evaluated via energy-dispersive X-ray spectroscopy (EDS) on a JEOL system 840A scanning electron microscope (SEM), equipped with an IXRF X-ray analyzer system and a Kevex Quantum light element detector. Typical data collections utilized a beam of approximately 20kV and 0.3nA to gain a count rate of about 2500 s^{-1}. Standards were measured to ensure proper calibration.

Magnetic Susceptibility Measurements

Where appropriate, magnetizations for the compounds were measured with a Quantum Design MPMS SQUID magnetometer from 6 to 300 K in a field of 3 T. Powdered samples of 30 - 60 mg were loaded into a container that sandwiched the material between the flat ends of two glass rods inside a concentric 3 mm i.d. fused-silica tube. This container was loaded inside the He-filled dry box, capped with a plug, and sealed outside the box using a natural gas/oxygen torch. The raw data were corrected for the diamagnetism of both the atomic cores and sample holders.

Electrical Resistivity Measurements

Resistivities of powdered, sized samples were collected using a Hewlett-Packard 4342A Q-meter. Measurements in this technique rely on the surface conduction of a sample to change the quality factor of a coil. For an average measurement of the surface area of the particles, the samples were passed through a sieve to collect particles having grain sizes between 250 and 425 μm in diameter for use. To minimize contact between particles, the samples were diluted with approximately 1 cm^3 of dry chromatographic Al_2O_3 inside a Pyrex tube. Each sample was loaded inside the He-filled dry box and later sealed inside the Pyrex tubing with a natural gas/oxygen torch.

The samples were measured in the Q-meter operating at 34 MHz between 100 and 300 K. The procedure involved measuring the quality factor of the coil with the sample both inside (Q) and outside (Q_0) at every temperature. This change in the quality factor ($\Delta 1/Q$) was used to calculate the sample resistivity (ρ) using the formula:[28,29]

$$\rho = \frac{B(Va)}{\Delta(1/Q)}$$

where B is a constant that is calibrated for every coil (4.84×10^5), V is the sample volume, a is the average particle radius, and $\Delta(1/Q)$ is $1/Q - 1/Q_0$.

Electronic Structure Calculations

Extended Hückel band calculations were carried out for many of the structures using the EHMACC[30] program operating on a PC. The calculations were carried out within the tight-binding approximation for the full structures at k-points spread out over the irreducible wedge. Suitable starting parameters, listed in the respective chapters, were obtained with the associated Iterate program,[30] and were used to calculate the densities of states (DOS) and crystal-orbital overlap populations (COOP) for each structure.

Dissertation Organization

This dissertation has been organized in the form of papers either formerly published or in a potentially publishable format. Chapters 2 - 5 belong to the former class, with the citation listed at the beginning of each, while chapters 6 - 8 fall in the later category. The appendices contain research results for which either no regular ordered solutions were found (Appendix A) or research which produced interesting, but divergent side products (Appendix B).

The thesis has been divided into parts A and B, to better delineate between the results for the binaries and ternaries.

References

(1) Menkov, A.A.; Komissarova, L.N.; Simanov, Yu.P.; Spitsyn, V.I. *Proc. Acad. Sci. USSR, Chem. Sect.* **1959**, *128*, 693.

(2) Menkov, A.A.; Komissarova, L.N.; Simanov, Yu.P.; Spitsyn, V.I. *Proc. Acad. Sci. USSR, Chem. Sect.* **1961**, *141*, 1137.

(3) White, J.G.; Dismukes, J.P. *Inorg. Chem.* **1965**, *4*, 1760.

(4) Corbett, J.D. *Acc. Chem. Res.* **1981**, *14*, 239.

(5) Simon, A.; Mattausch, HJ.; Miller, G.J.; Bauhofer, W.; Kremer, R.K. *Handbook on the Physics and Chemistry of Rare Earths, Vol. 15*; Elsevier Science Publishers: Ch. 100, **1991**.

(6) Poeppelmeier, K.R.; Corbett, J.D. *Inorg. Chem.* **1977**, *16*, 1107.

(7) Mattausch, HJ.; Hendricks, J.B.; Eger, R.; Corbett, J.D.; Simon, A. *Inorg. Chem.* **1980**, *19*, 2128.

(8) Hughbanks, T.; Corbett, J.D. *Inorg. Chem.* **1988**, *27*, 2022.

(9) Payne, M.W.; Corbett, J.D. *Inorg. Chem.* **1990**, *29*, 2246.

(10) Payne, M.W.; Dorhout, P.K.; Kim, S.-J.; Hughbanks, T.R.; Corbett, J.D. *Inorg. Chem.* **1992**, *31*, 1389.

(11) Steinwand, S.J.; Corbett, J.D. *Inorg. Chem.* **1997**, *36*, 6413.

(12) Payne, M.W.; Ebihara, M.; Corbett, J.D. *Angew. Chem., Int. Ed. Engl.* **1991**, *30*, 856.

(13) Hughbanks, T.M. *Prog. Solid St. Chem.* Vol. 19, **1989**, 329.

(14) Weirich, T.E.; Simon, A.; Pöttgen, R. *Z. Anorg. Allg. Chem.* **1996**, *622*, 630.

(15) Weirich, T.E.; Ramlau, R.; Simon, A.; Hovmöller, S.; Zou, X. *Nature* **1996**, *382*, 144.

(16) Owens, J.P.; Franzen, H.F. *Acta Crystallogr.* **1974**, *B30*, 427.

(17) Weirich, T.E.; Pöttgen, R.; Simon, A. *Z. Kristallogr.* **1996**, *211*, 929.

(18) Owens, J.P.; Conard, B.R.; Franzen, H.F. *Acta Crystallogr.* **1967**, *23*, 77.

(19) Weirich, T.E.; Pöttgen, R.; Simon, A. *Z. Kristallogr.* **1996**, *211*, 928.

(20) Harbrecht, B.; Leersch, R. *J. Alloys Compd.* **1996**, *238*, 13.

(21) Örlygsson, G.; Harbrecht, B. *Inorg. Chem.* **1999**, *38*, 3377.

(22) Simon, A. *Angew. Chem., Int. Ed. Engl.* **1981**, *20*, 1.

(23) Hwu, S.-J. Ph.D. Dissertation, Iowa State University, Ames, IA, 1985.

(24) Clark, C.M.; Smith, D.K.; Johnson, G.J. A Fortran IV Program for Calculating X-ray Powder Diffraction Patterns - Version 6, Department of Geosciences, Pennsylvania State University: University Park, PA, **1973**.

(25) Takusagawa, F. Ames Laboratory, Iowa State University, unpublished research, **1981**.

(26) TEXSAN, Version 6.0, Molecular Structure Corp., The Woodlands, Texas, 1990.

(27) Sheldrick, M. SHELXS-97. Universität Göttingen, Germany, 1997.

(28) Shinar, J.; Dehner, B.; Beaudry, B.J.; Peterson, D.T. *Phys. Rev.* **1988**, *37B*, 2066.

(29) El-Hunany, U. *Rev. Sci. Instrum.* **1973**, *44(8)*, 1067.

(30) Whangbo, M.-H.; et al. EHMACC, Department of Chemistry, North Carolina State University: Raleigh, NC, 1987.

PART 1. BINARY PHASES

CHAPTER 2. Sc_2Te: A NOVEL EXAMPLE OF CONDENSED METAL POLYHEDRA IN A METAL-RICH BUT RELATIVELY ELECTRON-POOR COMPOUND

A communication published in Angewandte Chemie

Angew. Chem., Int. Ed. Engl. **1997**, *36*, 1974

Paul A. Maggard and John D. Corbett

Department of Chemistry, Iowa State University, Ames, Iowa 50011

Introduction, Results and Discussion

The earlier transition-metal chalcogenides have both extended the boundaries of solid state chemistry and challenged our understanding of stability, structure and bonding. Some recent examples of metal-rich chalcogenides of group 4 and 5 metals are Ti_9Se_2,[1] Zr_3Te,[2] Hf_3Te_2,[3] Ta_3S_2,[4] and Ta_2Se.[5] Highly reduced binary compounds of the earliest transition metals Sc, Y, La have been limited to a few halides and to the monochalcogenides (NaCl-type), which may be significantly substoichiometric.[6] Only a few truly binary halides are known, Sc_7Cl_{10}, Y_2X_3, and LaI.[7] No phase diagrams exist for any of the scandium or yttrium chalcogenides, and the only binary Sc–Te phases reported are Sc_2Te_3 and ScTe.[8] This situation clearly results from a lack of investigation of these quite refractory compounds. This article describes the first example, Sc_2Te, an exceptional compound among chalcogenides in the nature of its metal–metal bonding.

A [010] projection of the Sc_2Te structure down the short (3.919 Å) axis is given in Figure 1. Both a large complex chain unit and a simple zig-zag chain of scandium are evident. The Sc-Sc distances vary from 3.05 Å upward with no distinctive breaks, but the justification of the 3.5 Å limit for "bonds" marked in Figure 1 will be given later. Considerably closer contacts and tighter bonding are found within the larger Sc chain, which is detailed in Figure 2 with atom numbers and independent distances (the Sc6–Sc6 and Sc4–Sc4 bonds lie on centers of symmetry). The central building block emphasized by the darker bonds is the same as can be visualized in Sc_7Cl_{10}[7] as well as in several interstitial derivatives such as Pr_3I_3Ru,[9] namely, the familiar pairs of quasi-infinite chains of distorted trans-edge-sharing metal octahedra (e.g., (1,1)–5–(6,6)–6) that are further co-condensed through sharing of Sc6–Sc6 side edges. (The choice of Sc1–Sc6 (3.49 Å) as the shared edges and Sc5, Sc6 (d = 3.52 Å) for the apices of the compressed octahedra is fairly arbitrary (below). The y coordinates around the periphery of the double chain alternate between ¼ and ¾.)

The shortest Sc–Sc distances in the structure lie within the double chain, 3.05 – 3.27 Å. Surprisingly, these values are the same to about 0.1 Å less than those in Sc_7Cl_{10}, while both the shared trans-edge Sc1–Sc6 and the chain repeat are about 0.4 Å longer. The first difference may reflect the presence of the Sc2, Sc3 appendages or the bonding within the chain (below), while the increased chain repeat, 3.92 Å, logically derives from the larger diameter of closed-shell Te. (An alternate description in terms of metal tetrahedra 1–5–6–6 that are more loosely coupled along the chains is more consistent with observed distances but less useful in comparing other structures.) There are no short Te–Te separations so their problematic bonding is not a concern. The metal environments of all tellurium atoms are monocapped trigonal prisms, and Sc–Te distances range between 2.86 and 3.14 Å, less than nearly all d(Sc–Sc).

Generally, the nonmetal:metal ratios in metal-rich compounds seem to be the major factor in determining structure, more overtly than electron counts. Although the similar double metal chains in Sc_7Cl_{10} [= $Sc^{3+}(Sc_6Cl_{10})^{3-}$] are easy to assess in terms of average oxidation state (+1.17), a similar partitioning in the more complex Sc_2Te is not very clear. The double-chain framework described above is further augmented by edge-sharing square pyramids (Sc1,2,3; open bonds in Figure 2) that also share Sc1–Sc1 edges along the double chains. The Sc–Sc distances within these appendages are the same or longer (3.25, 3.32, 3.42 Å), befitting the greater amount of tellurium bound to these atoms. The anion-poorer nature of the present compound also allows closer approaches between the metal building blocks. Finally, the 3.48 Å repeat in the Sc4–Sc4 zig-zag chain is somewhat larger than within the augmented double chain, and closer to what we assign as interchain separations, 3.53(x2) Å for Sc4–Sc6, 3.67 Å for Sc4–Sc1, 3.68 Å for Sc4–Sc2, and beyond. However, all of these are well segregated by overlap populations (below). The larger Sc–Sc separations appear to be attributable to matrix effects and the shortage of bonding electrons.

A novel way to view the Sc_2Te result is as a dissociation product of the metal frameworks in electron-richer chalcogenides of later transition metals with comparable stoichiometries. For example, the metal network in Ta_2Se contains layers of interpenetrating bcc Ta, as in the element,[5] and similar but more condensed frameworks appear in Ti_8S_3[10] and Ti_9Se_2.[1] Related building blocks can also be perceived in Ti_2S, Zr_2S, Zr_2Se (all Ta_2P-type),[11] and Hf_3Te_2.[3] A similar feature can be generated from Sc_2Te if each Sc4 is moved toward Sc6 in the closer chain, extended pairs of condensed Sc4–5–6–1 cubes centered by

Sc6. The Sc2,3 portions may be further fragments of what was once a sheet.

Extended-Hückel calculations have been carried out for the full structure at 48 k-points.[12] The total DOS shows a Te p-orbital-based valence band (with some Sc mixing through covalency) between about −14.0 and −10.8 eV. A large conduction band, Figure 3, is generated almost entirely from Sc 3d orbitals with only traces of Te p in the upper reaches. Six small DOS features between −7.0 and −8.5 eV all originate with the Sc1–5, 1–6, 5–6, 6–6 intracluster bonding interactions. The Fermi energy for such an electron-poor compound falls low in the band near −6.4 eV, while the Sc–Sc COOP functions show that the states remain bonding up to ~−6.0 eV. (In contrast, all bonding states are occupied in Hf_3Te_2.[3]) The compound appropriately exhibits a Pauli-like paramagnetism, $\chi_{M(298)} = 3.4 \times 10^{-4}$ emu mol^{-1}, and is logically presumed to be a metal.

Interesting features of the bonding are revealed by differences in pair-wise Sc–Sc Mulliken overlap populations (MOP) as a function of distance. These emphasize the strength and delocalization of the metal bonding in the double chain region, especially among Sc1, 5, 6, and the contrasting weakness of all bonding about Sc4. In fact, directly following the 0.306–0.172 MOP for the three shortest Sc–Sc separations (Figure 2) are those for the longish Sc1–Sc6 separation across the octahedral waist (3.49 Å, MOP 0.166) and for Sc5–Sc6 between its vertices (not interconnected in Figure 2 for clarity) (3.52 Å, 0.170). Next is that for the shorter Sc5–Sc6 (3.27 Å, 0.146) on the periphery of the chain. These contrasts presumably reflect an enhanced electron concentration and delocalization *within* the chains, and suggest a reason for the marked compression of the octahedra across Sc5–Sc6. Still lower populations order fairly well with increasing distances, including those within the

Sc1, Sc2, Sc3 appendages (0.119–0.069). Another irregularity appears for the Sc6–Sc6 and Sc3–Sc3 interactions along the chain (0.050–0.040), even at 3.92 Å! Finally, the longish 3.48 Å Sc4–Sc4 separations in the zig-zag chains have an MOP of only 0.026, followed by still lower populations for all interchain Sc4–ScX contacts. Thus bonding of Sc4 to all other scandium atoms appears to be weak and not an important part of the stability of this compound. Naturally, Sc4 and Sc2 have, in opposition, the largest Sc–Te overlap populations. A charge flow among the rather different types of scandium atoms from Sc–Sc and Sc–Te bonding is reflected in the relative MOP, largest for Sc6 and Sc1, least for Sc4 and Sc2.

Other highly reduced group-3 chalcogenides of this type are under study, for example, the result of condensation of four chains of edge-sharing octahedra into four-blocks in Sc_9Te_2.[13] A rich and novel chemistry of these chalcogenides is expected by virtue of the conflicts between the electron-poor but metal-rich characteristics.

Experimental Procedures

Sc_2Te_3[8] was prepared by reaction of 2:3 Sc and Te in fused SiO_2 at 900 °C for 72 h. A pressed pellet of Sc_2Te_3 and Sc foil with a Sc_2Te stoichiometry was arc-melted for 20 s per side, sealed into a tantalum tube, and reacted in a vacuum furnace at 1125 °C for 72 h, followed by cooling at 5 °C h^{-1} to 850 °C. The structure was determined from crystals in the product, which was later shown to be single phase Sc_2Te according to its Guinier pattern.[14]

References

[1] T. E. Weirich, A. Simon, R. Pöttgen, *Z. anorg. allg. Chem.* **1996**, *622*, 630

[2] B. Harbrecht, R. Leersch, *J. Alloys Compd.* **1996**, *238*, 13

[3] R. L. Abdon, T. Hughbanks, *Angew. Chem.* **1994**, *106*, 2414; *Angew. Chem. Int. Ed. Engl.* **1994**, *33*, 2328

[4] S.-J. Kim, K.S. Nanjundaswamy, T. Hughbanks, *Inorg. Chem.* **1991**, *30*, 159

[5] B. Harbrecht, *Angew. Chem.* **1989**, *101* 1696; *Angew. Chem. Int. Ed. Engl.* **1989**, *28*, 1660

[6] H. F. Franzen, *Eur. J. Solid State Inorg. Chem.* **1996**, *33*, 197

[7] a) K. R. Poeppelmeier and J. D. Corbett, *Inorg. Chem.* **1977**, *16*, 1107; b) H. Mattausch, J.B. Hendricks, R. Eger, J. D. Corbett, A. Simon, *ibid.* **1980**, *19*, 2128; c) J. D. Martin, J. D. Corbett, *Angew. Chem.* **1995**, *107*, 234; *Angew. Chem. Int. Ed. Engl.* **1995**, *34*, 233

[8] a) A. A. Men'kov, L. N. Komissarova, Ju. P. Simanov, *Dokl. Aka. Nauk. SSSR.* **1961**, *141*, 364; b) J. G. White, J. P. Dismukes, *Inorg. Chem.* **1965**, *4*, 1760

[9] J. D. Corbett, *J. Alloys Compd.* **1995**, *229*, 10

[10] J. P. Owens, H. F. Franzen, *Acta Crystallogr. Sect. B.* **1974**, *30*, 427

[11] H. F. Franzen, L. J. Norrby, *Acta Crystallogr. Sect. B.* **1968**, *B24*, 601

[12] R. Hoffman, *J. Chem. Phys.* **1963**, *39*, 1397; M. Whangbo, R. Hoffman, *J. Am. Chem. Soc.* **1978**, *100*, 6093. Energy parameters for scandium (3d, −6.12; 4s, −6.74; 4p, −3.38 eV) were obtained from charge iterative calculations on the smaller Sc_9Te_2 cell,[13] and tellurium parameters were taken from [4]. Orbital size parameters were all the program default values

[13] P. A. Maggard, J. D. Corbett, *J. Am. Chem. Soc.* **2000**, *122*, 838.

[14] Structure analysis of Sc_2Te: Orthorhombic with space group no. 62, *Pnma*, Z=12, and a = 20.178(5), b = 3.9186(7), c = 10.675(2) Å, V = 844.1(5) Å^3 refined from the Guinier powder pattern (λ = 1.540562 Å, 23 °C); 2229 reflections ($h,k,\pm l$; 2θ <54°) collected on CAD4 diffractometer (Mo $K\alpha$, $\omega-2\theta$, μ = 146.8 cm^{-1}) from a crystal 0.4 x 0.1 x 0.1 mm. The structure was solved by direct methods (SHELXS[15]) and refined with the package TEXSAN.[16] Anisotropic refinement gave $R(F)/R_w$ = 4.3/5.5% with 839 unique reflections ($I_o > 3\sigma_I$) and 56 variables; empirical absorption corrections with the aid of two Ψ-scans and later, after isotropic refinement, DIFABS[17] gave relative transmission coefficients of 0.470 – 1.00 (R_{ave} = 4.2%). The largest e.d residual was 2.5 e/Å^3, 0.79 Å from Te3. Further details of the structural investigation and results may be obtained from J.D.C. or from Fachinformationszentrum Karlsruhe, D-76344, Eggenstein-Leopoldshafen (FRG) on quoting the depository number CSD-406579, the authors, and the journal citation

[15] M. Sheldrick, SHELXS-86. Universität Göttingen, BRD, 1986.

[16] TEXSAN, version 6.0, Molecular Structure Corp., The Woodlands, Texas, 1990

[17] N. Walker, D. Stuart Acta Crystallogr. Sect. A, **1983**, *39*, 158

Supporting Information

Sc_2Te. A Novel Example of Condensed Metal Polyhedra in a Metal-Rich But Relatively Electron-Poor Compound

Paul A. Maggard and John D. Corbett

Table S1. Single Crystal X-ray Data Collection and Refinement Parameters for Sc_2Te.

Formula weight, g mol^{-1}	217.53
Space group, Z	*Pnma* (No. 62), 12
Lattice parameters,[a] Å	
a	20.178(5)
b	3.9186(7)
c	10.675(2)
V, (Å^3)	844.1(5)
d_{calc}, g/cm^3	5.134
Radiation; $2\theta_{max}$	Mo K_α; 54°
Octants measured	h, k, ±l
Temperature, °C	23
Absorp corr. method	psi-scan (2), DIFABS
Relative transmission range	0.470-1.000
μ, cm^{-1} (Mo K_α)	146.8
Reflections measured	2229
observed ($I \geq 3\sigma(I)$)	1654
unique observed	839
$R_{avg\,(I\,\geq\,3\sigma(I))}$, %	4.2
Number of variables	56
Residuals *R*; R_ω,[b] %	4.3; 5.5
Goodness of fit	1.84

[a] Guinier data with Si as an internal standard, λ = 1.540562 Å, 23° C.

[b] $R = \Sigma||F_o|-|F_c||/\Sigma|F_o|$; $R_\omega = [\Sigma\omega(|F_o|-|F_c|)^2/\Sigma\omega(F_o)^2]^{1/2}$, $\omega = 1/\sigma_F^2$.

Table S2. Positional and Isotropic Thermal Parameters for Sc_2Te.

Atom	Position	x	y	z	B_{eq}(Å^2)[a]
Te1	4c	0.07326(6)	0.25000	0.8569(1)	1.1(1)
Te2	4c	0.12603(6)	0.75000	0.2227(1)	0.8(1)
Te3	4c	0.23625(6)	0.75000	0.5302(1)	0.8(1)
Sc1	4c	0.1079(2)	0.75000	0.6606(3)	0.9(1)
Sc2	4c	0.1625(2)	0.75000	0.9638(3)	1.0(1)
Sc3	4c	0.2286(2)	0.25000	0.7457(3)	1.0(1)
Sc4	4c	0.0320(2)	0.25000	0.1204(3)	1.0(1)
Sc5	4c	0.1376(2)	0.25000	0.4307(3)	0.9(1)
Sc6	4c	0.9905(2)	0.25000	0.6078(3)	1.1(1)

[a] $B_{eq} = (8\pi^2/3)\Sigma_i\Sigma_j U_{ij} a_i^* a_j^* \vec{a}_i \vec{a}_j$.

Table S3. U values Å^2 for Sc_2Te.[a]

Atom	U_{11}[b]	U_{22}	U_{33}	U_{13}
Te1	0.0150(7)	0.0148(6)	0.0136(6)	0.0017(5)
Te2	0.0086(6)	0.0125(6)	0.0086(5)	0.0001(4)
Te3	0.0077(6)	0.0113(6)	0.0108(6)	0.0006(4)
Sc1	0.007(2)	0.017(2)	0.011(1)	0.000(1)
Sc2	0.009(2)	0.017(2)	0.010(1)	0.000(1)
Sc3	0.012(2)	0.015(2)	0.009(1)	0.000(1)
Sc4	0.012(2)	0.015(2)	0.013(2)	-0.001(1)
Sc5	0.013(2)	0.012(1)	0.010(1)	-0.001(1)
Sc6	0.009(2)	0.021(2)	0.013(1)	-0.000(1)

[a] U12 = U23 = 0.

[b] $T = \exp[-2\pi^2(U_{11}h^2a^{*2} + U_{22}k^2b^{*2} + U_{33}l^2c^{*2} + 2U_{12}hka^*b^* + 2U_{13}hla^*c^* + 2U_{23}klb^*c^*)]$.

Table S4. Selected Bond Distances in Sc_2Te (Å).[a]

Te1	Sc1	2x	2.952(3)	Sc1	Sc1	2x	3.9186(7)	Sc4	Sc6	2x	3.530(4)
	Sc2	2x	2.896(3)		Sc2		3.419(5)	Sc5	Sc1	2x	3.197(4)
	Sc4	2x	2.900(30		Sc3	2x	3.254(4)		Sc3	2x	3.787(4)
	Sc4		2.934(4)		Sc4		3.669(5)		Sc3		3.831(5)
	Te1	2x	3.919(1)		Sc5	2x	3.197(4)		Sc4		3.938(5)
					Sc6	2x	3.126(4)		Sc5	2x	3.919(1)
Te2	Sc2		2.860(3)	Sc2	Sc1		3.419(5)		Sc6	2x	3.268(4)
	Sc3		2.944(4)		Sc2	2x	3.919(1)		Sc6		3.519(5)
	Sc4	2x	2.938(3)		Sc3	2x	3.322(4)	Sc6	Sc1	2x	3.126(4)
	Sc5	2x	2.971(3)		Sc3		3.726(5)		Sc1		3.486(5)
	Sc6		2.966(4)		Sc4	2x	3.684(4)		Sc4	2x	3.530(4)
	Te2	2x	3.919(1)						Sc5	2x	3.268(4)
	Te3		3.965(2)	Sc3	Sc1	2x	3.254(4)		Sc5		3.519(5)
	Te3	2x	3.973(2)		Sc2	2x	3.322(4)		Sc6	2x	3.047(5)
					Sc2		3.726(5)		Sc6	2x	3.919(1)
Te3	Sc1		2.941(4)		Sc3	2x	3.919(1)				
	Sc2	2x	2.918(3)		Sc5	2x	3.878(4)				
	Sc3	2x	3.026(3)		Sc5		3.831(5)				
	Sc5	2x	2.988(3)								
	Te2		3.965(1)	Sc4	Sc1		3.669(5)				
	Te2	2x	3.973(2)		Sc2	2x	3.684(4)				
	Te3	2x	3.919(2)		Sc4	2x	3.481(6)				
					Sc4	2x	3.919(1)				
					Sc5		3.939(5)				

---

[a] Distances cutoffs: Sc–Sc, Te–Te, 4.0 Å; Sc–Te, 3.1 Å.

Table S5. Sc–Sc Distances and Overlap Populations in Sc_2Te.

Atom 1	Atom 2	Distance (Å)	Overlap population
Sc6	Sc6	3.05	0.366
Sc1	Sc6	3.13	0.228
Sc1	Sc5	3.20	0.172
Sc5	Sc6	3.52[a]	0.170
Sc1	Sc6	3.49[a]	0.166
Sc5	Sc6	3.27	0.146
Sc1	Sc3	3.25	0.119
Sc2	Sc3	3.32	0.087
Sc1	Sc2	3.42	0.069
Sc6	Sc6	3.92[b]	0.050
Sc3	Sc3	3.92[b]	0.040
Sc4	Sc6	3.53[c]	0.035
Sc4	Sc4	3.48	0.026
Sc1	Sc4	3.67[c]	0.025
Sc1	Sc1	3.92[b]	0.021

[a] Across octahedra.
[b] Chain repeat.
[c] Interchain distances.

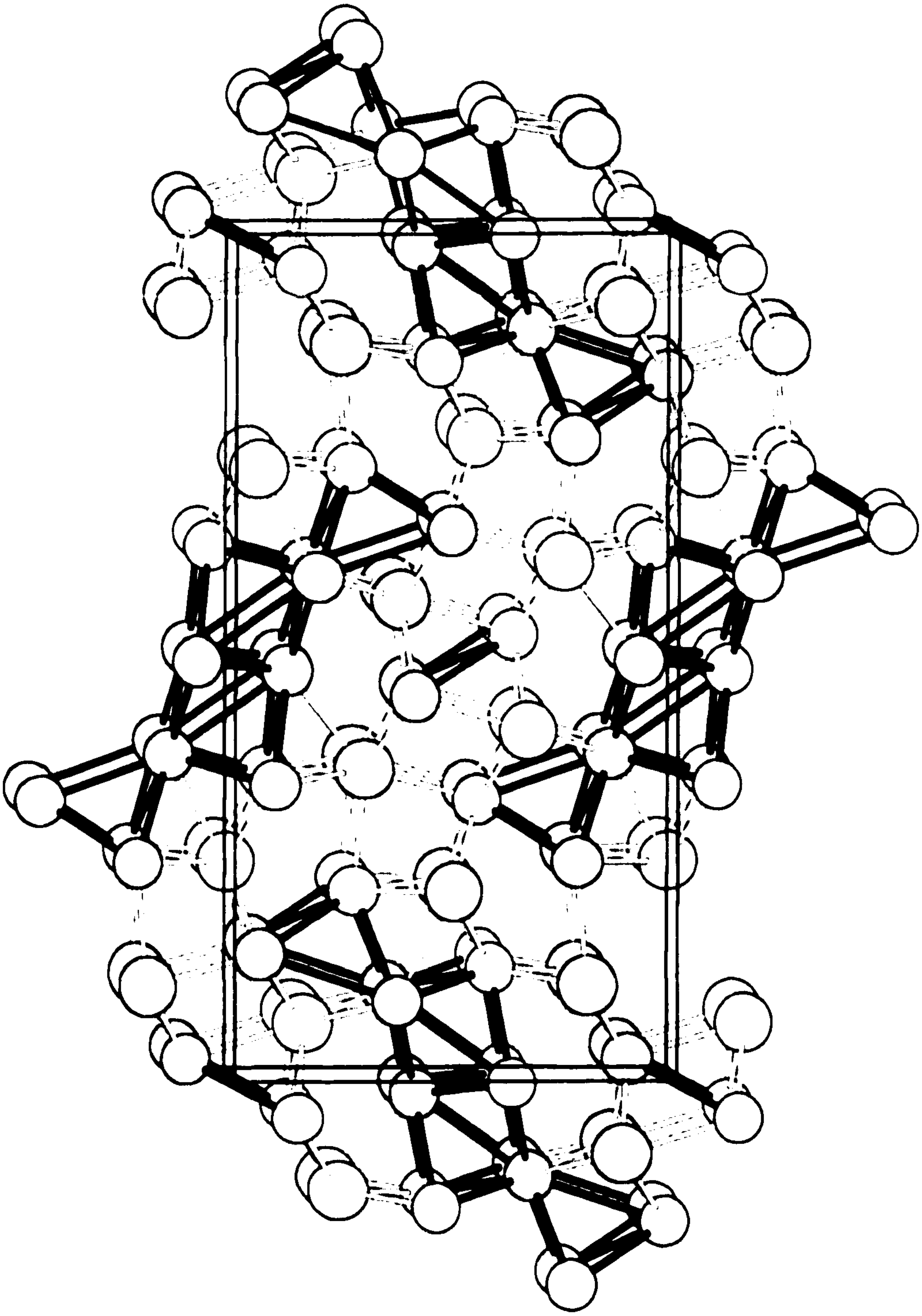

Figure 1. A view of the unit cell of Sc_2Te along [010] (Sc: small circles, Te: large circles). Bonds are drawn for $d(\text{Sc–Sc}) < 3.50$ Å and $d(\text{Sc–Te}) < 3.15$ Å. All atoms lie on mirror planes at $y = 1/4, 3/4$.

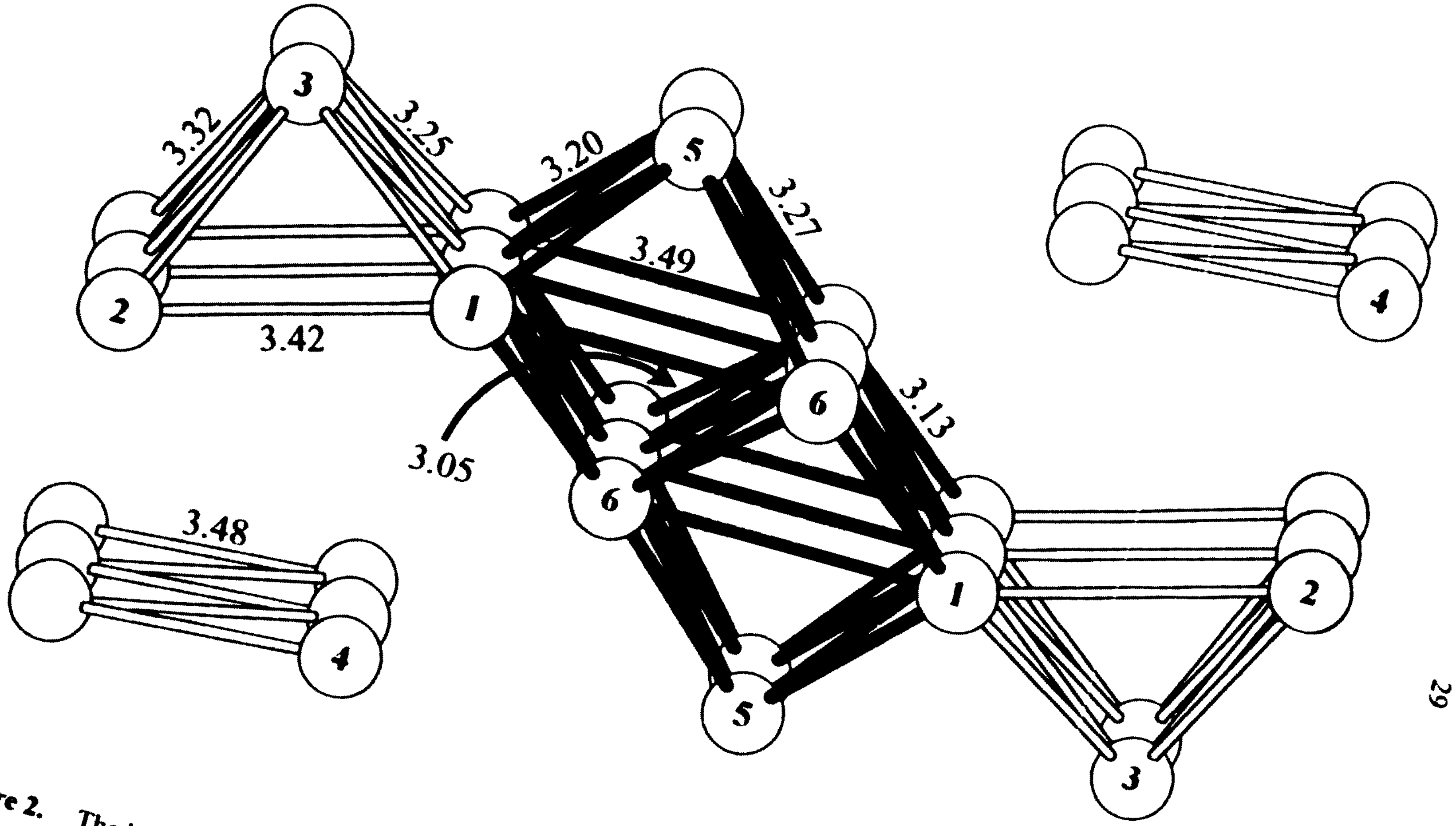

Figure 2. The highly condensed scandium chain and two zigzag chains with atomic labeling and independent distances ($\sigma \leq 0.005$ Å). Inversion centers lie on the Sc6– Sc6 and Sc4– Sc4 bonds.

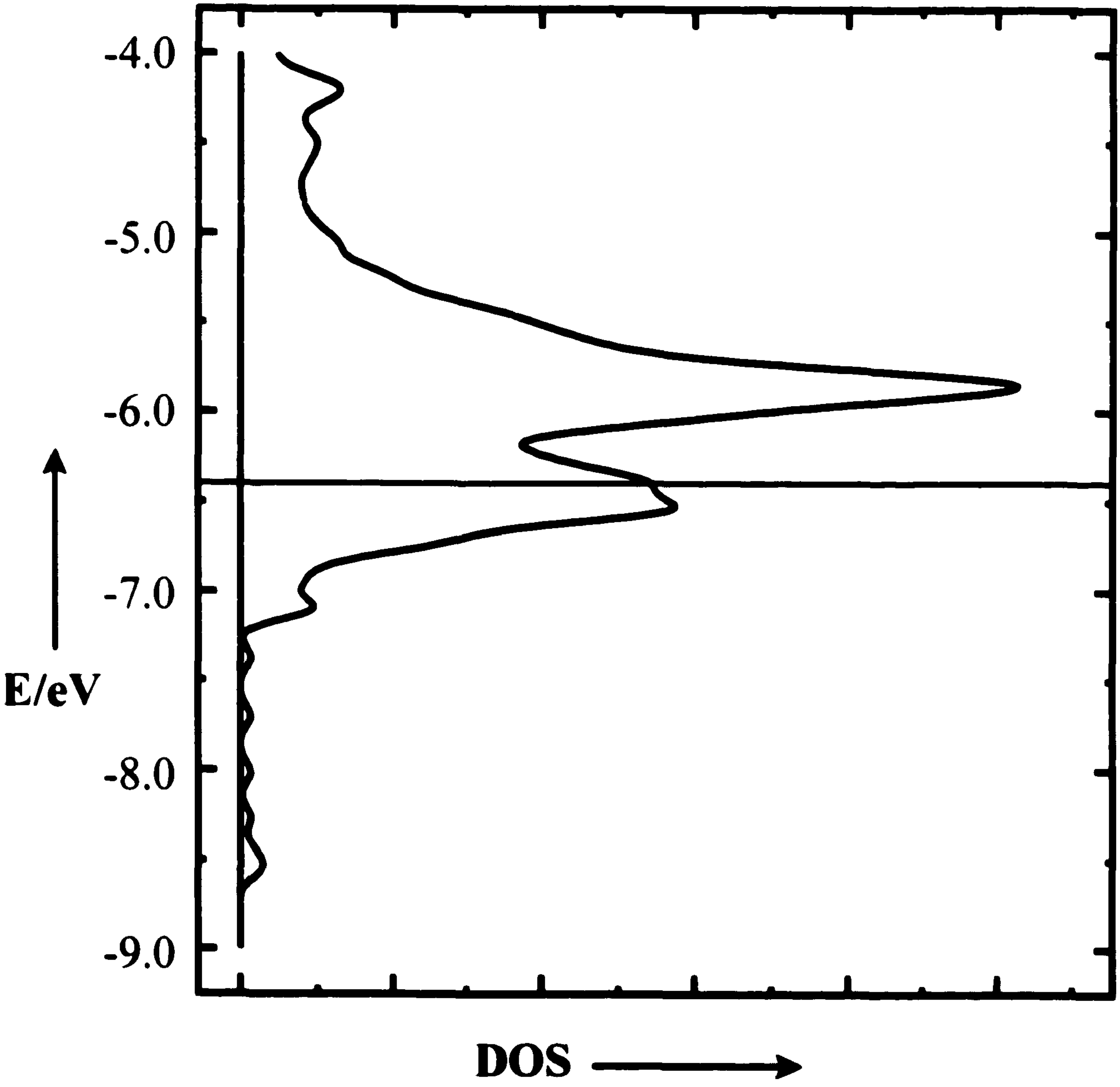

Figure 3. The total densities of states (DOS) for the conduction band in Sc_2Te.

CHAPTER 3. THE SYNTHESIS, STRUCTURE, AND BONDING OF Sc_8Te_3 AND Y_8Te_3. COOPERATIVE MATRIX AND BONDING EFFECTS IN THE SOLID STATE

A paper published in Inorganic Chemistry

Inorg. Chem. **1998**, *37*, 814

Paul A. Maggard and John D. Corbett

Department of Chemistry, Iowa State University, Ames, IA 50011

Abstract

Sc_8Te_3 and Y_8Te_3 have been prepared by high-temperature solid-state techniques. The structures of both were determined from single crystal and powder X-ray diffraction methods to be monoclinic, *C*2/*m* (No. 12) with *Z* = 8. Accurate lattice constants from Guinier powder film techniques at 23 °C are: Sc_8Te_3, a = 28.842(7), b = 3.8517(6), c = 22.352 (5) Å, β = 122.51(2)°; Y_8Te_3, a = 31.153(7), b = 4.0703(4), c = 24.375(5) Å, β = 122.80(2)°. The layered structure of the title compounds consists of a complex network of chains of trans-edge-sharing metal octahedra condensed into two types of corrugated sheets that are separated by tellurium. In terms of metal-metal bonding (as judged by overlap populations), the isotypic Ti_8S_3 and Ti_8Se_3 are more 3D in aggregation, while these scandium and yttrium tellurides are 2D. This difference in dimensionality is attributed to the cooperative effects of increased anion size and decreased valence electron concentration. This is described in detail for Sc_8Te_3. Contrasting paramagnetic properties are reported for the two, Pauli-like for Y_8Te_3 and temperature-dependent for Sc_8Te_3, in parallel with the behaviors of the parent

metals.

Introduction

The study of reduced chalcogenides of the early transition metals has led to a great variety of new chemistry and to a broader understanding of the bonding in solids. Examples of reduced group 4 chalcogenides include, but are not limited to, Ti_8Z_3[1,2] and Ti_2Z,[3,4] (Z=S,Se), $Ti_{11}Se_4$,[5] Ti_9Se_2,[6] Hf_2Te,[7] Hf_3Te_2,[8] Hf_2Se_3,[9] and Zr_3Te.[10] While the metal-rich chalcogenides of groups 4 and 5 transition metals have been heavily explored, those of the group 3 transition elements are almost unknown, the only example being the recently discovered Sc_2Te with a complex chain structure for scandium.[11] Examination of the literature for the Sc–Te and Y–Te binary systems reveals no investigations into the metal-rich parts of either, and the most reduced compounds reported in both systems are R_2Te_3 and RTe (R = Sc, Y).[12,13] This paper describes the first metal-rich yttrium chalcogenide, Y_8Te_3, and the isotypic Sc_8Te_3.

To a chemist, "understanding" a structure usually means justifying its existence and stability. For reduced chalcogenides of the early transition metals, this may mean only a conclusion that the distances and apparent bonding in the structure are "reasonable". The problem is how to justify, or understand, the relative stability of one unremarkable phase in a binary system that has a few electrons holding together a metal fragment with little to no discernible preference for electron counts or directional bonding. For reduced chalcogenides, innumerable structures may seem reasonable, but there is no delineation between an imaginary and an actual structure. Articles have provided theories justifying the existence of some particular reduced chalcogenide relative to known structural alternatives and the elements. Recently, the valence electron concentration together with the cohesive energy of the metal was used to rationalize the existence and structure type of Hf_2Te (Nb_2Se type).[7] Alternatively, the stabilities of Ti_2S and Ti_8S_3 were attributed to the enhanced efficiency of both metal-metal and nonmetal-metal bonding in each compared with those in the pure metal and TiS.[14]

Clearly, atom sizes, valence electron concentrations, and the metal-to-nonmetal proportions play key roles in the determination of structure features and types. The structural features seen in transition-metal-rich chalcogenides are predominantly condensed body-centered cubes or distorted octahedra. With the discovery of more reduced chalcogenides of the earliest transition metals, new insights into stability may be gained about the interplay of the above three variables and how they influence the structural features seen in more electron-rich systems, Ti_8S_3 and Ti_8Se_3 in particular. No thorough analysis of the structure and bonding features in these titanium compounds has appeared, however. Some analysis of "where the electrons are" and of the interplay of matrix and bonding effects may be found in the results of extended Hückel calculations. The new Sc_8Te_3 and Y_8Te_3 are significant in that they represent the electron-poorest, yet among the most metal-rich chalcogenides of the transition metals reported to date.

Experimental Section

Synthesis. All materials were handled in He-filled or N_2-filled gloveboxes to reduce contamination by "adventitious" impurities. The syntheses of both Sc_8Te_3 and Y_8Te_3 began with the preparation of the corresponding Sc_2Te_3 and Y_2Te_3 phases (NaCl-type with disordered cation vacancies). The elements were used as received (Sc turnings, 99.7%, Aldrich; Y sheet 99.8%, Alfa; Te powder, 99.99%, Aldrich) and were loaded in a 2:3 stoichiometry into a fused silica container. The fused silica container was evacuated, sealed off, and heated to 450 °C for 12 h, then to 900 °C for 72 h. The sample was allowed to cool radiatively to room temperature. Guinier film data confirmed the products were the R_2Te_3, NaCl-type phases. Appropriate amounts of these and scandium or yttrium metal to give the 8:3 stoichiometry were then pelletized inside a He-filled glovebox with the aid of a hydraulic press. The resulting pellets were arc-melted for 20 seconds per side with a current of 70 amps. Guinier patterns of the products at this point revealed a mixture of Sc_9Te_2[15] and Sc_2Te for the scandium reaction and a blurred pattern similar to that of Y_8Te_3 for the yttrium reaction. Each sample was then sealed inside tantalum tubing, annealed at 1150 °C for 72 hours, and allowed to radiatively cool. It should be noted that annealing temperatures 10–20 °C still higher resulted in reaction of the scandium products with the tantalum, and subsequent failure of the tubing. After annealing, Guinier powder diffraction film data showed that both Sc_8Te_3 and Y_8Te_3 had been obtained in apparently quantitative yields (single phase).

Powder X-ray Diffraction. The powder diffraction patterns of Sc_8Te_3 and Y_8Te_3 were obtained with the aid of an Enraf-Nonius Guinier powder camera and monochromatic Cu $K\alpha_1$ radiation. The samples were crushed into powder form, mixed with standard silicon (NIST), and placed between two strips of Scotch-brand tape on a frame for mounting on the camera rotation motor. Lattice parameters were obtained by least squares from 35 measured and indexed lines per sample. The lattice parameters are given in Table 1 along with those for the two titanium analogues for comparison.

Single Crystal Diffraction. Several black, irregularly shaped crystals were obtained from both the scandium and yttrium reactions. All crystals were mounted inside 0.3 mm i.d. glass capillaries that were sealed off and mounted on metal pins. Their crystal quality was checked by means of Laue photographs, and the best crystal from each group selected. A data set for the Sc_8Te_3 phase was collected on a CAD4 diffractometer (Mo $K\alpha_1$ radiation) at room temperature. Twenty-five centered reflections gathered from a random search were used to determine provisional lattice constants and the crystal system. Half a sphere of data was collected (h, $\pm k$, $\pm l$), and these were subsequently corrected for Lorentz and polarization effects. The data were further corrected for absorption with the aid of two averaged ψ-scans. Of 4310 measured reflections ($2\theta \leq 50°$), 2233 had $I > 3\sigma(I)$, and 1356 of these were unique. Extinction conditions suggested the possible space groups $C2$, Cm, and $C2/m$. Because the intensity statistics indicated a centrosymmetric space group, the structure was solved by direct methods (SHELXS[16]) and refined with the package TEXSAN in $C2/m$.[17] Subsequent refinements in the acentric space groups did not yield lower residuals or improved parameters. After isotropic refinement, the data were better corrected for absorption with respect to the third dimension of the crystal by means of DIFABS[18] and then averaged with R_{ave}= 9.0%. The final refinement converged at $R(F)/R_w$ = 3.7/3.7% for the loaded composition Sc_8Te_3. Selected crystallographic data, atomic positions, and isotropic-equivalent temperature factors are given in Tables 2 and 3. Additional data collection and refinement parameters, the anisotropic displacement parameters, and a complete distance list are in the Supporting Information. These, as well as the F_o/F_c listing, are also available from J.D.C.

The diffracting powers of the scandium crystals were in all cases much better than for the Y_8Te_3 crystals. A data set collected on the best diffractor among the yttrium crystals gave only ~20% observed reflections. The structure could be refined isotropically to $R_w < 8\%$ as isostructural with Sc_8Te_3, but the number of observed data were generally insufficient and these were very weak. Nonetheless, the atomic positions found and the observed X-ray powder diagrams made it clear that Y_8Te_3 has the same structure as Sc_8Te_3.

The unit cell choice for Table 3 needs to be made clear. We have retained the origin as reported for the original Ti_8S_3[1] (the center of the Sc16–Sc16 bond) but have transformed the cell to give the preferred cell with the smaller (obtuse) β angle. The later report on Ti_8Se_3 [2] has the same cell but with the origin displaced from ours by $c/2$.

Properties. Powdered samples of ~50mg of Sc_8Te_3 and Y_8Te_3 were each loaded inside a He-filled glovebox so that they were sandwiched between two glass rods inside a 3 mm i.d. fused silica tube. Magnetizations for the samples were measured from 6 to 300 K in a field of 3 T with the aid of a Quantum Design MPMS SQUID magnetometer. The data were corrected for diamagnetism of both the sample holder and atom cores. Resistivities of powdered, sized samples of ~50 mg of Sc_8Te_3 and Y_8Te_3 diluted with Al_2O_3 were each measured with a "Q" apparatus between 100 and 300 K.

Band Calculations. Extended Hückel calculations were carried out within the tight-binding approximation[19] for the full structure of Sc_8Te_3 at 32 k-points spread out over the irreducible wedge. H_{ii} parameters employed were the same as the charge-iterated values obtained previously for Sc_2Te[11] (in eV): Sc: 4s, -6.75; 4p, -3.38; 3d, -6.12; Te: 6s, -21.20; 6p, -12.00.

Results and Discussion

Structural Description. A near-[010] section of the Sc_8Te_3 structure down the short (3.85 Å) *b* axis is given in Figure 1. Evident are two separate and independent corrugated chains of scandium atoms along $\vec{a}$ that are separated by tellurium atoms along $\vec{c}$. The scandium atoms are further bonded down the short projection axis into layers (not shown). The shortest distance between the corrugated sheets is the 3.69 Å marked for Sc10–Sc14, which will be shown to be a nonbonding interaction. The Sc–Sc distances within these chains vary semi-continuously from 3.00 Å to 3.48 Å, as shown in Table 4 and marked separately on Figure 2. There are no distinctive breaks in this range, and the next larger value, 3.67 Å, is a fairly special interaction. This length trend is quite similar to that observed in Sc_2Te. The scandium–scandium distance limit in drawing bonds in the Figures has been set at 3.5 Å, in correspondence with the analysis of Sc_2Te and as likewise justified later in terms of overlap populations. The observed (12-bonded) and calculated single bond metallic distances for the pure metal are 3.24 Å and 2.88 Å,[20] so the observations for Sc_8Te_3 pertain to relatively electron-poor delocalized bonding.

Both corrugated sheets contain structural building blocks that are grossly similar to those in the isostructural Ti_8S_3 and Ti_8Se_3. The structure of Ti_8S_3 was described in terms of condensed body-centered-cubes,[1] while the structural features in Ti_8Se_3 were described as condensed, distorted octahedra.[2] Preference will be given to the condensed, distorted octahedra description here, with some mention of the body-centered-cubic features when appropriate. In the less condensed chain or sheet, Figure 2A, two main scandium units are evident, an infinite trans-edge-sharing chain of single octahedra (Sc5 and Sc6) and four infinite trans-edge-sharing chains of octahedra condensed through sharing of six side edges (not faces). (Such condensation, but only of a pair of chains, was first observed in Sc_7Cl_{10}.[21]) The quadruple chain is called the Z unit from here on (Sc3, Sc9, Sc11, Sc13, Sc15). The Z unit is also clearly two interpenetrating body-centered cubes centered by Sc15, e.g., Sc9, 11, 15, 13. The single edge-sharing octahedral chain has the shortest distance among the shared edges (Sc5–Sc5, 3.09 Å), and longer apex distances for the non-shared edges (Sc5–Sc6, 3.20 Å, 3.27 Å). The vertex–vertex distance, Sc6–Sc6, is correspondingly large. The Z unit likewise has the shortest distances among the shared edges of different octahedral chains (Sc15–Sc15, 3.00 Å; Sc13–Sc15, 3.14 Å), and longer distances among the outside (nonshared) and inside trans edges of the chains (3.14 Å – 3.43 Å). It is not by chance that the shorter scandium distances in the sheet are those furthest from the tellurium positions. The Z units and the single octahedral chains are connected via the lone Sc14 atoms (Sc5–Sc14, 3.35 Å; Sc9–Sc14, 3.30 Å) to generate the sheet, or puckered layer, but these are very weak bonds (below).

The repeating unit in the other more condensed corrugated sheet is shown in Figure 2B. The same Z unit can be discerned in the middle of the figure (Sc1, 2, 7, 8, 10). But this unit is now further condensed on both ends through two fairly short edges (Sc1–Sc7, 3.12 Å) to strings of three octahedral chains that share vertices internally. This assembly, repeated down the b-axis, generates the second puckered layer or sheet with more Sc–Sc bonding, shorter distances and, presumably, tighter bonding than the first one. Again, the shortest distances occur in the shared edges of different octahedral chains of higher connectivity (Sc8–Sc8, 3.06 Å, Sc8–Sc10, 3.11 Å, Sc1–Sc7, 3.12 Å), with the longer scandium distances around the periphery, as before (3.12 Å – 3.48 Å). The unique octahedral chain that does not share vertices, only waist atoms (Sc4, 16 in 2B), is more squashed and has a relatively shorter vertex–vertex distance (3.67 Å) and stronger bonding therewith (below). The sheet in 2B also has more body centered fragments, those centered by Sc8 and (distorted) Sc16. The characteristic body-centered cubic fragments are more pronounced in Sc_8Te_3 than in the electron-poorer Sc_2Te, and are even more pronounced in most of the electron-richer, metal-rich chalcogenides of the group 4 and 5 metals.

It should be noted that the relative cell dimensions and various modes of condensation seen in Figure 2 mean there are a wide variety of distances and distortions from idealized condensed octahedra. These occur particularly because of the long $\bar{b}$ repeat in the waist of all of the octahedra (3.85 Å) relative to the imagined shared trans edges near 3.30 Å. Thus the average scandium octahedron is also compressed along the vertex–vertex direction by about 0.4 Å relative to the ideal model. These differences are further compounded by the marked shortening of most of the side edges that are shared between octahedral chains. Notwithstanding, the octahedral units still remain the best overall descriptors for these structures.

All tellurium atoms in Sc_8Te_3 are surrounded by trigonal prisms of metal on which the rectangular faces are further capped one to three times by more scandium. The Sc–Te distances vary only from 2.91 to 3.01 Å. All Te–Te distances are ≥ 3.83 Å, and so Te–Te bonding is not a significant concern.

Although a good quality data crystal could not be found for Y_8Te_3, it is clearly isostructural with Sc_8Te_3. The change in the metal causes a shift to larger lattice constants (Table 1) and therefore longer metal–metal distances, by 0.25 to 0.40 Å or to ~10% greater than in Sc_8Te_3. The bonding trends and features in Sc_8Te_3 are equally valid for Y_8Te_3 save for one important feature, a changed size differentiation between R and Te in what can be called a matrix effect (below).

Calculations. Figure 3 shows the total DOS (densities of states) for Sc_8Te_3. The Fermi level (solid line) lies in a valley between two smallish peaks in a region that is dominated by scandium d orbital contributions; hence the solid is metallic. The dashed line is the projection of tellurium contributions, which are significant only in the upper energy levels, well above E_F. Figure 4 shows the COOP (crystal orbital overlap population) curve for the total Sc-Sc bonding in Sc_8Te_3. As in Sc_2Te, many metal-metal bonding states above E_F remain unoccupied. Two small peaks in the DOS around the Fermi level are both Sc-Sc bonding while the largest peak above them (-5.9 eV) is a mixture of nonbonding and antibonding states. As seen before in Sc_2Te, the interesting array of small peaks in the DOS at -7.0 eV and below arise from specific Sc-Sc interactions at shorter and shorter distances.

Such a complex structure as this provides a wide variety of distances and, presumably, bond strengths that need to be sorted out. Distances alone, although often taken to somehow vary inversely with the strength of the interactions, can be very misleading when these are determined largely or solely by matrix effects, that is, by just the contact sizes of the packed units. Examples can be clearly seen in Sc_2Te.[11] The interlayer (sheet) distances in the present structure, Sc10-Sc14 for example (Figure 1), are certainly of this character as these are established principally by the size of tellurium, with vanishingly small evidence of bonding according to the overlap population sum (OP) up to E_F for each atom pair.

For these purposes, pairwise overlap populations are used in Table 4 as the basis for ordering the listed distances. As expected, the overlap populations generally correlate with the bond distances, but there are some significant deviations that reflect important bonding details. The six largest overlap populations are associated by and large with the six shortest distances. One is the shared Sc5–Sc5 edge in the nearly isolated octahedral chain, but the other five short distances and large overlap populations pertain to the shared interior edges between octahedral chains (Sc pairs 15–15, 8–8, 8–10, 1–7, 13–15) at 3.00 – 3.14 Å. As found with Sc_2Te, the theme is that electrons are concentrated within the condensed units and thereby give rise to higher overlap populations. (Use of these pairwise measure may still leave delocalized (multicenter) bonding underappreciated.) In contrast, the outer regions of these, where scandium has fewer like and more tellurium neighbors, have low overlap populations relative to the distances. In the first category are the longer shared-waist distances that have relative high populations, namely atom pairs 1–10, 1-12, 2-8, 9–13 and 11–15 at 3.26 – 3.34 Å with OP values of 0.171 to 0.263. In contrast, the pair populations for the distances around the outside of the condensed units have low OP's relative to the distances, viz., 3–9, 3–13, 9–15 and 11–13 in Fig. 2A and 1–16, 2–8, 2–10, 4–16 (×2), 7–10 and 12–16 in Fig. 2B. Unshared trans vertices in octahedra give rise to relatively high OP's and short bonds, i.e., about Sc6 in the lone single chain (2A) and for the trans Sc4–Sc4 pair (2B), where a long 3.67 Å separation in the latter has an OP value of 0.141. The last is the only contradiction to the 3.50 Å upper limit used for bonds in the figures. The single octahedral chain of Sc5 and Sc6 is relatively isolated since the overlap populations for the "bonds" to the bridging Sc14 are only 0.04 and 0.05. Of course, significant bonding along *b*, the 3.85 Å projection axis, is expected for what is described as a 2D corrugated sheet structure, and 10 of the 16 Sc_i–Sc_i overlap populations are large enough to appear in Table 4.

Evidence that electrons are preferentially delocalized within the aggregated cluster sheets while being removed from the outlying Sc atoms with more Te neighbors is a recurrent theme. The shortest interlayer distance, 3.69 Å for Sc10–Sc14 in Figure 1, has an overlap population of only ca. 5×10^{-4}! Interactions between filled, low lying tellurium orbitals with higher lying orbitals on nearest neighbor scandium atoms have the effect of pushing the latter even higher in energy, so that they do not interact and bond as well with interior scandium atoms. Drawing bonds in this structure based only on distances is misleading. In a relatively electron-poor but metal-rich system, geometry, efficient packing, and stoichiometry dictate that some metal atoms must be packed close together even if there are no electrons for their bonding. Thus, scandium pairs such as 9–14 and 5–14 with small OP's are held together not by bonding electrons, but through common electrostatic and covalent interactions with their anionic tellurium neighbors. This is similar to the way in which lithium atoms in LiF are held close by surrounding fluorine atoms, and the zig-zag scandium chain in Sc_2Te, by surrounding tellurium atoms. In other words, these group 3 chalcogenides all illustrate how matrix effects, dictated by simple geometry and efficient packing considerations, cooperate with the "electronics" or bonding within the solid to generate stable phases in a relatively electron-poor system. While the overlap populations should in the simplest cases correlate with distances (and Pauling bond orders), both the positions of the "bonds" relative to the metal aggregate and the number of anion neighbors have a considerable effect on the actual overlap between a particular pair of metal atoms. In Sc_8Te_3 and Sc_2Te, the scandium bonding is primarily within and between the trans-edge sharing octahedra chains, while the outlying scandium atoms are held together more by a cooperative network of tellurium atoms.

Property Measurements. Because of the nature of the metal-metal bonding and the sizable densities of states at E_F from extended Hückel calculations, both Sc_8Te_3 and Y_8Te_3 are expected to be metallic and Pauli-paramagnetic. High frequency measurements of resistivities of the polycrystalline R_8Te_3 phases over 100–300 K showed that both are metallic, but rather different. The resistivity of Sc_8Te_3 is ~143 μΩ.cm at 298 K, 2.5 times that of the metal,[22] with a temperature dependence of 0.16% K^{-1}, while that for Y_8Te_3 is 226 μΩ.cm, 3.8 times that of the metal[22] and with a variation of 0.39% K^{-1}. Both reflect the higher anisotropy of the binary structure type. The magnetic differences are also sizable. Figure 5 shows that Y_8Te_3 exhibits a Pauli-like, temperature-independent paramagnetism of about 1.25×10^{-3} emu mol−1, seven times that for pure yttrium metal, which is ~1.8×10^{-4} emu mol^{-1} and also temperature-independent.[23] The ratio of susceptibilities is roughly proportional to the 8:1 molar ratio of yttrium atoms in the two. Although nonmagnetic impurities in yttrium metal (such as oxygen or hydrogen) are reported to reduce the magnetic susceptibility,[23] the large structural change for Y_8Te_3 makes improbable its interpretation as essentially yttrium metal with tellurium as an impurity. The substantial rearrangement and changed bonding still appears to give about the same DOS at E_F judging from the susceptibility data, and then perhaps a similar number of conduction electrons, but this is not reflected in the resistivity results, perhaps because of the higher anisotropy. In further contrast, Sc_8Te_3 exhibits a quite different and more complex paramagnetic behavior, Figure 6A, with an appreciable temperature dependence. The effective moment vs. temperature is shown in Figure 6B. The data cannot be fit well by a simple nonlinear least squares function that includes Curie-Weiss and van Vleck-like terms. Pure scandium metal over ~70–300 K shows a smaller temperature dependence.[22] Although the earlier data have been described with a Curie-Weiss fit, $\mu_{eff} = 1.65\ \mu_B$, $\theta \sim -850$ K, this is not a realistic treatment. The 25% increase observed in the scandium metal susceptibility between 300 (2.95×10^{-4} emu mol^{-1}) and 75 K could well arise from a temperature dependence of the density of states at E_F and thence of the observed χ_P. In fact, band calculations for scandium show a large peak at E_F.[24] The situation with Sc_8Te_3 is clearly not so simple. The room temperature value per scandium in Sc_8Te_3 is about one-fourth of that of the metal, and the temperature dependence, nearly five times greater. This may represent intermediate interactions in which itinerant electrons gain small orbital contributions at particular cores.[25] With 16 unique Sc atoms in this structure, the possibilities are large, and the answer, probably complex.

Structural Comparisons. Although Sc_8Te_3 and Y_8Te_3 are isotypic with both Ti_8S_3 and Ti_8Se_3, and the four structures do share approximately the same atomic positions, there are many differences in these relatively complex arrangements. The metal–metal bonding within the group 3 chalcogenides occurs in essentially 2D corrugated sheets, as judged by both distances and overlap populations, but the titanium examples differ appreciably in the number of metal-based electrons and the size of the chalcogen spacers. Figure 7, shows an equivalent [010] view of the Ti_8S_3 structure, with the two corrugated sheets in this structure labeled A and B in analogy to Figure 2 and "bonds" drawn out to a limit of 3.2 Å. The intrasheet Ti–Ti distances in the sulfide range from 2.71 Å upward, with an average of 2.99 Å. To further aid the comparison, the metal–metal bonds marked in Figure 2 are shown as solid lines here, while any additional "bonds" are drawn as open connections. To make clear that the cutoff is not arbitrarily influencing the conclusion, an extended Hückel calculation and analysis on Ti_8S_3 was used to verify that 3.2 Å is a suitable limit for good bonding, as 3.5 Å is in Table 4.

Although the gross features of the corrugated sheets in Ti_8S_3, Figure 7, are the same as with Sc_8Te_3, Figure 2, there are in detail two significant differences. First, reflecting the greater number of valence electrons is the generally greater condensation and increase in

Ti–Ti bonding. Particularly chain A, Figure 7, is seen to contain many more "bonds" than does Figure 2A. The chain is internally more kinked and condensed, i.e., between the equivalent of atoms 5–9, 6–11 and 9–11 in Figure 2A. Two octahedral chains are also more squashed, and the trans-edge distances fall above the bond distance limit (11–15). The already more condensed chain B is less changed, but has gained an additional 2–4 crosslink. Second and most important, distinctly more close contacts occur between the titanium sheets, from 3.15 Å down to a quite short 2.93 Å in what appears to be a more 3D metal–metal bonded structure. The decreased anion size ensures more close contacts between the sheets, and the system appears to react cooperatively to the additional electrons from titanium with more bonding, especially interchain and in chain A. Thus, cooperative effects of decreased anion size, increased valence electron concentration, and the resulting shorter metal–metal distances stabilize this flexible structure. What seems to be enlightening is that the analogous Ti_8Te_3, Sc_8S_3, or Y_8S_3 with different size proportions have not been found, although this may result at least in part from inadequate efforts. The overall picture suggests there may be some kind of "magic" electron count needed to stabilize each structure, its features, or simply, the number of metal–metal bonds in a metal-rich compound. Electron count alone as a stability factor in metal-rich phases is perhaps less definite because of the delocalized bonding, while matrix effects are also a major factor.

Conclusions. The isotypic Sc_8Te_3 and Y_8Te_3 are significant in that they represent the electron-poorest, but yet the metal-richest chalcogenides reported for the early transition metals. Their chemistry relative to those of other early transition metal chalcogenides such as Ti_8Ch_3 provides insight regarding the bonding and existence of this novel structure type. Extended Hückel calculations help one to roughly "locate" the electrons in the solid and also allow one to assess the cooperative effects of anion size, cation positions, and valence electron concentration. Although Sc_8Te_3 and Y_8Te_3 exist in the same structure type as the sulfide and selenide of their electron-richer neighbor titanium, there are clear differences with the increased anion size, fewer elections, and larger metal distances in the former. This suggests a particular but flexible electron count or valence electron concentration is necessary to stabilize what is also a flexible structure. Magnetic susceptibility measurements on both compounds show quite different results, but more similar to the differences in the pure metals themselves.

Acknowledgements

The authors thank Jerry Ostensen for the magnetic measurements, and Len Thomas for upkeep of the single crystal diffractometer. This work was supported by the National Science Foundation, Solid State Chemistry, via grant DMR-9510278 and was carried out in the facilities of the Ames Laboratory, U.S. Department of Energy.

Supporting Information Available

Tables of additional crystallographic and refinement parameters, anisotropic thermal parameters, and a complete listing of nearest-neighbor distances in Sc_8Te_3 (4 pages). Ordering instructions are given on any current masthead page.

References

(1) Owens, J. P.; Franzen, H. F. *Acta Cryst.* **1974**, *B30*, 427.

(2) Weirich, T. E.; Pöttgen, R.; Simon, A. *Z. Kristallogr.* **1996**, *211*, 929.

(3) Owens, J. P.; Conard, B. R.; Franzen, H.F. *Acta Cryst.* **1967**, *23*, 77.

(4) Weirich, T. E.; Pöttgen, R.; Simon, A. *Z. Kristallogr.* **1996**, *211*, 928.

(5) Weirich, T. E.; Ramlau, R.; Simon, A.; Hovmöller, S.; Zou, X. *Nature*. **1996**, *382*, 144.

(6) Weirich, T. E.; Simon, A.; Pöttgen, R. *Z. Anorg. Allg. Chem.* **1996**, *622*, 630.

(7) Harbrecht, B.; Conrad, M.; Degen, T.; Herbertz, R. *J. Alloys Compd.* **1997**, *255*, 178.

(8) Abdon, R. L.; Hughbanks, T. *Angew. Chem. Int. Ed. Engl.* **1994**, *106*, 2414.

(9) Schewe-Miller, I. M.; Young, Y. G. *J. Alloys Compd.* **1994**, *216*, 113.

(10) Harbrecht, B.; Leersch, R. *J. Alloys Compd.* **1996**, *238*, 13.

(11) Maggard, P. M.; Corbett, J. D. *Angew. Chem., Int. Ed. Engl.* **1997**, *36*, 1974.

(12) a) Men'kov, A. A.; Komissarova, L. N.; Simonav, Ju.P. *Dokl. Aka.* Nauk. *SSSR*. **1961**, *141*, 364; b) White, J. G.; Dismukes, J. P. *Inorg. Chem.* **1965**, *4*, 1760.

(13) Dismukes, J. P.; White, J. G. *Inorg. Chem.* **1965**, *4*, 970.

(14) Franzen, H. F. *Proc. 50th Anniv. Conf. Korean Chem. Soc.* **1996**, p. 635.

(15) Maggard, P.; Corbett, J. D., unpublished research (Sc_9Te_2)

(16) Sheldrick, M. SHELXS-86. Universität Göttingen, Germany, 1986.

(17) TEXSAN, version 6.0, Molecular Structure Corp., The Woodlands, Texas, 1990.

(18) Walker, N.; Stuart, D. *Acta Crystallogr. Sect. A*. **1983**, *39*, 158.

(19) Hoffman, R. *J. Chem. Phys.* **1963**, *39*, 1397; Whangbo, M.; Hoffman, R. *J. Am. Chem. Soc.* **1978**, *100*, 6093.

(20) Pauling, L. *The Nature of the Chemical Bond*; Cornell University Press: Ithaca, NY, 1960, p. 400.

(21) Hwu, S.-J.; Corbett, J. D.; Poeppelmeier, K. F. *J. Solid State Chem.* **1985**, *57*, 43.

(22) Spedding, F. H.; Croat, J. J. *J. Chem. Phys.* **1973**, *58*, 5514.

(23) Spedding, F. H.; Croat, J. J. *J. Chem. Phys.* **1973**, *59*, 2451.

(24) Theisen, C. M. Ph.D. Dissertation, Iowa State University, 1983; Harmon, B. N. private communication.

(25) Jiles, D. *Introduction of Magnetism and Magnetic Materials*, 2nd ed. 1998; Chapman & Hall: London, p. 316.

Table 1. Comparison of lattice parameters (Å, deg) and cell volumes (Å^3) for known M_8Ch_3 phases (Ch=S, Se, Te).

Compound	*a*	*b*	*c*	*β*	*V*
Ti_8S_3[a]	25.13(1)	3.327(2)	19.36(2)	123.1(5)	1356(7)
Ti_8Se_3[b]	25.562(4)	3.4411(5)	19.701(6)	122.25(1)	1466(1)
Sc_8Te_3[c]	28.842(7)	3.8517(6)	22.352(5)	122.51(2)	2094(2)
Y_8Te_3[c]	31.153(7)	4.0703(4)	24.375(5)	122.80(2)	2598(2)

[a] Ref. 1, converted to the same setting as for Sc_8Te_3.

[b] Ref. 2.

[c] For λ = 1.540562 Å, 23 °C, space group *C*2/*m*.

Table 2. Selected crystal and refinement data for Sc_8Te_3.[a]

Form. wt.	742.45
Space group, Z	$C2/m$ (No. 12), 8
d_{calc}, g cm^{-3}	4.710
μ(Mo Kα), cm^{-1}	130.4
rel. transm. coeff. range	0.832–1.00
R, R_w,[b] %	3.7, 3.7

[a] Lattice dimensions in Table 1.

[b] $R = \Sigma||F_o| - |F_c||/\Sigma|F_o|$; $R_w = [\Sigma w(|F_o| - |F_c|)^2/\Sigma w(F_o)^2]^{1/2}$; $w = 1/\sigma_F^2$.

Table 3. Positional and Isotropic Thermal Parameters for Sc_8Te_3.[a]

Atom	x	z	$B_{eq}(Å^2)$[b]
Te1	0.74108(6)	0.2799(1)	0.76(5)
Te2	0.89524(6)	0.3142(1)	0.72(6)
Te3	0.05620(6)	0.8265(1)	0.80(6)
Te4	0.42614(6)	0.8074(1)	0.72(6)
Te5	0.86962(6)	0.9628(1)	0.85(6)
Te6	0.86855(6)	0.4690(1)	0.77(6)
Sc1	0.4081(1)	0.5890(2)	0.9(2)
Sc2	0.2773(2)	0.3979(2)	0.8(2)
Sc3	0.3029(2)	0.2457(2)	1.0(2)
Sc4	0.4262(2)	0.4318(3)	1.2(2)
Sc5	0.4371(2)	0.9468(2)	0.7(2)
Sc6	0.0087(2)	0.9131(2)	0.9(2)
Sc7	0.9383(2)	0.7147(2)	1.0(2)
Sc8	0.7987(2)	0.5304(3)	1.2(2)
Sc9	0.7116(2)	0.1334(2)	0.9(2)
Sc10	0.6712(2)	0.3443(2)	1.0(2)
Sc11	0.6340(2)	0.9376(2)	0.7(2)
Sc12	0.4615(2)	0.2859(2)	0.7(2)
Sc13	0.8329(2)	0.1532(3)	1.3(2)
Sc14	0.1507(2)	0.1911(2)	0.5(1)
Sc15	0.2398(2)	0.0431(3)	1.7(2)
Sc16	0.9882(2)	0.5681(2)	1.2(2)

[a] All atoms in position 4*i*, $y = 0$.

[b] $B_{eq} = (8\pi^2/3)\Sigma_i\Sigma_j U_{ij} a_i^* a_j^* \vec{a}_i \vec{a}_j$.

Table 4. Selected pairwise distances in Sc_8Te_3 ordered according to their corresponding overlap populations.

Atom 1	Atom 2	Distance(Å)	Overlap
Sc15	Sc15	3.00(1)	0.343
Sc5	Sc5	3.09(1)	0.334
Sc8	Sc8	3.058(7)	0.316
Sc8	Sc10	3.113(5)	0.316
Sc1	Sc7	3.119(4)	0.312
Sc13	Sc15	3.142(5)	0.297
Sc1	Sc12	3.265(5)	0.263
Sc9	Sc13	3.282(6)	0.220
Sc5	Sc6	3.195(5)	0.209
Sc2	Sc8	3.339(6)	0.204
Sc4	Sc16	3.130(5)	0.178
Sc1	Sc10	3.334(6)	0.176
Sc3	Sc9	3.138(5)	0.174
Sc11	Sc15	3.425(6)	0.171
Sc5	Sc6	3.272(5)	0.155
Sc4	Sc16	3.214(5)	0.149
Sc9	Sc15	3.196(6)	0.149
Sc3	Sc13	3.265(5)	0.146
Sc4	Sc4	3.672(9)	0.141
Sc1	Sc16	3.230(5)	0.140
Sc2	Sc10	3.251(5)	0.139
Sc11	Sc13	3.289(5)	0.129
Sc16	Sc16	3.456(9)	0.124
Sc11	Sc15	3.425(6)	0.119
Sc7	Sc10	3.308(5)	0.119

Table 4. (continued)

Sc10	Sc10	3.8517(6)	0.119
Sc13	Sc13	3.8517(6)	0.117
Sc16	Sc16	3.8517(6)	0.114
Sc8	Sc8	3.8517(6)	0.114
Sc15	Sc15	3.8517(6)	0.111
Sc2	Sc8	3.301(5)	0.106
Sc1	Sc8	3.306(5)	0.100
Sc12	Sc16	3.373(5)	0.099
Sc7	Sc12	3.479(5)	0.093
Sc7	Sc7	3.8517(6)	0.074
Sc1	Sc1	3.8517(6)	0.069
Sc3	Sc15	3.869(8)	0.064
Sc6	Sc6	3.8517(6)	0.060
Sc13	Sc15	3.709(8)	0.059
Sc9	Sc9	3.8517(6)	0.056
Sc5	Sc5	3.8517(6)	0.055
Sc9	Sc14	3.299(5)	0.048
Sc8	Sc10	3.794(7)	0.043
Sc5	Sc14	3.352(5)	0.040

Supplementary Material
The Synthesis, Structure and Bonding of Sc_8Te_3 and Y_8Te_3. Cooperative Matrix and Bonding Effects in the Solid State

Paul A. Maggard and John D. Corbett

Table S1. Single Crystal X-ray Data Collection and Refinement Parameters for Sc_8Te_3.

Formula weight	742.45
Space group, Z	$C2/m$ (No. 12), 8
Crystal Dimensions, mm	0.1 × 0.3 × 0.4
Lattice parameters, Å, $Å^3$ [a]	
a	28.842(7)
b	3.8517(6)
c	22.352(5)
β	122.51(2)
V	2094(2)
d_{calc}, g/cm^3	4.710
Radiation; $2\theta_{max}$	Mo K_α; 50°
Octants measured	h, ±k, ±l
Scan method	ω
Temperature, °C	23
Absorption corr. method	ψ-scans, DIFABS
μ, cm^{-1} (Mo K_α)	130.36
Relative transmission range	0.832–1.00
Number of reflections:	
measured	4310
observed ($I \geq 3\sigma(I)$)	2233
unique	1356
Number of variables	133
R_{avg} ($I \geq 3\sigma(I)$), %	9.0

Table S1. (continued)

Residuals R; R_ω,[b] %	3.7; 3.7
Goodness of fit	1.01
Secondary Ext. (10^{-7})	1.24(7)

---

[a] Guinier data, Cu Kα, 22°C.

[b] $R = \Sigma||F_o|-|F_c||/\Sigma|F_o|$; $R_\omega = [\Sigma\omega(|F_o|-|F_c|)^2/\Sigma\omega(F_o)^2]^{1/2}$, $\omega = 1/\sigma^2$.

Table S2. U_{ij} values for Sc_8Te_3 ($Å^2/8\pi^2$).[a]

Atom	U_{11}[b]	U_{22}	U_{33}	U_{13}
Te1	0.0128(8)	0.0078(9)	0.0085(8)	0.0059(7)
Te2	0.0091(8)	0.0096(9)	0.0073(8)	0.0035(7)
Te3	0.0102(8)	0.0107(9)	0.0089(3)	0.0049(7)
Te4	0.0110(8)	0.0080(9)	0.0080(8)	0.0050(7)
Te5	0.0117(8)	0.0081(9)	0.0117(9)	0.0059(7)
Te6	0.0100(8)	0.0092(8)	0.0101(8)	0.0055(7)
Sc1	0.013(2)	0.014(3)	0.010(2)	0.008(2)
Sc2	0.012(2)	0.011(3)	0.008(2)	0.007(2)
Sc3	0.011(2)	0.012(3)	0.015(3)	0.007(2)
Sc4	0.016(2)	0.013(3)	0.017(3)	0.010(2)
Sc5	0.013(2)	0.010(3)	0.008(2)	0.008(2)
Sc6	0.008(2)	0.009(2)	0.016(3)	0.007(2)
Sc7	0.013(2)	0.012(3)	0.012(3)	0.007(2)
Sc8	0.022(3)	0.012(3)	0.022(3)	0.017(2)
Sc9	0.010(2)	0.015(3)	0.008(2)	0.003(2)
Sc10	0.009(2)	0.020(3)	0.008(2)	0.003(2)
Sc11	0.014(2)	0.004(2)	0.007(2)	0.003(2)
Sc12	0.011(2)	0.006(3)	0.010(2)	0.006(2)
Sc13	0.013(2)	0.024(3)	0.013(2)	0.009(2)
Sc14	0.007(2)	0.003(2)	0.008(2)	0.004(2)
Sc15	0.011(2)	0.019(3)	0.036(3)	0.011(2)
Sc16	0.012(2)	0.020(3)	0.011(2)	0.005(2)

[a] $T = \exp[-2\pi^2(U_{11}h^2a^{*2} + U_{22}k^2b^{*2} + U_{33}l^2c^{*2} + 2U_{12}hka^*b^* + 2U_{13}hla^*c^* + 2U_{23}klb^*c^*)]$.

[b] $U_{12} = U_{23} = 0$.

Table S3. Bond Distances in Sc_8Te_3 (Å).[a]

Te1	Sc2	2×	2.966(4)
	Sc3	2×	2.989(4)
	Sc9		2.908(5)
	Sc10		3.042(5)
	Sc14	2×	2.980(3)
	Te1	2×	3.852(1)
	Te2		4.086(2)
	Te4		4.118(2)
	Te6		3.831(3)
Te2	Sc3	2×	2.960(3)
	Sc4	2×	2.983(4)
	Sc12	2×	3.010(4)
	Sc13		3.038(5)
	Sc16		2.952(5)
	Te1		4.086(2)
	Te2	2×	3.852(1)
	Te3		4.072(2)
	Te6		3.927(2)
Te3	Sc6		2.911(5)
	Sc7		2.946(5)
	Sc11	2×	2.987(3)
	Sc12	2×	2.984(4)
	Sc13		2.980(5)
	Te2		4.072(2)
	Te3	2×	3.852(1)
	Te4	2×	4.030(2)
	Te5		3.991(3)
Te4	Sc5		2.957(5)
	Sc6	2×	2.985(4)
	Sc7	2×	2.984(4)
	Sc10		3.023(5)
	Sc14	2×	2.951(3)
	Te1		4.118(2)
	Te3	2×	4.030(2)
	Te4	2×	3.852(1)
Te5	Sc5	2×	2.895(3)
	Sc6		3.090(5)
	Sc9	2×	2.899(4)
	Sc11	2×	2.989(4)
	Sc14		3.163(5)
	Sc15		3.088(5)
	Te3		3.991(3)
	Te5	2×	3.852(2)
Te6	Sc1	2×	2.986(1)
	Sc2	2×	2.943(3)
	Sc4	2×	2.940(4)
	Sc8		2.986(5)
	Sc16		2.933(5)
	Te1		3.831(3)
	Te2		3.927(2)
	Te6	2×	3.852(2)
Sc1	Te6	2×	2.986(1)
	Sc4		3.819(6)
	Sc7	2×	3.119(4)
	Sc8	2×	3.306(5)
	Sc10		3.334(6)
	Sc12		3.265(5)
	Sc16	2×	3.230(5)
Sc2	Te1	2×	2.966(4)
	Te6	2×	2.943(3)
	Sc8	2×	3.301(5)
	Sc8		3.339(6)
	Sc10	2×	3.251(5)
Sc3	Te1	2×	2.989(4)
	Te2	2×	2.960(3)
	Sc4		3.747(7)
	Sc9	2×	3.138(5)
	Sc13	2×	3.265(5)
Sc4	Te2	2×	2.983(4)
	Te6	2×	2.940(4)
	Sc4		3.819(6)
	Sc4		3.747(7)
	Sc4		3.672(9)
	Sc16	2×	3.214(5)
	Sc16	2×	3.130(5)
Sc5	Te4		2.957(5)
	Te5	2×	2.895(3)
	Sc5		3.089(9)
	Sc6	2×	3.195(5)
	Sc6	2×	3.272(5)
	Sc9		3.654(6)
	Sc14	2×	3.351(5)
Sc6	Te3		2.911(5)
	Te4	2×	2.985(4)
	Te5		3.090(5)
	Sc5	2×	3.195(5)
	Sc5	2×	2.272(5)
	Sc7		3.756(7)
Sc7	Te3		2.946(5)
	Te4	2×	2.984(4)
	Sc1	2×	3.119(4)
	Sc10	2×	3.308(5)
	Sc12	2×	3.479(5)
Sc8	Te6		2.986(5)
	Sc1	2×	3.306(5)
	Sc2	2×	3.301(5)
	Sc2		3.339(6)
	Sc8	2×	3.058(7)
	Sc10	2×	3.113(5)
	Sc10		3.794(7)
Sc9	Te1		2.908(5)
	Te5	2×	2.899(4)
	Sc3	2×	3.138(5)
	Sc5		3.654(6)
	Sc11		3.693(6)
	Sc13		3.282(6)
	Sc14	2×	3.299(5)
	Sc15	2×	3.196(6)
Sc10	Te1		3.042(5)
	Te4		3.023(5)
	Sc1		3.334(6)
	Sc2	2×	3.251(5)
	Sc7	2×	3.308(5)
	Sc8	2×	3.113(5)
	Sc8		3.794(7)
	Sc14	2×	3.690(5)
Sc11	Te3	2×	2.987(3)
	Te5	2×	2.989(4)
	Sc9		3.693(6)
	Sc13	2×	3.289(5)
	Sc15	2×	3.294(5)
	Sc15		3.425(6)

Table S3. (continued)

Sc12	Te2	2×	3.010(4)
	Te3	2×	2.984(4)
	Sc1		3.265(5)
	Sc7	2×	3.479(5)
	Sc13	2×	3.800(6)
	Sc16	2×	3.373(5)
Sc13	Te2		3.038(5)
	Te3		2.980(5)
	Sc3	2×	3.265(5)
	Sc9		3.282(6)
	Sc11	2×	3.289(5)
	Sc15	2×	3.142(5)
	Sc15		3.709(8)
Sc14	Te1	2×	2.980(3)
	Te4	2×	2.951(3)
	Te5		3.163(5)
	Sc5	2×	3.351(5)
	Sc9	2×	3.299(5)
	Sc10	2×	3.690(5)
Sc15	Te5		3.088(5)
	Sc9	2×	3.196(6)
	Sc11	2×	3.294(5)
	Sc11		3.425(6)
	Sc13	2×	3.142(5)
	Sc13		3.709(8)
	Sc15	2×	3.00(1)
Sc16	Te2		2.952(5)
	Te6		2.933(5)
	Sc1	2×	3.230(5)
	Sc4	2×	3.214(5)
	Sc4	2×	3.130(5)
	Sc12	2×	3.373(5)
	Sc16		3.456(9)

---

[a] Distances listed out to Sc–Sc = 3.84 Å, Sc–Te =3.1 Å, and Te–Te = 4.2 Å.

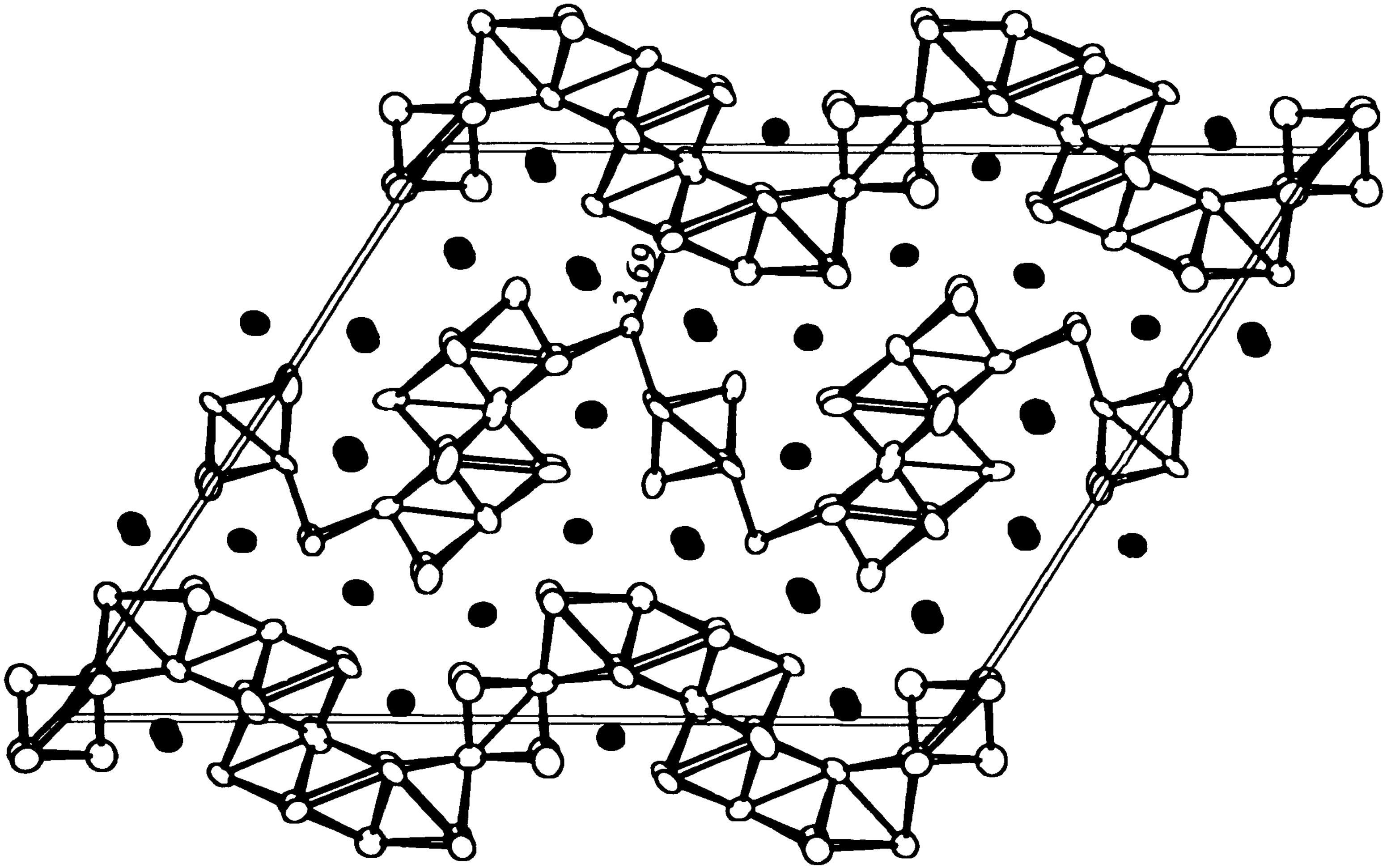

Figure 1. Near-[010] projection of the unit cell of Sc_8Te_3 (99.9% probability thermal ellipsoids) with bonds drawn for d(Sc–Sc) ≤ 3.50 Å. The shortest intersheet distance, Sc10–Sc14, is marked. Dark atoms are tellurium; light atoms, scandiums.

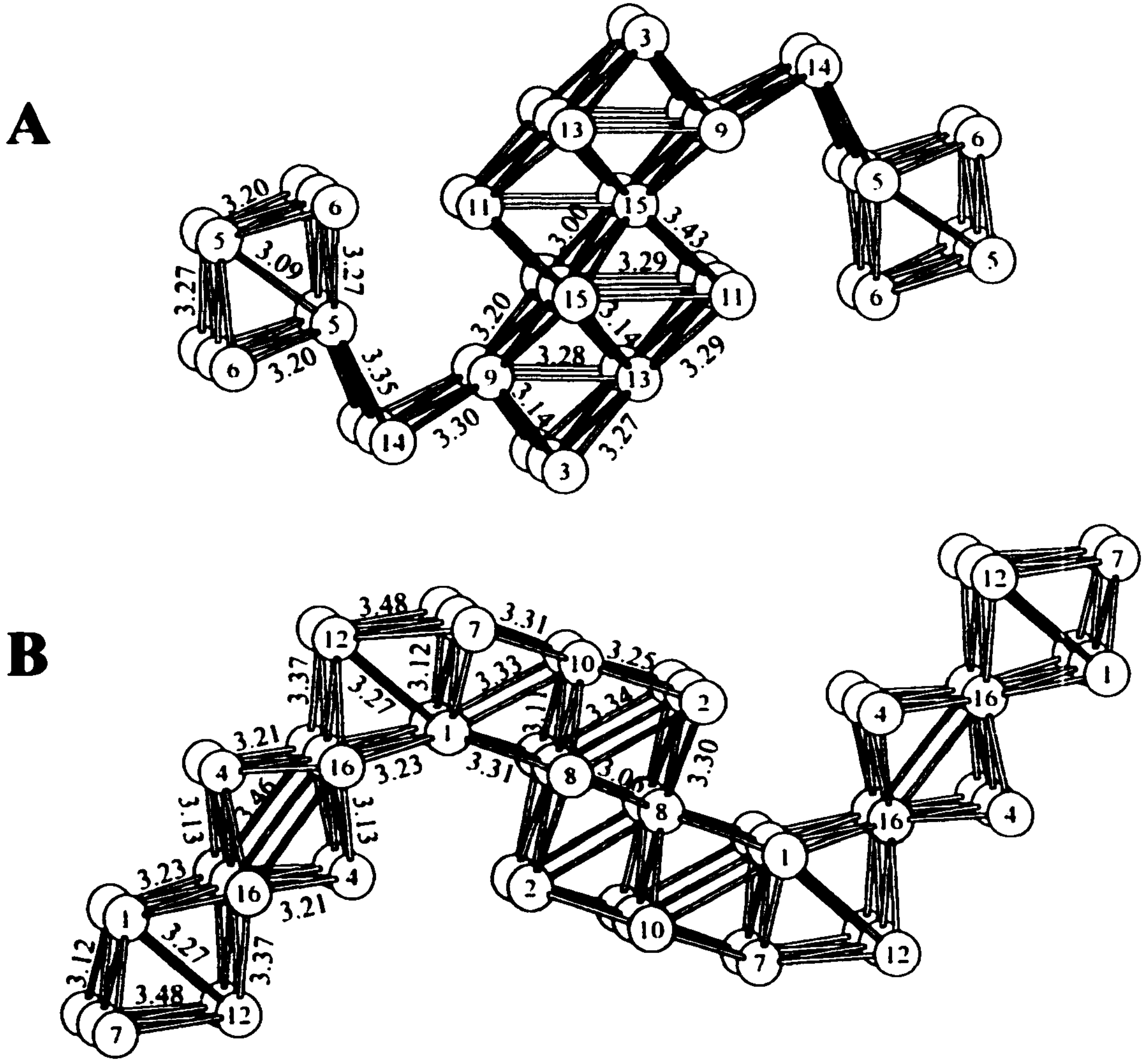

Figure 2. (A) More open corrugated sheet in Sc_8Te_3 with bond distances marked. The sheet is infinite along the projection axis. Two-fold axes pass through the centers of the Sc5–Sc5 and Sc15–Sc15 bonds. (B) More condensed corrugated sheets in Sc_8Te_3. Two-fold axes pass through the centers of the Sc8–Sc8 and Sc16–Sc16 bonds.

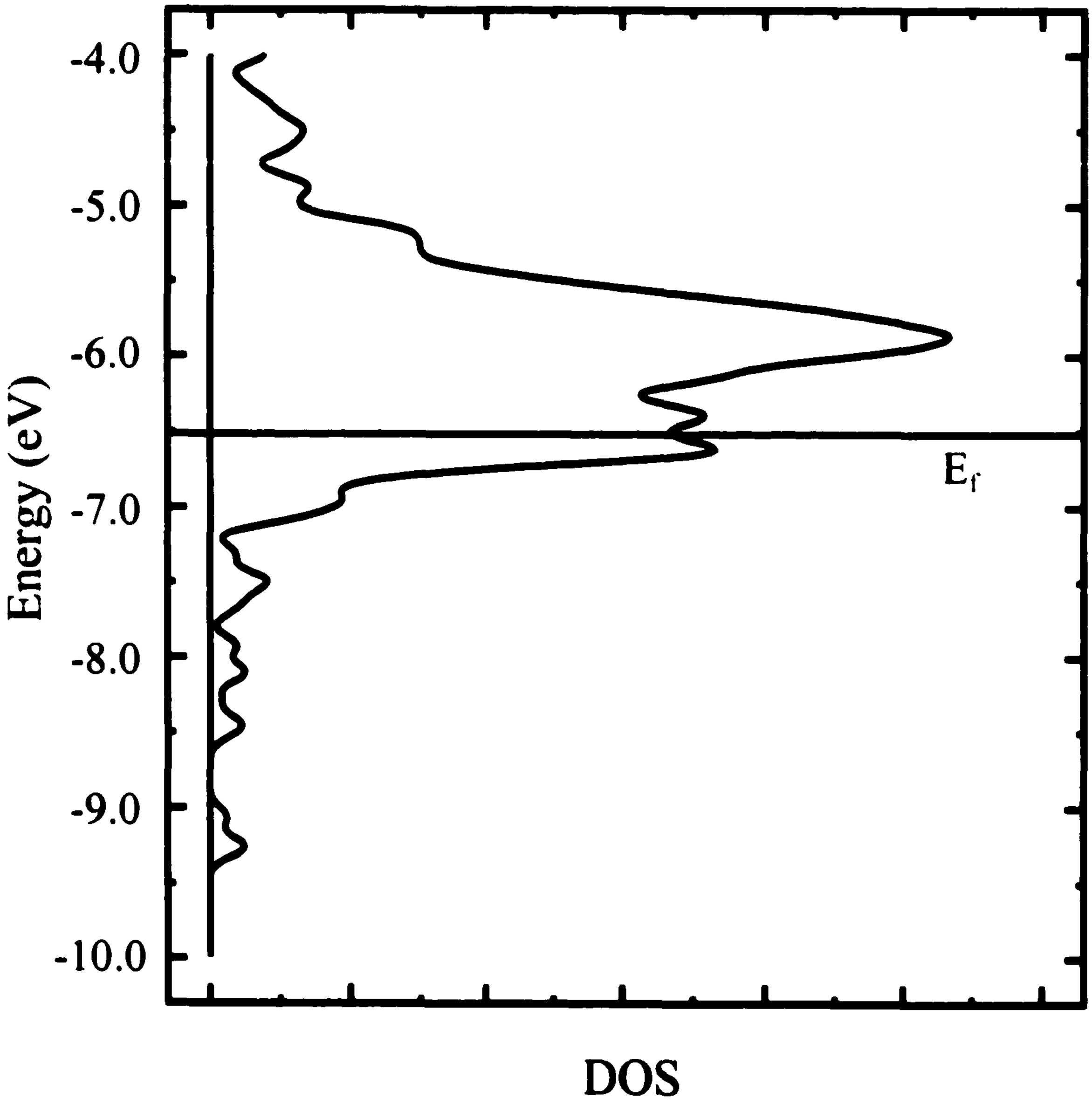

Figure 3. Total densities of states (DOS) for Sc_8Te_3.

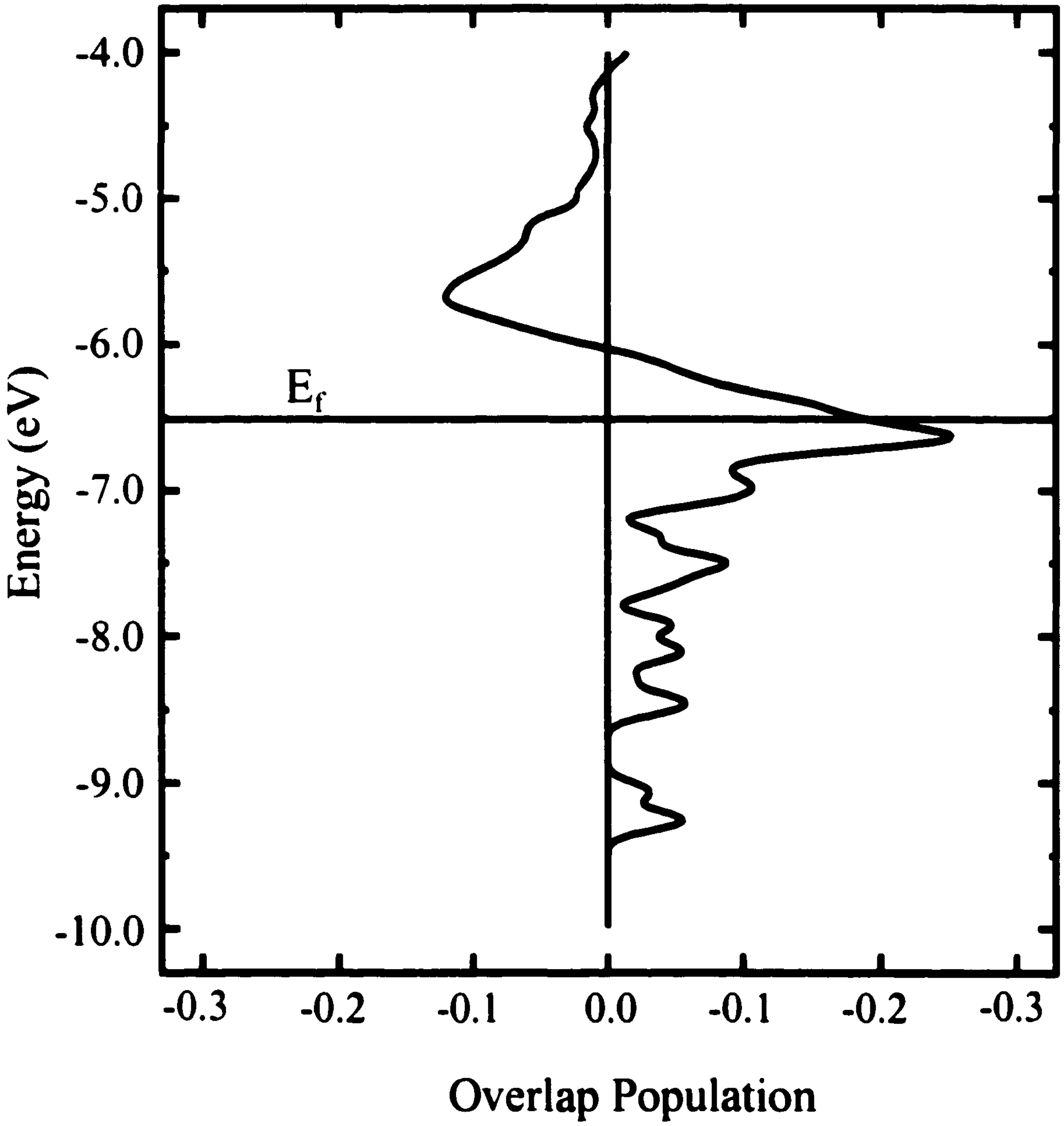

Figure 4. Total Sc–Sc crystal orbital overlap population out to 3.8 Å.

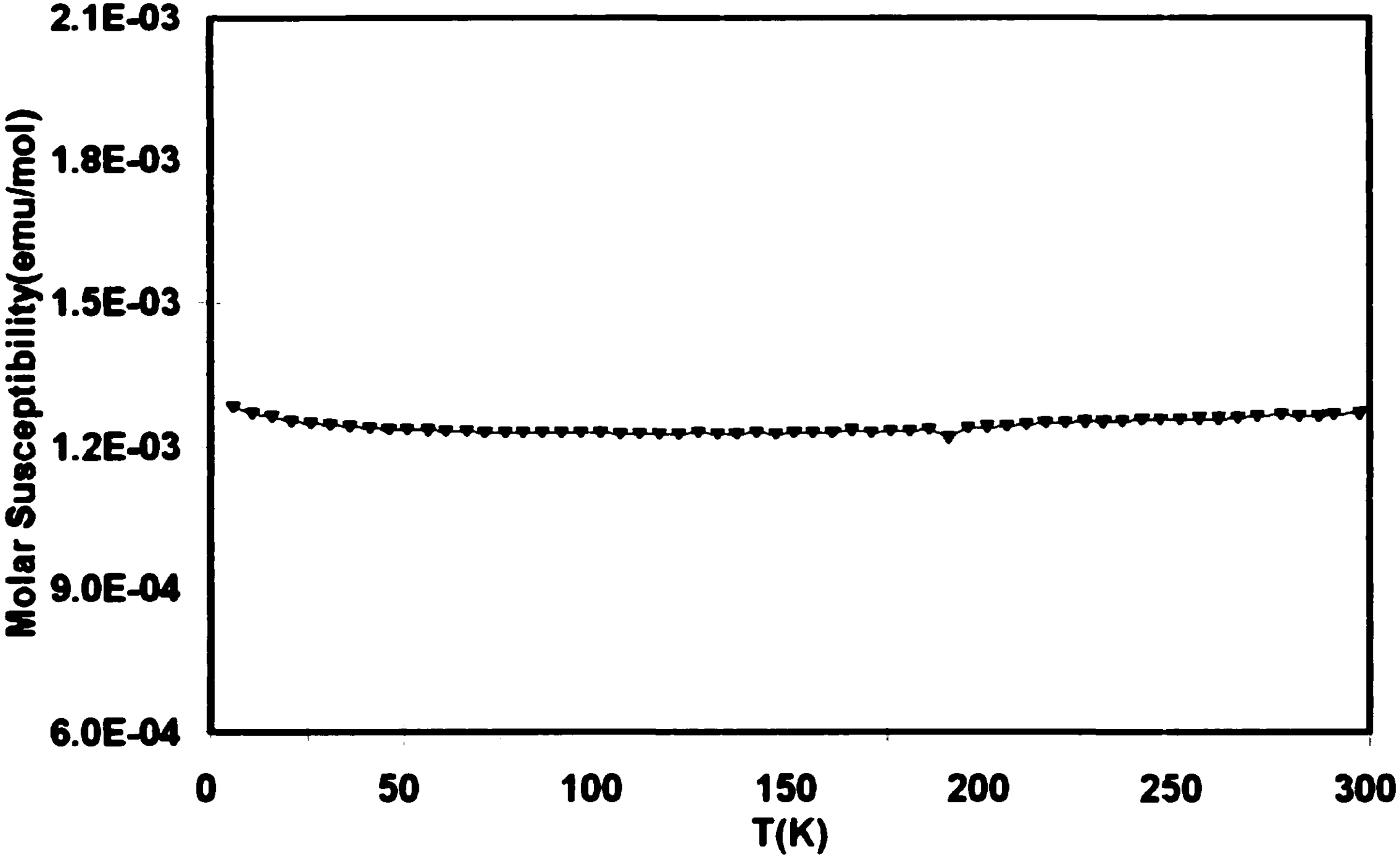

Figure 5. Molar magnetic susceptibility of Y_8Te_3 as a function of temperature (K).

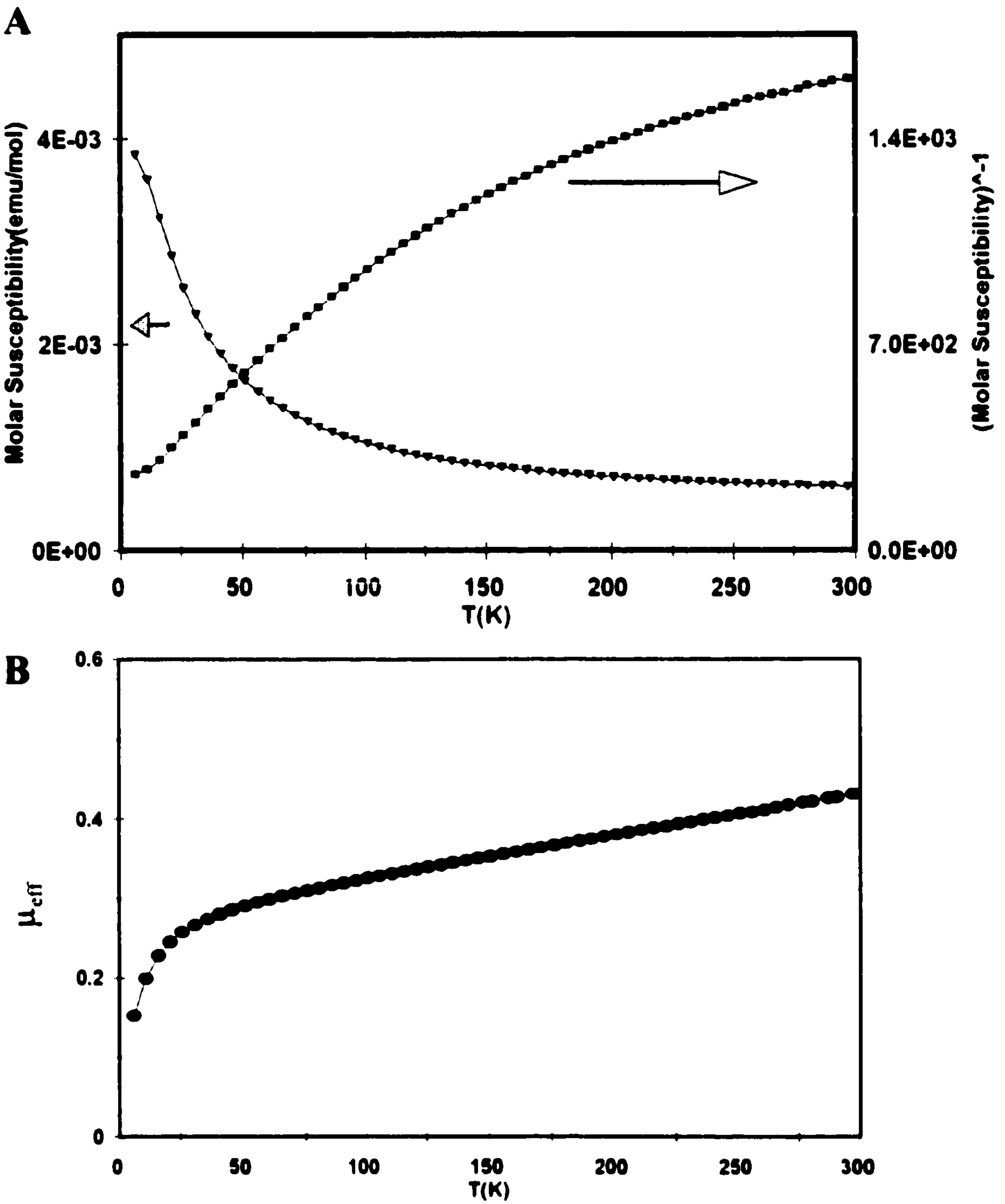

Figure 6. (A) Molar magnetic susceptibility of Sc_8Te_3 and its inverse as a function of temperature. (B) M μ_{eff} vs temperature for Sc_8Te_3.

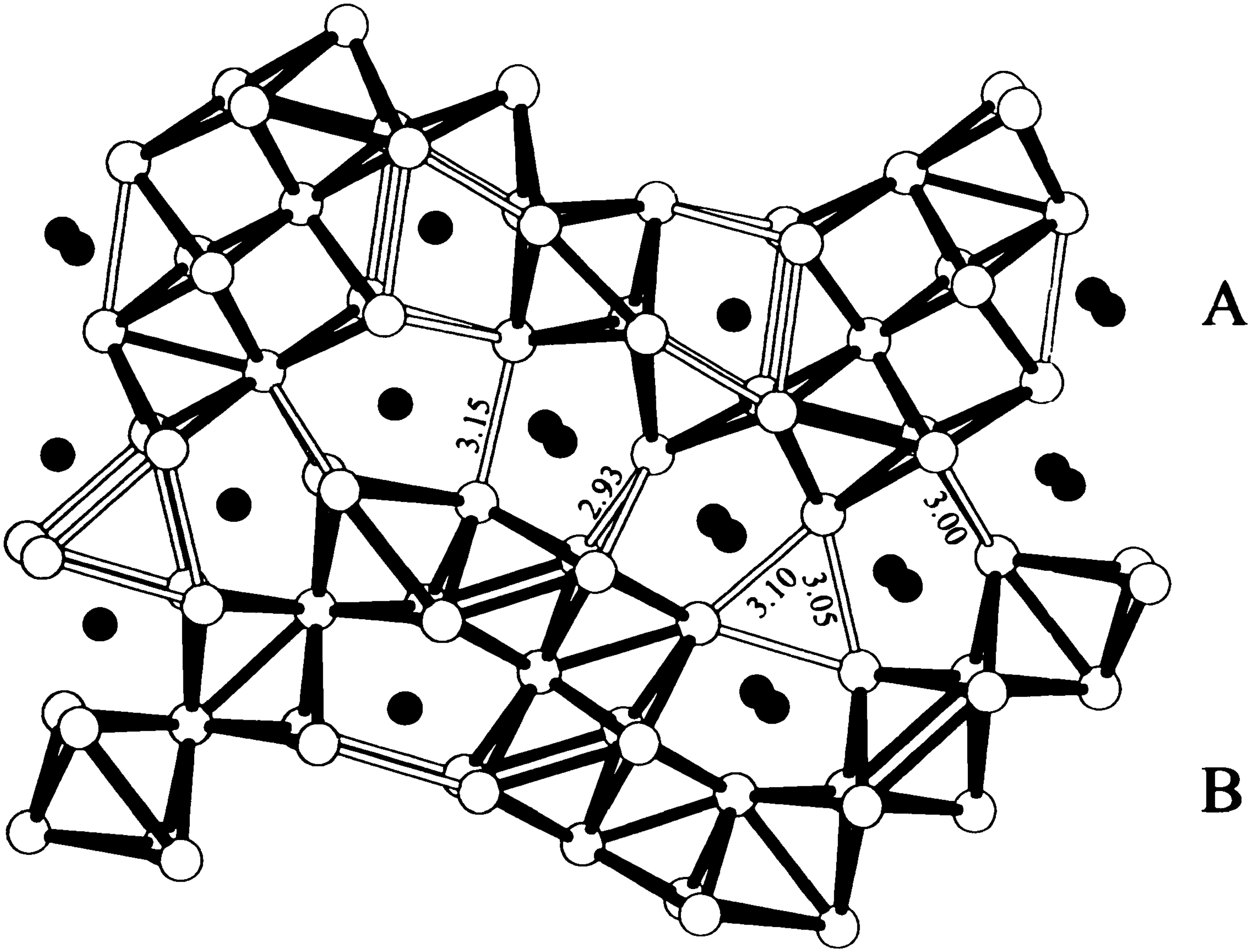

Figure 7. Near-[010] projection of the corrugated sheets in Ti_8S_3, with bonds drawn for $d(\text{Ti–Ti}) < 3.20$ Å. Dark bonds are comparable to those in the chains shown in Figure 2, while open bonds are additional interactions in this structure. The interlayer distances are marked. Dark atoms are sulfur, light atoms, titanium.

CHAPTER 4. Sc_9Te_2: A TWO-DIMENSIONAL DISTORTION WAVE IN THE SCANDIUM-RICHEST TELLURIDE

A paper published in Journal of the American Chemical Society

J. Am. Chem. Soc. **2000**, *122*, 838

Paul A. Maggard and John D. Corbett

Department of Chemistry, Iowa State University, Ames, IA 50011

Abstract

Sc_9Te_2 was prepared by high-temperature solid-state techniques, and the structure was determined by single crystal X-ray diffraction to be monoclinic, *Cc* (No. 9, $Z = 8$) with $a = 7.7576(1)$ Å, $b = 15.654(3)$ Å, $c = 17.283(3)$ Å, and β=90.01(3)° at 23 °C. The structure of metallic Sc_9Te_2 can be viewed as columns built either from distorted 3×3 b.c.c. metal atoms or from distorted edge-sharing octahedra along $\vec{a}$ that are joined via intercolumn bonds on opposite sides into 2D layers along $\vec{b}$. A corrugated layer of Te atoms separates the metal layers in the *c* direction. This structure derives from the Ti_9Se_2 structure, with doubled *a* and *b* dimensions and a lower symmetry. Magnetic susceptibility measurements on Sc_9Te_2 show a substantially temperature-independent paramagnetism that is much smaller per metal atom than those for other scandium-rich tellurides or scandium metal. Extended Hückel band calculations reveal a clear distinction between high overlap populations for Sc–Sc interactions in the interior of the condensed metal structure and lower values for those on the

exterior that have Te neighbors. The distortion generally enhances the overlap populations of occupied states.

Introduction

The nature of metal-metal bonding has been an important aspect of inorganic chemistry since the days of Pauling.[1] Metal-metal bonding in low-dimensional structures has been cited as a key component in synthesizing materials that contain metal–lattice modulations, or charge density waves.[2,3] The study of metal-metal bonding in early transition-metal compounds, chalcogenides especially, has received increased attention over the past 30 years. Voluminous expressions of lower-dimensional metal-metal bonding have been uncovered in such examples as Ti_8Ch_3[4,5] and Ti_2Ch[6,7] (Ch = S, Se), $Ti_{11}Se_4$,[8] Ti_9Se_2,[9] Ti_5Te_4,[10] Hf_2Te,[11] Hf_3Te_2,[12] Hf_2Se_3,[13] Zr_3Te,[14] Zr_5Te_4,[15] and Zr_2Te.[16] This chemistry has only recently been extended to the earliest and electron-poorest transition metals, namely Sc_2Te[17] and R_8Te_3 ® = Sc, Y).[18] Structural and bonding relationships among these electron-impoverished tellurides and the electron-richer Ti, Zr, Hf chalcogenides have given good insights regarding the importance of atom sizes, valence electron concentrations, and proportions in the determination of stability and structural features.

Often little insight can be offered about the bonding or other features that drive the structural outcomes. One might think that well established interrelationships between electron counts, steric/matrix effects, and bond distances upon which the foundation of rational chemistry is based are too complex to be understood. However, the interrelationships previously outlined[18] for one case, M_8Ch_3, have proven valuable in understanding the chemistry. A great many of the metal-rich phases can be described as chains of octahedra sharing vertices or edges that may be further condensed in diverse ways into infinite single, double, or quadruple chains. The majority (>95%) of these metal-rich phases share one common feature, a short repeat axis that appears to be determined primarily by the van der Waals radii of the anions. The metal-metal bonds repeat along this short axis as well, but these distances are usually determined by anion-anion contacts. Additionally, neighboring metal atoms often occupy alternating positions along the short axis, e.g., at 1/4 and 3/4, and this arrangement may have a distinct impact on all metal-metal distances. As for Sc_8Te_3 vs $Ti_8(S,Se)_3$, a cooperative result of the effects of metal-based electron counts (valence electron concentration per atom, VEC), anion sizes, and the degree of M-M bonding appear to be involved. An increase in VEC plus a decrease in anion size together afford more short metal-metal contacts and bonding. This effect seems to be at work in the present Sc_9Te_2, which is related to Ti_9Se_2[9] via a predicted discontinuous symmetry-lowering metal lattice distortion. This article also presents an analysis of the electronic structures and distortion wave that relates Ti_9Se_2 to Sc_9Te_2, the metal-richest binary telluride known among the electron-poorest transition metals.

Experimental Section

Syntheses. All materials were handled in a He-filled glovebox. The synthesis of Sc_9Te_2 began with the preparation of Sc_2Te_3 (NaCl type with disordered cation vacancies). The elements as received (Sc turnings 99.7%, Aldrich-APL; Te powder 99.99%, Alfa-AESAR) were loaded in a 2:3 stoichiometry into a fused silica container. This was evacuated, sealed, and heated to 450 °C for 12 hrs, and then to 900°C for 72 hours. Guinier film data confirmed the production of only the target product. This and the appropriate amount of scandium turnings to give a 9:2 stoichiometry were then pelletized with a hydraulic press within a glovebox. The pellet was arc-melted in the glovebox for 20 seconds per side with a current of 70 amps. A Guinier pattern of the product at this point revealed single phase (>95%) monoclinic Sc_9Te_2. This was annealed at 1135°C for 72 hours inside a welded tantalum container and then allowed to cool radiatively. It should be noted that still higher annealing temperatures resulted in reaction of the sample with and subsequent failure of the tantalum tubing. After annealing, powder diffraction data revealed that Sc_9Te_2 had been obtained in evidently quantitative yield, and single crystals therein were selected for structural analysis. We have not been able to prepare a Y_9Te_2 analogue.

Single Crystal Diffraction. Several black, irregularly shaped crystals were mounted inside 0.3-mm i.d. glass capillaries. Crystal qualities were checked with Laue photographs, and the best crystal was taken for a data set collection on a Bruker CCD diffractometer operating at room temperature with Mo $K\alpha_1$ radiation. Ninety reflection frames collected with 15-second exposures were analyzed and yielded an orthorhombic unit cell with a = 7.821 Å, b = 17.285 Å, and c = 3.879 Å, with a few weak reflections not included. This cell was the same as obtained earlier from diffractometers equipped with point detectors, from which a Ti_9Se_2-type structure (*Pnma*) had been solved, but with much apparent disorder (some extreme ellipsoids). A set of ninety reflection frames recollected with 45-second exposures revealed additional reflections that doubled both the a and c axes and gave a = 7.7576 (3) Å, b = 15.654 (3) Å, and c = 17.283 (3) Å in the standard setting. One sphere of reflections (±*h*, ± *k*, ±*l*) was collected to $2\theta \sim 56°$. The reflection frames when integrated and filtered with SAINTPLUS[19] gave 7239 reflections, of which 2141 were unique and observed ($I > 3\sigma_I$). Comparison of reflection intensities clearly demonstrated that there was no mirror plane normal to *a* (or *c*), which with the distorted supercell reduces the original *Pnma* to monoclinic *Cc*. An absorption correction was applied with the package program SADABS.[20] Additional observational conditions suggested the possible space group *Cc*. Structural models were obtained and successfully refined with the SHELXTL[21] program. Some data collection and refinement parameters are given in Table 1. The refinement converged at R1/wR2 = 0.031/0.098. For the subcell, 1069 observed unique reflections yielded *R*1/w*R*2 = 0.030/0.088, while 1072 observed reflections unique to the supercell gave *R*1/w*R*2 = 0.040/0.110. On average, the subcell reflections were about 3 times the intensity of the unique supercell data. The complete positional and isotropic-equivalent thermal parameters for Sc_9Te_2 are given in Table 2. Additional data collection, refinement and anisotropic displacement parameters as well as all interatomic distances are given in the Supporting Information. These as well as the F_o/F_c listing are available from J.D.C.

Properties. A weighed, powdered sample of ~50 mg of Sc_9Te_2 was loaded inside the glovebox so that it was sandwiched between two close-fitting rods inside a 5 mm o.d. fused silica tube. Magnetizations of the samples were measured from 6 to 300 K at a field of 3 T with a Quantum Design MPMS SQUID magnetometer. Also, the magnetization versus field properties were checked at 80 K and 160 K, and the M values were found to intercept M = 0 at H = 0, suggesting that the temperature dependencies are intrinsic, the same as determined earlier for the other scandium-rich phases. The data were corrected for the diamagnetism of both the sample holder and the atom cores.

Resistivities of powdered ~50-mg samples of Sc_9Te_2 diluted with Al_2O_3 powder were measured with a "Q" apparatus at ~35 MHz between 100 and 300 K.

Band Calculations. Extended Hückel band calculations were carried out within the tight-binding approximation[22] for the full structure of Sc_9Te_2 at 75 k-points spread out over the irreducible wedge. H_{ii} parameters employed were those values iterated to charge consistency for Sc_2Te (eV):[17] Sc 4s, -6.75; 4p -3.38; 3d, -6.12; Te 6s, -21.20; 6p, -12.00.

Results and Discussion

Structural Description. A near-[100] section of the Sc_9Te_2 structure is shown in Figure 1, and the more significant (nearest neighbor) scandium–scandium distances are given in Table 3. The atom distribution can be viewed as corrugated multi-layers of scandium atoms (white) that stack normal to $\vec{c}$ and are separated into 2D sheets by isolated tellurium atoms (gray). The most conspicuous building block of the metal substructure is approximately a 1D square column of scandium, three atoms in width and height, that extends infinitely along $\vec{a}$. Adjoining columns are identical but displaced by $a/2$, which allows the display of all independent atom numbers as these alternate along the columns. This 3 × 3 cluster block can be described as the side-by-side condensation product of four infinite trans-edge-sharing chains of octahedra. (Note in the Figure that the shared edge (waist) and vertex positions alternate by $a/2$, with the waist of the octahedron assigned to the clearly shorter trans distance.) Similar infinite chains of condensed octahedra have been useful in the earlier description of Sc–Sc bonding in Sc_2Te, Sc_8Te_3, and Sc_7Cl_{10},[23] where possible close-packed or condensed b.c.c. features are less apparent. Each column here is bonded to parallel units on opposed faces (at atoms 5, 6, 15, 16) by another chain of edge-sharing octahedra to generate corrugated sheets of these columns normal to $\vec{c}$. The latter connections, marked in Figure 1, range over 3.18 – 3.29 Å, while edges on the opposing column faces (6–16 and 5–15) are much shorter, 3.05 Å. The shortest metal–metal distance between sheets, 3.48 Å (4–11), is marked in Figure 1, although the corresponding overlap population is relatively small (below).

Significant distortions in this structure relative to Ti_9Sc_2 occur along the individual columns, and these are better seen in Figure 2 in which the chain axis ($\vec{a}$) is horizontal. This pattern is comprised of four crystallographically distinct octahedra, two "squashed" (18, 9, 13, 12, 15, 3; 17, 16, 11, 14, 10, 2) and two more regular octahedra (18, 11, 16, 14, 10, 1; 17, 12, 15, 9, 13, 4), with the latter highlighted. The distances within one of each type of octahedron are marked in Figure 2, those in the other pair being fairly similar. The Sc–Sc distances around the more regular octahedron vary from 3.1– 3.3 Å, with waists of ~3.5 Å (9–12 or 13–15) and heights of 4.4 Å (4–17). Distances around the "squashed" octahedra vary from 3.1 – 3.4 Å, with shorter height distances of ~3.5 Å (marked, 2–17) and longer waists of ~4.3 Å (10–11, 14–16), along the chain, that is, compressed by about 0.8 Å so that the height and waist proportions of the octahedra have been reversed but remain comparable. One regular and one "squashed" octahedron share a vertex (17,18) and are connected via two shared edges along $\vec{a}$ to another such pair with the distortion reversed with respect to the first one. In this way, the regular octahedra in this view occupy opposed positions across the chain, in concert with the alternation of "squashed" octahedra. Finally, the sides on these chains of octahedra are augmented by metal atoms (5,8; 6,7) that simultaneously cap faces of adjoining octahedra and "squashed" octahedra and define bridges to the adjoining column, Figure 1. The distances to the shared vertices of the octahedra are fairly constant, slightly less than 3.4 Å (5–17, 7–17, 6–18, 8–18). All tellurium atoms are located within tricapped trigonal prismatic scandium figures, with Sc–Te distances in a 2.9–3.2 Å range. Appropriate to the electron richness of this compound, all Te–Te distances are 4.0 Å or greater and nonbonding.

The parent from which this zigzag pattern of distorted octahedra can be derived is shown in Figure 3, the undistorted, or structurally averaged, Sc_9Te_2 that corresponds to the Ti_9Se_2-type structure.[9] Here the waists and heights of the octahedra are both ~3.9 Å, quite long for good bonding, and the overall column structure is just a simple but rather extensive condensation of these. The observed superstructure is achieved by splitting the five independent metal positions into four or two sites each, as keyed with a superscript for the former sites on the atom numbers in Table 2. The descent in space group symmetry from *Pbam* for Ti_9Se_2 to *Cc* for Sc_9Te_2 is not direct, but is predicted to require two steps,[24] so the transition must be first order rather than continuous. The major displacements, marked on Figure 3 by arrows, occur along the short $\vec{a}$ axis, while neighboring columns displace out of phase so as to yield a doubled *b* axis as well, Figure 2.

Physical Properties. Sc_9Te_2 exhibits a paramagnetic susceptibility with a small temperature-dependence at the lowest temperatures, as shown in Figure 4 along with data for other metal-rich scandium phases for comparison, all as χ/mole Sc. The temperature dependence here is much less than observed for both Sc_2Te and Sc_8Te_3, and the result is quite Pauli-like from 50 – 300K. The room temperature susceptibility of scandium metal[27] is two to four times greater than that for any of the scandium-rich tellurides investigated, with Sc_9Te_2 being the lowest. What is different is that the two other scandium-rich phases have greater temperature dependencies at lower temperatures. High-frequency measurements of the resistivity of the polycrystalline Sc_9Te_2 phase over 100 – 300 K show metallic behavior. The resistivity is ~220 $\mu\Omega\cdot$cm at 298 K, four times that of the metal, with a temperature dependence of $-0.57\%K^{-1}$, characteristic of a metallic compound. Neither χ or ρ gave any evidence for a phase transition over the temperature regions studied.

Theoretical Calculations. Although the metal–metal bonded nature of Sc_9Te_2 suggests delocalization of conduction electrons, the unusual distortions away from the more symmetrical Ti_9Se_2 type also suggest electronic driving forces. Band calculations seem necessary to understand this aspect better. Figure 5 shows the total DOS and the total Sc–Sc COOP curve (sum of overlap-weighted bond populations) for Sc_9Te_2 as functions of energy. As is usual for such compounds, the Fermi level is located on the low energy side of a large conduction band that is composed almost entirely of scandium d and s states. The COOP curve shows that these are highly bonding up to and beyond E_F, which is typical for these electron-deficient compounds. Figure 5 suggests the valence electrons are delocalized within a broad conduction band, but it does not give any hint about the distortion.

We have already seen many examples in which overlap populations may not vary inversely with metal–metal distances, particularly when their locations within a low dimensional network are distinctly different.[17,18] However, an analysis of all of the individual distances and Sc–Sc overlap populations in this complex structure would be cumbersome. Table 3 lists the Sc–Sc distances under 4.0 Å and the overlap populations for those with values of the latter above 0.02, along with a key to describe the location of each in the structure. The Sc–Sc overlap populations are listed in descending order, and the first 20 to 30, all of which lie within the chains, parallel increases in distances fairly well. Notable deviations then begin to occur everywhere on the list, depending on the environment of the metal–metal bond. For example, the overlap population for the atom pair 7–12 (0.182) occurs very low on the list considering its distance (3.11 Å), but this bond occurs on the periphery of the 2D sheet. Contrastingly, that for 5–6 (0.214) lies high on the list for its distance (3.29 Å), but this bond occurs between columns within the 2D sheet. This correlation is summarized in Figure 6, part A, where all of the independent Sc–Sc overlap populations are plotted as a function of distance. The data fall basically into two distinct populations, corresponding to either internal or surface (exterior) Sc–Sc bonding. Those for internal Sc–Sc bonds in and between columns, labeled i1 and i2, respectively (following Table 3) together with data for the shortest axial repeats i3 all fall on the upper empirical curve with higher overlap populations for the corresponding distances. The surface and interlayer (exterior) Sc–Sc bonds with Te neighbors (e1 and e2, respectively) occur on a lower curve and have lower overlap populations for their distances. Although we have seen such qualitatively parallel trends before,[17,18] this clear segregation of the Sc–Sc bonds in Sc_9Te_2 into internal and external bond classes has never been quite so conspicuous and compelling. The usual explanation has been that metal-based electrons on Sc atoms with anionic tellurium near neighbors are repelled or, equivalently, that the d states on these metal atoms are raised (become relatively oxidized) through mixing with Te states. Thus, metal bonds located on the external part of the aggregate follow a different bond order–bond length relationship than those located within the metal aggregates.

Since the Sc_9Te_2 structure is a distorted version of the Ti_9Se_2 structure type, it seemed necessary to determine whether there are conspicuous bonding differences between the two structure types that might justify the distortion. The same calculations were therefore performed for Sc_9Te_2 with an undistorted, or structurally averaged, Ti_9Se_2-type structure. The lower half (B) of Figure 6 shows the same plot of Sc–Sc overlap populations versus distances, with the number of data points greatly reduced because of the higher symmetry of the structure. Again, the Sc–Sc bonding is differentiated into the two categories, interior and exterior distances, but to a lesser extent. A significant difference is that some of the populations for internal Sc–Sc bonding along the short *a* axis (grouped as i3) are relatively large, given their distances, compared with the other internal bonding (i1, i2) and with that in the real structure. This distinction was noted as well in the electron-poorer compounds Sc_2Te and Sc_8Te_3 with ~1D blades and 2D sheets, respectively. The distortion essentially disproportionates the strong ~3.9 Å bonds along the short axis, $\vec{a}$, into shorter and stronger at ~3.5 Å bonds well up on the curve in Figure 6(A) plus longer inconsequential separations near 4.3 Å (off-scale), Figure 2. Such distortions should be spontaneous given the logarithmic dependence of bond order on distance if the elastic energies and bonding changes elsewhere in the structure are not too important. The distortion in general raises the curve of overlap populations as a function of distance, curve i1, i2 in Figure 6B lying closer to e1, the exterior populations in the real structure, Figure 6A, than to curve defined by interior bonding i1, i2, i3. In other words, the distortion has logically emptied the moderate or less bonding states in the Ti_9Se_2 arrangement and lowered the energy of those that are more bonding. The effects are difficult to discern with only a collective COOP curve comparison. There are appreciable changes during this distortion, however, and over 80 distinct Sc–Sc contacts would need separate analysis. The symmetry reduction found for Sc_9Te_2 relative to a Ti_9Se_2-type aristotype may take place at elevated temperatures, but it must occur above 1135 °C where the crystals were grown.

Such a differentiation does not occur for Sc_8Te_3, which occurs in a Ti_8Se_3 structure type but with clear responses to the larger anion and smaller number of valence electrons. On the other hand, the interior metal positions for Y_8Te_3 refine with somewhat extreme thermal ellipsoids suggestive of a missing superstructure, but no evidence for this can be found.[28] Some incommensurate behavior may be possible.

Conclusions. The structure of Sc_9Te_2 consists of distorted 3×3 columns of scandium metal that extend infinitely down the *a* axis, and are joined laterally into 2D layers along the *b* axis. A corrugated layer of tellurium atoms separates the rumpled metal layers in the $\vec{c}$ direction. The Sc_9Te_2 structure is the result of distortion of the Ti_9Se_2 structure type with doubled *a* and *b* axes and alternating long and short Sc–Sc distances along the columns. Extended Hückel calculations show that the distortion to lowered symmetry generates more regular Sc–Sc bond order – distance relationships (Figure 6A) that clearly distinguish between inner and outer positions on the metal columns or layers.

Acknowledgements

We thank Jerry Ostenson for the magnetic susceptibility measurements and Ilia Guzei for help with the CCD diffractometer. This work was supported by the National Science Foundation, Solid State Chemistry, via grants DMR-9510278 and -9809850 and was carried out in the facilities of the Ames Laboratory, U.S. Department of Energy.

Supporting Information Available

Tables of additional crystallographic and refinement parameters, anisotropic thermal parameters, and a complete listing of nearest neighbor distances. This material is available free-of-charge via the Internet at http//pubs.acs.org.

References

(1) Pauling, L. *Phys. Review.* **1938**, *54*, 899.; Pauling, L. *The Nature of the Chemical Bond;* Cornell University Press: Ithaca, N.Y., **1960**, p. 400.

(2) Whangbo, M. H.; Canadell, E.; Foury, P. *Science* **1991**, *252*, 96.

(3) Thorne, R. E. *Physics Today* **1996**, *49*, 42.

(4) Owens, J. P.; Franzen, H. F. *Acta Crystallogr.* **1974**, *B30*, 427.

(5) Weirich, T. E.; Pöttgen, R.; Simon, A. *Z. Kristallogr.* **1996**, *211*, 929.

(6) Owens, J. P.; Conard, B. R.; Franzen, H. F. *Acta Crystallogr.* **1967**, *23*, 77.

(7) Weirich, T. E.; Pöttgen, R.; Simon, A. *Z. Kristallogr.* **1996**, *211*, 928.

(8) Weirich, T. E.; Ramlau, R.; Simon, A.; Hovmöller, S.; Zou, X. *Nature* **1996**, *382*, 144.

(9) Weirich, T. E.; Simon, A.; Pöttgen, R. *Z. Anorg. Allg. Chem.* **1996**, *622*, 630.

(10) Gronvold, F.; Kjekshus, A.; Raaum, F. *Acta Cryst.* **1961**, *14*, 930.

(11) Harbrecht, B.; Conrad, M.; Degen, T.; Herbertz, R. *J. Alloys Compd.* **1997**, *255*, 178.

(12) Abdon, R. L.; Hughbanks, T. *Angew. Chem., Int. Ed. Engl.* **1994**, *33*, 2414.

(13) Schewe-Miller, I. M.; Young, Y. G. *J. Alloys Compd.* **1994**, *216*, 113.

(14) Harbrecht, B.; Leersch, R. *J. Alloys Compd.* **1996**, *238*, 13.

(15) Brattas, L.; Kjekshus, A. *Acta Chem. Scand.* **1971**, *25*, 2350.

(16) Orlygsson, G.; Harbrecht, B. *Inorg. Chem.* **1999**, *38*, 3377.

(17) Maggard, P. A.; Corbett, J. D. *Angew. Chem., Int. Ed. Engl.* **1997**, *36*, 1974.

(18) Maggard, P. A.; Corbett, J. D. *Inorg. Chem.* **1998**, *37*, 814.

(19) *SAINTPLUS*; Bruker AXS, Inc.: Madison, Wisconsin 53719, **1996**.

(20) Blessing, R. H. *Acta Cryst.* **1995**, *A51*, 33.

(21) Sheldrick, G. M. SHELXS-86, Universität Göttingen, Germany, 1986.

(22) Hoffman, R. *J. Chem. Phys.* **1963**, *39*, 1397; Whangbo, M.; Hoffman, R. *J. Am. Chem. Soc.* **1978**, *100*, 6093.

(23) Poeppelmeier, K. R.; Corbett, J. D. *Inorg. Chem.* **1977**, *16*, 1107.

(24) Group theoretical methods[25,26] predict the descent in symmetry involves at least two steps: a transition corresponding to the U_1 irreducible representation of *Pbam* ($\vec{k} = \frac{a^* + c^*}{2}$) to give $Cmc2_1$ followed by another transition at the Γ_4 point of $Cmc2_1$ ($\vec{k} = 0$) to yield *Cc*. However, the first step does not meet the Lifshitz criterion and may not be continuous. One could reverse the order of the transitions, which would make $P2_1/c$ the intermediate, and the second step would be unallowed by the Lifshitz criterion.

(25) Stokes, H. T.; Hatch, D. M. *Isotropy Subgroups of the 230 Crystallographic Space Groups*; World Scientific Publishing Co.: Singapore, 1988.

(26) Franzen, H. F. *Physical Chemistry of Solids;* World Scientific Publishing Co.: Singapore, 1994.

(27) Spedding, F. H.; Croat, J. J. *J. Chem. Phys.* **1973**, *59*, 2451.

(28) Maggard, P. A.; Corbett, J. D., unpublished results.

Table 1. Single Crystal X-ray Data Collection and Refinement Parameters for Sc_9Te_2.

Formula weight	659.84
Space group, Z	Cc (No. 9), 8
Lattice parameters and cell volume	
a (Å)	7.7576(1)
b (Å)	15.654(3)
c (Å)	17.283(3)
β (deg.)	90.01(3)
V (Å^3)	2098.8(6)
d_{calc} (g/cm^3)	4.176
μ (Mo K_α) (cm^{-1})	108.10
Residuals $R1$, w$R2$ (×100)[a]	3.1; 9.8

[a] $R1 = \Sigma||F_o| - |F_c||/\Sigma|F_o|$; $wR2 = [\sum w(|F_o|^2-|F_c|^2)^2/\sum w(|F_o|^2)^2]^{1/2}$, $w = 1/(\sigma_F{}^2)^2$.

Table 2. Positional and Isotropic-Equivalent Thermal Parameters for Sc_9Te_2.

Atom^a	x	y	z	U_{eq}(Å^2)^b
Te1	0.96968(8)	0.38090(4)	0.98396(4)	0.0080(2)
Te2	0.96841(9)	0.62951(3)	0.88165(4)	0.0061(2)
Te3	0.46538(9)	0.62949(3)	0.88165(4)	0.0062(2)
Te4	0.46386(8)	0.38088(4)	0.98397(4)	0.0082(2)
Sc1^1	0.7179(3)	0.4849(1)	0.8945(1)	0.0074(5)
Sc2^1	0.2174(3)	0.4759(1)	0.8819(2)	0.0073(5)
Sc3^1	0.2178(4)	0.2260(1)	0.9855(2)	0.0076(5)
Sc4^1	0.2178(4)	0.7350(1)	0.9743(2)	0.0080(5)
Sc5^2	0.7156(3)	0.6808(1)	0.7633(2)	0.0083(5)
Sc6^2	0.7152(3)	0.4316(2)	0.1025(2)	0.0076(5)
Sc7^2	0.2155(3)	0.4245(1)	0.1089(1)	0.0090(5)
Sc8^2	0.2157(3)	0.6741(1)	0.7576(1)	0.0071(5)
Sc9^3	0.9908(3)	0.5740(1)	0.0469(1)	0.0102(5)
Sc10^3	0.9905(3)	0.8247(1)	0.8200(1)	0.0093(5)
Sc11^3	0.9409(3)	0.3247(1)	0.8198(1)	0.0085(5)
Sc12^3	0.4406(3)	0.5740(1)	0.0470(1)	0.0098(5)
Sc13^4	0.4918(3)	0.2624(1)	0.1272(1)	0.0101(5)
Sc14^4	0.4927(3)	0.5120(1)	0.7389(1)	0.0109(5)
Sc15^4	0.9389(3)	0.2623(1)	0.1272(1)	0.0080(5)
Sc16^4	0.9375(3)	0.4881(1)	0.2388(1)	0.0081(5)
Sc17^5	0.2166(4)	0.6147(1)	0.1994(2)	0.0078(4)
Sc18^5	0.7166(4)	0.3651(1)	0.6660(2)	0.0089(4)

[a] Superscripts 1–5 denote corresponding metal positions within the Ti_9Se_2 structure.

[b] $U_{eq} = (1/3)\Sigma_i\Sigma_j U_{ij}a_i^*a_j^*\vec{a}_i\vec{a}_j$.

Table 3. Sc–Sc Distances (Å) and Corresponding Overlap Populations (OP).

Atom 1	Atom 2	Distance	OP	i,e[a]	Atom 1	Atom 2	Distance	OP	i,e[a]
7	8	3.00	0.363	i1	14	16	3.45	0.153	i3
14	17	3.00	0.306	i2	13	15	3.47	0.149	i3
13	18	3.00	0.305	i2	10	11	3.49	0.145	i3
15	18	3.01	0.298	i2	9	12	3.49	0.142	i3
16	17	3.01	0.298	i2	6	12	3.23	0.141	e1
6	16	3.05	0.274	i1	6	9	3.24	0.140	e1
5	15	3.05	0.273	i1	5	10	3.25	0.137	e1
6	14	3.05	0.273	i1	5	11	3.25	0.137	e1
9	18	3.11	0.272	i2	4	15	3.18	0.137	e1
5	13	3.06	0.272	i1	5	16	3.18	0.133	e1
12	18	3.12	0.268	i2	5	14	3.19	0.132	e1
10	17	3.12	0.267	i2	4	13	3.20	0.130	e1
11	17	3.13	0.263	i2	6	15	3.20	0.130	e1
16	18	3.13	0.233	i2	6	13	3.19	0.130	e1
15	17	3.14	0.229	i2	1	16	3.21	0.127	e1
14	18	3.15	0.226	i2	1	14	3.24	0.120	e1
13	17	3.15	0.224	i2	3	13	3.29	0.114	e1
5	6	3.29	0.214	i1	4	12	3.30	0.112	e1
12	17	3.22	0.213	i2	4	9	3.32	0.108	e1
9	17	3.23	0.209	i2	1	11	3.31	0.108	e1
11	18	3.24	0.206	i2	3	15	3.32	0.108	e1
8	13	3.26	0.204	i1	2	14	3.32	0.106	e1
11	16	3.25	0.204	i1	3	9	3.36	0.104	e1
7	14	3.26	0.203	i1	1	10	3.33	0.104	e1
8	15	3.27	0.202	i1	2	10	3.35	0.104	e1
10	14	3.25	0.202	i2	9	16	3.60	0.103	i2
10	18	3.25	0.201	i2	12	14	3.60	0.103	i2
7	16	3.27	0.201	i1	7	13	3.34	0.102	e1
12	15	3.26	0.200	i2	8	14	3.34	0.100	e1
9	13	3.26	0.199	i2	2	11	3.37	0.100	e1
7	12	3.11	0.182	e1	3	12	3.38	0.100	e1

Table 3. (continued)

7	9	3.11	0.181	e1
7	17	3.36	0.179	i2
8	11	3.13	0.176	e1
6	18	3.37	0.176	i2
10	8	3.13	0.175	e1
5	17	3.39	0.171	i2
8	18	3.38	0.170	i2
3	18	3.43	0.164	i2
2	17	3.46	0.155	i2
2	16	3.34	0.100	e1
7	15	3.34	0.100	e1
11	13	3.62	0.100	i2
10	15	3.62	0.099	i2
8	16	3.35	0.098	e1
17	18	3.93	0.041	i3
4	11	3.48	0.025	e2
4	10	3.49	0.024	e2

[a] i = interior Sc–Sc bond; i1 – inside 3 × 3 column ; i2 – inside the octahedral chain shared between columns; i3 – along short axis repeat; e = exterior; e1 – on exterior of 3 × 3 block; e2 – interlayer.

Supporting Information
Sc_9Te_2: A 2D Distortion Wave in the Scandium-Richest Telluride

Paul A. Maggard and John D. Corbett

Table S1. Single Crystal X-ray Data Collection and Refinement Parameters for Sc_9Te_2.

Formula weight	659.84
Space group, Z	Cc (No. 9), 8
Lattice parameters, volume (Å, deg., Å^3)	
a	7.7576(1)
b	15.654(3)
c	17.283(3)
β	90.01(3)
V	2098.8(6)
d_{calc} g/cm^3	4.176
Radiation; $2\theta_{max}$	Mo Kα; 56°
Octants measured	±h, ±k, ±l
Diffractometer, scan method	Bruker CCD, area detector
Temperature, °C	23
Absorption method	SADABS
μ, Mo K_α (cm^{-1})	108.10
Rel. transm. coeff. range	0.542–1.00
Reflections: Total measured	7239
Unique ($I \geq 3\sigma(I)$)	2141
Number of variables	200
Residuals R_1, w$R2$ (×100)[a]	3.1; 9.8
Goodness of fit	0.89
Secondary ext.	0.00016(4)

[a] $R1 = \Sigma||F_o| - |F_c||/\Sigma|F_o|$; $wR2 = [\sum w(|F_o|^2-|F_c|^2)^2/\sum w(|F_o|^2)^2]^{1/2}$, $w = 1/(\sigma_F^2)^2$.

Table S2. U_{ij} (Å^2) values for Sc_9Te_2.

Atom	U_{11}[a]	U_{22}	U_{33}	U_{12}	U_{13}	U_{23}
Te1	0.0073(3)	0.0079(4)	0.0089(5)	-0.0016(3)	-0.0005(3)	0.0002(3)
Te2	0.0061(4)	0.0055(3)	0.0062(4)	-0.0015(3)	0.0004(3)	0.0003(3)
Te3	0.0065(4)	0.0057(3)	0.0060(4)	-0.0015(3)	0.0001(3)	0.0003(3)
Te4	0.0081(4)	0.0077(4)	0.0088(5)	-0.0017(3)	-0.0008(3)	0.0005(3)
Sc1	0.0064(8)	0.0080(8)	0.0078(1)	0.0010(8)	-0.0017(8)	0.0001(8)
Sc2	0.0055(8)	0.0077(8)	0.009(1)	0.0009(7)	0.0003(8)	0.0014(7)
Sc3	0.0085(5)	0.0063(8)	0.008(1)	-0.0020(7)	-0.0019(8)	0.0013(8)
Sc4	0.0092(8)	0.0049(8)	0.010(1)	-0.0020(7)	0.0008(8)	-0.0004(8)
Sc5	0.0082(9)	0.0078(9)	0.009(1)	0.0023(8)	-0.0001(8)	0.0000(8)
Sc6	0.0092(9)	0.0041(9)	0.010(1)	0.0015(8)	0.0000(8)	-0.0002(7)
Sc7	0.0083(9)	0.0054(9)	0.013(1)	-0.0002(8)	0.0004(9)	-0.0008(7)
Sc8	0.0091(9)	0.0062(9)	0.006(1)	-0.0011(8)	-0.0011(8)	-0.0004(7)
Sc9	0.0137(2)	0.0070(8)	0.0108(9)	0.0010(6)	-0.0012(9)	-0.0006(6)
Sc10	0.0147(1)	0.0065(8)	0.0067(9)	0.0001(6)	-0.0008(9)	0.0013(6)
Sc11	0.012(1)	0.0059(8)	0.0067(9)	-0.0004(6)	0.0001(9)	-0.0008(6)
Sc12	0.012(1)	0.0064(8)	0.0105(9)	0.0013(6)	-0.0008(9)	-0.0005(6)
Sc13	0.0154(1)	0.0080(9)	0.0079(9)	-0.0005(6)	0.001(1)	-0.0001(6)
Sc14	0.016(1)	0.0050(8)	0.0103(9)	-0.0003(6)	0.003(1)	0.0019(7)
Sc15	0.009(1)	0.0079(9)	0.0070(8)	-0.0001(6)	-0.0032(9)	0.0004(6)
Sc16	0.009(1)	0.0052(8)	0.0105(9)	0.0002(6)	-0.0032(9)	-0.0006(6)
Sc17	0.0074(7)	0.0061(8)	0.010(1)	-0.0010(6)	-0.0027(8)	0.0007(6)
Sc18	0.0084(6)	0.0066(8)	0.012(1)	0.0020(7)	0.0011(8)	0.0010(6)

[a] $T = \exp[-2\pi^2(U_{11}h^2a^{*2} + U_{22}k^2b^{*2} + U_{33}l^2c^{*2} + 2U_{12}hka^*b^* + 2U_{13}hla^*c^* + 2U_{23}klb^*c^*)]$.

Table S3. Interatomic Distances (< 4.0 Å) for Sc_9Te_2.

Te1	Sc1	2.976(2)	Te4	Sc4	3.021(2)	Sc2	Sc14	3.316(4)
	Sc2	3.002(3)		Sc6	2.937(3)		Sc16	3.339(3)
	Sc3	3.096(2)		Sc7	2.974(3)		Sc17	3.458(4)
	Sc4	3.011(2)		Sc10	2.975(3)			
	Sc6	2.953(3)		Sc12	3.219(2)	Sc3	Te1	3.096(2)
	Sc7	2.961(3)		Sc13	3.100(2)		Te2	3.047(3)
	Sc9	3.217(2)					Te3	3.056(3)
	Sc11	2.979(2)	Sc1	Te1	2.976(2)		Te4	3.086(2)
	Sc15	3.103(2)		Te2	2.991(2)		Sc4	3.886(4)
				Te3	3.001(2)		Sc5	3.905(4)
Te2	Sc1	2.991(2)		Te4	2.988(3)		Sc7	3.769(4)
	Sc2	3.084(2)		Sc2	3.891(4)		Sc9	3.357(3)
	Sc3	3.047(3)		Sc2	3.884(4)		Sc10	3.879(4)
	Sc4	3.005(3)		Sc5	3.814(4)		Sc11	3.899(4)
	Sc5	2.946(3)		Sc6	3.690(4)		Sc12	3.378(3)
	Sc8	2.961(3)		Sc9	3.655(3)		Sc13	3.292(3)
	Sc9	2.990(3)		Sc10	3.327(3)		Sc15	3.316(4)
	Sc10	3.240(2)		Sc11	3.310(3)		Sc18	3.430(4)
	Sc16	3.088(2)		Sc12	3.676(3)			
				Sc14	3.235(4)	Sc4	Te1	3.011(2)
Te3	Sc1	3.001(2)		Sc16	3.213(4)		Te2	3.005(3)
	Sc2	3.079(2)					Te3	2.997(3)
	Sc3	3.056(3)	Sc2	Te1	3.002(3)		Te4	3.021(2)
	Sc4	2.997(3)		Te2	3.084(2)		Sc3	3.886(4)
	Sc5	2.932(3)		Te3	3.079(2)		Sc6	3.792(4)
	Sc8	2.973(3)		Te4	2.997(2)		Sc8	3.864(4)
	Sc11	3.243(2)		Sc1	3.884(4)		Sc9	3.320(3)
	Sc12	2.992(3)		Sc1	3.891(4)		Sc10	3.492(3)
	Sc14	3.084(2)		Sc8	3.774(4)		Sc11	3.478(3)
				Sc9	3.684(3)		Sc12	3.303(3)
Te4	Sc1	2.988(3)		Sc10	3.352(3)		Sc13	3.200(4)
	Sc2	2.997(2)		Sc11	3.370(3)		Sc15	3.179(3)
	Sc3	3.086(2)		Sc12	3.674(3)			

Table S3. (continued)

Sc5	Te2	2.946(3)	Sc7	Sc3	3.769(4)	Sc9	Sc4	3.320(3)
	Te3	2.932(3)		Sc6	3.884(4)		Sc6	3.235(3)
	Sc1	3.814(4)		Sc6	3.880(4)		Sc7	3.109(3)
	Sc3	3.905(4)		Sc8	2.997(2)		Sc12	3.489(2)
	Sc6	3.289(2)		Sc9	3.109(3)		Sc13	3.260(3)
	Sc8	3.881(4)		Sc12	3.110(3)		Sc16	3.604(3)
	Sc8	3.882(4)		Sc13	3.336(3)		Sc17	3.229(4)
	Sc10	3.253(3)		Sc14	3.264(3)		Sc18	3.110(3)
	Sc11	3.251(3)		Sc15	3.340(3)			
	Sc13	3.055(4)		Sc16	3.268(3)	Sc10	Te2	3.240(2)
	Sc14	3.185(3)		Sc17	3.363(3)		Te4	2.975(3)
	Sc15	3.054(3)					Sc1	3.327(3)
	Sc16	3.183(3)	Sc8	Te2	2.961(3)		Sc2	3.352(3)
	Sc17	3.386(3)		Te3	2.973(3)		Sc3	3.879(4)
				Sc2	3.774(4)		Sc4	3.492(3)
Sc6	Te1	2.953(3)		Sc4	3.864(4)		Sc5	3.253(3)
	Te4	2.937(3)		Sc5	3.882(4)		Sc8	3.126(3)
	Sc1	3.690(4)		Sc5	3.881(4)		Sc11	3.494(2)
	Sc4	3.792(4)		Sc7	2.997(2)		Sc14	3.251(3)
	Sc5	3.289(2)		Sc10	3.126(3)		Sc15	3.622(3)
	Sc7	3.880(4)		Sc11	3.125(3)		Sc17	3.124(3)
	Sc7	3.884(4)		Sc13	3.264(3)		Sc18	3.249(3)
	Sc9	3.235(3)		Sc14	3.340(3)			
	Sc12	3.230(3)		Sc15	3.269(3)	Sc11	Te1	2.979(2)
	Sc13	3.193(3)		Sc16	3.347(3)		Te3	3.243(2)
	Sc14	3.053(3)		Sc18	3.382(3)		Sc1	3.310(3)
	Sc15	3.195(3)					Sc2	3.370(3)
	Sc16	3.051(3)	Sc9	Te1	3.217(2)		Sc3	3.899(4)
	Sc18	3.368(3)		Te2	2.990(3)		Sc4	3.478(3)
				Sc1	3.655(3)		Sc5	3.251(3)
Sc7	Te1	2.961(3)		Sc2	3.684(3)		Sc8	3.125(3)
	Te4	2.974(3)		Sc3	3.357(3)		Sc10	3.494(2)

Table S3. (continued)

Sc11	Sc13	3.619(3)	Sc14	Te3	3.084(2)	Sc16	Sc8	3.347(3)
	Sc16	3.248(3)		Sc1	3.235(4)		Sc9	3.604(3)
	Sc17	3.131(3)		Sc2	3.316(4)		Sc11	3.248(3)
	Sc18	3.239(3)		Sc5	3.185(3)		Sc14	3.451(2)
				Sc6	3.053(3)		Sc17	3.013(3)
Sc12	Te3	2.992(3)		Sc7	3.264(3)		Sc18	3.131(3)
	Te4	3.219(2)		Sc8	3.340(3)			
	Sc1	3.676(3)		Sc10	3.251(3)	Sc17	Sc2	3.458(4)
	Sc2	3.674(4)		Sc12	3.603(3)		Sc5	3.386(3)
	Sc3	3.378(3)		Sc16	3.451(2)		Sc7	3.363(3)
	Sc4	3.303(3)		Sc17	2.999(3)		Sc9	3.229(4)
	Sc6	3.230(3)		Sc18	3.146(3)		Sc10	3.124(3)
	Sc7	3.110(3)					Sc11	3.131(3)
	Sc9	3.489(2)	Sc15	Te1	3.103(2)		Sc12	3.220(3)
	Sc14	3.603(3)		Sc3	3.316(4)		Sc13	3.154(3)
	Sc15	3.257(3)		Sc4	3.179(3)		Sc14	2.999(3)
	Sc17	3.220(3)		Sc5	3.054(3)		Sc15	3.142(3)
	Sc18	3.119(3)		Sc6	3.195(3)		Sc16	3.013(3)
				Sc7	3.340(3)		Sc18	3.934(4)
Sc13	Te4	3.100(2)		Sc8	3.269(3)			
	Sc3	3.292(3)		Sc10	3.622(3)	Sc18	Sc3	3.430(4)
	Sc4	3.200(4)		Sc12	3.257(3)		Sc6	3.368(3)
	Sc5	3.055(4)		Sc13	3.468(3)		Sc8	3.382(3)
	Sc6	3.193(3)		Sc17	3.142(3)		Sc9	3.110(3)
	Sc7	3.336(3)		Sc18	3.012(3)		Sc10	3.249(3)
	Sc8	3.264(3)					Sc11	3.239(3)
	Sc9	3.260(3)	Sc16	Te2	3.088(2)		Sc12	3.119(3)
	Sc11	3.619(3)		Sc1	3.213(4)		Sc13	2.998(3)
	Sc15	3.468(3)		Sc2	3.339(3)		Sc14	3.146(3)
	Sc17	3.154(3)		Sc5	3.183(3)		Sc15	3.012(3)
	Sc18	2.998(3)		Sc6	3.051(3)		Sc16	3.131(3)
				Sc7	3.268(3)		Sc17	3.934(4)

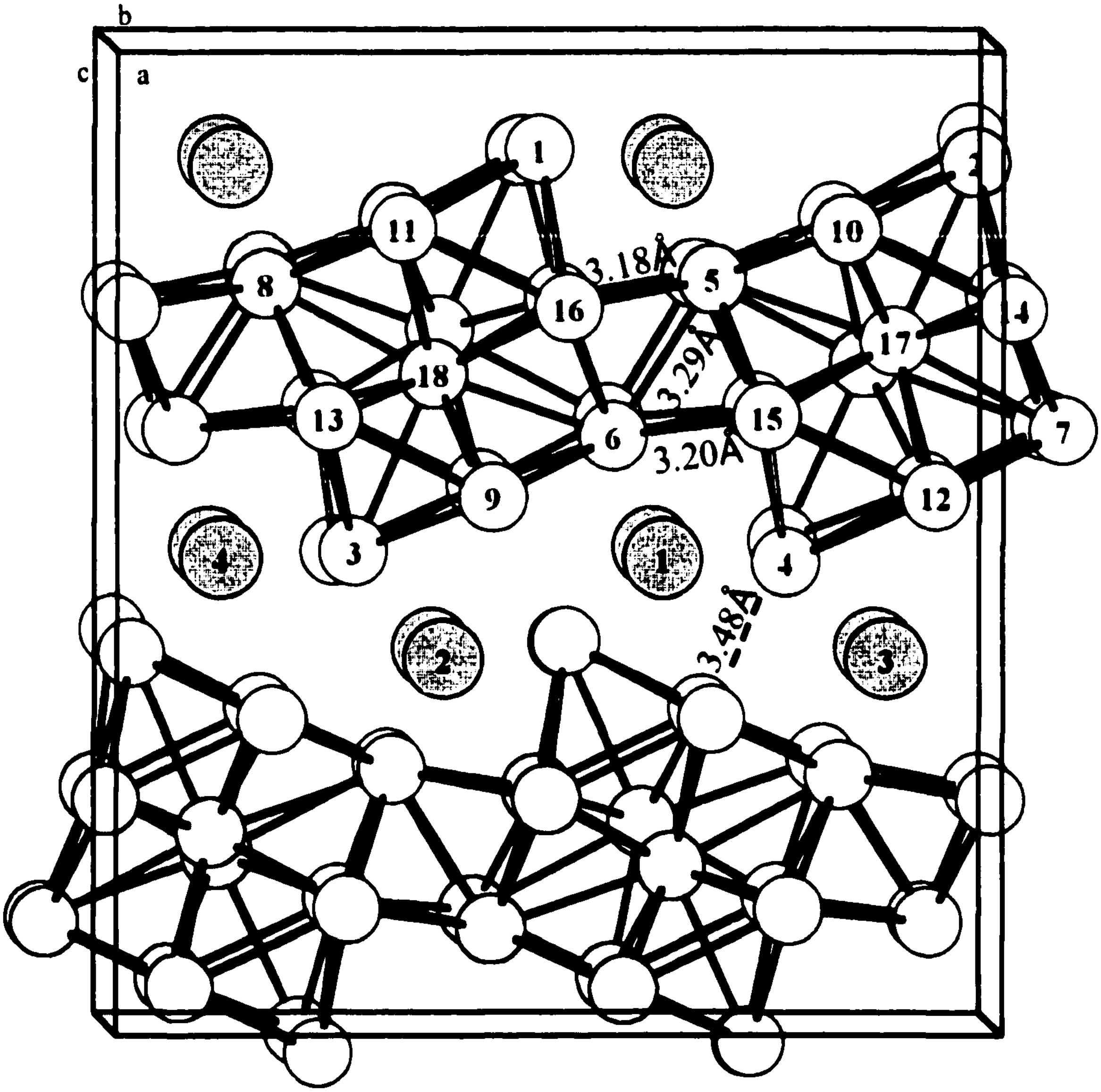

Figure 1. ~[100] section of the unit cell of monoclinic Sc_9Te_2. The pairs of similar but independent metal atoms within the 3 × 3 columns that alternate down the short *a* axis (1–2, 3–4, 5–8, 6–7, 9–12, 10–11, 13–15, 14–16, 17–18), as marked on separate columns. White atoms are scandium; gray atoms are tellurium.

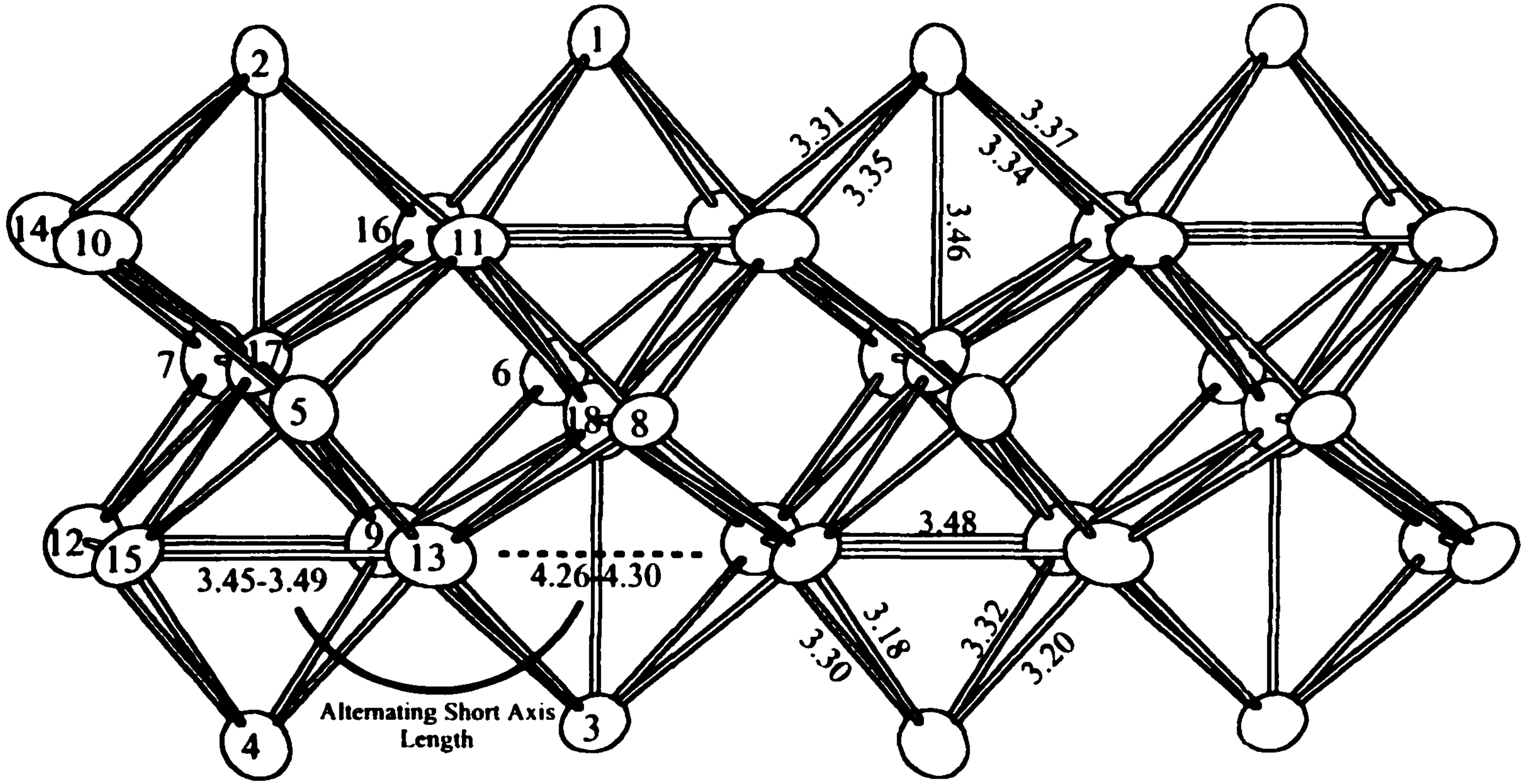

Figure 2. The repeating patterns of shared, distorted, octahedra along the short *a* axis of Sc_9Te_2 drawn with 99% probability thermal ellipsoids and distances marked in Å. The darker bonds emphasize the zigzag arrangement of octahedra, and the arcs, the alternating octahedral waist (A) and height (B) pattern.

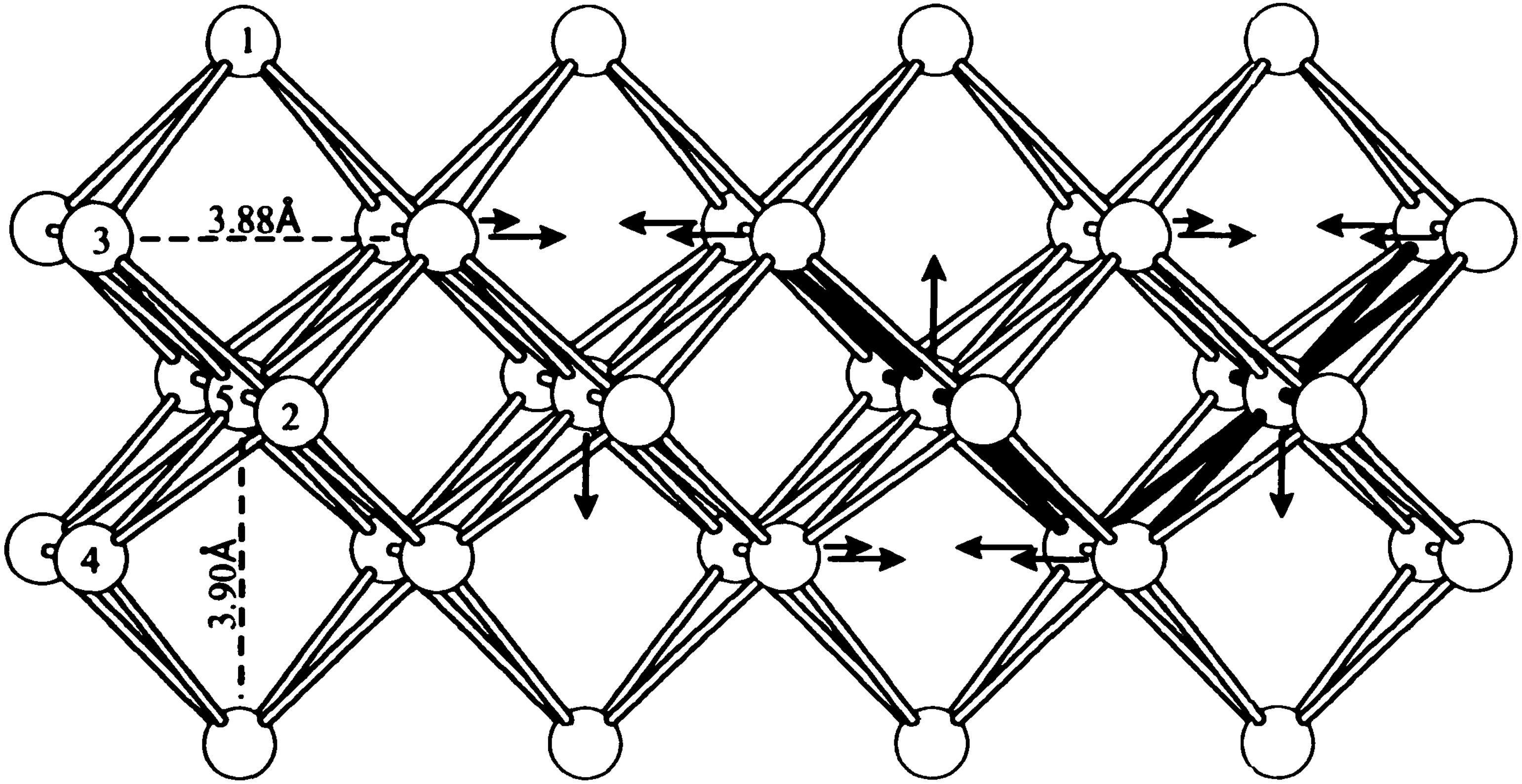

Figure 3. A view along the short *a* axis of the ideal undistorted, or structurally averaged, Sc_9Te_2 in the orthorhombic Ti_9Se_2 structure type. The average distances of the waist and height dimensions of the octahedra are marked as well as the metal displacement pattern that produces the observed distorted structure in Figure 2.

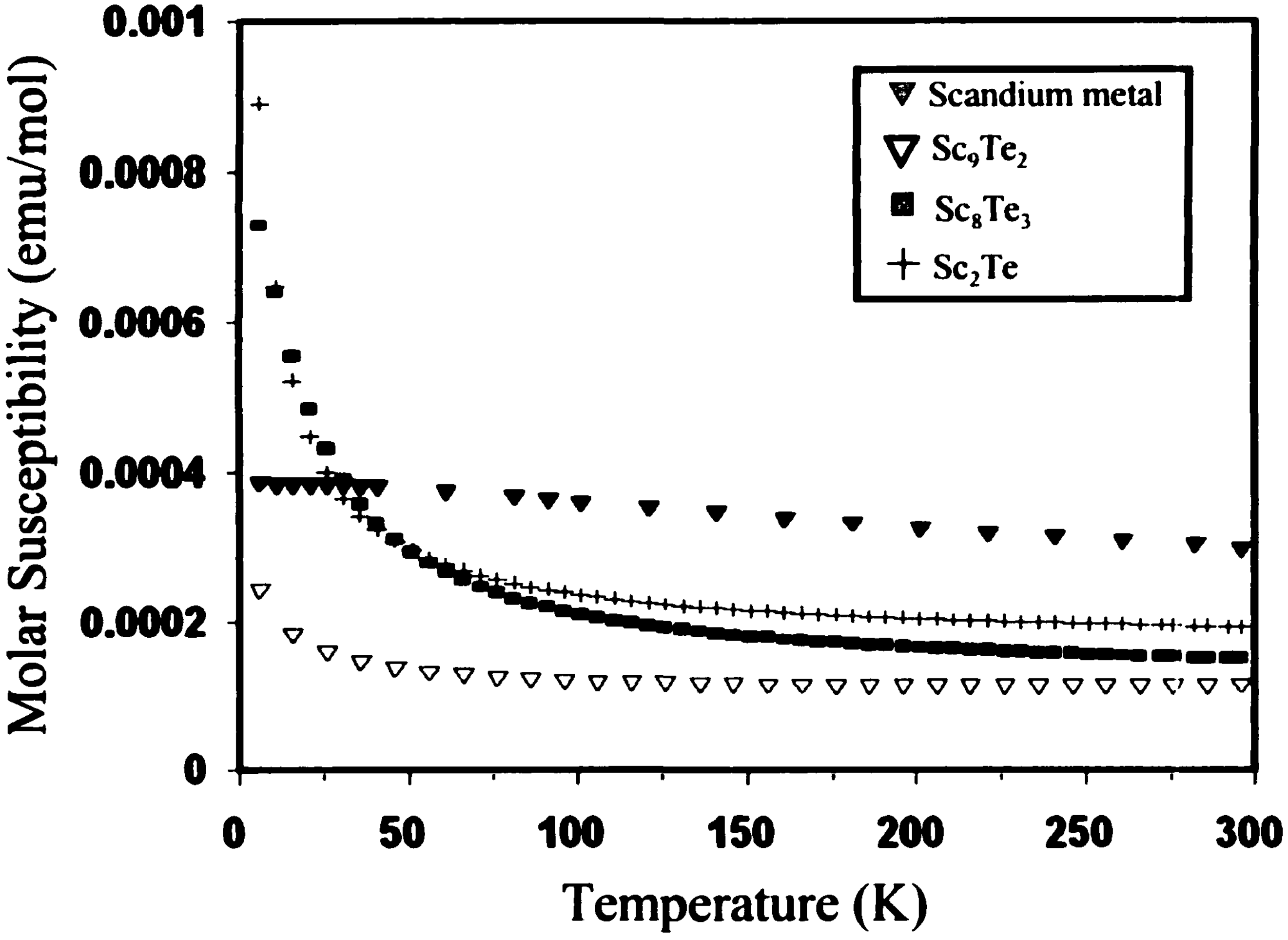

Figure 4. Molar magnetic susceptibilities per scandium versus temperature for Sc_9Te_2, other scandium-rich tellurides, and the metal.

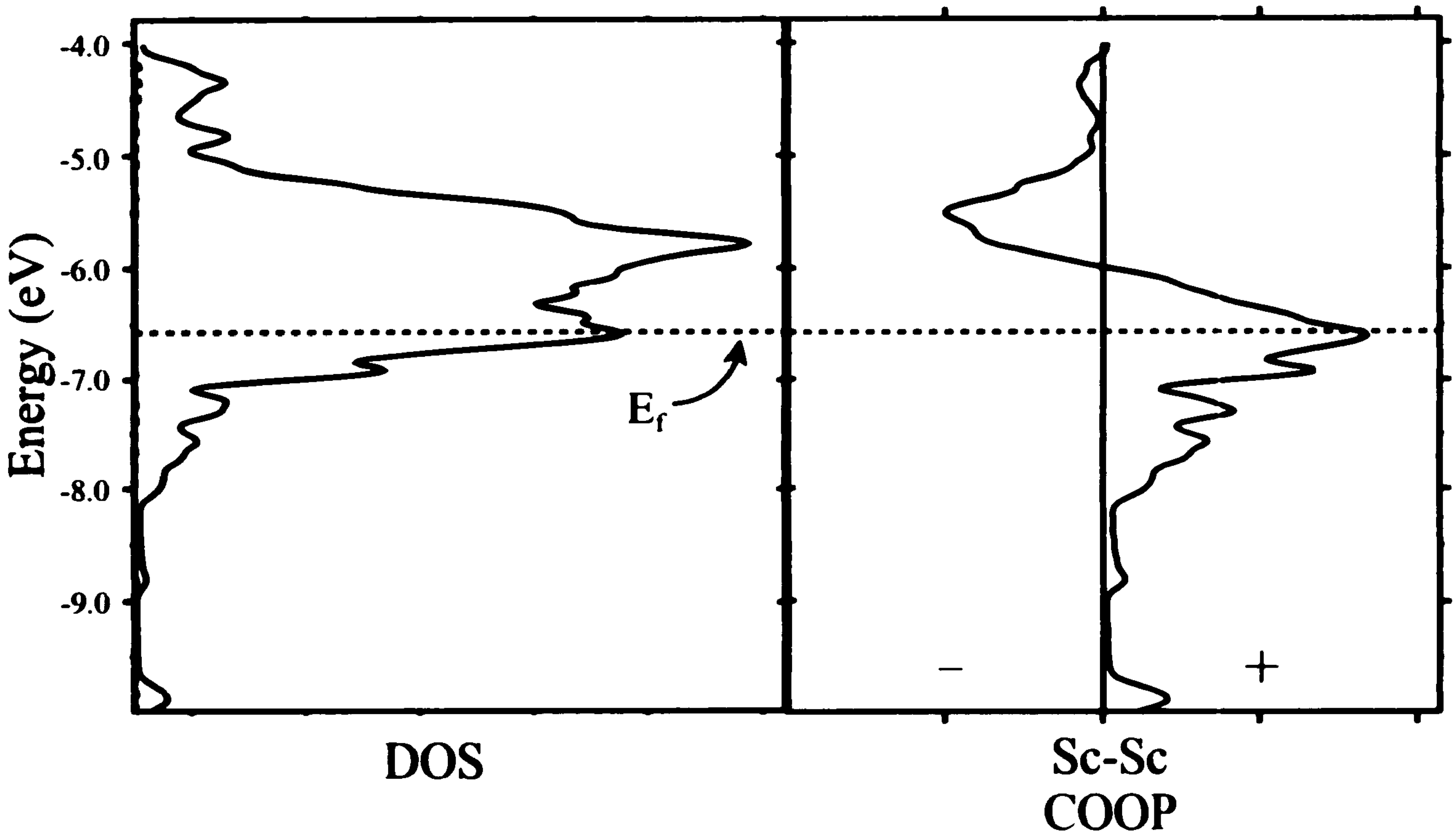

Figure 5. Total densities of states (DOS) (left) and Sc–Sc crystal orbital overlap populations (COOP) (right) curves for Sc_9Te_2. The minute Te contributions (dashed) are projected out in the former.

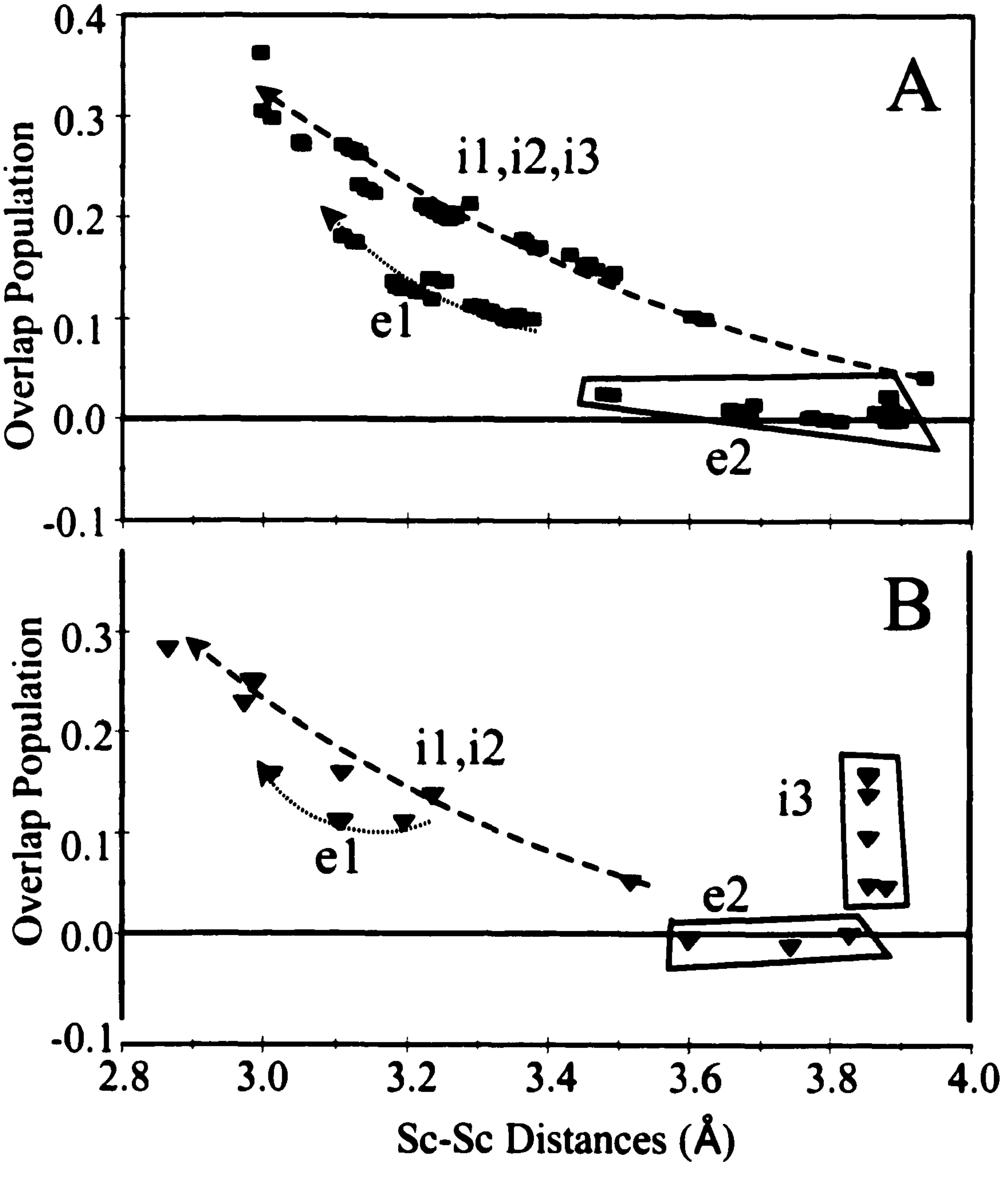

Figure 6. Sc–Sc overlap populations versus distances for the real Sc_9Te_2 structure (A) and the equivalent undistorted Ti_9Se_2 aristotype (B). Note the clear distinction in A between interior (i) and exterior (e) bond populations within the layer of bridged columns. The categories i3 and e2 refer to values along the short axis and between layers, respectively (see Table 3).

PART 2. RELATED TERNARY PHASES

CHAPTER 5. $Sc_5Ni_2Te_2$: SYNTHESIS, STRUCTURE, AND BONDING OF A METAL–METAL BONDED CHAIN PHASE, A RELATIVE OF Gd_3MnI_3

A paper published in Inorganic Chemistry

Inorg. Chem. **1999**, *38*, 1945

Paul A. Maggard and John D. Corbett

Department of Chemistry, Iowa State University, Ames, IA 50011

Abstract

$Sc_5Ni_2Te_2$ has been prepared by high-temperature solid-state techniques, and the structure determined at 23 °C by single crystal and powder X-ray diffraction methods to be orthorhombic, *Pnma* (No. 62) with $Z = 4$, $a = 17.862(1)$, $b = 3.9533(3)$, $c = 10.6398(6)$ Å. The structure contains pairs of eclipsed zigzag chains of nickel atoms that are sheathed by scandium atoms and demarcated from other chains by tellurium atoms. The structure is isotypic with that of $Hf_5Co_{1-x}P_{3-x}$, but shifted atomic positions and a different ordering of the main group and late transition elements give it a clearly 1D character. The differences in dimensionality, ordering and bonding are discussed, and comparisons are made with Gd_3MnI_3 and rare-earth-metal cluster halides in general.

Introduction

The plethora of new metal-rich chalcogenide phases among the early transition metals have been important for understanding the expression of and interrelationships between metal–metal bonding features among these many compounds. Incorporation of late transition metals has long been known to stabilize both metal-rich halides[1] and chalcogenides that are otherwise unstable with respect to electron count and other binary phases. Recently reported ternary chalcogenides and phosphides of this type include $Ta_9M_2S_6$,[2] $Ta_{11}M_2Se_8$ (M = Fe, Co, Ni),[3] Ta_8NiSe_8 (M = Co, Ni),[4] Hf_8MTe_6 (M = Co, Ni, Ru),[5] $Zr_9M_2P_4$ (M = Co, Ni),[6] $Hf_5Co_{1+x}P_{3-x}$, $(0 < x < 0.5)$,[7] Hf_2NiP,[8] and ScNiP.[9]

The study of bonding features in metal-rich chalcogenides of the early transition metals has only recently been extended to group 3 examples, namely, to Sc_2Te[10] and Sc_8Te_3.[11] Their structural and bonding relationships to those of later electron-richer analogues allow one to assess the importance of atom sizes, valence electron concentrations, and metal–to–nonmetal proportions in the structure and bonding. The smaller number of metal-based electrons for the earlier transition metals appears to force a reduction in the metal–metal framework dimensionality, as shown in particular for Sc_8Te_3 and Y_8Te_3, relatives of Ti_8Ch_3, Ch = S, Se.[12,13] Stoichiometry and efficient packing apparently dictate that some metal atom pairs may be in close proximity even though theory indicates that there are relatively few or no electrons involved in their bonding, i.e., a classical result of matrix effects.

Metal-rich chalcogenides of scandium and yttrium also show some notable contrasts with parallel structures and stoichiometries of their most reduced halides. The latter are known only with proportionately more nonmetal atoms. Twice as many halogen atoms per chalcogen would be expected for the same electron count per metal atom, and in fact somewhat more (2<X/R<3) are observed in isolated cluster halides. Condensed chains or tetramers built of recognizable octahedra span a range of $1 < X/R < 2$. The halides structurally serve to sheath the metal cores, in all cases leading to clearer definition of the building blocks. Furthermore, with few exceptions, the known reduced halides are so electron-poor that they also require interstitial heteroatoms ($Sc_2Cl_{12}C$, Y_4I_5C, etc.) which afford central bonding and additional bonding electrons.[14]

In analogy with studies on later transition-metal–chalcogen systems, this article presents the first results of the expansion of this chemistry to ternary systems of scandium, in this case with the incorporation of nickel. The early–late transition metal bonding involved appears to reflect the extra stability of such polar interactions that were first noted by Brewer and Wengert.[15] Mixed-metal features in chalcogenides and phosphides are largely multicapped trigonal prisms of the earlier transition metal centered by a late transition metal. The nonmetals in these generally prefer a similar environment, a tricapped trigonal prism (tetrakaidecahedron). In some ternary phases, the late-transition metal and nonmetal (e.g., Co and P, or Ni and S) may exhibit unusual mixed metal/nonmetal occupancies of the same sites, as in ($Hf_5Co_{1+x}P_{3-x}$),[7] evidently because of their similar sizes and site preferences. In the title compound $Sc_5Ni_2Te_2$, the late-transition metal and the nonmetal have markedly different sizes, and mixed occupancy is not a factor. Furthermore, the relative electron deficiency of the host metal and the larger anion ensure a cooperative reduction in dimensionality of the metal–metal bonded framework as compared with that in $Hf_5Co_{1+x}P_{3-x}$, etc. The new $Sc_5Ni_2Te_2$ is significant in that it represents the extension of early–late transition metal chemistry to ternary chalcogenides of the electron-poorer scandium.

Experimental Section

All materials were handled in He-filled or N_2-filled gloveboxes to reduce contamination by adventitious impurities. The elements were used as received: Sc turnings, Aldrich 99.7%; Te powder, Aldrich 99.99%; Ni powder, Alfa 99.95%. The synthesis of $Sc_5Ni_2Te_2$ began with the preparation of Sc_2Te_3 as described previously.[10] The Sc_2Te_3, Ni, and Sc to give a 3:1:1 (Sc:Ni:Te) stoichiometry were first loaded into a tantalum tube welded at one end. The other end of the tube was then crimped shut inside the glovebox, transferred to an arc-welder, and the tube sealed after the welder had been evacuated and backfilled with argon. Such containers were then sealed inside evacuated and well flamed fused silica jackets, heated at 1000 °C for 24 hours, cooled to 700 °C at 5 °C/hr, and then allowed to cool in air. Guinier powder diffraction on the product of the first reaction showed what was subsequently found to be $Sc_5Ni_2Te_2$ had been obtained in $\geq$ 80% yield, plus ScTe. Further reactions with the indicated 5:2:2 stoichiometry at higher or lower temperatures only yielded a neighboring ternary phase Sc_6NiTe_2,[16] or ScTe and ScNi. Also, arc-melting reactions at the 5:2:2 composition did not yield $Sc_5Ni_2Te_2$. But reactions loaded off-stoichiometry (~Sc_3NiTe) yielded higher quantities of $Sc_5Ni_2Te_2$, evidently because some Ni had been lost into the container in the former reactions. The same synthetic techniques with Fe, Co, and Cu (M) as the late transition metal did not yield any of the analogous $Sc_5M_2Te_2$.

Powder X-ray Diffraction. The powder diffraction patterns of $Sc_5Ni_2Te_2$ were obtained with the aid of an Enraf-Nonius Guinier powder camera and monochromatic Cu $K\alpha_1$ radiation. The samples were powdered, mixed with standard silicon (NIST), and placed between two strips of cellophane tape on a frame that mounted on the sample rotation motor.

Lattice parameters were obtained with the aid of least squares refinement of 58 indexed lines with 2θ values calibrated by a nonlinear fit to the positions of the standard Si lines (Table 1).

Single crystal diffraction. Several irregularly shaped, silvery crystals were mounted inside 0.3 mm i.d. glass capillaries that were sealed off and mounted on metal pins. Their quality was checked by means of Laue photographs. A diffraction data set for the best crystal was measured on a Rigaku AFC6R diffractometer (monochromated Mo $K\alpha_1$ radiation) at room temperature. Twenty-five centered reflections gathered from a random search were used to determine provisional lattice constants and the crystal system. Two octants of data were collected (*h*, *k*, ±*l*) to $2\Theta_{max} = 60°$ and corrected for Lorentz and polarization effects. The data further corrected for absorption with the aid of two ψ-scans. Of 4627 measured reflections, 1938 had $I > 3\sigma(I)$ and 653 of these were unique. Extinction conditions and statistical evidence for centricity indicated one possible space group, *Pnma*. The structure was solved by direct methods (SHELXS[17]) and refined with the package TEXSAN[18] in this space group. After isotropic refinement, the data averaged with R_{ave}= 9.2%, and the final anisotropic refinement converged at $R(F)/R_w$ = 3.2/3.2% for the composition $Sc_5Ni_2Te_2$. Some data for these processes are listed in Table 1, and the atomic positions and isotropic-equivalent temperature factors are given in Table 2. Additional data collection and refinement parameters, the anisotropic displacement parameters, and a complete distance list are in the Supporting Information. These as well as the F_o/F_c listing are also available from J.D.C.

Band Calculations. Extended Hückel calculations were carried out within the tight-binding approximation[19] for the full structure of $Sc_5Ni_2Te_2$ at 48 k-points spread out over the irreducible wedge. H_{ii} parameters employed were the values iterated to charge consistency for Sc from Sc_2Te, and for Ni from Sc_6NiTe_2 (eV): Sc: 4s, -6.75; 4p, -3.38; 3d, -6.12;[10] Ni: 4s, -5.58; 4p, -2.41; 3d, -7.82;[16] Te: 6s, -21.20; 6p, -12.00.[10] Very similar energies were also obtained for the first two from charge iteration on ScNi (CsCl type). The charge iteration for Ni gave much more suitable results for this polar compound than those from density functional theory (-8.13, -4.18, -12.40 eV, respectively[20]).

Results and Discussion

Structural Description. A near-[010] section of the $Sc_5Ni_2Te_2$ structure viewed along the short 3.95 Å axis is given in Figure 1. The atom distribution can be viewed as pairs of extended zig-zag chains of nickel (black) that are sheathed by scandium (open) and are in turn well separated by single tellurium atoms (grey). The shortest distance between separate metal chains, *d*(Sc2-Sc3) = 3.68 Å (marked), is at best a weak interaction (below). Figure 2 illustrates the repeat unit in one chain along with atom labels and distances with appreciable overlap populations (vide infra). To help understand the structure, Figure 3 shows a side view of one-half of the composite chain as viewed more or less along [301], Figure 1. The repeat units here are rectangular scandium pyramids [Sc2, Sc1(×2), Sc4(×2) and Sc3, Sc4 (×2), Sc5 (×2)] (one is highlighted) that share Sc4–Sc4 edges in pairs and Sc1-Sc4-Sc5 edges infinitely along $\vec{b}$. Each rectangular pyramid has a nickel atom 0.54 Å outside of the base. Two of these composites are then assembled base-to-base with a relative displacement of *b*/2 to generate the full chains seen in Figures 1 and 2. This assembly generates additional Sc1-Sc5 (top and bottom) and Sc4-Sc4 bonds across the Figure plus the pair of parallel zig-zag chains of nickel that run down the central channel of the chain. The Ni–Ni distance within the zig-zag chains is 2.66 Å (the single bond distance is given as 2.31 Å[21]) while the closest separation between the eclipsed Ni chains is 3.27 Å. The scandium atoms about the two nickel strings exhibit Sc–Ni distances over 2.62–2.87 Å, while Sc–Sc distances around the outside of the chain span 3.17–3.48 Å.

Numerous older structures have demonstrated that a preferred environment for the late transition metal is in the center of a multicapped trigonal prism of the early transition metal.[2-8] In the present structure, four such chains of nickel centered within confacial scandium trigonal prisms can be viewed as having been condensed together, but the relationship is not as clear and direct. One such Sc2-capped member in the upper right of Figure 2 consists of Sc1(×2) and Sc4(×2) as two of the side edges, with the third edge Ni2–Ni1 pair which also centers the next interpenetrating trigonal prism. The 2:5 ratio of nickel to scandium, relative to that in Sc_6NiTe_2,[14] predicates such condensation. Another description of this one-dimensional array is in terms of zigzag chains. If the Sc–Ni connectivity of the structure is neglected for the moment, it can be seen in Figure 2 that the outside shell of the chain is composed entirely of zigzag Sc–Sc chains along *b* that share vertices, the comparable Ni–Ni chains being added internally. While the later interpretation is not the most useful in terms of understanding the local bonding, it is visually helpful.

The description of all of the pairwise atom–atom distances within the Sc_5Ni_2 chain is fairly involved. Some of these are marked in Figure 2, and they are also listed in order of decreasing pairwise overlap populations in Table 3. (The complete distance listing is given in the Supporting Information.) It should be noted that the chain is centrosymmetric and only one-half of the interactions need to be considered. While Sc1 is bonded twice to Ni1 (2.62 Å) and once to Ni2 (2.87 Å, across the double Ni chain), Sc5 is connected in parallel but more tightly, twice to Ni2 (2.61 Å) and once to Ni1 (2.65 Å). Sc1 and Sc5 also form a zig-zag pattern atop the double nickel chains with Sc1–Sc5 = 3.32 Å (×2). Internally, Sc4 occupies a special position more inside of the chain, and the farthest from any tellurium atom. The Sc4 has two short contacts to each of Ni1 and Ni2, 2.64 and 2.62 Å, respectively, and long diagonals across the chain center to both Ni (2.86 Å). Interestingly, there are also short distances between Sc4 and both Sc1 and Sc5, edges in the square pyramids (3.27 and 3.31 Å), perhaps because of their common nickel neighbors. Finally, the comparable Sc2 and Sc3 atoms, the apices of the rectangular pyramids described earlier, are also bonded to their basal Ni1 (2.70 Å) and Ni2 (2.67 Å), respectively, and also twice each to Sc4 and Sc1 or Sc5 at 3.17 – 3.48 Å. The two opposed double chains of rectangular pyramids, $Sc_2(Sc_{6/2})Ni_2$, left and right in Figure 2, are then interconnected through Sc1–Sc5, Sc4–Sc4, and Ni1–Ni2 bonding. (This description is helpful later in understanding the overlap populations.) The nonequivalent nickel atoms are reflected in the unequal but generally similar distances about them, the most disparate of which being Ni1–Sc5, 2.65 Å and Ni2–Sc1, 2.87 Å (not drawn) which reflect the skewness of the centrosymmetric chain. Fourier difference maps do not show any extra electron density in the central channel of the chain. The chains are not significantly interbonded, as will be shown for the shortest separation of this kind marked in Figure 1, 3.68 Å for Sc2•••Sc3. The Te–Te distances are all ≥3.95 Å. These structural motifs and atomic distances support the 1D chain assignment to $Sc_5Ni_2Te_2$.

Remarkably similar structural characteristics are found in the chains in Gd_3MnI_3,[22] the $(Gd_3Mn)_2$ portion of which is shown along the short 4.13 Å axis in Figure 4.[23] This is very similar to the upper or lower half of the Sc_5Ni_2Te chain (Figures 2,3). The iodide was likewise described as the base-to-base assembly of two chains of trans-edge-sharing rectangular pyramids, which is a very atypical halide structure. This has been classified as a distortion extreme of a family of compounds originating with $Pr_3(Ru)I_3$, viz., double chains of Z-centered R_6 octahedra that share trans edges and are further condensed side-by-side. Their progressive distortions in other examples can be described as the partial fusion of the recognizable twin octahedral chains in Pr_3I_3Ru etc. as two adjoining octahedra begin to merge and the Z elements approach one another.[24] Although the $Sc_5Ni_2Te_2$ and Gd_3MnI_3 compositions and geometries may be readily interrelated, the electron-poorer interstitial Mn also exhibits significant Mn–Mn bonding .

Theoretical Calculations. Intuitively, the character of the bonding in $Sc_5Ni_2Te_2$ must be highly delocalized, the bonded metal neighbors ranging from five about Sc2 and Sc3 through eight for Sc1 and Sc5, 10 for each Ni and 14 for Sc4. Band calculations seemed necessary to clarify the situation. Figure 5 shows the total DOS for $Sc_5Ni_2Te_2$. Typical for these relatively electron-poor compounds, the Fermi level resides on the low energy side of a prominent conduction band composed of about 90% scandium d and s orbitals and 10% nickel contributions. The nickel d (and Sc d) states comprise all of the lower valence bands between ~–8.5 and –7.0 eV, with tellurium states being the majority at still lower energies (off scale). A near gap at ~–6.9 eV occurs with 36 of the 47 total electrons per formula unit.

The band below there can be described simply, but not rigorously, as 2 Ni (d^{10}) and 2 Te (s^2p^6), with the 11 electrons left over in the conduction band.

Figure 6 shows the COOP curves for total Ni–Ni, Sc–Sc and Sc–Ni bonding. E_F falls largely within bonding regions for both Sc–Sc and Sc–Ni and 0.4 eV below the onset of Sc–Sc antibonding states. On the other hand, the Fermi level falls in a nonbonding region for Ni–Ni interactions, these being virtually closed shell above ~–7.0 eV. This is a common behavior for M–M bonding of late transition metals as they achieve a closed shell d^{10} configuration, as noted in La_2Ni_2I.[25] Other cases of early–late transition metal chalcogenide structures have been observed to optimize the M–Ni bonding as revealed by COOP curves.[4] It is interesting that this is not the situation here, albeit in a structure that does not involve the trigonal prisms in a linear face-sharing motif as before.

A complex structure such as this presents an ample variety of distances and bond strengths. Comparisons of bond distances with overlap populations allow one to ascertain where matrix effects, separations fixed more by geometric relationships, may be more important than bonding in near-neighbor contacts. For this purpose, pairwise overlap populations for Sc–Sc, Sc–Ni, and Ni–Ni are listed in Table 4 in decreasing magnitude along with the corresponding distances. These change in parallel fairly well, but there are some significant deviations that assist in highlighting important bonding details. For one, the Sc1–Sc5 bridging interactions at 3.32 Å lie fairly low in the list (0.093). The natural assumption is that this distance is moderately to heavily influenced by matrix effects, in concert with the suggestion made earlier that the structure could be described as two edge-sharing sheets built from square pyramids and "glued" together by Ni–Sc (and Ni–Ni) bonding, Figure 2. The other cross-distance, Sc4–Sc4, is longer but more central and it has only a slightly lower population, 0.082 at 3.53 Å. The Sc and Ni orbital energies are close enough that they do mix well and give substantial overlap populations, while this is not true for the Ni–Ni bonding when the atoms are this well reduced and have virtually closed shells. In this case, the observed distance in the zig-zag chain is quite misleading regarding the actual bonding effects.

Other noteworthy differences are the relatively large overlaps for Sc2–Sc2 (0.045) and Sc4–Sc4 (0.037) (but not for Sc1–Sc1, Sc3–Sc3, and Sc5–Sc5) along the 3.95 Å chain repeat. This result is not surprising for Sc4, which resides centrally within the chain and shows effects that parallel those noted for Sc_2Te and Sc_8Te_3 where electrons appear to be concentrated within metal-rich cluster chains that are isolated by nonmetals neighbors.[9,10] But strong bonding along the chain for Sc2 as well seems unusual as these atoms reside more on the periphery of the chains, with three tellurium near neighbors. The larger population here may mean additional bonding takes place for scandium that otherwise has fewer (five) near metal neighbors. Scandium 3 has the largest number of close Te neighbors (4) and thence little Sc3–Sc3 bonding.

The interchain Sc–Sc distances lie near the bottom of the overlap population list. The shortest distance between the chains (Sc2–Sc3, 3.68 Å) has an overlap population of 0.036, followed by smaller values for analogous but longer distances (Sc1–Sc3, 0.028; Sc1–Sc2, 0.018). There are evidently only meager amounts of electron density between the chains (<~15% of the larger internal populations), but whether these are remarkable or substantial is doubtful.

The notion was posited before that Sc–Ni bonding holds the chain together, an idea that goes back to the original studies of early–late transition metal bonding by Brewer and Wengert.[15] These overlaps are given at the bottom of Table 3. The seven shorter types of Sc–Ni contacts around 2.61–2.70 Å have overlap populations of about 0.17 to 0.21, while the three longer contacts of 2.86 Å involving Sc4 or a long diagonal to Sc1 have lower values, ~0.10. One important detail is that the Ni2–Sc3 distance to the apex of one rectangular pyramid has a somewhat larger overlap population than for the analogous Ni1–Sc2 (0.209 vs 0.174), in parallel with the generally different distances about these two-pseudo-equivalent atoms (i.e., Sc2–Sc1 vs Sc3–Sc5). Similarly the "equivalent" Sc1–Ni2 and Sc5–Ni1 diagonals differ by 0.22 Å and in parallel, so do the overlap populations. The causes of these distortions are complex and perhaps tied up with the factors behind optimization of overall bonding.

Structural Comparisons. $Sc_5Ni_2Te_2$ is nominally isotypic with $Hf_5Co_{1+x}P_{3-x}$, but there are in detail many differences in the bonding. These involve the ordering pattern, the sizes of the nonmetals and the transition metals, and, presumably, the electron counts. Figure 7 shows the $Hf_5Co_{1+x}P_{3-x}$ structure[7] nearly along [010], with the bonds in the double zigzag chain unit that are comparable to those in Figure 1 outlined in black, and the additional metal–metal interactions about it, as open bonds. The Hf–Hf and Hf–Co bonding in this occurs in essentially a 3D arrangement, as judged by distances and, especially, overlap populations.[7] The few Hf–Hf distances displayed on the structure show that the equivalent "interchain" distances are approximately equal to or less than those within. This condensation of the building units expresses the greater number of metal-based electrons for hafnium compared with scandium and, most certainly, the smaller size of phosphorus compared with tellurium. Once again, as was the case for the M_8Ch_3 phases (M = Sc, Y; Ch = Se, Te vs Te_8Ch_3, Ch = S, Se),[9] there is a cooperative effect of increased anion size and decreased valence electron concentration that acts to reduce the dimensionality of the scandium interactions.

In addition to the reduction in dimensionality in $Sc_5Ni_2Te_2$, there is also a substantial difference in ordering of the nonmetal and transition metal atoms. In $Hf_5Co_{1+x}P_{3-x}$,[7] a phase width ($0 \leq x \leq 0.5$) arises from the varying occupancy of one intrachain position by cobalt (gray) and phosphorus (black). The authors attributed this in part to the similar atomic sizes and their distances to hafnium. For $Sc_5Ni_2Te_2$, the intrachain zigzag chains are composed solely of nickel atoms, and the interchain cavities are filled only by tellurium, which emphasize the lowered dimensionality. This new ordering rests with the fact that tellurium and nickel have disparate atomic sizes and very different bonding characteristics to scandium. Furthermore, a large phase width is no longer a structural feature. The resultant ordering generates only fairly weak Ni–Ni bonding. The variability among these structures is remarkable.

There are interesting parallels and contrasts between the metal-rich chalcogenide compounds of the rare-earth elements and the longer known halides. Twice as many halide as chalcogen atoms would be needed to achieve the same electron count per metal, and this anion preponderance alone would produce better separation of the metal-bonded units and reduction of the dimensionality of the halides, as observed. Isolated halide clusters are thus much more common, and chains of edge-sharing metal octahedra are relatively fewer (Y_2Cl_3,

Sc_5Cl_8C, Y_4I_5C, etc.). The halides are in fact generally so electron-poor that interstitial heteroatoms are nearly always required for stability. Including the electron count of the interstitial gives 2.3 – 2.8 electrons per cluster metal, 2.8–3.2 e^- in chains, and X/R values of roughly 1.0 (condensed clusters) to 2.0 (isolated).[14] (The odd binary Y_2Cl_3 and Sc_7Cl_{10} remain exceptions at 1.8 e^-/R.) The binary chalcogenides Sc_2Te and Sc_8Te_3 achieve only slightly lower electron counts than cluster halides, 2.0–2.25 per metal, but with disproportionately lower Ch/R values, 0.5 – 0.38. In other words, the grossest analysis suggests that both classes of the metal-richest group 3 compounds achieve similar electron counts per metal, ca. 2.0–2.5, but at greatly different stoichiometries: 1.3–1.7 X/R vs $\leq$0.5 Ch/R.[26] The latter nicely correlates with the notably greater aggregation found in the metal-richest chalcogenides. As with later transition-metal chalcogenides, these too would appear to be driven by M–M bonding when the anion number is insufficient to give good sheathing of the metal aggregate. It's harder to compare these two families of compounds electronically when they contain late transition metal components (Gd_3MnI_3 vs. $Sc_5Ni_2Te_2$), but if we ignore the contributions of the latter the difference in VEC is similarly low (2.0 vs. 2.2).

Finally, the roles of the anions are rather different, evidently because of differences in their quantity. Halides (Cl, Br, I) generally exhibit several very discrete functions on these clusters or chains, being two to four coordinate as they bridge all exposed edges and bond exo at all vertices of the cluster units. Exceptions are rare.[14] The greatly reduced telluride numbers lead to much higher coordination numbers and less regular geometries, usually some form of an augmented trigonal prism. In the present compound, two different tellurides have each 6 – 7 neighbors at 2.91–3.06 Å, plus two more contacts at 3.16 Å. These marked differences have generally led us to include the halides in illustrations, but to omit the less specific chalcogenide environments. One would in fact expect the chalcogenide–metal interactions to be somewhat more covalent.

Conclusions. $Sc_5Ni_2Te_2$ is significant because it represents the first extension of early–late transition metal bonding in chalcogenides to the earliest, and most electron-impoverished transition metals. The structure is built up from double nickel zigzag chains sheathed by scandium atoms and separated from other Sc_5Ni_2 chains by tellurium atoms. The metal substructure can be envisaged as trans-edge-shared double square pyramid chains "glued" together at their bases mainly by Sc–Ni bonding. Reduction in dimensionality compared with $Hf_5Co_{1+x}P_{3-x}$ results from a new ordering of the nonmetal and late transition metal and the different anionic nature of tellurium. A decreased number of metal-based electrons is in concert with the absence of interchain bonds via tellurium in this new phase. These structural interrelationships aid in the understanding of this new ternary phase.

Acknowledgements

This work was supported by the National Science Foundation, Solid State Chemistry, via grants DMR-9510278 and -9809850 was carried out in the facilities of the Ames Laboratory, U.S. Department of Energy.

Supporting Information Available

Tables of additional crystallographic and refinement parameters, anisotropic thermal parameters, and a complete listing of nearest-neighbor distances (4 pages). Ordering instructions are given on any current masthead page.

References

(1) Corbett, J. D. *J. Alloys Compd.* **1995**, *229*, 10.

(2) Harbrecht, B.; Franzen, H. F. *J. Less-Common Met.*, **1985**, *113*, 349; Harbrecht, B. *J. Less-Common Met.*, **1986**, *124*, 125.

(3) Harbrecht, B. *J. Less-Common Met.*, **1988**, *182*, 118.

(4) Conard, M.; Harbrecht, B. *J. Alloys Compd.*, **1993**, *197*, 57.

(5) Abdon, R. L.; Hughbanks, T. *Chem. Mater.*, **1994**, *6*, 424.

(6) Kleinke, H.; Franzen, H. F. *Inorg. Chem.*, **1996**, *35*, 5272.

(7) Kleinke, H.; Franzen, H. F. *J. Alloys Compd.*, **1996**, *238*, 68; Kleinke, H.; Franzen, H. F. *J. Alloys Compd.*, **1997**, *255*, 110.

(8) Kleinke, H.; Franzen, H. F. *J. Angew. Chem., Int. Ed. Engl.* 1997, *36*, 513.

(9) Kleinke, H.; Franzen, H. F. *J. Solid State Chem.* **1988**, *137*, 218.

(10) Maggard, P. A.; Corbett, J. D. *Angew. Chem., Int. Ed. Engl.* **1997**, *18*, 36.

(11) Maggard, P. A.; Corbett, J. D. *Inorg. Chem.*, **1998**, 37, 814.

(12) Owens, J. P.; Franzen, H. F. *Acta Crystallogr.* **1994**, *B30*, 427.

(13) Weirich, T. E.; Pöttgen R.; Simon, A. *Z. Kristallogr.* **1996**, *211*, 927.

(14) Corbett, J. D. in *Modern Perspectives in Inorganic Crystal Chemistry*, Parthé, E. Ed.; NATO ASI Series C; Kluwer Academic Publishers: Dordrecht, The Netherlands, 1992; pp 27--56.

(15) Brewer, L.; Wengert, P. R. *Metallurg. Trans.* **1973**, 4, 2674.

(16) Maggard, P. A.; Corbett, J. D. unpublished.

(17) Sheldrick, M. SHELXS-86. Universität Göttingen, Germany, 1986.

(18) TEXSAN, Version 6.0, Molecular Structure Corp., The Woodlands, Texas, 1990.

(19) Hoffman, R. *J. Chem. Phys.* **1963**, 39, 1397; Whangbo, M.; Hoffman, R. *J. Am. Chem. Soc.* **1978**, 100, 6093.

(20) Vela, A.; Gázquez, J. L. *J. Phys. Chem.* **1988**, 92, 5688.

(21) Pauling, L. *The Nature of the Chemical Bond*; Cornell University Press: Ithaca, NY, 1960, p. 400.

(22) Ebihara, M.; Martin, J. D.; Corbett, J. D. *Inorg. Chem.* **1994**, *33*, 2078.

(23) This relationship was pointed out to us by a perceptive reviewer.

(24) Payne, M. W.; Dorhout, P. K.; Kim, S.-J.; Hughbanks, T. R.; Corbett, J. D. *Inorg. Chem.* **1992**, *32*, 1389.

(25) Hong, S.-T.; Martin, J. D.; Corbett, J. D. *Inorg. Chem.* **1998**, *37*, 3385.

(26) The lowest X/R in individual closed-shell clusters is about 1.7 [$Sc(Sc_6Cl_{12}N)$, $Y_6I_{10}Os$]. Oxidation to give larger X/R values and less interbridged cluster arrays, up to X/R = 3 (R_6X_{18}), are compensated by incorporation of electron-richer Z or additional alkali metals, or both, the e^-/R remaining close to 2.3 throughout.

Table 1. Some Data Collection and Refinement Parameters for $Sc_5Ni_2Te_2$.

Formula weight	597.42
Space group, Z	*Pnma* (No. 62), 4
Lattice parameters,[a] (Å, Å^3)	
a	17.862(1)
b	3.9533(3)
c	10.6398(6)
V	751.3(1)
d_{calc}, g/cm^3	5.281
μ, cm^{-1} (Mo K_α)	167.35
R; R_w,[b] %	3.2, 3.2

[a] Guinier data, Cu Kα, 23 °C, 58 lines.

[b] $R = \Sigma||F_o| - |F_c||/\Sigma|F_o|$; $R_w = [\Sigma w(|F_o| - |F_c|)^2/\Sigma w(F_o)^2]^{1/2}$; $w = \sigma_F^{-2}$.

Table 2. Positional and Isotropic-Equivalent Thermal Parameters for $Sc_5Ni_2Te_2$.[a]

Atom	x	z	B_{eq}(Å^2)[b]
Te1	0.10736(6)	0.5103(1)	0.71(4)
Te2	0.73263(6)	0.3098(1)	0.71(4)
Ni1	0.9159(1)	0.1038(2)	0.83(7)
Ni2	0.9939(1)	0.8261(2)	0.84(8)
Sc1	0.1526(2)	0.7819(3)	0.7(1)
Sc2	0.2730(2)	0.4786(3)	0.8(1)
Sc3	0.8663(2)	0.6963(3)	0.8(1)
Sc4	0.5740(2)	0.4410(3)	0.8(1)
Sc5	0.9808(2)	0.3281(3)	0.8(1)

[a] All atoms on m, y = ¼.

[b] $B_{eq} = (8\pi^2/3)\sum_i\sum_j U_{ij}a_i^*a_j^*\vec{a}_i\vec{a}_j$.

Table 3. Selected Metal–Metal Distances (Å) and Overlap Populations in $Sc_5Ni_2Te_2$.

Atom 1	Atom 2	Distance		Overlap pop. per pair
Sc1	Sc2	3.17	×2	0.199
Sc1	Sc4	3.27		0.194
Sc4	Sc5	3.31	×2	0.172
Sc2	Sc4	3.48	×2	0.102
Sc3	Sc4	3.44	×2	0.108
Sc3	Sc5	3.38	×2	0.099
Sc1	Sc5	3.32	×2	0.093
Sc4	Sc4	3.53	×2	0.082
Sc2	Sc2	3.95[a]	×2	0.045
Sc4	Sc4	3.95[a]	×2	0.037
Sc2	Sc3	3.68[b]		0.036
Sc1	Sc3	3.83[b]	×2	0.028
Sc1	Sc2	3.88[b]	×2	0.018
Sc1	Sc1	3.95[a]	×2	0.015
Sc5	Sc5	3.95[a]	×2	0.009
Ni1	Ni2	2.66	×2	0.020
Ni1	Ni2	3.27[c]		-0.007
Ni2	Sc3	2.67		0.209
Ni2	Sc4	2.62	×2	0.191
Ni2	Sc5	2.61	×2	0.192
Ni1	Sc1	2.62	×2	0.184
Ni1	Sc4	2.64	×2	0.178
Ni1	Sc2	2.70		0.174
Ni1	Sc5	2.65		0.174
Ni2	Sc4	2.86		0.107
Ni1	Sc4	2.86		0.104
Ni2	Sc1	2.87		0.098

[a] Unit cell repeat in the chain.

[b] Interchain distance.

[c] Shortest distance between two nickel chains.

Supporting Information
$Sc_5Ni_2Te_2$: Synthesis, Structure, and Bonding of a Metal–Metal–Bonded Chain Phase, A Relative of Gd_3MnI_3

Paul A. Maggard and John D. Corbett

Table S1. Single Crystal X-ray Data Collection and Refinement Parameters for $Sc_5Ni_2Te_2$.

Formula weight	597.42
Space group, Z	*Pnma* (No. 62), 4
Crystal Dimensions, mm	0.1×0.1×0.4
Lattice parameters,[a] (Å, Å^3)	
a	17.862(1)
b	3.9533(3)
c	10.6398(6)
V	751.3(1)
d_{calc}, g/cm^3	5.281
Radiation; $2\theta_{max}$	Mo K_α; 60°
Octants measured	h, ±k, ±l
Scan method	ω–2θ
Temperature, °C	23
Number of reflections:	
measured	4627
observed ($I \geq 3\sigma(I)$)	1938
unique	653
μ, cm^{-1} (Mo K_α)	167.35
Absorption corr. method	2 ψ-scans
Relative transmission range	0.806–1.000
R_{ave} ($I \geq 3\sigma(I)$), %	9.2
Number of variables	56
Residuals R; R_ω,[b] %	3.2, 3.2
Goodness of fit	1.20
Sec. extinct. coeff.	9.9(4) x 10^{-7}

[a] Guinier data, Cu Kα, 23°C, 58 lines.

[b] $R = \Sigma||F_o| - |F_c||/\Sigma|F_o|$; $R_w = [\Sigma w(|F_o| - |F_c|)^2/\Sigma w(F_o)^2]^{1/2}$; $w = \sigma_F^{-2}$.

Table S2. U_{ij} (Å^2) values for $Sc_5Ni_2Te_2$.

Atom	U_{11}[a]	U_{22}	U_{33}	U_{13}
Te1	0.0110(5)	0.0097(4)	0.0070(5)	-0.0006(4)
Te2	0.0091(5)	0.077(5)	0.010(2)	-0.001(4)
Ni1	0.011(1)	0.0092(8)	0.011(1)	-0.002(8)
Ni2	0.013(1)	0.0091(9)	0.010(1)	-0.004(9)
Sc1	0.010(1)	0.008(1)	0.007(1)	-0.001(1)
Sc2	0.011(2)	0.010(1)	0.011(1)	0.001(1)
Sc3	0.012(1)	0.009(1)	0.011(1)	0.001(1)
Sc4	0.014(1)	0.007(1)	0.008(1)	-0.001(1)
Sc5	0.011(1)	0.009(1)	0.011(1)	0.001(1)

[a] $U_{12} = U_{23} = 0$.

Table S3. Selected Distances (Å) in $Sc_5Ni_2Te_2$.

Te1	Te1	2x	3.9533(3)	Ni2	Ni1	2x	2.657(2)	Sc3	Te1	2x	2.994(2)
	Te2	2x	3.967(1)		Ni1		3.267(3)		Te2	2x	2.914(2)
	Te2		4.075(2)		Sc1		2.874(4)		Ni2		2.665(4)
	Sc1		3.000(3)		Sc3		2.665(4)		Sc4	2x	3.438(4)
	Sc2		2.978(3)		Sc4	2x	2.622(3)		Sc5	2x	3.381(4)
	Sc3	2x	2.994(2)		Sc4		2.862(4)				
	Sc5		2.978(3)		Sc5	2x	2.608(2)	Sc4	Te2		3.158(3)
	Sc5	2x	3.056(3)						Ni1	2x	2.635(3)
				Sc1	Te1		3.000(3)		Ni1		2.864(4)
Te2	Te1	2x	3.967(1)		Te2	2x	3.010(3)		Ni2	2x	2.622(3)
	Te1		4.075(2)		Ni1	2x	2.624(2)		Ni2		2.862(4)
	Te2	2x	3.9533(3)		Ni2		2.874(4)		Sc1		3.266(4)
	Sc1	2x	3.010(3)		Sc2	2x	3.171(3)		Sc2	2x	3.480(4)
	Sc2		3.152(3)		Sc3		3.825(4)		Sc3	2x	3.438(4)
	Sc2	2x	2.998(2)		Sc4		3.266(4)		Sc4	2x	3.533(5)
	Sc3	2x	2.914(2)		Sc5	2x	3.310(3)		Sc5		3.312(4)
	Sc4		3.158(3)								
				Sc2	Te1		2.978(3)	Sc5	Te1	2x	3.056(3)
Ni1	Ni2		3.267(3)		Te2	2x	2.998(2)		Te1		2.978(3)
	Ni2	2x	2.657(2)		Te2		3.153(3)		Ni1		2.653(4)
	Sc1	2x	2.624(2)		Ni1		2.699(4)		Ni2	2x	2.608(2)
	Sc2		2.699(4)		Sc1	2x	3.171(3)		Sc1	2x	3.310(3)
	Sc4	2x	2.635(3)		Sc3		3.683(4)		Sc3	2x	3.381(4)
	Sc4		2.864(4)		Sc4	2x	3.480(4)		Sc4		3.312(4)
	Sc5		2.653(4)								

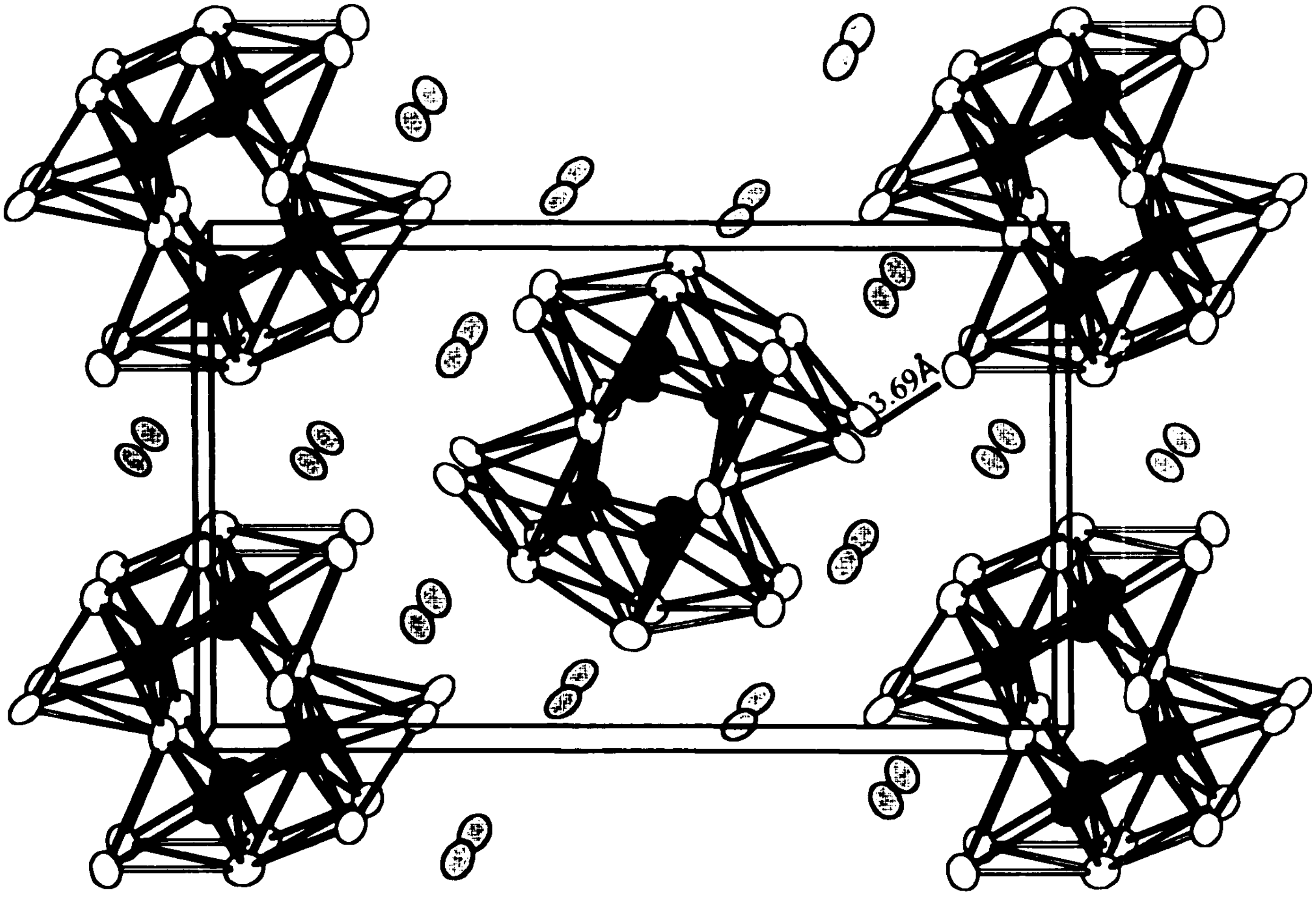

Figure 1. Near-[010] section of the chain structure of $Sc_5Ni_2Te_2$ (99.9% probability ellipsoids). The Ni atoms are black, Sc, white, and Te, gray ellipsoids. The shortest interchain distance is marked. The *a* axis is horizontal.

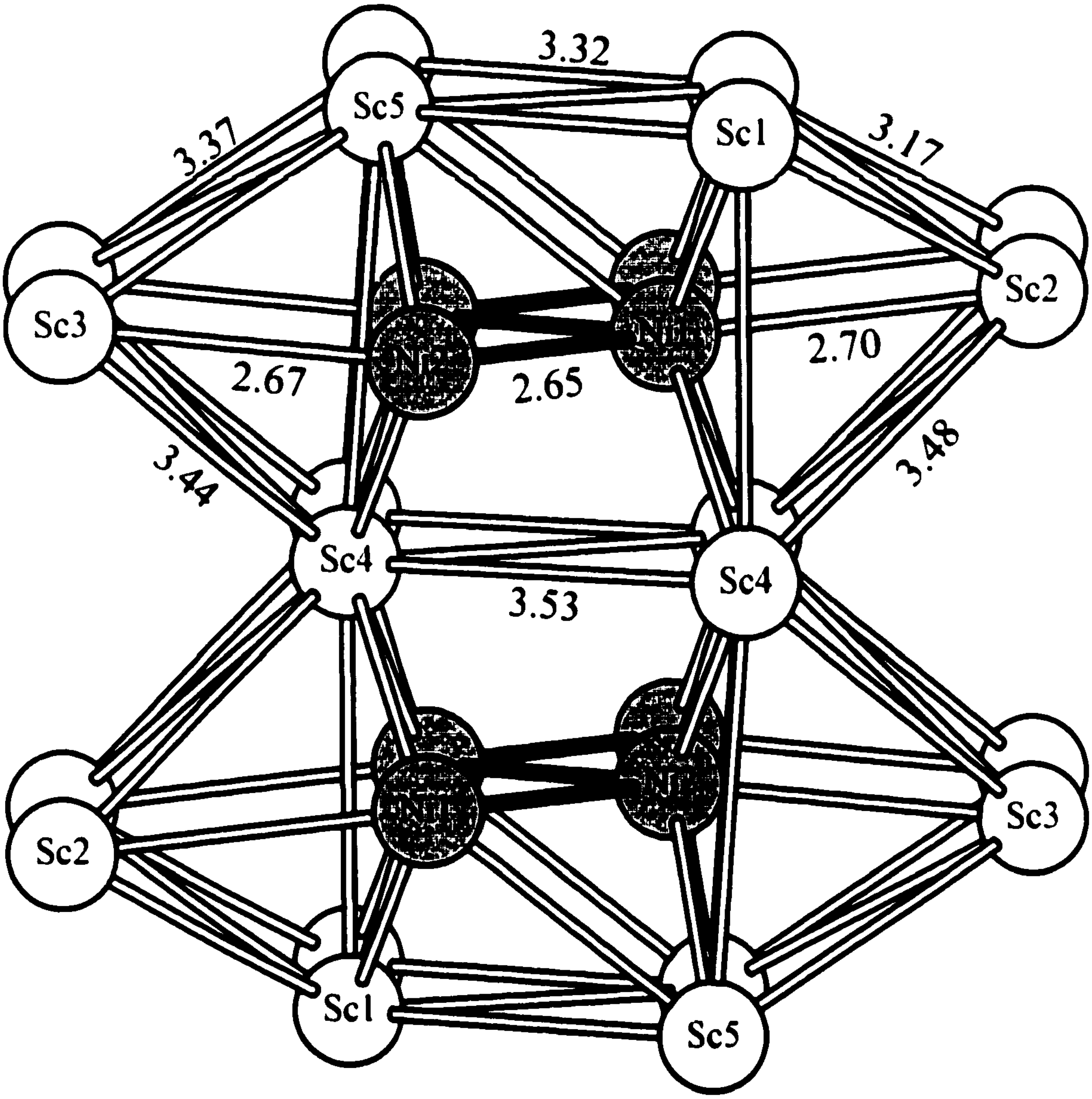

Figure 2. The centrosymmetric repeat unit in the Sc_5Ni_2 chain, with the numbering scheme and independent distances marked. Nickel atoms and Ni–Ni bonds are darker.

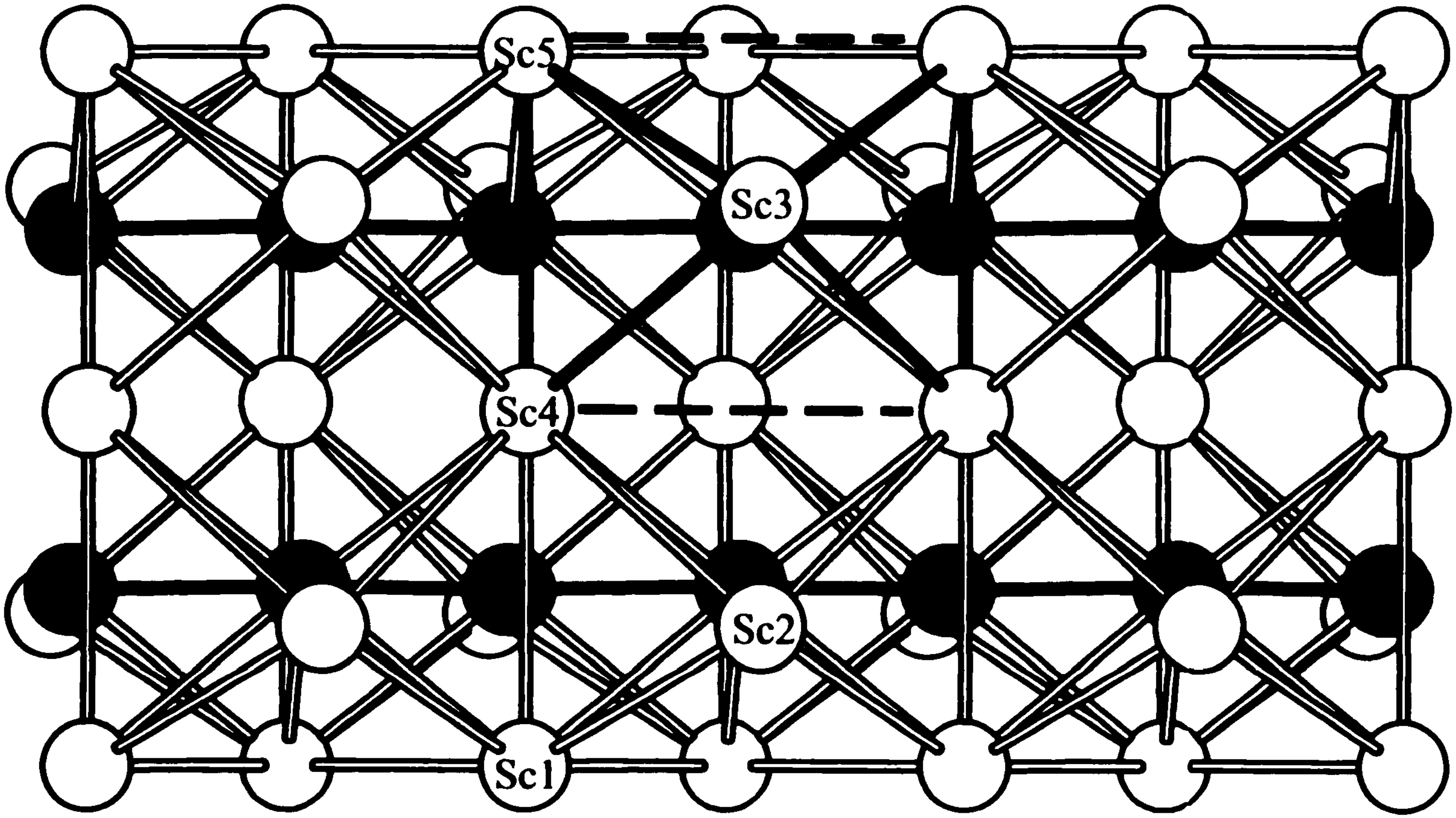

Figure 3. Side view of the Sc_5Ni_2 metal chain (Figure 2), with the short b = 3.95 Å repeat horizontal. The Ni atoms are darkened with the gray one further away. Note the construction of Ni-based rectangular pyramids of Sc; one is marked by a heavier outline.

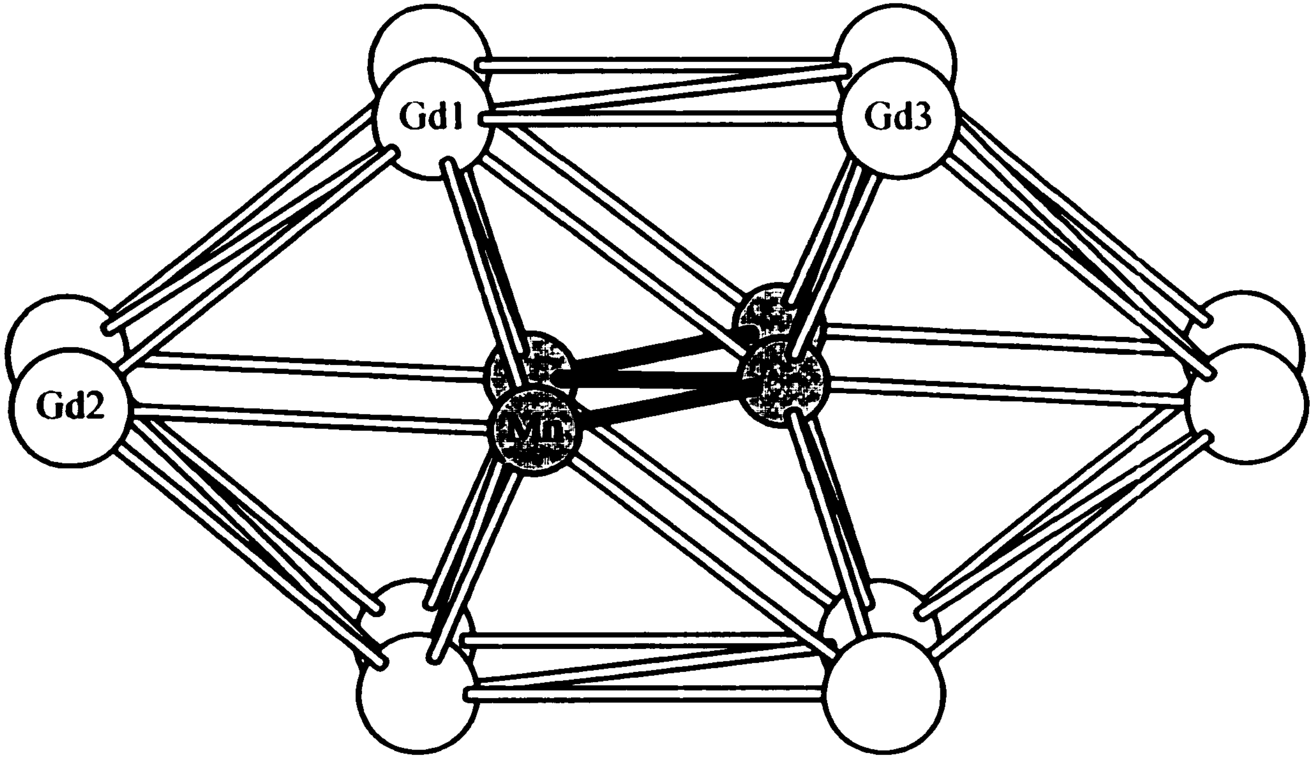

Figure 4. A[010] view of the metal chain in Gd_3MnI_3[22] along the short repeat. Compare with the top or bottom half of the Sc_5Ni_2 chain in Figure 3.

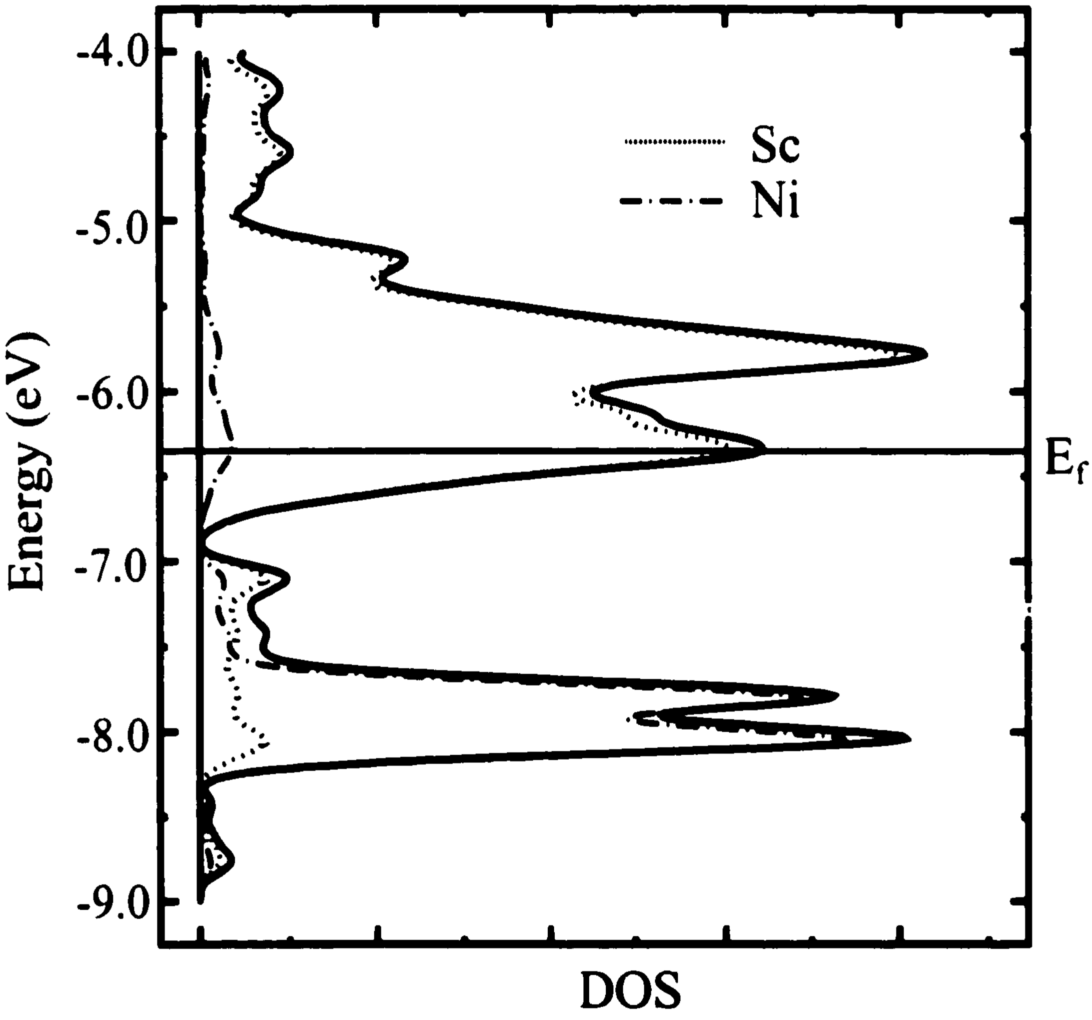

Figure 5. The densities-of-states from EHTB band calculations for $Sc_5Ni_2Te_2$. The separate Sc and Ni contributions are projected out.

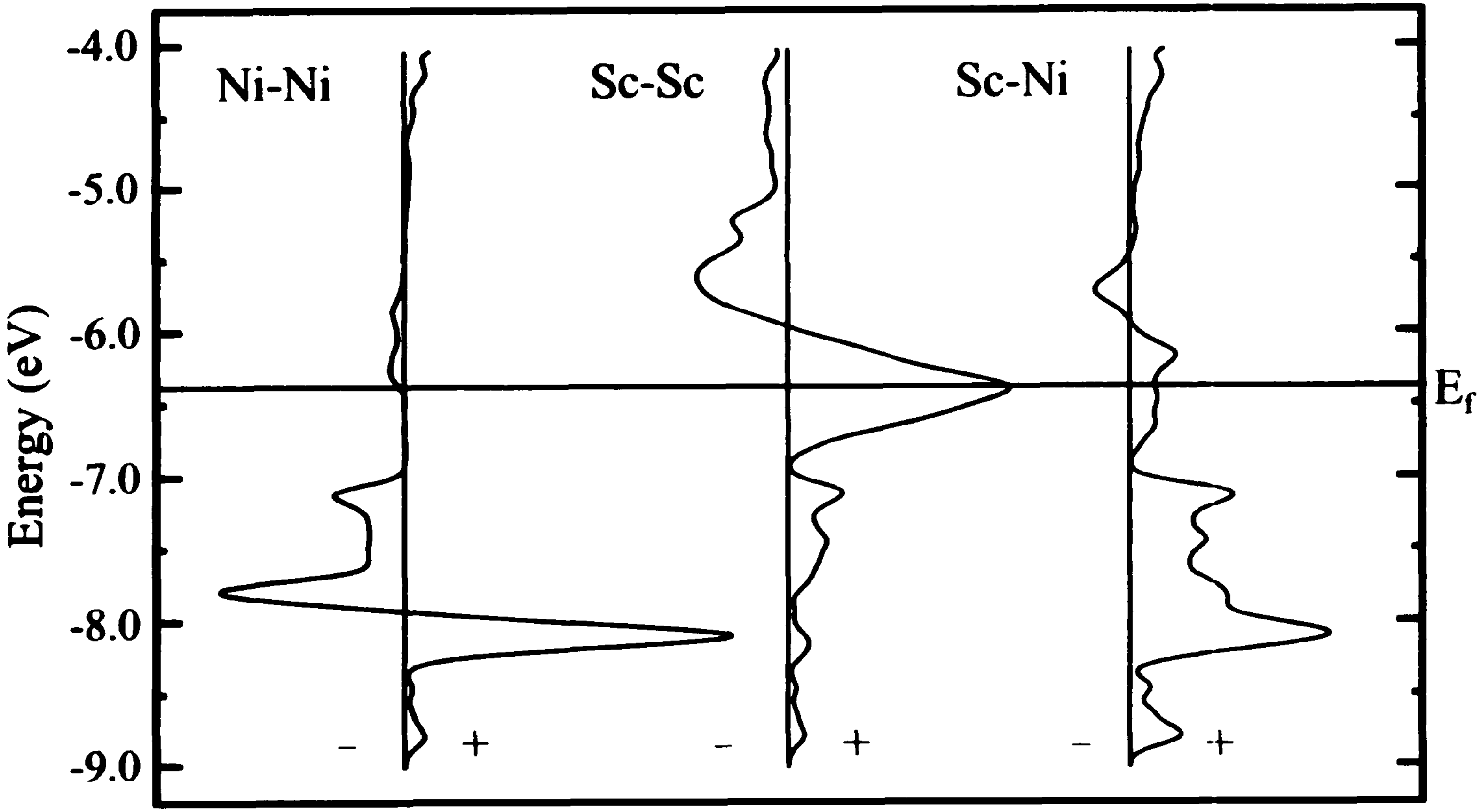

Figure 6. Total COOP (overlap-weighted orbital populations) curves for pairwise interactions in $Sc_5Ni_2Te_2$.

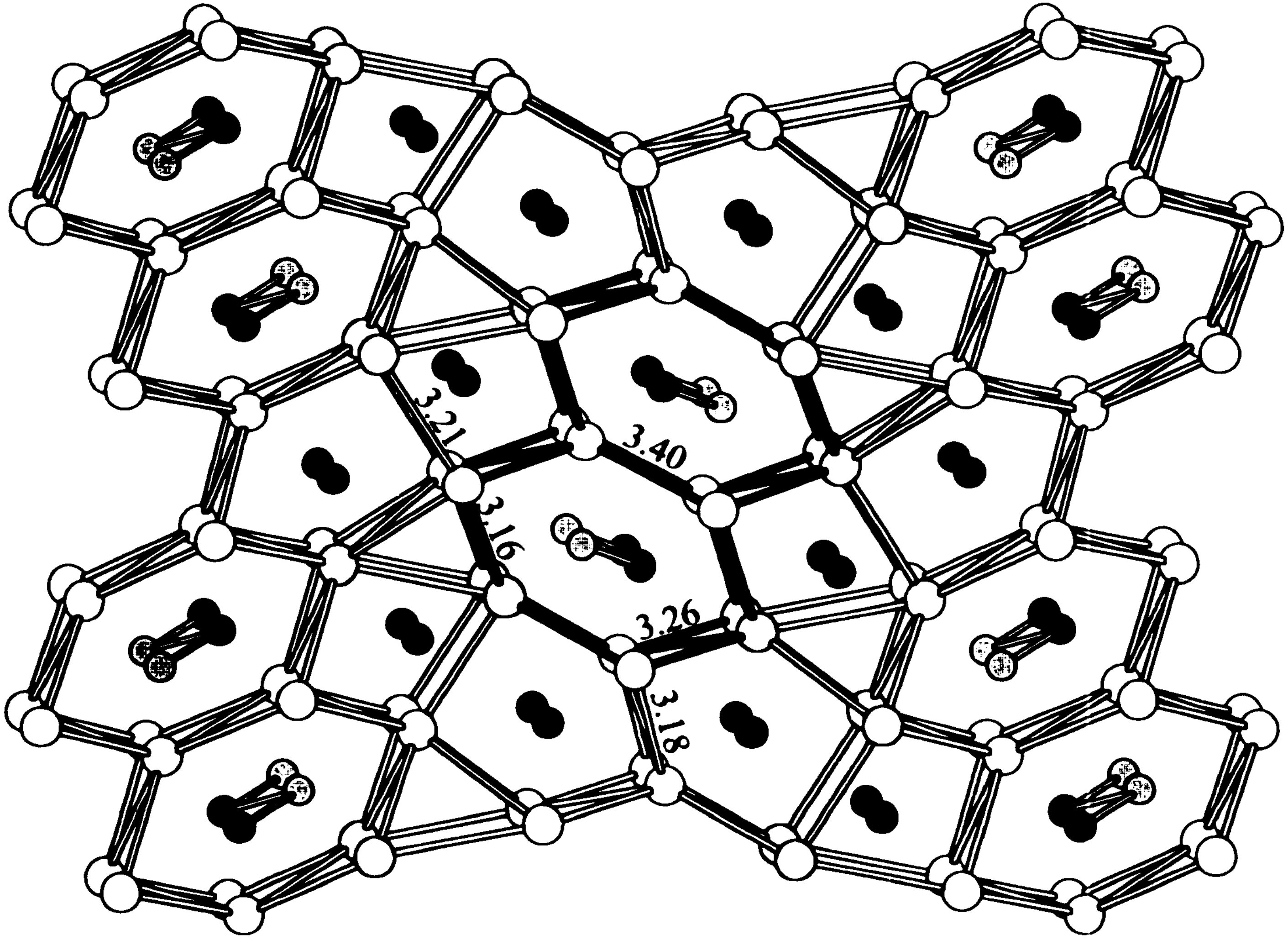

Figure 7. Near-[010] projection of the structure of Hf$_5$Co$_{1+x}$P$_{3-x}$ ($0 \le x \le 0.5$) with Co gray, P black.[7] The chain unit evident in Sc$_5$Ni$_2$Te$_2$ (Figure 1) is outlined.

CHAPTER 6. TWO-DIMENSIONAL METALLIC COMPOUNDS $Y_5M_2Te_2$ (M = Fe, Co, Ni) THAT ARE RELATED TO Gd_3MnI_3. HYDROGEN ABSORPTION IN THE $Y_5Ni_2Te_2H_x$ DERIVATIVE

A paper prepared for submission to the Journal of the American Chemical Society

Paul A. Maggard, Robert W. Henning and John D. Corbett

Iowa State University, Ames, IA 50011
Intense Pulsed Neutron Source, Argonne National Laboratory, Argonne, IL 60439

Abstract

$Y_5M_2Te_2$ (M = Fe, Co, Ni) have been prepared by high-temperature solid-state techniques, and shown to be isostructural and orthorhombic *Cmcm* (No. 63) with $Z = 4$. The structure was established by X-ray single crystal methods at 23 °C for M = Fe, with a = 3.9594(3)Å, b = 15.057(1)Å, and c = 15.216(1)Å. The new structure contains zigzag chains of late-transition metals sheathed by yttrium atoms that are condensed through trans vertices to yield 2D bimetallic layers separated by single layers of tellurium atoms. Reaction of hydrogen with $Y_5Ni_2Te_2$ causes a rumpling of the Y–Ni layers as determined from combined X-ray single crystal and neutron powder diffraction for $Y_5Ni_2Te_2D_{0.41(1)}$: *Pnma* (No. 62) with $Z = 4$. Lattice constants from Guinier powder diffraction at 23 °C and neutron techniques at -259 °C, respectively are: a = 14.3678(7), 14.3282(2)Å, b = 4.0173(2), 4.01167(5)Å, and c = 15.8787(7), 15.8359(2)Å. The hydrogen is accommodated in a tetrahedral yttrium environment within the 2D bimetallic layers. Lattice constant trends indicate that a more fully hydrided version exists. Band structure calculations confirm the 2D metal-bonded

character of the compounds, and also help illustrate the bonding/matrix changes with the absorption of hydrogen. The ternary structures for both $Y_5M_2Te_2$ and $Sc_5Ni_2Te_2$ derive from that of Gd_3MnI_3, and illustrate three different kinds of metal chain condensation.

Introduction

The understanding of metal-metal bonding and its consequences has experienced much growth since the early empirical studies on metals by Pauling.[1] Our research group has focused considerable attention on the early transition-metal-rich chemistry of the halides and chalcogenides to uncover the many different expressions of metal-metal bonding and their import. Examples of group III chalcogenides include Sc_2Te,[2] $(Sc,Y)_8Te_3$,[3] and Sc_9Te_2,[4] while representatives from the complementary binary halides include Sc_7Cl_{10},[5] Y_2Cl_3,[6] and LaI.[7] The chalcogenide and halide compounds share one similar feature, that each contains trans-edge-shared metal octahedral chains linked via vertices or edges to form diverse 1D and 2D metal-bonded structures. The halide metal structures have relatively more anions and naturally tend to be less condensed. Close structural relationships have been found with compounds in electron- richer binary systems, such as between Sc_8Te_3 and Ti_8Ch_3[8, 9] (Ch = S, Se), or Sc_2Te and Zr_2Te.[10] Later transition metals have long been known to stabilize early transition metal clusters in the halides,[11] and research in ternary chalcogenide chemistry has uncovered more structural interrelationships between $Sc_5Ni_2Te_2$,[12] Gd_3MnI_3,[13] and $Hf_5Co_{1+x}P_{3-x}$ $(0 < x < 0.5)$.[14] These relationships have helped us to assess how anion sizes, metal-electron concentrations and metal-to-nonmetal proportions influence structural features. A new linkage in cluster condensation among the bimetallic layered compounds is reported here for $Y_5M_2Te_2$ (M = Fe, Co, Ni), with its close electronic and structural interrelationships to Gd_3MnI_3 and $Sc_5Ni_2Te_2$ giving further clues as to factors that contribute to the dimensionality and persistent features of metal-metal bonding.

From another perspective, combinations of early with late transition metals in binary systems has been descried as important as hydrogen storage materials, as in $LaNi_5$.[15] The Y-M (M = Fe, Co, Ni) systems have also been considered to be very promising for hydrogen storage[16] because yttrium's lower atomic mass compared with those of the heavier lanthanides increases the amount of hydrogen absorbed per unit weight,[17] and YNi_3 does in fact absorb more hydrogen (by weight) than $LaNi_5$.[16] The phases YNi_2, Y_2Ni_7 and YNi_3 have been studied earlier as hydrogen storage materials, and all are reported to keep their respective structure type, even with up to four bound hydrogen atoms per formula unit.[16] We report here the hydrogen absorption within the 2D Y-Ni layers of $Y_5Ni_2Te_2$ and the resulting structural and bonding transformations.

Experimental Section

Syntheses. All materials were handled in a He-filled glovebox. The sources (yttrium sheets, iron chunks, cobalt, nickel and tellurium powder, all with reported purities of > 99.9%), and the preparation of Y_2Te_3, were described before.[3, 12]

$Y_5M_2Te_2$ (M = Fe, Co, Ni). Appropriate amounts of the elements and Y_2Te_3 to give the $Y_5M_2Te_2$ (M = Fe, Co, Ni) stoichiometry (~300 mg total) were pelletized with the aid of a hydraulic press and sealed inside tantalum tubing. These were heated to 1050 °C for 84 h inside fused-silica containers and then allowed to radiatively cool inside the furnace. Guinier powder patterns at this point revealed yields from 75 to 95% $Y_5M_2Te_2$, with small amounts of yttrium metal (visual), YTe, and the appropriate late-transition metal as impurities.

$Y_5M_2Te_2H_x$. This compound was initially synthesized via an adventitious hydrogen contamination of newly prepared yttrium powder. A yttrium rod (Ames Laboratory > 99.9% purity) had been hydrided by slow heating (~10 °C/hr) to 700 °C in a fused-silica apparatus under a hydrogen pressure of 0.8 atm, kept there for 5 hours, and allowed to cool radiatively in the furnace. The sample was powderized in an alumina mortar, and Guinier patterns taken at this point revealed a mixture of YH_2 and YH_3. A pure sample of YH_3 was later prepared according to the known *P-T-c* diagram[18] by reacting a similar mixture at 200 °C for 36 h under 1 atm of H_2. To prepare granular yttrium metal, the powdered hydride sample was placed inside a high-temperature vacuum furnace and dehydrided by heating to 750 °C for 48 hours until the vacuum pressure decreased to 3×10^{-8} atm. Apparently, the yttrium was not sufficiently dehydrided (below) under these conditions, although it had started to sinter.

Use of this yttrium powder to prepare the $Y_5M_2Te_2$ phases according to the procedure above resulted in an unidentified product for M = Ni. To confirm suspicions about hydride, this phase was converted to the known $Y_5Ni_2Te_2$ compound (above) and back to the unknown by first heating it to 950 °C for 24 hours in the high-temperature furnace under dynamic vacuum and then by reaction with small amounts of YH_3 (in fused silica) in a tube furnace. The supposed $Y_5Ni_2Te_2H_x$ phase was then prepared from Y_2Te_3, Ni, YH_3 and non-hydrided yttrium sheet as before for the loaded compositions x = 0.4, 0.6, 0.8, 1.0, 2.0, 3.0, and 4.0 under the reaction conditions described before for the ternaries. A reaction, on a 5 gram scale, was also performed with YD_3 at the loaded composition $Y_5Ni_2Te_2D_{1.5}$ for the neutron data collection. Similar reactions with iron and cobalt in place of nickel and loaded as $Y_5M_2Te_2H_2$ gave no evidence of a hydride. All of the lattice constant results are listed in Table 1.

Powder X-ray Diffraction. The powder diffraction patterns of all phases were obtained with the aid of an Enraf-Nonius Guinier powder camera and monochromatic Cu $K\alpha_1$ radiation. The samples were crushed into powder form, mixed with standard silicon (NIST), and placed between two strips of Scotch-brand tape on a frame for mounting on the camera rotation motor. Lattice parameters were obtained by least squares of the measured and indexed lines in each sample referenced to silicon. Lattice parameters for the $Y_5M_2Te_2$ (M = Fe, Co, Ni) phases and the $Y_5Ni_2Te_2H_x$ series of hydrides are given in Table 1.

Single-Crystal Diffraction. $Y_5Fe_2Te_2$. Several black, irregularly shaped crystals were obtained from reactions loaded $Y_5Fe_2Te_2$ and mounted inside 0.3 mm i.d. glass capillaries that were sealed off and affixed to metal pins. Their crystal quality was checked by means of Laue photographs, and the best crystal was selected for data collection on a Rigaku AFC6R rotating-anode diffractometer (Mo Kα radiation, graphite monochromator) at 23°C. Twenty-five reflections were located from a random search, centered, and used to determine provisional lattice constants and crystal system. Four octants of data were collected (h, $\pm k$, $\pm l$) to $2\theta_{max} = 56°$ and corrected for Lorentz and polarization effects. The data were further corrected for absorption with the aid of three ψ-scans. Of 3106 measured reflections, 305 were unique and observed ($I > 3\sigma_I$). Extinction conditions and statistical evidence for centricity indicated one possible space group, *Cmcm*. The structure was solved by direct methods (SHELXS[19]) and refined with the package TEXSAN[20] in this space group.

The final anisotropic refinement converged at $R(F)/R_w = 4.6/4.2\%$ for the composition $Y_5Fe_2Te_2$. Some data for these processes are given in Table 2, and the atomic positions and isotropic-equivalent thermal parameters are given in Table 3. Additional data collection and refinement parameters, the anisotropic displacement parameters, and a complete distance list are in the Supporting Information. These as well as the F_o/F_c listing are available from J.D.C.

$Y_5Ni_2Te_2H_x$. Crystals from the reaction loaded $Y_5Ni_2Te_2H$ were mounted and checked, and the best was taken for a data set collection on a Bruker CCD diffractometer operating at room temperature with Mo Kα radiation. Ninety reflection frames collected with 30-s exposures were analyzed and yielded an orthorhombic unit cell and provisional lattice parameters. One sphere of reflections was collected ($\pm h$, $\pm k$, $\pm l$) to $2\theta_{max} = 56°$ and, when integrated and filtered with SAINTPLUS[21] gave 7740 reflections, of which 784 were unique and observed ($I > 3\sigma_I$). An absorption correction was applied with the program package SADABS.[22] Extinction conditions and statistical evidence for centricity indicated one possible space group, *Pnma*, and the structural model was obtained and successfully refined with the SHELXTL[19] program. Some data collection and refinement parameters are given in Table 2. The refinement converged at $R1/wR2 = 3.4/7.8\%$ for the composition $Y_5Ni_2Te_2$. The hydrogen positions could not be detected or refined in the structure. The positional and isotropic-equivalent temperature parameters for the heavy atoms are given in Table 4. Additional data are available as described earlier.

Neutron Powder Diffraction. Atomic positions and isotropic displacement parameters for the deuteride $Y_5Ni_2Te_2D_{0.41(1)}$ were established with the aid of neutron powder diffraction data collected at −259 °C on the General Purpose Powder Diffractometer (GPPD) at the Intense Pulsed Neutron Source (IPNS) facility at Argonne National Laboratory.[23] The GPPD is a time-of-flight diffractometer with multidetector arrays at fixed scattering angles, and the high-resolution data from the $2\theta = 90.0$ and 145.9° backscattering detector banks were used for refinement. The powder data were refined using the Rietveld method[24] with the PC version of the General Structure Analysis System (GSAS),[25] starting with the positional data taken from the single crystal X-ray study. The final refinement included data in the range $0.6 < d < 3.0$ Å.

The heavy-atom structure, determined from X-ray diffraction, readily refined and revealed a single deuterium position in a yttrium tetrahedral interstice. Fractional refinements of this position gave a D occupancy of 41.1(1)%. Three impurity phases, YTe, YNi, and YD_2 were also observed and refined to the relative amounts of 13.0(1), 7.8(1), and 1.28(9)% (by weight), respectively. The background function was a cosine Fourier series with 6 coefficients, and the final conventional agreement indices were $R_p/R_{wp} = 3.2/4.6\%$ with a reduced χ^2 of 3.509. Some neutron data collection and refinement parameters are listed in Table 5. The neutron diffraction patterns in Figure 1 show the raw intensity data and, from top to bottom in each range, the background, and the individual contributions from the main $Y_5Ni_2Te_2D_{0.41(1)}$ and impurity phases, and the difference between the calculated and observed intensity profiles. Each profile includes tick marks to show the locations of the calculated reflections. A full distance list is available in the Supporting Information.

Band Calculations. Extended Hückel band calculations were carried out within the tight-binding approximation[26] for the full structures of $Y_5Fe_2Te_2$ and $Y_5Ni_2Te_2D_{0.5}$ by removal of two well-separated D per unit cell at 96 k-points spread out over the irreducible wedge. H_{ii} parameters employed for Y, Ni, and Fe were iterated to charge consistency for their respective structures (eV): Y 5s, -6.61; 5p, -4.18; 4d, -6.27. Fe 4s, -6.20; 4p, -3.00; 3d, -7.97. Ni 4s, -6.62; 4p, -3.19; 3d, -9.44. Te 5s, -21.20; 5p -12.00.[2] D 1s -13.60.

Results and Discussion

Syntheses. Synthesis of the ternary $Y_5M_2Te_2$ (M = Fe, Co, Ni) phases were straightforward, and their lattice constants are listed in Table 1. The series of reactions loaded $Y_5Ni_2Te_2H_x$, $x = 0.4 - 4.0$, were performed to aid in determining the possible range of hydrogen absorption into the structure (middle and lower parts of Table 1). The series of reactions loaded $x = 0.4$, 0.6, 0.8, 1.0, 2.0, 3.0 and 4.0 had yields of approximately 85% (first three), 75%, 60%, 50% and 30% $Y_5Ni_2Te_2H_x$, respectively. All products contained Y_2Te_3 and YNi impurities, but YH_2 was only observed as a side product at $Y_5Ni_2Te_2H_2$ and beyond. Inspection of the lattice dimensions obtained for the $x = 0.4 - 2.0$ series shows a fairly constant volume at ~915 Å^3, while the volume for $x = 3.0 - 4.0$ distinctly increases to plateau at ~924 Å^3. The high yields for $x = 0.4 - 1.0$ imply a single structure type with no detectable trend in lattice constants. The neutron data sample, loaded $Y_5Ni_2Te_2D_{1.5}$, had a refined composition of $Y_5Ni_2Te_2D_{0.41(1)}$ and a cell volume consistent with the lower range of x (Table 1). This suggests a higher hydrogen occupancy is probable for the reactions with $x = 3.0 - 4.0$, and lower % yields. An X-ray single crystal structure determination for $x = 4.0$ was attempted, but only could show a consistent unit cell dimension and crystal system due to the poor crystal quality.

Similar reactions were loaded with iron and cobalt in place of nickel. The lattice constants of reactions loaded $Y_5Fe_2Te_2H_2$ and $Y_5Co_2Te_2H_2$, upper half of Table 1, are statistically unchanged from those for pure $Y_5Fe_2Te_2$ and $Y_5Co_2Te_2$, which implies no hydride is formed.

Structural Description.

$Y_5Fe_2Te_2$. A near-[100] section of the structure viewed along the short 3.95 Å axis is drawn in Figure 2, with 99.9% probability thermal ellipsoids. In this view, any Y-Fe bonds have been omitted for clarity, and will be highlighted/discussed later. In general, the atom distribution can be viewed as extended zigzag chains of iron (gray) that are sheathed within yttrium (open) columns that are further connected via trans-vertices into 2D metallic layers well-separated by a single layer of tellurium atoms (black). The yttrium atoms in the apparent six-membered rings alternate in the projection by $a/2$. A side view in Figure 3 better illuminates this and the connectivity along a. A face-sharing yttrium trigonal-prismatic chain surrounds each iron zigzag chain, with each yttrium chain contributing capping atoms to the neighboring ones, to form the bimetallic layer.

Selected metal-metal distances for $Y_5Fe_2Te_2$ are listed in Table 6 and marked on the Figures. The shortest distance between two Y_5Fe_2 sheets, d(Y1-Y1) = 3.78 Å, is a weak interaction (below). The shortest yttrium-yttrium distances in the structure are within the bimetallic layer around Y3, Y3-Y1 and Y3-Y2 at 3.54 and 3.55 Å, respectively, which define elongated body-centered cubes around Y3. These cubes (offset by ½ a) are connected to each other at the top and bottom through Y1-Y2 at 3.70Å, forming the shell around the iron chain. A similar condensation around a late transition-metal chain has been described for

$Sc_5Ni_2Te_2$,[12] in which a pair of edge-sharing square-pyramidal chains interconnect to form the sheath. In $Y_5Fe_2Te_2$, the yttrium body-centered cubes may be similarly described as two vertex and basal-shared square pyramids. Longer yttrium distances occur on the edges (dashed) of the body-centered cubes (through the yttrium shell interior) for Y1-Y1 and Y2-Y2 at 3.99 and 3.80 Å. The body centered cubes form a face-sharing chain down the short *a* axis, for which all atoms repeat at 3.95 Å, Figure 3.

The near-[001] section of the structure in Figure 3 reveals the Y-Fe bonding more clearly. Each iron is surrounded by a yttrium trigonal prism at distances of 2.87 - 2.95 Å. The trigonal prisms around both iron positions are capped three times, once by Y3 on opposite sides at 3.05 Å for Fe1 and 3.32 Å for Fe2 respectively, and twice by the opposing iron atoms, Fe1 and Fe2, at 2.30 Å. In this arrangement, the capping nickel atoms for one trigonal prism are centering atoms for the next on each side, forming interpenetrating trigonal prisms, as in $Sc_5Ni_2Te_2$. Surprisingly, this Fe–Fe bond length is shorter than Pauling's single-bond distance, 2.33 Å.[1] This perhaps originates with matrix effects from the strong Y–Fe bonding, as the calculated overlap population per bond is less than expected (below).

The tellurium atoms sandwiched between the bimetallic layers are bound in bicapped trigonal prisms of yttrium, with Y-Te distances of 3.15-3.33 Å, a typical environment for tellurium in these metal-rich phases.[2-4] The closest Te–Te distance is 3.71 Å (marked), ~0.15 Å shorter than that normally seen in metal-rich telluride compounds or van der Waals separations. This Te–Te distance is fixed more by matrix effects, as the Y-Te bonds have some covalency, and the Te–Te interaction is calculated to be antibonding (below).

$Y_5Ni_2Te_2D_{0.41(1)}$. A near-[010] section of the structure, analogous to the [100] section of $Y_5Fe_2Te_2$, is shown in Figure 4 with marked atoms and distances, and Figure 5 is again the comparable view normal to the sheets. The atom distribution and coding is the same as in $Y_5Fe_2Te_2$, but that the bimetallic layers are rumpled to accommodate the deuterium (hatched).

Selected metal-metal distances for $Y_5Ni_2Te_2D_{0.41(1)}$ are reported in Table 7 and marked on Figures. The shortest distance between the bimetallic layers, *d*(Y1-Y2) = 3.91 Å (marked) is again a weak interaction (below), while the shorter distances and stronger interactions are located within the 2D layer. Compared with Y3 in $Y_5Fe_2Te_2$ (Figure 2), the equivalent Y4 centers a more distorted cube, with two similar by short yttrium distances, Y5-Y4 at 3.59Å and Y1-Y4 at 3.55Å, around D, and two comparably longer distances, Y2-Y4, 3.77Å; Y3-Y4, 3.72Å. The Y4 centered distorted cube is connected to another through Y1-Y3 at 3.62Å and Y3-Y5, 3.63Å, forming the sheath around the nickel zigzag chain. The edges of the distorted Y4-centered cubes, Y1-Y2 at 3.50Å and Y3-Y5 at 3.58Å, are ~0.4 Å shorter than in $Y_5Fe_2Te_2$. These distance changes likely reflect a reapportioning of the metal-based electrons away from the Y4 cube center (Y2-Y4, Y3-Y4) and towards the cube edges (Y1-Y2, Y3-Y5) (below). All atoms, including the yttrium body-centered cubes, repeat down the short axis at 4.01 Å.

Figure 5 reveals the Y-Ni and Y-D bonding more clearly. Each nickel is again surrounded in a distorted yttrium trigonal prism at distances of 2.7 - 2.8 Å. However, the distance to one Y vertice of the trigonal prism, that is shifted closer to deuterium, is increased (not marked), Y1-Ni2 at 3.14 Å, and Y5-Ni1 at 3.18Å. Each nickel trigonal prism is capped three times, once each by Y4–Ni1 and Y4–Ni2 at 3.13 and 3.09 Å, and twice by opposing nickel atoms, Ni1–Ni2 at 2.69 Å, close to that in $Sc_5Ni_2Te_2$, 2.66 Å.[12]. Again, Pauling's Ni–Ni single-bond distance is much less, 2.30 Å,[1] and so possible matrix effects in the parent $Y_5Fe_2Te_2$ structure type have disappeared with the structural change. The Y–Ni distribution is such that the capping nickel atom of one trigonal prism is the centering atom in the next, to form the interpenetrating trigonal prisms. The added deuterium atom is bound in a yttrium tetrahedron with Y–D distances of 2.26 - 2.32 Å, a chain of these tetrahedra sharing vertices in an eclipsed conformation down the *b* axis. This distance compares well with 2.24Å for the crystal radius for Y^{3+} (VI) and a general value of 1.10Å for H .

Tellurium atoms sandwiched between the bimetallic layers are again bound in a bicapped trigonal prism of yttrium, with Y–Te distances of 3.10–3.32 Å. The closest Te–Te distance is 4.01Å down the short *b* axis, ~0.3 Å longer than before. The shortest Te–Te distance in $Y_5Fe_2Te_2$, marked at 3.71 Å in Figure 2, has increased to 4.58 Å in $Y_5Ni_2Te_2D_{0.41(1)}$ as a result of the structural distortion. As will be noted in the next section on electronic calculations and matrix effects, hydrogen absorption apparently relieves the structural compression. However, it is not yet not possible to fully quantify these matrix/bonding effects.

Theoretical Calculations. Band calculations seemed necessary to understand better the metal-metal bonding in $Y_5Fe_2Te_2$ and $Y_5Ni_2Te_2D_{0.41(1)}$, as conclusions based on atomic distances alone can be misleading.[2-4] Figures 6 and 7 show the total densities of states (DOS) and selected crystal orbital overlap population (COOP) curves for $Y_5Fe_2Te_2$ and

$Y_5Ni_2Te_2D_{0.5}$, respectively. Transition metal contributions have each been projected out in the respective DOS.

The Fermi level in the iron compound resides in a broad conduction band composed of ~65% yttrium and ~35% iron d-character, hence the solid is expected to be metallic. Iron is the major contributor to the bands between ~8.0 and -9.0 eV, while yttrium is at higher energies. The COOP curves at the Fermi level reveal Y-Y bonding and Fe-Fe antibonding character up to -5.5eV, to reveal the electron poor character of this compound, and with Y-Fe bonding being within 0.5 eV of optimization.

For $Y_5Ni_2Te_2D_{0.5}$, the Fermi level resides in a conduction band composed of ~85% yttrium and ~15% nickel d-character, and again the solid is metallic. As expected intuitively from the composition, to vary the hydrogen site occupancy from one to zero results in an insignificant change, ±0.03eV, in the Fermi level. Nickel is the major contributor to the conduction band below ~8.6eV, while at higher energies yttrium is. The nickel d-states fall lower and are much narrower in energy (~1.0eV) and more core-like than were the iron states. This is a common observation and arises in part from the fact that the yttrium d and s atomic orbitals are 1.5eV closer to the iron d orbitals than to the nickel states. The COOP curves reveal Y-Y and Y-Ni bonding character remain well above E_F, but mostly nonbonding Ni-Ni interactions once the d core becomes filled about 1 eV below there. The Y-Ni interactions are farther from optimization than Y-Fe in $Y_5Fe_2Te_2$, by ~1.5eV.

Comparison of bond distances with pairwise overlap populations allows one to ascertain where matrix effects, separations that are fixed more by geometric relationships, appear to be more important than bonding via near-neighbor contacts. For this purpose, pairwise overlap populations for Y-Y, Y-M, and M-M for $Y_5Fe_2Te_2$ and $Y_5Ni_2Te_2D_{0.5}$ are listed in decreasing magnitude with the distances in Tables 6 and 7.

In $Y_5Fe_2Te_2$, the highest Y-Y overlap populations (OP) occur within the Y3 centered cube, Y3-Y1 and Y3-Y2 at ~0.23 for both, and also along the notably longer repeat distance *a*, 0.16, for only Y3-Y3, around which Y-Y bonding dominates. The next highest Y-Y overlap populations include the connection between two cube chains that form the sheath, Y1 -Y2 at 0.11, and down the cube edges, Y1-Y1 and Y2-Y2 at 0.11 and 0.16 respectively. The Y1-Y1 interlayer contact falls fairly low on the list at 0.051, a weak interaction. The pairwise Y-Fe overlap populations are fairly unstriking, with distances from 2.7 to 3.3 Å that inversely parallel the OP range 0.29-0.17. The Y3 with more yttrium neighbors also exhibits a larger OP, 0.28, for its distance to Fe1 at 3.05 Å. A similar skewing of the environment around the late transition metal was noted in $Sc_5Ni_2Te_2$.

The Fe-Fe contact is found to be bonding, OP = 0.29, even though its distance is 0.03Å less than for an Fe-Fe single bond (Pauling). Its environment is certainly unlike that in elemental iron, and has self-bonding distances strongly influenced by covalent yttrium neighbors, in what has been called a matrix effect in metal-rich structures before.[2-4] The shortest Te-Te interaction, 3.71 Å, has an antibonding OP of -0.033. Clearly, this tellurium separation is fixed mainly by the strong Y-Te interactions. The strongest Y-Y bonding and smallest volume (structural compression) of the three new non-hydride phases is for M = Ni, which may provide the driving force for the hydrogen absorption (below).

In $Y_5Ni_2Te_2D_{0.5}$, the Y-Y pairwise overlap populations (Table 7) parallel decreases in distance much better than for $Y_5Fe_2Te_2$. The largest deviation on the list, Y1-Y3 at 3.62Å, exhibits a low OP of 0.15, an expected effect on the basis of its location on the periphery of the metal-layer and closeness to tellurium atoms. The same occurs for the equivalent Y2-Y5, but slightly less. This effective oxidation of external metal-cluster bonds has been seen more clearly before.[4] The shortest and internal Y-Y bonds, Y1-Y2, Y1-Y4, Y3-Y5 and Y4-Y5 all have OP's greater than 0.20, while those just mentioned on the periphery have lower values. Comparison of $Y_5Ni_2Te_2D_{0.5}$ with $Y_5Fe_2Te_2$ shows that the metal-based electrons are redistributed away from the equivalent centered cubes and on the outside of the fold at deuterium, (Y4-Y2, Y4-Y3 at ~ 0.15 vs. Y1-Y3, Y2-Y3 at ~0.23 respectively) and towards the cube edges (Y1-Y2, Y3-Y5 at ~0.22 vs. Y1-Y1, Y2-Y2 at ~0.16–0.11 respectively). This noticeable Y-Y bonding change on incorporation of hydrogen may arise from the relative oxidizing ability of hydrogen on neighboring metal atoms. The interlayer contact, Y1-Y2 falls fairly low on the list at 0.048, and is again a weak interaction.

The Y-Ni pairwise interactions neatly parallel decreases in distances with ranges of 2.7-3.2 Å for 0.24–0.10 OP's and no statistically discernable deviations, in contrast to those for Y-Fe in $Y_5Fe_2Te_2$. The Y-Ni distances are ~0.14Å less than the stronger Y-Fe interactions, but the former leaves more electrons available for Y-Y bonding and allows for the contraction of the yttrium cage around it, in what may be called a cooperative size and valence effect. Lastly, the Ni-Ni interaction is weakly bonding with an OP of only 0.019, while Te–Te down the short *b* axis has an OP of -0.006 (as expected from their distances). Also, the slightly antibonding Te–Te interaction in $Y_5Fe_2Te_2$ is now nonbonding (OP = 0) in $Y_5Ni_2Te_2D_{0.5}$. Matrix effects are clearly less significant here.

Generally, the electronic calculations reveal the largely 2D metal-bonded character for both of the title compounds, and Y-M overlap populations that parallel well with the corresponding inverse distances. Hydrogen absorption evidently diminishes compression on the Te–Te and M-M neighbors, which is greatest for M = Ni from the volume trends, and also results in a better correspondence between bond lengths and bond orders for Y-Y and Y-M. The latter has been suspected as a possible contributing factor to a metal lattice instability in Sc_9Te_2.[4] Additionally, the hydrogen absorption effects a redistribution of metal-based electrons away from the neighboring Y-Y bonds and less optimized and strong Y-M bonding.

Structural Comparisons. The $Y_5M_2Te_2$ (M = Fe, Co, Ni) compounds share very striking close structural relationships with both $Sc_5Ni_2Te_2$ and Gd_3MnI_3, as shown in Figure 8. The longest known, Gd_3MnI_3, contains single zigzag chains of Mn sheathed by a gadolinium framework (which may be traced to a substantial distortion of pairs of condensed octahedral chains), to form an isolated 1D metallic chain. This can be seen to be structurally related to that shown for $Sc_5Ni_2Te_2$ and the title compounds. The present results shows that replacement of iodine in Gd_3MnI_3 by tellurium, and necessary changes in composition and interstitials to give the $R_5Ni_2Te_2$ ® = Sc, Y) compounds allows condensation of the isolated chains to proceed in one of two ways: 1) the formation of a Sc_5Ni_2 double chain motif by the sharing of two vertices on the same edge (A), or 2) the formation of Y_5Ni_2 by the sharing of the trans vertices (B). The sharing of trans-vertices results in the continuous polymerization of the metallic Gd_3Mn-like rods into 2D sheets, while a sharing of two vertices on a single edge halts the condensation at the dimer stage. Why a metallic structure prefers one mode of condensation over another may be significantly influenced by matrix effects because of the structure-directing features described here and before, while electron count alone as a stability factor in metal-rich phases is less clear because of the delocalized bonding.[3] A good way to approach this problem quantitatively is not evident. Progress in the synthesis of low-dimensional metallic phases far exceeds the theoretical predictability, while experiments continue to lead the way.

Conclusions. The $Y_5M_2Te_2$ (M = Fe, Co, Ni) and $Y_5Ni_2Te_2D_{0.41}$ compounds have been synthesized by high-temperature solid-state techniques. Their structures comprise zigzag chains of the late-transition metal sheathed by yttrium atoms and condensed through trans vertices to form 2D bimetallic layers separated by a single layer of tellurium atoms. Only $Y_5Ni_2Te_2$ is found to absorb hydrogen, which caused a rumpling of the bimetallic sheets through the binding of hydrogen in tetrahedral yttrium cavities. Band structure calculations confirm the largely 2D metal-bonded character of both title compounds, and show that hydrogen absorption and change in M reduces the structural compressions in the $Y_5Fe_2Te_2$ structure type. The structure type derives from Gd_3MnI_3 by a new type of metal condensation that contrasts with another mode in $Sc_5Ni_2Te_2$.

Acknowledgements

We thank Ilia Guzei for help with the CCD diffractometer. This work was supported by the National Science Foundation, Solid State Chemistry, via Grants DMR-9510278 and DMR-9809850 and was carried out in the facilities of the Ames Laboratory, U.S. Department of Energy. The neutron diffraction studies were carried out at Argonne National Laboratory under Contract W-31-109-ENG-38.

Supporting Information Available

Tables of additional crystallographic and refinement parameters, and a complete listing of nearest neighbor distances. This material is available free-of-charge via the Internet at http//pubs.acs.org. See any current masthead page for ordering and Web access instructions.

References

(1) Pauling, L. *Phys. Rev.* **1938**, *54*, 899. Pauling L. *The Nature of the Chemical Bond*; Cornell University Press: Ithaca, NY, 1960.

(2) Maggard, P.A.; Corbett, J.D. *Angew. Chem., Int. Ed. Engl.* **1997**, *36*, 1974

(3) Maggard, P.A.; Corbett, J.D. *Inorg. Chem.* **1998**, *37*, 814.

(4) Maggard, P.A.; Corbett, J.D. *J. Am. Chem. Soc.* **2000**, *122*, 838.

(5) Poeppelmeier, K.R.; Corbett, J.D. *Inorg. Chem.* **1977**, *16*, 1107.

(6) Mattausch, J.B.; Hendricks, J.B.; Eger, R.; Corbett, J.D.; Simon A. *Inorg. Chem.* **1980**, *19*, 2128.

(7) Martin, J.D.; Corbett, J.D. *Angew. Chem., Int. Ed. Engl.* **1995**, *34*, 233.

(8) Owens, J.P.; Franzen, H.F. *Acta Crystallogr.* **1974**, *B30*, 427.

(9) Weirich, T.E.; Pöttgen, R.; Simon, A. *Z. Kristallogr.* **1996**, *211*, 929.

(10) Örlygsson, G.; Harbrecht, B. *Inorg. Chem.* **1999**, *38*, 3377.

(11) Corbett, J.D. *J. Alloy Compd.* **1995**, *229*, 10.

(12) Maggard, P.A.; Corbett, J.D. *Inorg. Chem.* **1999**, *38*, 1945.

(13) Ebihara, M.; Martin J.D.; Corbett, J.D. *Inorg. Chem.* **1994**, *33*, 2078.

(14) (a) Kleinke, H.; Franzen, H.F. *J. Alloys Compd.* **1996**, *238*, 68. (b) Kleinke, H.; Franzen, H.F. *ibid.* **1997**, *255*, 110.

(15) Furrer, A.; Fischer, P.; Hälg, W.; Schlapbach, L. *Hydrides for Energy Storage, Proceedings of an International Symposium*; Norway 1977.

(16) Burnasheva, V.V.; Tarasov, B.P. *Russian J. Inorg. Chem.* **1984**, *29*, 651.

(17) van Essen, R.H.; Buschow, K.H.J. *J. Less-Common Met.* **1980**, *70*, 189.

(18) Lundin, C.E.; Blackledge, J.P. *J. Electrochem Soc.* **1962**, *109*, 838.

(19) Sheldrick, M. *SHELXS-86*. Universität Göttingen, Germany, 1986.

(20) *TEXSAN*, Version 6.0, Molecular Structure Corp., The Woodlands, Texas, 1990.

(21) *SAINTPLUS*; Bruker AXS, Inc.: Madison, WI, 1996.

(22) Blessing, R.H. *Acta Crystallogr.* **1995**, *A51*, 33.

(23) Jorgensen, J.D.; Faber Jr, J.; Carpenter, J.M.; Crawford, R.K.; Haumann, J.R.; Hitterman, R.L.; Kleb, R.; Ostrowski, G.E.; Rotella, F.J.; Worlton, T.G. *J. Appl. Cryst.* **1989**, *22*, 321.

(24) Rietveld, H.M. *Acta Crystallogr.* **1967**, *22*, 151.

(25) Larson, A.C.; Von Dreele, R.B. *General Structure Analysis System*; Report LAUR 86-748; Los Alamos National Laboratory: Los Alamos, NM, 1995.

(26) Hoffman, R.J. *Chem. Phys.* **1963**, *39*, 1397. Whangbo, M.; Hoffman, R. *J. Am. Chem. Soc.* **1978**, *100*, 6093.

Table 1. Lattice parameters for the $Y_5M_2Te_2$ (*Cmcm*) and $Y_5Ni_2Te_2H_x$ (*Pnma*) phases.[a]

compound	*a*(Å)	*b*(Å)	*c*(Å)	*V*(Å^3)
$Y_5Fe_2Te_2$	3.9594(3)	15.057(1)	15.216(1)	907.1(2)
$Y_5Co_2Te_2$	3.9421(6)	15.092(2)	15.021(2)	893.7(4)
$Y_5Ni_2Te_2$	3.977(1)	15.035(2)	14.857(3)	888.4(5)
loaded compositions				
$Y_5Fe_2Te_2H_2$	3.958(1)	15.058(6)	15.214(7)	906.7(6)
$Y_5Co_2Te_2H_2$	3.942(2)	15.090(5)	15.020(4)	893.4(5)
$Y_5Ni_2Te_2H_{0.4}$[b]	14.359(4)	4.020(1)	15.858(3)	915.5(4)
$Y_5Ni_2Te_2H_{0.6}$	14.353(1)	4.0213(4)	15.853(1)	915.0(1)
$Y_5Ni_2Te_2H_{0.8}$	14.354(3)	4.0163(7)	15.866(2)	914.7(3)
$Y_5Ni_2Te_2H_{1.0}$	14.364(1)	4.0172(4)	15.880(1)	916.4(1)
$Y_5Ni_2Te_2H_{2.0}$	14.352(1)	4.0132(5)	15.876(1)	914.4(2)
$Y_5Ni_2Te_2H_{3.0}$	14.368(1)	4.0302(4)	15.951(1)	923.7(1)
$Y_5Ni_2Te_2H_{4.0}$	14.369(2)	4.0327(5)	15.951(2)	924.3(2)
refined composition				
$Y_5Ni_2Te_2H_x$[c]	14.356(2)	4.0209(3)	15.857(1)	915.3(1)
$Y_5Ni_2Te_2D_{0.41(1)}$[d]	14.3678(7)	4.0173(2)	15.8787(7)	916.50(9)
$Y_5Ni_2Te_2D_{0.41(1)}$[e]	14.3282(2)	4.01167(5)	15.8359(2)	910.25(2)

[a] Lattice constants from guinier powder diffraction data at 23 °C.

[b] All hydrides, with the unit cell transformation to the new space group (**a**, **b**, **c**) → (**b**, **c**, **a**).

[c] Sample used in the X-ray single crystal structure determination for heavy atom refinement.

[d] Lattice constants from X-ray powder diffraction at 23 °C.

[e] Lattice constants from neutron powder diffraction data at −259 °C.

Table 2. Single crystal X-ray data collection and refinement parameters for $Y_5Fe_2Te_2$ (1st value) and $Y_5Ni_2Te_2H_x$ (2nd value).

Crystal Data	
Formula weight,g mol^{-1}	811.42, 817.12
Crystal System	Orthorhombic
Space group, Z	*Cmcm* (No. 63), 4; *Pnma* (No. 62), 4
ρ_{calc}, g/cm^3	5.976, 5.897
μ (Mo K$_\alpha$), cm^{-1}	41.421, 41.265
Data Collection	
Diffractometer	Rigaku AFC6R, Bruker AXS CCD
Temperature, °C	23
Radiation, $2\theta_{max}$	Mo K$_\alpha$, 56°
Reflections measured	(h, ±k, ±l), (±h, ±k, ±l)
Refinement	
Number of measured reflections	3106, 7740
Number of unique observed reflections ($I > 3\sigma_I$)	305, 784
Number of variables	31, 56
$R(F_o, F_o^2)$; R_w,^{a,b} %	4.6, 4.2; 3.4, 7.8

[a] $R = \Sigma||F_o|-|F_c||/\Sigma|F_o|$; $R_\omega = [\Sigma w(|F_o|-|F_c|)^2/\Sigma w(F_o)^2]^{1/2}$, $w = 1/\sigma^2$.

[b] $R = \Sigma|F_o^2-F_c^2|/\Sigma F_o^2$; $R_\omega = [\Sigma w((F_o^2-F_c^2)^2/\Sigma wF_o^2)^2]^{1/2}$, $w = 1/\sigma^2$.

Table 3. Positional and isotropic-equivalent thermal parameters for $Y_5Fe_2Te_2$.

Atom[a]	y	z	B_{eq} (Å^2)[b]
Te1	0.3831(2)	0.5388(3)	0.89(7)
Y1	0.0369(2)	0.6187(2)	0.9(1)
Y2	0.2556(2)	0.3750(2)	1.0(1)
Y3	0.6061(3)	1/4	1.0(2)
Fe1	0.4034(4)	1/4	1.0(3)
Fe2	0.8263(5)	1/4	1.0(2)

[a] All atoms on m or $m2m$ with $x = 0$.

[b] $B_{eq} = (8\pi^2/3)\Sigma_i\Sigma_j U_{ij} a_i^* a_j^* \vec{a}_i \vec{a}_j$.

Table 4. Positional and isotropic-equivalent thermal parameters from the single crystal X-ray data, $Y_5Ni_2Te_2H_x$ (1st line), and neutron powder data, $Y_5Ni_2Te_2D_{0.41(1)}$ (2nd line).

Atom[a]	x	z	B_{eq} (Å^2)[b]
Te1	0.96613(6)	0.62734(6)	0.85(2)
	0.9659(3)	0.6264(5)	0.27(4)
Te2	0.95423(7)	0.12999(6)	0.94(2)
	0.9552(2)	0.1278(5)	0.27(4)
Y1	0.1489(1)	0.74196(9)	0.84(2)
	0.1483(2)	0.7427(2)	0.23(6)
Y2	0.8864(1)	0.81019(9)	0.86(2)
	0.8857(3)	0.8098(2)	0.26(6)
Y3	0.8823(1)	0.44668(9)	0.94(2)
	0.8816(3)	0.4460(2)	0.38(6)
Y4	0.2079(1)	0.37406(3)	0.91(2)
	0.2071(2)	0.3736(4)	0.28(5)
Y5	0.1376(1)	0.00103(9)	0.93(2)
	0.1392(2)	0.0001(2)	0.28(6)
Ni1	0.7405(1)	0.3218(1)	0.93(3)
	0.7413(2)	0.3217(2)	0.53(5)
Ni2	0.2470(1)	0.5655(1)	1.02(3)
	0.2465(2)	0.5653(2)	0.27(5)
D	0.2204(6)	0.873(1)	0.9(2)

[a] All atoms on m, with $y = 1/4$.

[b] $B_{eq} = (8\pi^2/3)\Sigma_i\Sigma_j U_{ij} a_i^* a_j^* \vec{a}_i \vec{a}_j$.

Table 5. Powder neutron data collection and refinement parameters for $Y_5Ni_2Te_2D_{0.41(1)}$.

Formula weight	817.99
Space Group, Z	*Pnma* (No. 62), 4
Temperature (°C)	-259
d_{calc} (g/cm^3)	5.969
Number of data	8486
Number of reflections (fitted)	3707
Variables	72
Residuals; R_p, R_{wp}[a] (%)	3.19, 4.59
χ^2	3.509
Scattering lengths (10^{-12}cm)[b]	Y, 0.775
	Ni, 1.030
	Te, 0.580
	D, 0.667

[a] $R_p = [\Sigma(|I_o - I_c|)/\Sigma I_o]$; $R_{wp} = [\Sigma(I_o - I_c)^2/\Sigma w I_o^2]^{1/2}$.

[b] Reference 24.

Table 6. Selected metal-metal distances (Å) and the corresponding pairwise overlap populations in $Y_5Fe_2Te_2$.

atom 1	atom 2	distance	OP	atom 1	atom 2	distance	OP
Y1	Y3	3.543(4)	0.233	Y1	Fe2	2.870(6)	0.287
Y2	Y3	3.551(3)	0.231	Y3	Fe1	3.051(9)	0.278
Y3[a]	Y3	3.9594(3)	0.163	Y2	Fe2	2.944(3)	0.267
Y2[b]	Y2	3.8042(3)	0.160	Y1	Fe1	2.953(3)	0.249
Y1	Y2	3.699(3)	0.108	Y2	Fe1	2.928(6)	0.244
Y1[b]	Y1	3.987(3)	0.107	Y3	Fe2	3.316(9)	0.167
Y1[c]	Y1	3.779(6)	0.051				
Y2[a]	Y2	3.9594(3)	0.044	Fe1	Fe2	2.296(4)	0.289
Y1[a]	Y1	3.9594(3)	0.035				

[a] Short axis distance.

[b] Intralayer distance.

[c] Interlayer distance.

Table 7. Selected metal-metal distances (Å) and the corresponding pairwise overlap populations in $Y_5Ni_2Te_2D_{0.5}$.[a]

atom 1	atom 2	distance	OP	atom 1	atom 2	distance	OP
Y1[b]	Y2	3.502(5)	0.232	Ni1	Y2	2.715(4)	0.237
Y1	Y4	3.552(5)	0.219	Ni2	Y3	2.725(3)	0.234
Y3[b]	Y5	3.577(5)	0.215	Ni1	Y1	2.750(3)	0.231
Y4	Y5	3.590(5)	0.200	Ni2	Y5	2.788(3)	0.219
Y2	Y5	3.634(5)	0.158	Ni1	Y3	2.814(5)	0.207
Y3	Y4	3.715(6)	0.151	Ni2	Y2	2.808(5)	0.206
Y1	Y3	3.624(4)	0.150	Ni2	Y4	3.088(7)	0.127
Y2	Y4	3.772(6)	0.140	Ni1	Y4	3.131(7)	0.116
Y1[c]	Y2	3.910(5)	0.048	Ni2	Y1	3.142(5)	0.107
				Ni1	Y5	3.180(5)	0.102
D	Y4	2.259(4)	0.165				
D	Y1	2.31(2)	0.133	Ni1	Ni2	2.694(2)	0.019
D	Y5	2.32(2)	0.125				

[a] Distances are calculated from the more accurate neutron powder diffraction results.

[b] Intralayer distance.

[c] Interlayer distance.

Supporting Information
Two-Dimensional Metallic Compounds $Y_5M_2Te_2$ (M = Fe, Co, Ni) That are Related to Gd_3MnI_3. Hydrogen Absorption in the $Y_5Ni_2Te_2H_x$ Derivative

Paul A. Maggard, Robert W. Henning, and John D. Corbett

Table S1. Single Crystal X-ray Data Collection and Refinement Parameters for $Y_5Fe_2Te_2$.

Formula weight, g mol^{-1}	811.42
Space group, *Z*	*Cmcm* (No. 63), 4
Lattice parameters, Å	
a	3.9594(3)
b	15.057(1)
c	15.216(1)
V, (Å^3)	907.1(2)
d_{calc}, g/cm^3	5.976
Radiation; $2\theta_{max}$	Mo K_α; 56°
Octants measured	h, ±k, ±l
Scan method	ω-2θ
Temperature, °C	23
Absorption Method	2 ψ-scans, DIFABS
Relative transmission range	0.48 - 1.43
μ, cm^{-1} (Mo K_α)	41.421
Number of reflections:	
measured	3106
unique observed ($I \geq 3\sigma(I)$)	305
Number of variables	31
Residuals *R*; R_ω,[a] %	4.6; 4.2
Goodness of fit	1.39
Secondary Ext.	2.8(2) x 10^{-7}

[a] $R = \Sigma||F_o|-|F_c||/\Sigma|F_o|$; $R_\omega = [\Sigma\omega(|F_o|-|F_c|)^2/\Sigma\omega(F_o)^2]^{1/2}$, $\omega = 1/\sigma^2$.

Table S2. U_{ij} (Å^2) values for $Y_5Fe_2Te_2$.

Atom	U11	U22	U33	U12	U13	U23
Te1	0.0109(8)	0.011(1)	0.011(1)	0	0	0
Y1	0.013(1)	0.014(2)	0.009(1)	0	0	0
Y2	0.012(1)	0.011(2)	0.013(2)	0	0	0
Y3	0.012(2)	0.012(2)	0.015(2)	0	0	0
Fe1	0.017(3)	0.015(4)	0.007(3)	0	0	0
Fe2	0.008(3)	0.016(3)	0.012(3)	0	0	0

Table S3. Interatomic distances < 4.0Å in $Y_5Fe_2Te_2$.

Atom	Atom	x	Distance	Atom	Atom	x	Distance
Te1	Te1	2x	3.9594(3)	Y3	Te1	2x	3.217(2)
	Te1		3.714(5)		Y1	4x	3.543(4)
	Y1	2x	3.281(3)		Y2	4x	3.551(3)
	Y1	2x	3.334(3)		Fe1		3.051(9)
	Y2		3.146(3)		Fe2		3.316(9)
	Y2	2x	3.162(3)				
	Y3		3.217(2)	Fe1	Y1	4x	2.953(3)
					Y2	2x	2.928(6)
Y1	Te1	2x	3.281(3)		Y3		3.051(9)
	Te1	2x	3.334(3)		Fe2	2x	2.296(4)
	Y1		3.779(6)				
	Y2	2x	3.699(3)	Fe2	Y1	2x	2.870(6)
	Y3	2x	3.543(4)		Y2	4x	2.944(3)
	Fe1	2x	2.953(3)		Y3		3.316(9)
	Fe2		2.870(6)		Fe1	2x	2.296(4)
Y2	Te1		3.146(3)				
	Te1	2x	3.162(3)				
	Y1	4x	3.699(3)				
	Y2		3.8042(3)				
	Y3	2x	3.551(3)				
	Fe1		2.928(6)				
	Fe2	2x	2.944(3)				

Table S4. Single Crystal X-ray Data Collection and Refinement Parameters for $Y_5Ni_2Te_2(H)$.

Formula weight,g mol^{-1}	817.12
Space group, Z	*Pnma* (No. 62), 4
Lattice parameters, Å	
a	14.384(4)
b	4.026(2)
c	15.895(7)
V, (Å^3)	920.5(6)
d_{calc}, g/cm^3	5.897
Radiation; $2\theta_{max}$	Mo K_α; 56°
Octants measured	±h, ±k, ±l
Scan method	ω-2θ
Temperature, °C	23
Absorption Method	SADABS
Relative transmission range	0.73 - 1.69
μ, cm^{-1} (Mo K_α)	41.265
Number of reflections:	
measured	7740
unique observed ($I \geq 3\sigma(I)$)	784
Number of variables	56
Residuals R; R_ω,^{a} %	3.4; 7.8
Goodness of fit	0.58
Secondary Ext.	1.3(2) x 10^{-3}

[a] $R = \Sigma |F_o^2-F_c^2|/\Sigma F_o^2$; $R_\omega = [\Sigma\omega((F_o^2-F_c^2)^2/\Sigma\omega F_o^2)^2]^{1/2}$.

Table S5. U_{ij} (Å^2) values for $Y_5Ni_2Te_2H$.

Atom	U11	U22	U33	U12	U13	U23
Te1	0.0109(5)	0.0127(5)	0.0089(5)	0	0.0001(4)	0
Te2	0.0131(5)	0.0102(4)	0.0122(5)	0	-0.0016(4)	0
Y1	0.0098(7)	0.0118(7)	0.0103(7)	0	-0.0005(5)	0
Y2	0.0110(7)	0.0119(7)	0.0099(7)	0	0.0002(5)	0
Y3	0.0140(8)	0.0130(7)	0.0087(7)	0	-0.0014(5)	0
Y4	0.0120(7)	0.0112(6)	0.0112(7)	0	-0.0003(6)	0
Y5	0.0136(8)	0.0118(7)	0.0100(7)	0	0.0007(5)	0
Ni1	0.010(1)	0.012(1)	0.0138(9)	0	-0.0005(7)	0
Ni2	0.012(1)	0.013(1)	0.013(1)	0	-0.0001(8)	0

Table S6. Interatomic distances < 4.0Å in $Y_5Ni_2Te_2$(H).

Atom 1	Atom 2	Mult.	Distance	Atom 1	Atom 2	Mult.	Distance
Te1	Y1		3.199(2)	Y2	Y1		3.929(2)
	Y2		3.125(2)		Y1		3.514(2)
	Y3		3.114(2)		Y4	2x	3.804(2)
	Y3	2x	3.192(2)		Y5	2x	3.630(2)
	Y4	2x	3.212(2)		Ni1	2x	2.723(2)
					Ni2		2.814(2)
Te2	Y1	2x	3.224(2)				
	Y2	2x	3.196(2)	Y3	Te1		3.114(2)
	Y4		3.544(2)		Te1	2x	3.192(2)
	Y5		3.341(2)		Y1	2x	3.639(2)
	Y5	2x	3.184(2)		Y4	2x	3.722(2)
					Y5		3.616(2)
Y1	Te1		3.199(2)		Ni1		2.847(2)
	Te2	2x	3.224(2)		Ni2	2x	2.748(2)
	Y2		3.929(2)				
	Y2		3.514(2)	Y4	Te1	2x	3.212(2)
	Y3	2x	3.639(2)		Te2		3.544(2)
	Y4	2x	3.564(2)		Y1	2x	3.564(2)
	Ni1	2x	2.759(2)		Y2	2x	3.804(2)
	Ni2		3.140(3)		Y3	2x	3.722(2)
					Y5	2x	3.614(2)
					Ni1		3.148(3)
Y2	Te1		3.125(2)		Ni2		3.094(3)
	Te2	2x	3.196(2)				

Table S6. (continued)

Y5	Te2		3.341(2)	Ni2	Y1		3.140(3)
	Te2	2x	3.184(2)		Y2		2.814(2)
	Y2	2x	3.630(2)		Y3	2x	2.748(2)
	Y3		3.616(2)		Y4		3.094(3)
	Y4	2x	3.614(2)		Y5	2x	2.802(2)
	Ni1		3.181(3)		Ni1	2x	2.701(2)
	Ni2	2x	2.802(2)				
Ni1	Y1	2x	2.759(2)				
	Y2	2x	2.723(2)				
	Y3		2.847(2)				
	Y4		3.148(3)				
	Y5		3.181(3)				
	Ni2	2x	2.701(2)				

Table S7. Interatomic distances < 4.0Å in $Y_5Ni_2Te_2D_{0.41(1)}$.

Atom 1	Atom 2	Mult.	Distance	Atom 1	Atom 2	Mult.	Distance
Te1	Y1		3.196(6)	Y2	Y1		3.910(5)
	Y2		3.124(9)		Y1		3.502(5)
	Y3		3.102(9)		Y4	2x	3.772(6)
	Y3	2x	3.180(5)		Y5	2x	3.634(5)
	Y4	2x	3.189(4)		Ni1	2x	2.715(4)
					Ni2		2.808(5)
Te2	Y1	2x	3.229(6)				
	Y2	2x	3.193(5)	Y3	Te1		3.102(9)
	Y4		3.554(4)		Te1	2x	3.180(5)
	Y5		3.322(6)		Y1	2x	3.624(4)
	Y5	2x	3.155(7)		Y4	2x	3.715(6)
					Y5		3.577(5)
Y1	Te1		3.196(6)		Ni1		2.814(5)
	Te2	2x	3.229(6)		Ni2	2x	2.725(3)
	Y2		3.910(5)				
	Y2		3.502(5)	Y4	Te1	2x	3.189(4)
	Y3	2x	3.624(4)		Te2		3.554(4)
	Y4	2x	3.552(5)		Y1	2x	3.552(5)
	Ni1	2x	2.750(3)		Y2	2x	3.772(6)
	Ni2		3.142(5)		Y3	2x	3.715(6)
	D		2.31(2)		Y5	2x	3.590(5)
					Ni1		3.131(7)
Y2	Te1		3.124(9)		Ni2		3.088(7)
	Te2	2x	3.193(5)		D	2x	2.259(4)

Table S7. (continued)

Y5	Te2		3.322(6)	Ni2	Y1		3.142(5)
	Te2	2x	3.155(7)		Y2		2.808(5)
	Y2	2x	3.634(5)		Y3	2x	2.725(3)
	Y3		3.577(5)		Y4		3.088(7)
	Y4	2x	3.590(5)		Y5	2x	2.788(3)
	Ni1		3.180(5)		Ni1	2x	2.694(2)
	Ni2	2x	2.788(3)				
	D		2.32(2)	D	Y1		2.31(2)
					Y4	2x	2.259(4)
Ni1	Y1	2x	2.750(3)		Y5		2.32(2)
	Y2	2x	2.715(4)				
	Y3		2.814(5)				
	Y4		3.131(7)				
	Y5		3.180(5)				
	Ni2	2x	2.694(2)				

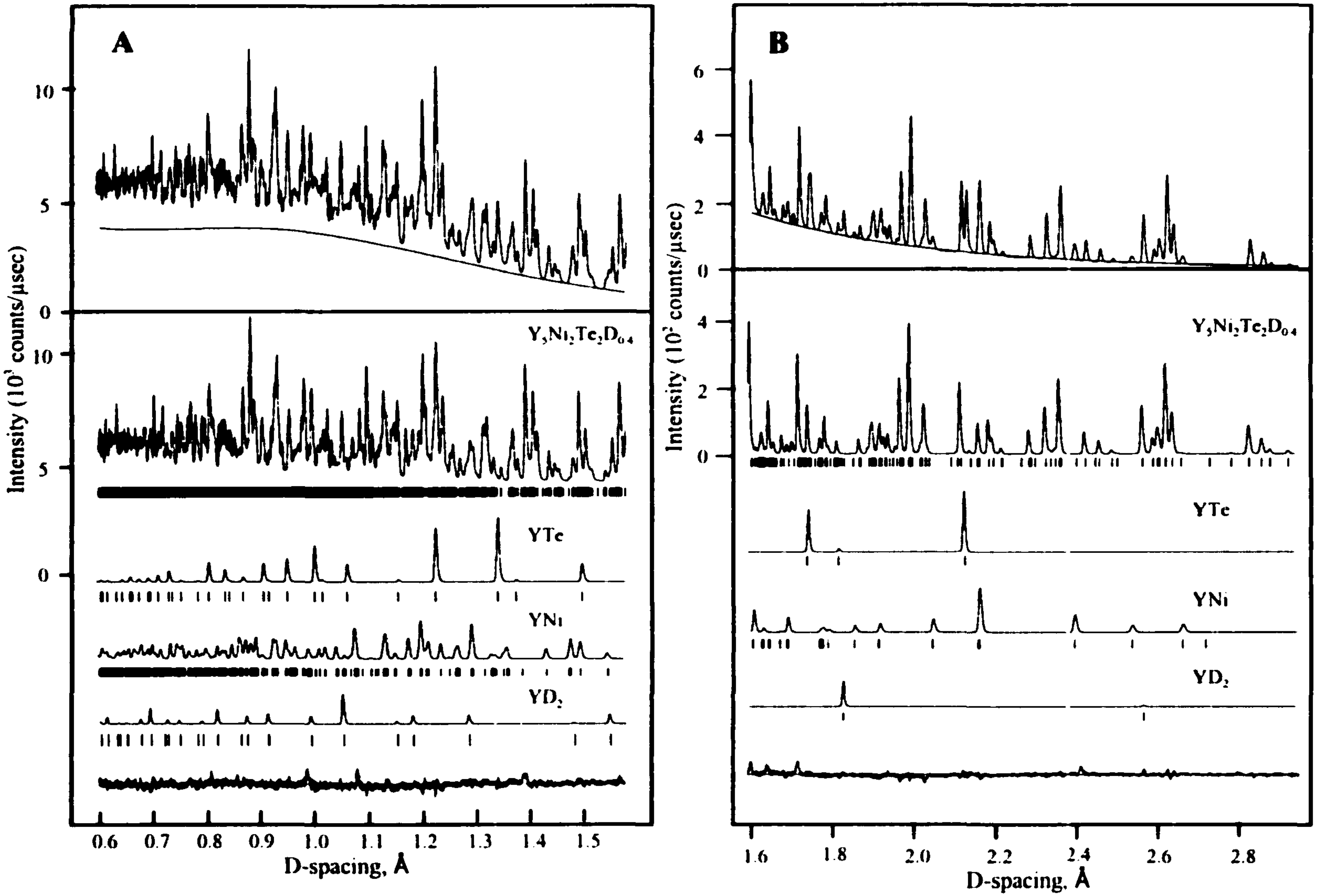

Figure 1. Neutron powder pattern of $Y_5Ni_2Te_2D_{0.41}$ divided into two regions, *d* = 0.6–1.6 (A) and 1.6–3.0Å (B). Shown in each are, from top to bottom, the experimental pattern with fitted background; the calculated patterns for the major and impurity phases, the reflections used (tick marks), and the difference spectrum; Scales are drawn for the experimental and major phases and to define the zero intensities, with all phases drawn to same scaling.

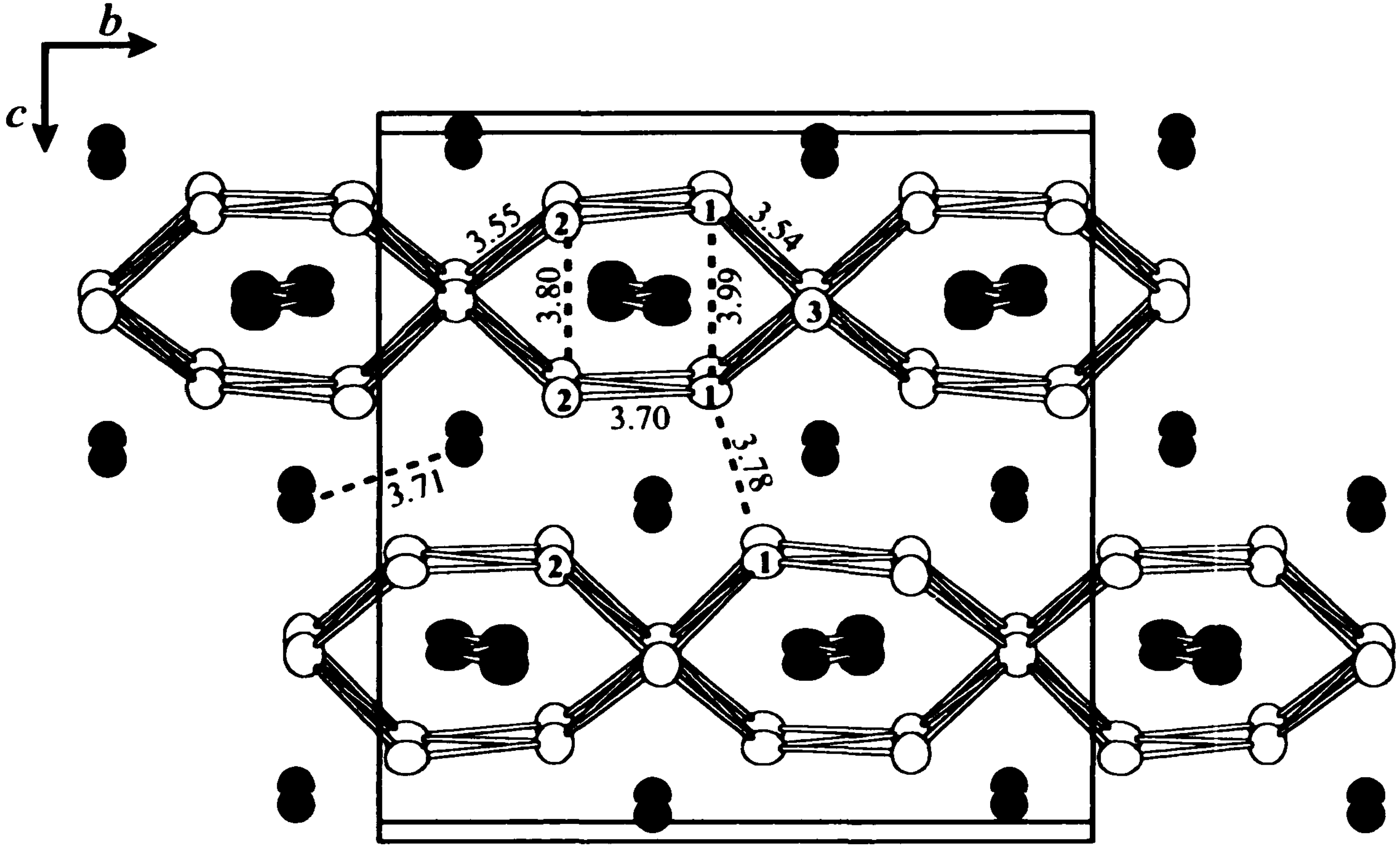

Figure 2. Unit cell of $Y_5M_2Te_2$ (M = Fe, Co, Ni) viewed down the [100] axis, with 99.9% thermal ellipsoids. Y - Y distances labeled in Å for M = Fe, while the shortest interlayer and Te—Te distances highlighted with dashed lines. Dark atoms are Te; lightly shaded, M; unfilled, Y.

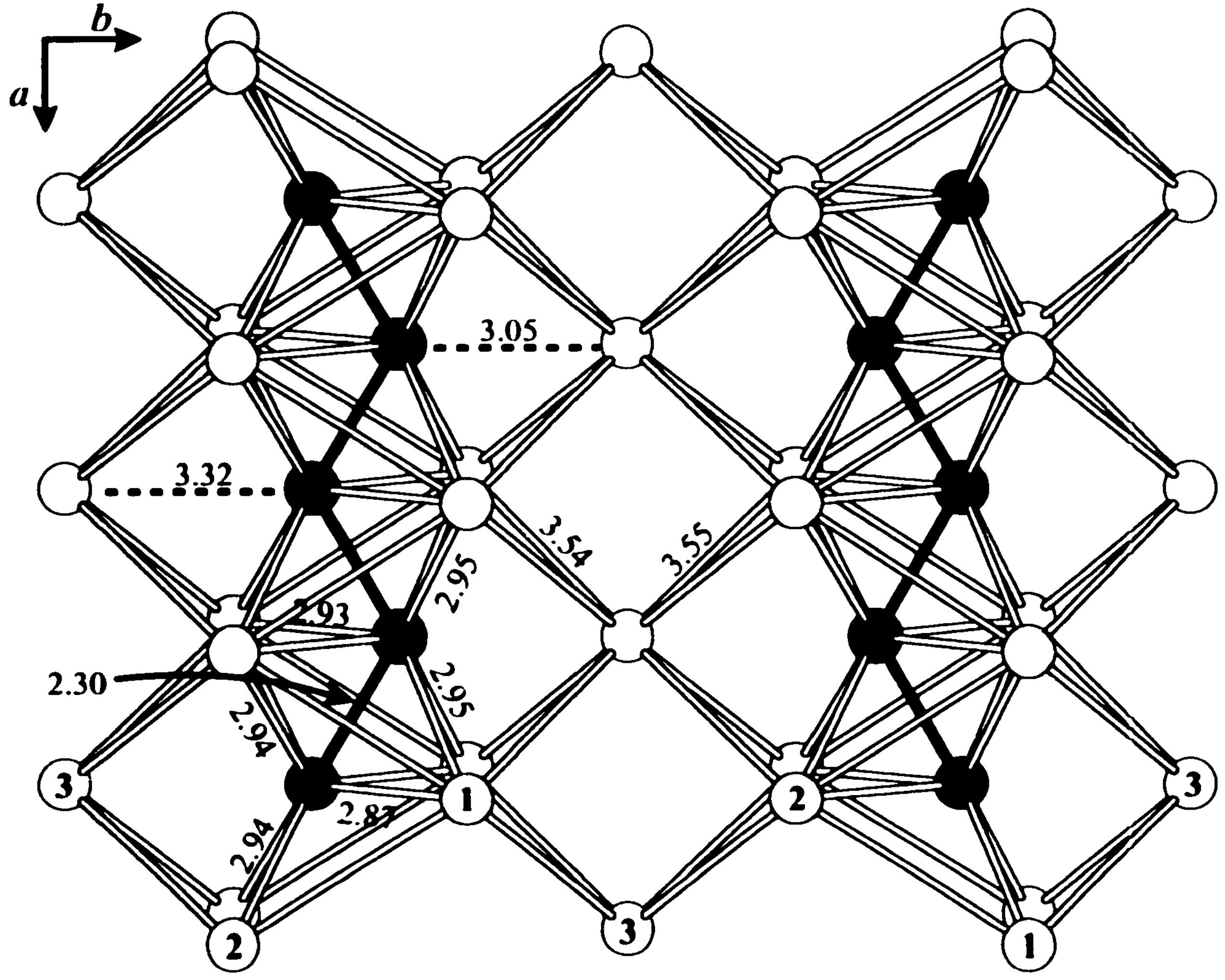

Figure 3. Near-[001] view of a single infinite Y_5M_2 sheet normal to that in Figure 2. The Y-M, M-M and Y-Y distances are labeled in Å for M = Fe. Dark atoms are M; unfilled, Y. Mirror planes lie in horizontally through M1 and M2 and in the plane.

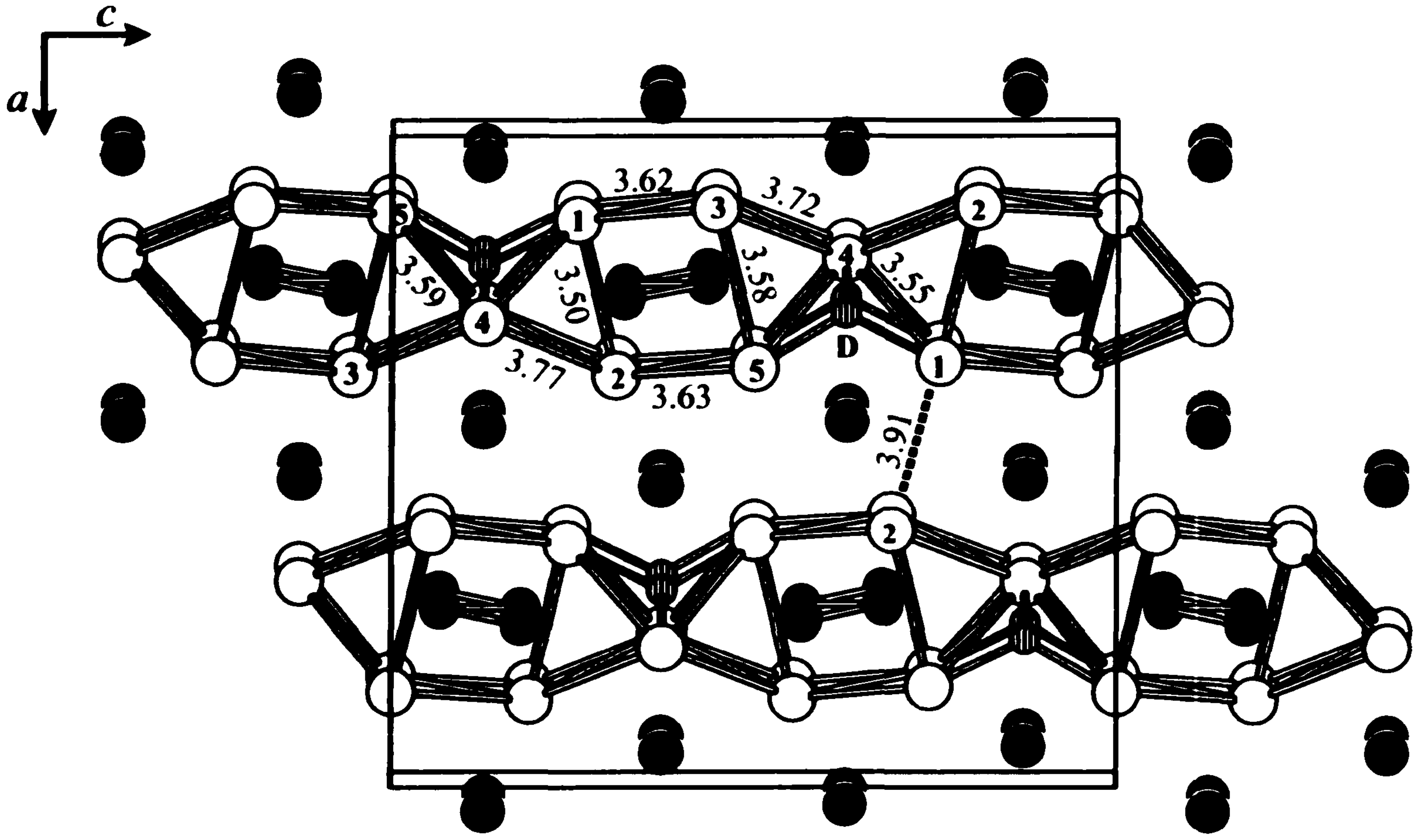

Figure 4. Near-[010] section of the $Y_5Ni_2Te_2D_{0.41(1)}$ unit cell, with Y - Y distances labeled in Å. Dark atoms are Te; lightly shaded, Ni; unfilled, Y; hatched, D.

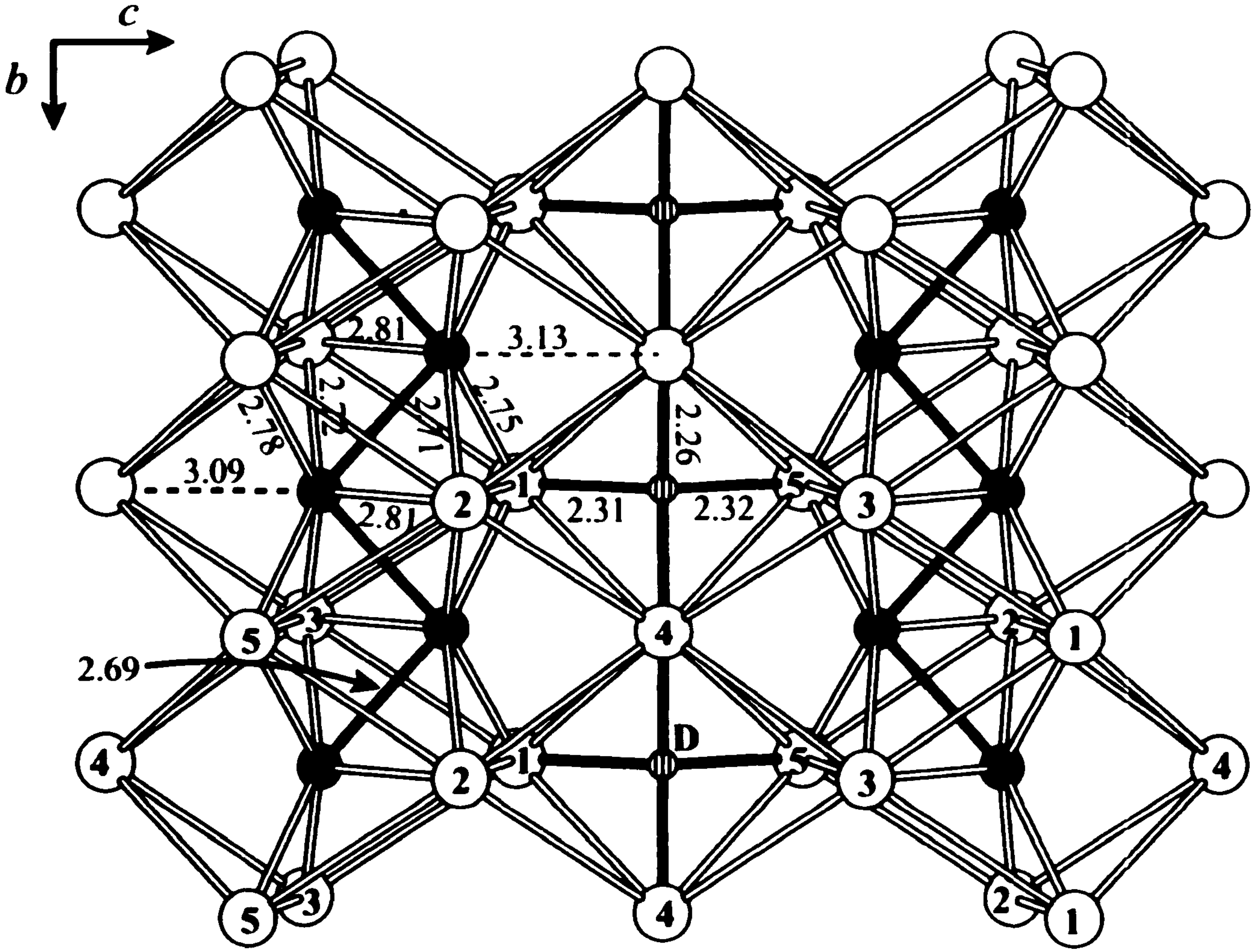

Figure 5. Near-[100] view of a single infinite Y_5Ni_2D sheet, with Y–Ni, Ni–Ni, and Y–D distances labeled in Å. Shaded atoms are Ni; unfilled, Y; hatched, D. Bonds in the tetrahedral yttrium environment about deuterium are shaded for clarity. Horizontal mirror planes contain all atoms.

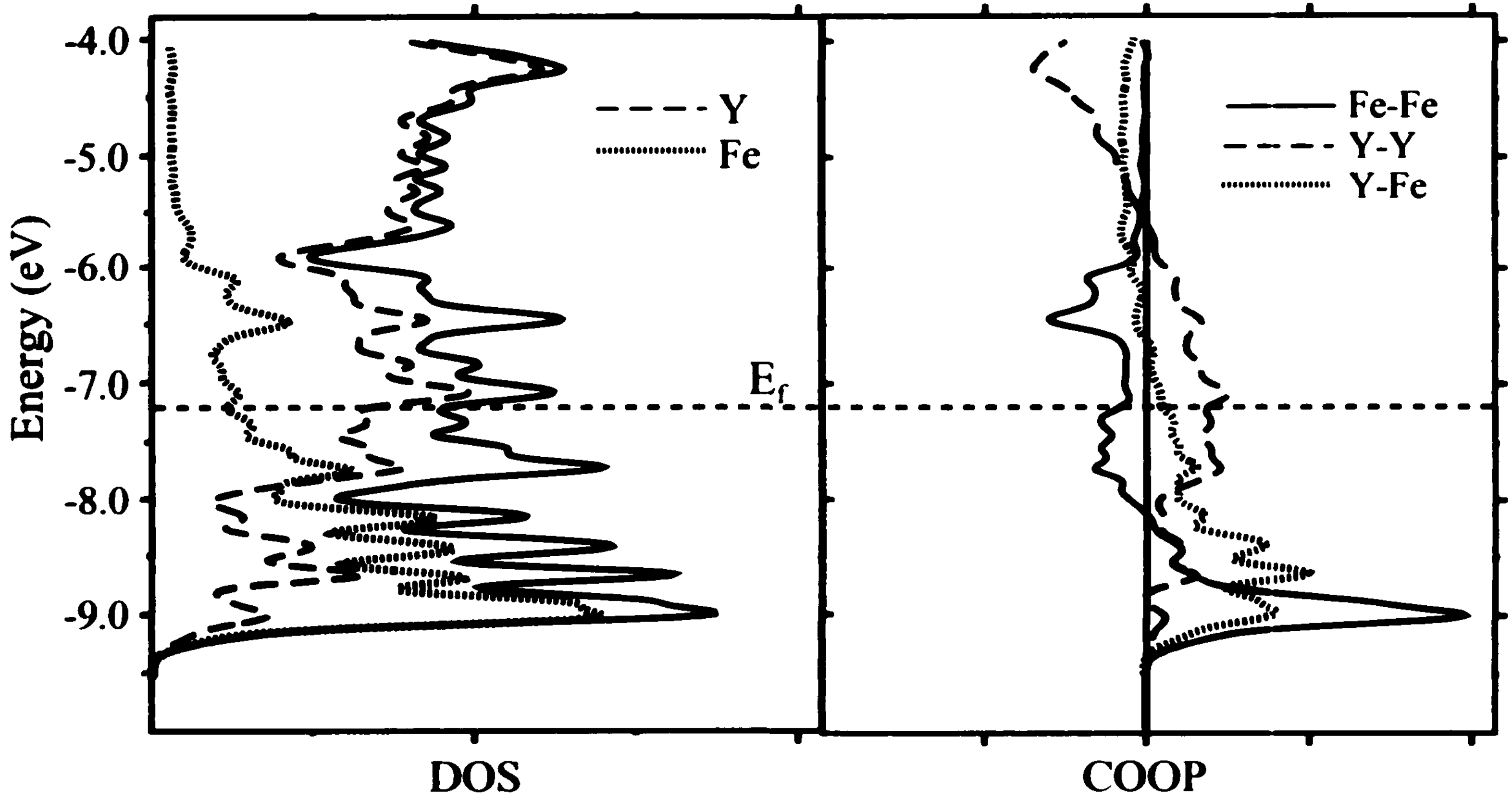

Figure 6. Total densities-of-states (DOS, left) and metal–metal crystal orbital overlap populations (COOP, right) curves for $Y_5Fe_2Te_2$. The separate yttrium and iron contributions are projected out. The COOP curves are for indicated pairwise interactions, all drawn to the same scale.

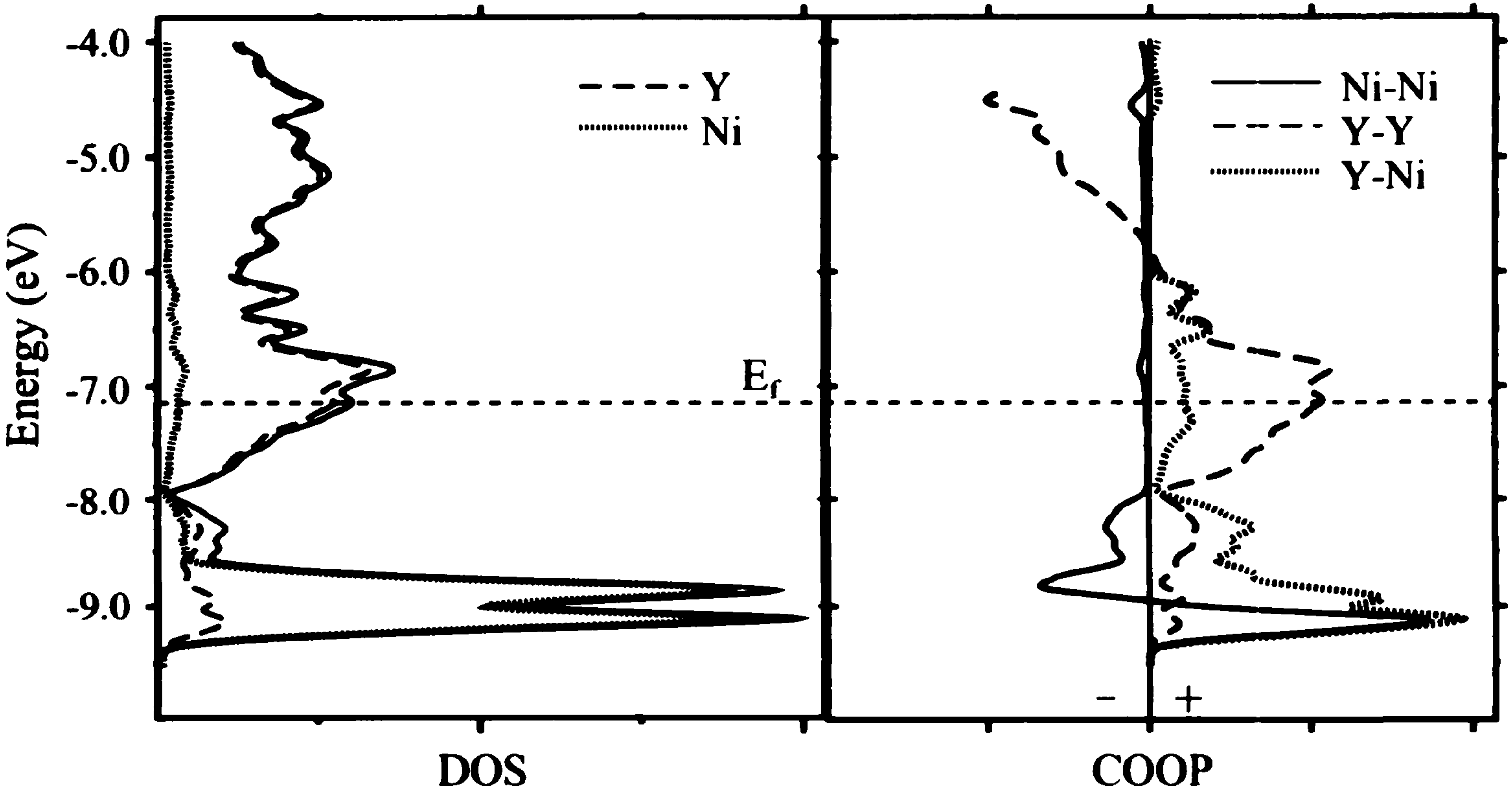

Figure 7. Total densities-of-states (DOS, left) and metal–metal crystal orbital overlap populations (COOP, right) curves for $Y_5Ni_2Te_2D_{0.5}$. The separate yttrium and nickel contributions are projected out. The COOP curves are for indicated pairwise interactions, all drawn to the same scale.

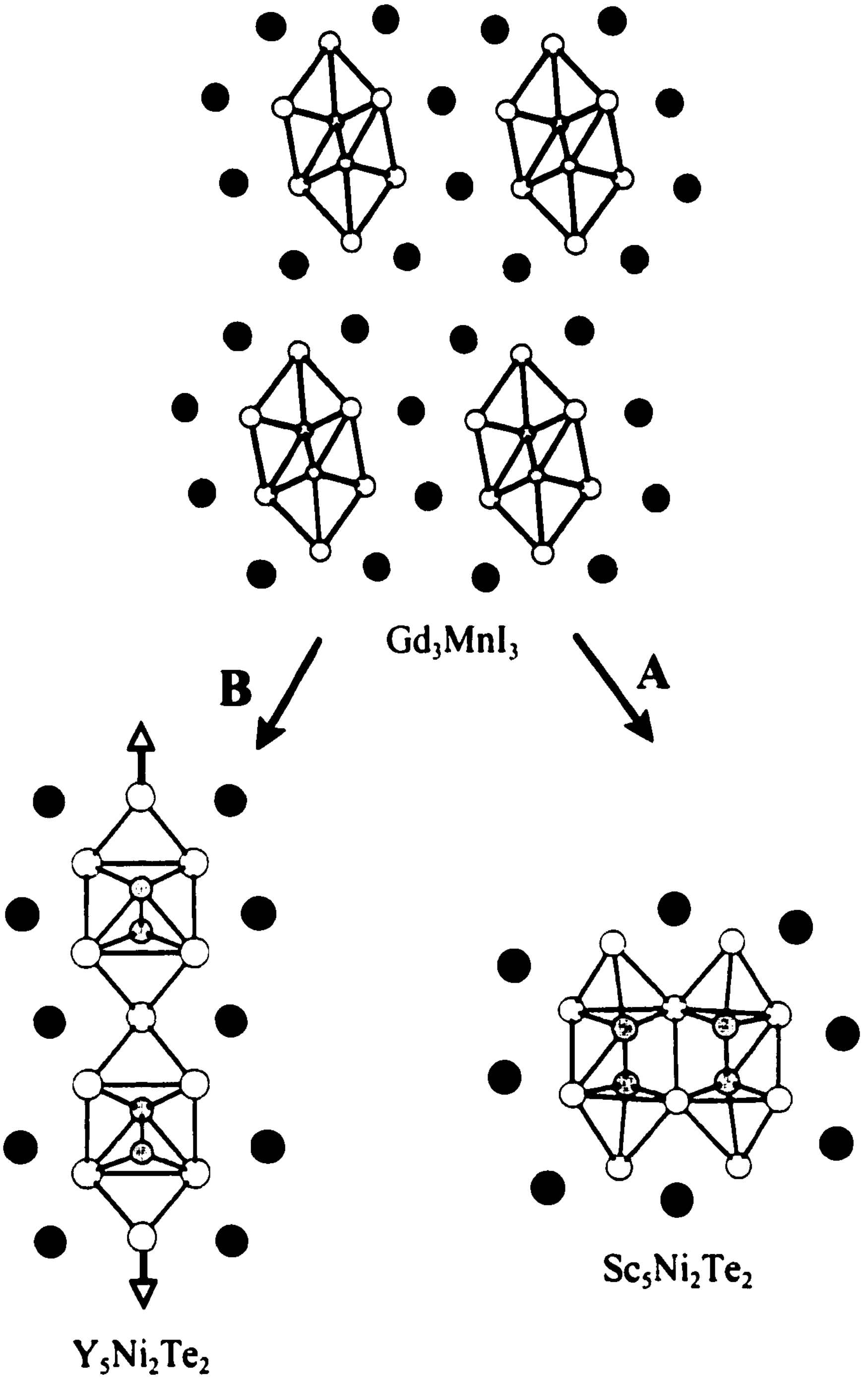

Figure 8. Two methods of condensation of the single 1D chains in Gd_3MnI_3 to (A) pairs of the 1D chains in $Sc_5Ni_2Te_2$ and (B) infinite chains in the 2D layers in $Y_5Ni_2Te_2$. Dark atoms are Te or I; lightly shaded, Ni or Mn; unfilled, Sc, Y, or Gd, according to respective structures.

CHAPTER 7. Sc_6MTe_2 (M = Mn, Fe, Co, Ni): MEMBERS OF THE FLEXIBLE Zr_6CoAl_2 -TYPE FAMILY OF COMPOUNDS

A paper submitted to Inorganic Chemistry

Paul A. Maggard and John D. Corbett

Department of Chemistry, Iowa State University, Ames, IA 50011

Abstract

Sc_6MTe_2 (M = Mn, Fe, Co, Ni) compounds have been prepared by high-temperature solid-state techniques, and their structures determined to be hexagonal $P\bar{6}2m$ (no. 189) with $Z = 1$, a = 7.662(1), 7.6795(2), 7.6977(4), 7.7235(4)A, c = 3.9041(9), 3.8368(2), 3.7855(3), 3.7656(3)A and V = 198.51(8), 195.96(2), 194.26(3), 194.53(2)A^3, for M = Mn, Fe, Co and Ni respectively. Single crystal structures were determined for M = Fe and Ni, while M = Mn and Co were assigned on the basis of powder diffraction data. The Sc_6MTe_2 compounds belong to a large family with the Zr_6CoAl_2 type structure, an ordered variant of the Fe_2P structure. The structure contains face-shared tricapped trigonal prisms of scandium centered by either the late transition metal or tellurium atoms. The Sc_6MTe_2 compounds are the electron-poorest examples of this structure type. Extended Hückel band calculations for M = Fe and Ni show both compounds are predicted to be metallic and largely 1D in metal-metal bonding.

Introduction

The study of metal - metal bonding in solid-state compounds has been facilitated by the discovery of many new phases of the group 3 transition-metal chalcogenides. These include Sc_2Te,[1] $(Sc,Y)_8Te_3$,[2] and Sc_9Te_2.[3] However, the chemistry and metal - metal bonding can be enriched and enlarged by the addition of a third metal which stabilizes new metal frameworks, i.e. a late transition metal. Inclusion of a late transition metal in the $Sc_5Ni_2Te_2$,[4] and $Y_5M_2Te_2$ (M = Fe, Co, Ni)[5] have provided insight into the factors that influence metal-bonded structures. Interestingly, $Sc_5Ni_2Te_2$ contains double 1D metal chains and $Y_5Ni_2Te_2$, 2D metal layers, and both may be shown to arise from the condensation of the Gd_3I_3Mn type phases[6] that contain single 1D metal chains.

A growing list of compounds are known to crystallize in the ordered variant of the Fe_2P structure type known as the Zr_6CoAl_2 type.[7,8] In this instance, the unit cell of Fe_2P is tripled, with the early transition metal on the iron positions and the late transition metal and main-group element ordered between the two independent phosphorus sites. Recent examples of this type include Zr_6MTe_2 (M = Mn, Fe, Co, Ni, Ru, Pt),[9] Hf_6MSb_2 (M = Fe, Co, Ni),[10] Zr_6CoAs_2,[11] Dy_6MTe_2 (M = Fe, Co, Ni),[12] and R_6CoTe_2 ® = Y, La).[12] Crystallization of these phases in the Zr_6CoAl_2 structure type has been attributed to the size mismatch of the late transition metals and main-group elements.[9] A similar analogy was found between the $Sc_5Ni_2Te_2$[4] and $Hf_5Co_{1-x}P_{3-x}$[13] compounds, with the former is an ordered variant of the latter. Concomitant with this ordering is a decrease in the metal-framework dimensionality from 3D to 1D. Described in this paper is a series of new Sc_6MTe_2 (M = Mn, Fe, Co, Ni) compounds which represent the electron-poorest Zr_6CoAl_2 types that have been reported.

Experimental Section

Syntheses. The synthetic methods for the Sc_6MTe_2 phases were parallel to those that have been described elsewhere.[4] The elements were used as received: Sc turnings, Aldrich 99.7%; Te powder, Aldrich 99.99%; Ni powder, Alfa 99.95%. Preparation of Sc_2Te_3 has been described previously.[4] An appropriate mixture of Sc_2Te_3, Sc, and Mn, Fe, Co or Ni was pelletized, wrapped in molybdenum foil, and loaded into tantalum tubing inside a He-filled glovebox. (At high temperatures, the late transition metals in contact with the tantalum will dissolve, but this occurs to a much smaller extent when the container wall is protected by molybdenum foil.) The tantalum tubing was then arc-welded shut under argon and further sealed inside evacuated fused-silica tubing. Heating between 950 °C and 1025 °C for 72 to 168 hours and slow cooling (5 °C/hr) provided ≥ 90% yields of the four compounds according to Guinier powder diffraction data. The impurities were ScTe, unreacted scandium metal (visual identification), and the appropriate late transition metal.

Powder X-ray Diffraction. The powder diffraction patterns of Sc_6MTe_2 were obtained with the aid of an Enraf-Nonius Guinier powder camera and monochromatic Cu $K\alpha_1$ radiation. The powdered samples were mixed with standard silicon (NIST) and placed between two strips of cellophane tape on a frame that mounted on the sample rotation motor. Lattice parameters (Table 1) were obtained with the aid of least squares refinement of the indexed lines with the 2θ values calibrated by a nonlinear fit to the positions of the standard silicon lines.

Single Crystal Diffraction. Several irregularly shaped, silvery crystals were mounted inside 0.3-mm i.d. glass capillaries and then sealed off and mounted on metal pins. The crystal qualities were checked by means of Laue photographs. Diffraction data sets for the best crystals from reactions loaded as Sc_6FeTe_2 and Sc_6NiTe_2 were measured on a Rigaku AFC6R diffractometer (with monochromated Mo $K\alpha_1$ radiation) at room temperature. Twenty-five centered reflections gathered from a random search were used to determine provisional lattice constants and the probable crystal systems. The data were corrected for Lorentz and polarization effects, and further corrected for absorption with the aid of 3 and 2 ψ-scans, respectively. Out of 1258 (Fe) and 902 (Ni) measured reflections to $2\theta_{max} = 60°$ and 54°, 1225 and 863 had $I > 3\sigma_I$, and 253 and 239 of these were unique, respectively. Extinction conditions and statistical evidence for noncentricity indicated four possible space groups. Attempts to solve the structures by direct methods (SHELXS[14]) and to refine these with the package TEXSAN[15] were successful only in space group $P\bar{6}2m$ (no. 189). After isotropic refinement, the data averaged with $R_{ave} = 6.4$ and 5.5% for $I > 0$. The final anisotropic refinements were $R(F)/R_w = 3.8/3.3$ and 3.1/4.0% for the compositions Sc_6FeTe_2 and Sc_6NiTe_2. Some refinement data for these studies are listed in Table 2, and the atomic positions and isotropic-equivalent temperature factors are given in Table 3. Additional data collection and refinement parameters, the anisotropic displacement parameters, and the complete distance tabulations are in the Supporting Information. These as well as the F_o/F_c listing are also available from J.D.C.

Band Calculations. Extended Hückel calculations were carried out within the tight-binding approximation[16] for the full structures of Sc_6FeTe_2 and Sc_6NiTe_2 at 140 k-points spread over the irreducible wedge. H_{ii} parameters employed were the values iterated to charge consistency for Sc from Sc_2Te,[1] and for Fe and Ni from Sc_6FeTe_2 and Sc_6NiTe_2 (this work) (eV): Sc 4s, -6.75; 4p, -3.38; 3d, -6.12; Fe 4s, -5.50; 4p, -2.45; 3d, -6.86; Ni 4s, -5.58; 4p, -2.41; 3d, -7.82; Te 6s, -21.20; 6p, -12.00.

Results and Discussion

Structural Description. The structure along (001) is illustrated in Figure 1 for Sc_6NiTe_2, with selected scandium distances marked. The late transition metal (M) centers the tricapped trigonal prisms (or tetrakaidecahedra) of scandium that stack and share faces along the *c* axis to form a linear chain. The tricapped trigonal prismatic chains are interconnected via Sc1 - Sc2 bonds at 3.460(2)A and 3.411(3)A for M = Fe and Ni, respectively. The shorter scandium distances are around the triangular faces of the trigonal prisms, Sc1 - Sc1, at 3.151(3) Å and 3.201(5) Å, and also on the capped rectangular faces, Sc1 - Sc2, at 3.234(1) Å and 3.248(2) Å for M = Fe and Ni as before. The next shortest scandium distances in the structure are along the *c* axis for both Sc1 - Sc1 and Sc2 - Sc2, 3.8368(2) Å (Fe) and 3.7656(3) Å (Ni). Generally, the *c* axis and interchain distances contract between Fe and Ni, while the triangular faces and capping distances around the scandium trigonal prisms (Sc1–Sc2) expand.

An isolated Sc$_6$M trigonal prismatic chain is shown in Figure 2 with the repeat and Sc - M distances for nickel. The shaded bonds emphasize the scandium trigonal-prismatic environment around the late transition metal, with Sc1 - M lengths of 2.644(1)A and 2.638(2)A, for M = Fe and Ni respectively, while the capping atoms, Sc2 - M, are at 2.982(2)A and 3.032(3)A.

The tricapped trigonal prisms about the tellurium atoms, highlighted with dashed lines in Figure 1, are arranged and stacked in an analogous fashion as around the late transition metal, but with some expansion. Six of the Te-centered chains surround each Sc$_{6/2}$M chain with internal Sc2–Te bonds of 3.0547(6) Å and 3.0340(8) Å, while the capping distances to Sc1 are 3.000(1) Å and 3.004(2) Å for M = Fe and Ni, respectively. The bonds defining the trigonal prisms are expanded compared with the face-capping distances and also expanded compared with the late transition metal environment, as would be expected from size differences.

Calculations. The Zr$_6$CoAl$_2$-type compounds containing scandium are the electron-poorest known in this group, while Zr$_6$MTe$_2$ (M = Mn, Fe, Co, Ni, Ru, Pt),[9] Hf$_6$MSb$_2$ (M = Fe, Co, Ni),[10] and Zr$_6$CoAs$_2$[11] all contain electron-richer transition metals, and with metal-metal bonding arrays that have been reported to be fully three-dimensional. Similar comparisons of other scandium systems such as (Sc,Y)$_8$Te$_3$[2] and Sc$_5$Ni$_2$Te$_2$[4] with electron-richer analogues also show that the lowered electron concentrations in the former lead to both overall weakening of metal - metal interactions and lowered dimensionality. Electronic calculations seemed necessary to understand this aspect in the Sc$_6$MTe$_2$ phases better.

Figure 3 shows the total DOS for Sc_6FeTe_2 and Sc_6NiTe_2 with the two transition-metal contributions projected out. The Fermi level falls within a large conduction band composed primarily of scandium d states intermixed with some late transition metal d character. Iron d orbitals are higher in energy (about -7.2 eV) and mix more with the scandium d states than do those for nickel (about -8.0 eV). This results in the larger contribution of the iron d states at the Fermi level.

The COOP (crystal orbital overlap population) curves for the total Sc - M and Sc - Sc bonding interactions for both systems are plotted in Figure 4. (The M - M interactions are very small.) In both cases, the Sc - M interactions appear to be optimized, with the Fermi level lying close to the crossover between bonding and antibonding states. The host-interstitial bonding is likewise optimized for the systems Zr_6MTe_2 (M = Mn, Fe, Co, Ni, Ru, Pt)[9] and Zr_6CoAs_2.[11] On the other hand, the Sc - Sc COOP data show that many bonding states remain above the Fermi level.

Comparisons of bond distances with overlap populations allow one to ascertain where matrix effects may be important in determining distances as opposed to real bonding effects. For this purpose, pairwise overlap populations (OP) and distances in Sc_6FeTe_2 and Sc_6NiTe_2 are given for Sc - Sc, Sc - M, and M - M in Table 4. The first large Sc - Sc OP, and presumably a strong bond, occurs for Sc1–Sc1 on the triangular (end) faces of the trigonal prisms, 0.228 and 0.219 for M = Fe and Ni. The face caps on the trigonal prism, Sc1 - Sc2, likewise have sizable 0.141 and 0.146 values. Two of the three next largest overlap populations (≤0.056) occur for Sc1 - Sc1 and Sc2 - Sc2 down the short *c* axis for interactions that appear to be weaker. The interchain overlap populations for Sc1 - Sc2 (0.036 to 0.041), which reflect the dimensionality of the metal-metal bonding, are ≤ 20% of the larger internal populations. Whether these are very significant is doubtful; as usual, bonds located on the periphery of the metal cluster chains have substantially lower bond populations.[2] The metal-metal bonding is, at the least, located preferentially within the 1D chains of tricapped trigonal prisms, while bond populations fall off regularly with an increased number of tellurium neighbors.

The Sc - M overlap populations show similar trends for M = Fe and Ni. The Sc1 - M overlap populations for each contact within the trigonal prisms (0.267, 0.189) are about twice as large as those for the capping Sc2 - M populations (0.140, 0.087), in parallel with the distances and always less for nickel. Contrastingly, M–M interactions between the late transition metal neighbors along the chain are very small and slightly antibonding.

The overall trend from Fe to Ni is that four out of the five Sc - Sc overlap populations increase, while those for both Sc - M bonds decrease. This represents a reapportioning of the metal electrons from the Sc - M framework to the Sc - Sc bonds as the late transition metal d orbitals fall in energy and take on a more core-like character.

Conclusions. New phases of the composition Sc_6MTe_2 (M = Mn, Fe, Co, Ni) have been synthesized in the Zr_6CoAl_2 type structure. A growing number of examples for this structural type demonstrates its structural and electronic flexibility. Size differences between the later transition metal and the main-group element result in the ordered occupancy of the two phosphorus sites in Fe_2P. The metal - metal bonding character is more 1D in character than for electron-richer analogues of zirconium, etc., while the overlap population trends reflect how the metal-based electrons redistribute from Sc - M to Sc - Sc bonds between Fe and Ni, and probably over the whole series Mn–Ni.

Acknowledgements

The authors would like to thank R. Jacobson for provision of diffractometer time. This research was supported by the National Science Foundation, Solid State Chemistry, via grants DMR-9510278 and DMR-9809850, and was carried out in the facilities of Ames Laboratory, U.S. Department of Energy.

Supporting Information Available

Tables of additional crystallographic information, anisotropic thermal parameters, and a complete listing of nearest neighbor distances in Sc_6FeTe_2 and Sc_6NiTe_2. The material is available free-of-charge via the Internet at http://pubs.acs.org.

References

(1) Maggard, P. A.; Corbett, J. D. *Angew. Chem., Int. Ed. Engl.* **1997**, *18*, 336.

(2) Maggard, P. A.; Corbett, J. D. *Inorg. Chem.* **1998**, *37*, 814.

(3) Maggard, P. A.; Corbett, J. D. *J. Am. Chem. Soc.* **2000**, *122*, 838.

(4) Maggard, P. A.; Corbett, J. D. *Inorg. Chem.* **1999**, *38*, 1945.

(5) Maggard, P. A.; Corbett, J. D. manuscript in preparation.

(6) Ebihara, M.; Martin, J. D.; Corbett, J. D. *Inorg. Chem.* **1994**, *33*, 2078.

(7) Kwon, Y.-U.; Sevov, S. C.; Corbett, J. D. *Chem. Mater.* **1990**, *2*, 550.

(8) Villars, P.; Calvert, L. D. *Pearson's Handbook of Crystallographic Data for Intermetallic Phases*, 3rd ed.; American Society for Metals: Materials Park, OH, 1985; Vol. 1.

(9) Wang, C.; Hughbanks, T. *Inorg. Chem.* **1996**, *35*, 6987.

(10) Kleinke, H. *J. Alloys Compd.* **1998**, *270*, 136.

(11) Kleinke, H. *J. Alloys Compd.* **1997**, *252*, L29.

(12) Bestaoui, N.; Corbett, J. D. unpublished research, 1998.

(13) (a) Kleinke, H.; Franzen, H. F. *J. Alloys Compd.* **1996**, *238*, 68. (b) Kleinke, H.; Franzen, H. F. *J. Alloys Compd.* **1997**, *255*, 110.

(14) Sheldrick, M. SHELXS-86, Universität Göttingen, Germany, 1986.

(15) TEXSAN, Version 6.0, Molecular Structure Corp., The Woodlands, Texas, 1990.

(16) (a) Hoffman, R. *J. Chem. Phys.* **1963**, *39*, 1397. (b) Whangbo, M.; Hoffman, R. *J. Am. Chem. Soc.* **1978**, *100*, 6093.

Table 1. Lattice Constants (Å) and Cell Volumes (Å^3) for Sc_6MTe_2 (M = Mn, Fe, Co, Ni).

Compound	*a*	*c*	*V*
Sc_6MnTe_2	7.662(1)	3.9041(9)	198.51(8)
Sc_6FeTe_2	7.6795(2)	3.8368(2)	195.96(2)
Sc_6CoTe_2	7.6977(4)	3.7855(3)	194.26(3)
Sc_6NiTe_2	7.7235(4)	3.7656(3)	194.53(2)

[a] Guinier data, Cu Kα_1, 23 °C, with 11, 15, 18, 17 indexed lines for Mn, Fe, Co, and Ni, respectively.

Table 2. Some Data Collection and Refinement Parameters for Sc_6MTe_2, M = Fe (1st value) and Ni (2nd value).[a]

formula weight	597.42, 583.67
space group, *Z*	$P\bar{6}2m$ (no. 189), 1
d_{calc}, g/cm^3	4.921, 4.982
μ, cm^{-1} (Mo Kα_1)	139.29, 145.99
R/R_w[b] (%)	3.8/3.3, 3.1/4.0

[a] Lattice parameters in Table 1.

[b] $R = \sum||F_o|-|F_c||/\sum|F_o|$; $R_w = [\sum w(|F_o|-|F_c|)^2/\sum w(F_o)^2]^{1/2}$, $w = 1/\sigma^2$.

Table 3. Positional and Isotropic-Equivalent Thermal Parameters for Sc_6MTe_2, M = Fe and Ni, respectively.

Atom	x	y	z	$B_{eq}(Å^2)^a$
Sc1	0.2369(2)	0	½	0.77(6)
Sc2	0.6117(3)	0	0	0.80(6)
M	0	0	0	1.24(4)
Te	1/3	2/3	½	0.62(2)

[a] $B_{eq} = \Sigma_i\Sigma_j U_{ij}a_i^*a_j^*{}_{ij}$.

Table 4. Selected Metal-Metal Distances (A) and Overlap Populations in Sc_6MTe_2 (M = Fe, Ni).

		distance			overlap population per bond	
atom 1	atom 2	Fe	Ni		Fe	Ni
Sc1	Sc1[a]	3.151(3)	3.201(5)	×2	0.228	0.219
Sc1	Sc2	3.234(1)	3.248(2)	×4	0.141	0.146
Sc1	Sc1[b]	3.8368(2)	3.7656(3)	×2	0.048	0.056
Sc1	Sc2[c]	3.460(2)	3.411(3)	×2	0.036	0.041
Sc2	Sc2[b]	3.8368(2)	3.7656(3)	×2	0.002	0.014
Sc1	M	2.644(1)	2.638(2)	×2	0.267	0.189
Sc2	M	2.982(2)	3.032(3)		0.140	0.087
M[b]	M	3.8368(2)	3.7656(3)	×2	-0.008	-0.007

[a] Distance within the triangular faces of the trigonal prism.

[b] Distance along *c* axis.

[c] Interchain separation.

Supporting Information

Sc_6MTe_2 (M = Mn, Fe, Co, Ni): Members of the Flexible Zr_6CoAl_2-Type Family of Compounds

Paul A. Maggard and John D. Corbett

Table S1. Single Crystal X-ray Data Collection and Refinement Parameters for Sc_6MTe_2, M = Fe (1st value) and M = Ni (2nd value).

Formula weight	580.81, 583.67
Space group, Z	$P\bar{6}2m$ (no. 189), 1
Lattice parameters and cell volume	
a (Å)	7.6795(2), 7.7235(4)
c (Å)	3.8368(2), 3.7656(3)
V, (Å^3)	195.96(2), 194.53(2)
d_{calc} g/cm^3	4.921, 4.982
Radiation; $2\theta_{max}$	Mo Kα; 60°, 54°
Octants measured	+h, ±k, ±l (×2)
Temperature, °C	23
Absorption method	3ψ-scans, 2ψ-scans
μ, Mo K_α (cm^{-1})	139.29, 145.99
Reflections: measured	1258, 902
observed and unique ($I \geq 3\sigma$)	253, 239
Number of variables	14 (both)
R_{ave}, % ($I > 3\sigma_I$)	6.4, 5.5
Residuals R, R_ω,[b] (based on F), %	3.8, 3.3; 3.1, 4.0
Goodness of fit	2.22, 1.85
Secondary ext. coeff.	3.0(9) × 10^{-5}, 3.5(2) × 10^{-4}

[a] Guinier data, Cu $K\alpha_1$, 23 °C, with 11, 15, 18, 17 indexed lines for Mn, Fe, Co, and Ni, respectively.

[b] $R = \Sigma||F_o|-|F_c||/\Sigma|F_o|$; $R_\omega = [\Sigma w(|F_o|-|F_c|)^2/\Sigma w(F_o)^2]^{1/2}$, $w = 1/\sigma^2$.

Table S2. U_{ij} (Å^2) values for Sc_6MTe_2, for Fe and Ni, respectively.

Atom	U11	U22	U33
Sc1	0.0078(5) 0.009(1)	0.0077(7) 0.009(1)	0.0137(7) 0.013(1)
Sc2	0.0103(6) 0.009(1)	0.0095(7) 0.009(1)	0.0103(6) 0.008(1)
Fe, Ni	0.0193(7) 0.020(1)	U11	0.0087(7) 0.008(1)
Te	0.0075(3) 0.0081(5)	U11	0.0086(3) 0.0067(6)

Table S3. Interatomic Distances (< 4.0Å) for Sc$_6$MTe$_2$.

Atom 1	Atom 2	#	Distance(Å)	Atom 1	Atom 2	#	Distance
			Sc$_6$FeTe$_2$				
Te	Te	2x	3.8368(2)	Sc2	Te	4x	3.0547(6)
	Sc1	3x	3.000(1)		Sc1	4x	3.234(1)
	Sc2	6x	3.0547(6)		Sc1	2x	3.460(2)
					Sc2	2x	3.8368(2)
Sc1	Te	2x	3.000(1)		Fe		2.982(2)
	Sc1	2x	3.151(3)				
	Sc1	2x	3.8368(2)	Fe	Sc1	6x	2.644(1)
	Sc2	4x	3.234(1)		Sc2	3x	2.982(2)
	Sc2	2x	3.460(2)		Fe	2x	3.8368(2)
	Fe	2x	2.644(1)				
			Sc$_6$NiTe$_2$				
Te	Te	2x	3.7656(3)	Sc2	Te	4x	3.0340(8)
	Sc1	3x	3.004(2)		Sc1	4x	3.248(2)
	Sc2	6x	3.0340(8)		Sc1	2x	3.411(3)
					Sc2	2x	3.7656(3)
Sc1	Te	2x	3.004(2)		Ni		3.032(3)
	Sc1	2x	3.201(5)				
	Sc1	2x	3.7656(3)	Ni	Sc1	6x	2.638(2)
	Sc2	4x	3.248(2)		Sc2	3x	3.032(2)
	Sc2	2x	3.411(3)		Ni	2x	3.7656(3)
	Ni	2x	2.638(2)				

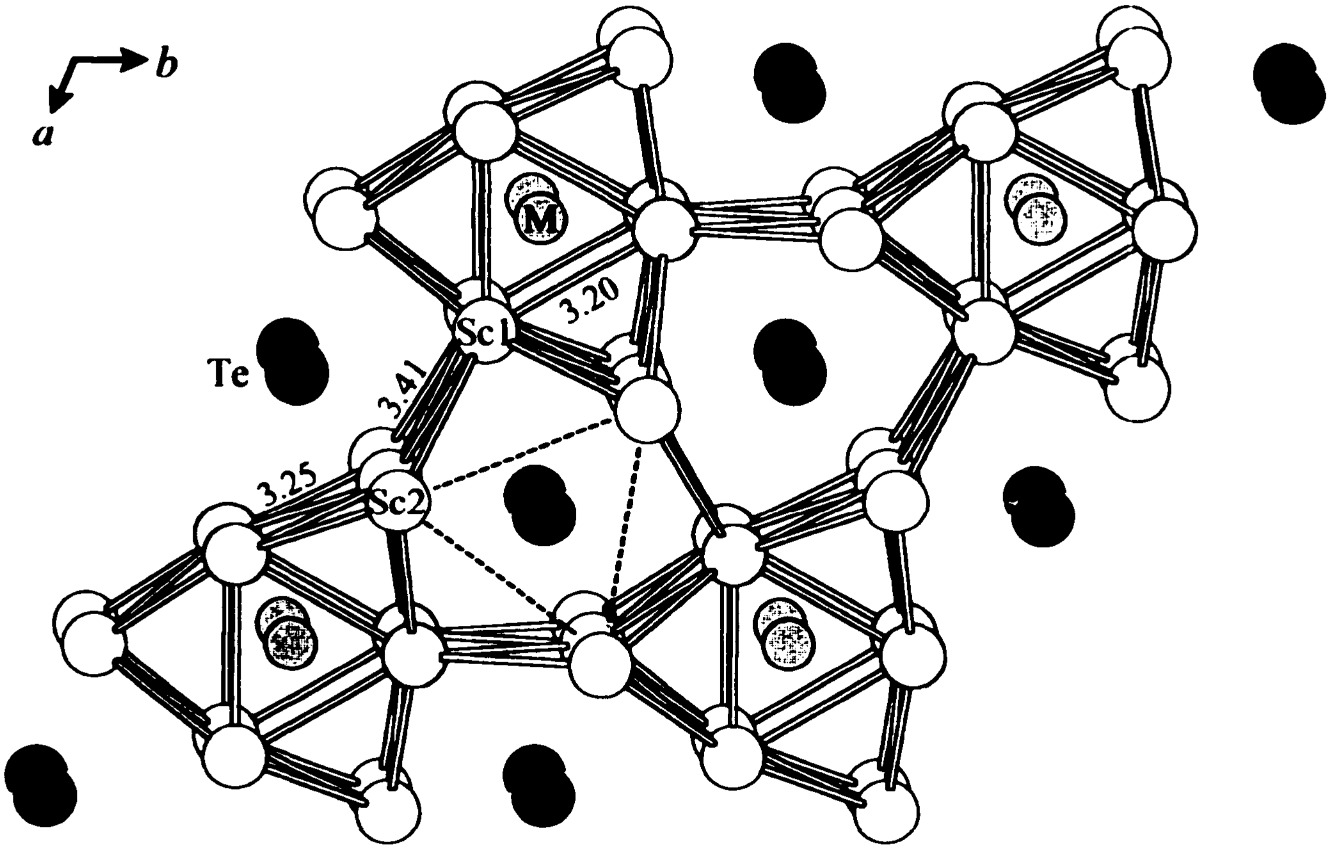

Figure 1. Near-[001] view of the Sc_6MTe_2 (M = Mn, Fe, Co, or Ni, gray atoms) structure. Sc–Sc distances are marked in Å for M = Ni, and dashed lines highlight trigonal prism around tellurium, black atoms. The symmetries at M and Te are -62m and -6.

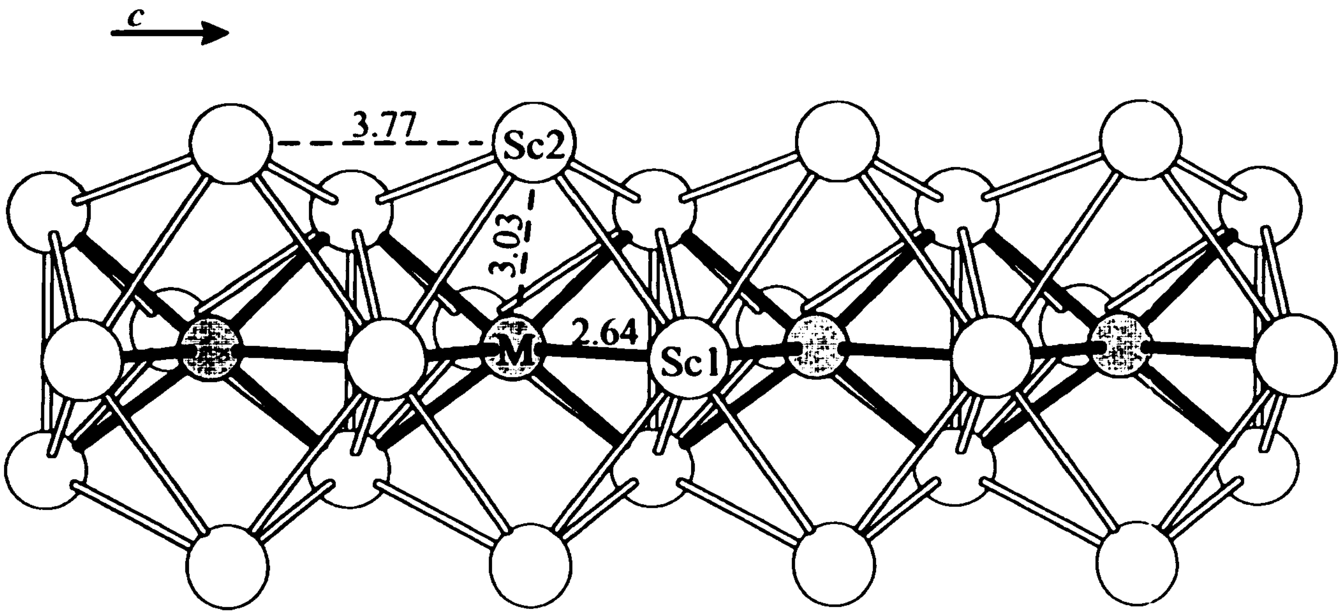

Figure 2. A side view of the isolated Sc_6M metal chain (Figure 1). Sc–M and repeat distances marked in Å for M = Ni. The darkened Sc–M bonds denote the Sc1 trigonal prismatic environment around M, which is tricapped by Sc2.

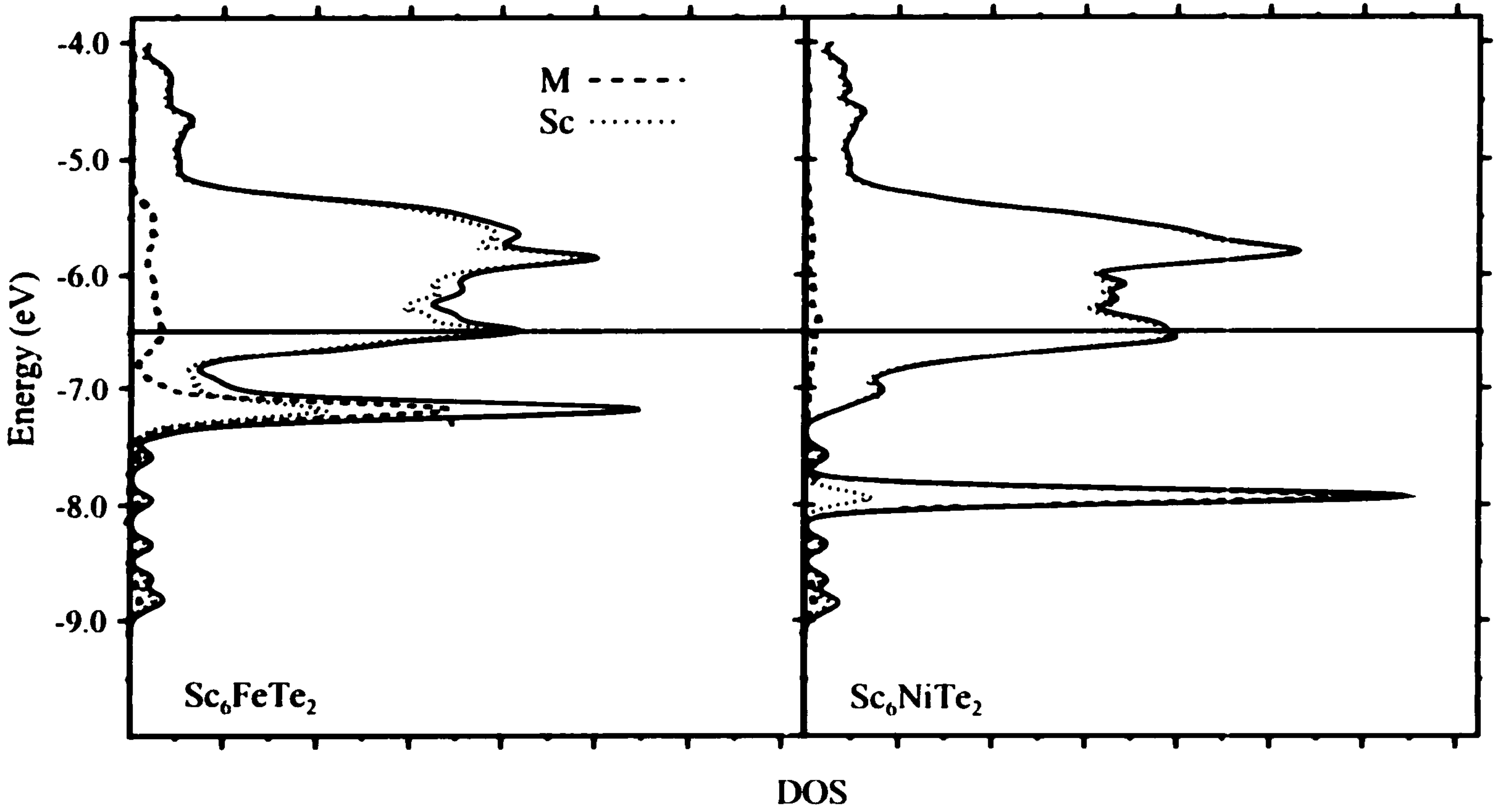

Figure 3. The densities-of-states from the EHTB band calculations for Sc_6MTe_2 (M = Fe, Ni). The separate M (larger dashed lines) and Sc contributions are projected out.

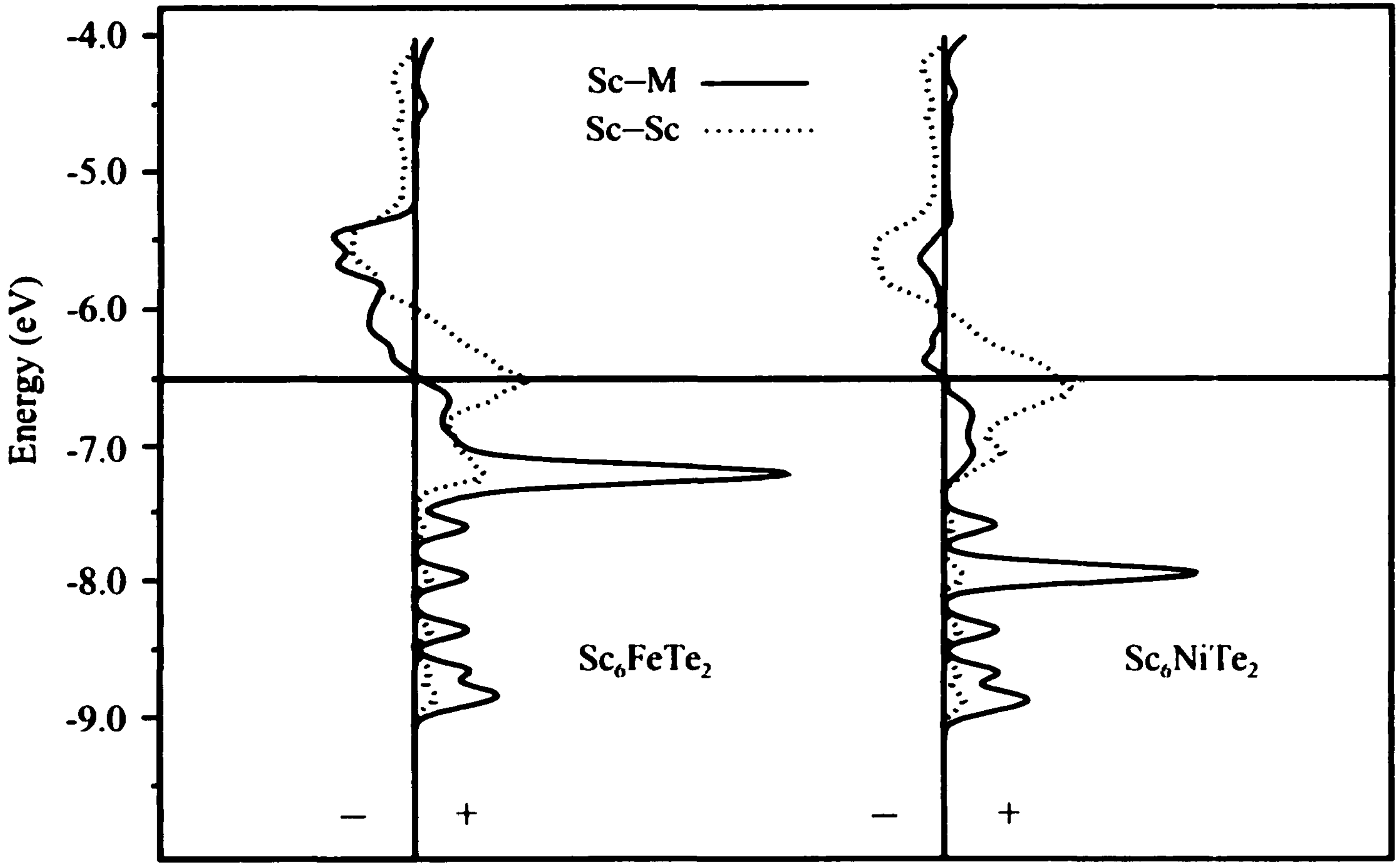

Figure 4. Total COOP (crystal orbital overlap populations) curves for indicated pairwise interactions in Sc$_6$MTe$_2$, M = Fe and Ni.

CHAPTER 8. SUBSTITUTIONAL CHEMISTRY IN Mn_5Si_3-TYPE SCANDIUM COMPOUNDS AND THE FORMATION OF QUASI-BINARY PHASES

A paper prepared for submission to Materials Chemistry

Paul A. Maggard, Douglas A. Knight and John D. Corbett

Department of Chemistry, Iowa State University, Ames, IA 50011

Abstract

The compounds $Sc_5B_{3-x}B'_x$ (B = Al or Ga; B' = Sn, Sb or Te) were prepared by high-temperature solid-state techniques, and their structures were determined from powder or single crystal X-ray diffraction as hexagonal Mn_5Si_3 type, $P6_3/mcm$ (No. 193), Z = 2. A given atom, Al or Ga (B), shows mixed occupancy with Sn, Sb, or Te (B') over different phase widths. For systems annealed at 1100 - 1575 °C, Single crystal x-ray data indicate that the phase widths of $Sc_5B_{3-x}B'_x$ extend over the ranges x = 1.38(6) - 2.25(2), 0.83(1) - 0.96(1), 0 - 2.25(6), and 0 - 1.25(3) for (B/B') Al/Sb, Al/Te, Ga/Sb and Ga/Te respectively. Powder x-ray data on the Sn systems shows phase width ranges of x = ~1.2 - 3.0 and 0.0 - 3.0 for B = Al and Ga respectively. No interstitial effects were evident. Lattice constant trends follow Vegard's law, with natural increases of a (b) and V with increasing x, but with irregular behaviors of c. Physical property measurements show many of the compounds display metallic characteristics, with positive temperature-dependent resistivities and Pauli-like

paramagnetic signals. These series of mixed compounds illustrate the effect of substitution of a larger B atom in the flexible Mn_5Si_3 type structure.

Introduction

The long and well-known history of the chemical flexibility of Mn_5Si_3-type phases and their interstitial derivatives has been described previously in reviews.[1,2] Pearson's handbook[3] lists 290 combinations of elements known to crystallize in the Mn_5Si_3 (A_5B_3) type structure through 1991. The A elements include groups 2 to 5, i.e. the early transition- or alkaline-earth metals, and the B elements include groups 13 to 15, i.e. main-group elements. Chemical alterations within this structure type allow the tuning of electron counts, lattice sizes, orbital characteristics, and physical properties within the single structure type. For chemists, this flexibility has served as a continual check of some of the most basic chemical ideas of bonding and properties, as well as an unrecognized source of significant experimental errors from impurities. Possible modifications of A_5B_3 include the addition of a third interstitial element Z, which can range up to 20(!) different examples within the confacial trigonal antiprisms formed by A, as in Zr_5Sb_3Z,[4] Zr_5Sn_3Z,[5] Zr_5Pb_3Z,[6] La_5Pb_3Z,[7] La_5Ge_3Z,[8] La_5Sn_3Z,[9] Ae_5Pn_3 (Ae = alkaline-earth metal; Pn = pnictogen),[10,11] and R_5Pn_3Br ® = rare-earth metal)[12] systems. Some of these phases require the presence of interstitial Z for stabilization in the Mn_5Si_3 structure type, i.e. Zr_5Sb_3Z and La_5Sn_3Z, and have historically been termed "Nowotny" phases. There are a few examples in which the B atom can also serve as the interstitial (self-stuffed Mn_5Si_3 or Ti_5Ga_4[13]), as in $A_5B_3(B)$ for $Zr_5Sb_{3.2}$,[4]

Zr_5Sn_4,[14] Zr_5Pb_4,[6] and Zr_5Al_4[15] which may or may not span the entire composition range from 5:3 to 5:4. More complexities arise when these interstitial sites are filled by both Z and B atoms, as in $Zr_5Sb_{3.3}Fe_{0.3}$.[16] Compounds are known with mixed occupancies on A positions, but no A elements are reported to disorder on the B or the interstitial sites.

There are a few reported explorations into the equilibrium chemistry of disorder on the B-site in these phases from different chemical groups, i.e., excluding mixed Ge-Si occupancy.[17-19] Boller and Parthé[20] in 1963 were interested in the formation of "pseudosilicides" by suitable B-site substitution in $Zr_5(Al, Ga, or In)_{3-x}Sb_x$, $Ti_5Ga_{3-x}Sb_x$, and $Hf_5In_{3-x}Sb_x$ systems at $x \approx 1.5$, which they thought might provide increased oxidation resistance and stability. More recently, Waterstrat, Kuentzler, and Müller[21] were interested in optimizing the T_c values for superconductivity with B-site substitutions in $Zr_5Ir_{3-x}T_x$ (T = Pt or Os).

Our own explorations into mixed B-site chemistry of Mn_5Si_3 phases started serendipitously with the identification of $Sc_5Al_{3-x}Te_x$ ($x \sim 0.8 - 1.0$) in this structure type. This contrasted with the fact that neither binary end-member, Sc_5Al_3 or Sc_5Te_3, was known or could be synthesized by us, implying some unusual electronic or size effects in the mixed system. In order to gain further views and insights about diverse changes in chemical and structural features, this chemistry has been explored for six systems, $Sc_5(Al or Ga)_{3-x}(Sn, Sb, or Te)_x$. The binary 5:3 phases are known among these only for scandium with gallium or tin.[3] Syntheses, phase widths, structural features, and resistivity and magnetic susceptibility properties are reported and discussed for these series. We will designate B as the triel element and B' as the Sn, Sb or Te that is substituted on these positions.

Experimental Section

Syntheses. All materials were handled in a He-filled glovebox. The elements were used as received (Sc turnings 99.7%, Aldrich-APL; Al rods 99.999%, United Mineral and Chemical; Ga chunks 99.99%, Johnson-Matthey; Sn chunks 99.999%, Johnson-Matthey; Sb powder 99.999%, Alfa-AESAR; Te powder 99.99%, Alfa-AESAR). Synthesis of $Sc_5Al_{3-x}Te_x$ and $Sc_5Ga_{3-x}Te_x$ began with the preparation of Sc_2Te_3 as described previously.[22] All other elements were used directly. Appropriate amounts of these compounds and the elements were weighed out to give ~ 300 - 350 mg total for the $Sc_5B_{3-x}B'_x$ (B = Al or Ga; B' = Sn, Sb or Te) compositions. The reactants were pelletized into 10mm diameter disks with a hydraulic press inside a glovebox and then arc-melted for 20-seconds per side with a current of 70 amps. Weight losses from the arc-melted pellets varied with the system and composition: $Sc_5Al_{3-x}Te_x$ (1 - 2 wt.%), $Sc_5Al_{3-x}Sb_x$ (2 - 4 wt.%), $Sc_5Al_{3-x}Sn_x$ (2 - 5 wt.%), $Sc_5Ga_{3-x}Te_x$ (1 - 3 wt.%), $Sc_5Ga_{3-x}Sb_x$ (3 - 6 wt.%), $Sc_5Ga_{3-x}Sn_x$ (2 - 6 wt.%). These weight losses were typically insignificant relative to the overall compositions, except when small amounts of one component were present, i.e. $Sc_5Ga_{2.75}Te_{0.25}$. These reactions were repeated multiple times with and without an excess of the supposedly volatilized component, and the phases formed and their lattice constants were found to be typically unaffected. Guinier X-ray powder patterns were usually not taken at this point, as the powder pattern lines were occasionally somewhat broadened after arc-melting. The arc-melted pellets were welded inside tubular tantalum containers and annealed at 1100 - 1575 °C from 1 - 5 days in a high temperature vacuum furnace. The reactions annealed at 1525 - 1575 °C for the systems $Sc_5Al_{3-x}Sb_x$ and $Sc_5Ga_{3-x}Sb_x$ and 1100 - 1200 °C for $Sc_5Al_{3-x}Te_x$ and $Sc_5Ga_{3-x}Te_x$ gave single crystals. Guinier patterns at this point were usually very sharp and indicated either the synthesis of >95% $Sc_5B_{3-x}B'_x$, or a biphasic product of the target phase and additional Sc_xB or Sc_xB' components, which indicated the respective phase width limits for the B and B' components had been surpassed.

Powder X-ray Diffraction. The powder diffraction patterns of the $Sc_5B_{3-x}B'_x$ phases were obtained with the aid of Enraf-Nonius Guinier powder cameras and monochromatic Cu $K\alpha_1$ radiation. The samples were ground, mixed with standard silicon (NIST), and placed between two strips of cellophane tape on a metal frame that mounted on the sample rotation motor. Lattice parameters were obtained with the aid of least-squares refinement of 15 - 30 lines per sample with 2θ values calibrated by a non-linear fit to the positions of the standard silicon lines (Table 1). The samples studied fell within the phase width limits and beyond to aid in the determination of their end points by lattice dimensions and product yields.

Single Crystal Diffraction. Several well-faceted crystals were selected from the six reactions with B = Al or Ga and B' = Sb or Te that produced samples containing excess aluminum, antimony or tellurium, as judged by the presence of Sc_2Al, Sc_5Sb_3 (Yb_5Bi_3 type), or ScTe in the powder patterns, respectively. These enabled the determination of the approximate phase boundaries of each system. Crystal qualities were checked with Laue or rotation photographs, and the best crystal mounted in each system was taken for data collection on a Rigaku AFC6R diffractometer (monochromated Mo Kα_1 radiation) at room temperature. Twenty-five centered reflections gathered from a random search were used to determine provisional lattice constants and the crystal system. Four octants of data were collected (h, ±k, ±l), in each case to $2\theta_{max} = 60°$ or 58°, and these were corrected for Lorentz and polarization effects. The data were further corrected for absorption with the aid of 2 - 3 ψ scans. Approximately 2,100 reflections were measured for each crystal from which 700 - 1,400 reflections had $I > 3\sigma$ and 118 - 172 were unique. Extinction conditions in all cases suggested the space groups 185 (*$P6_3cm$*), 188 (*$P\text{-}6c2$*) or 193 (*$P6_3/mcm$*). In all cases, the centricity statistics were ambiguous, but the structures were solvable only in space group 193. For every data set, trial models were obtained by direct methods (SHELXS[23]) and refined with the package TEXSAN.[24]

The refinement of the B-site with only Al, Ga, Sn, Sb, or Te for the mixed samples resulted in extremely large or small thermal parameters, depending on the situation, and led to the mixed-site refinements of Al or Ga with Sn, Sb or Te on the same site (assuming full occupancy). This result was buttressed by EDS and synthetic results, vide infra. Refinements of other combinations of mixed site occupancy on A, vacancies on unmixed B, or interstitial site occupation were unsuccessful. After isotropic refinement, the antimony-richest crystals were further corrected for absorption with the aid of DIFABS.[25] The data sets converged after anisotropic refinement at $R(F)/R_w < 5\%$ in all cases. The x-ray data collection and refinement parameters, atomic positions and site occupancies are given in

Table 2. Additional data collection, refinement, and anisotropic displacement parameters are in the Supporting Information. These as well as the F_o/F_c listings are available from J.D.C.

EDS. The elemental compositions of crystals from several different systems were determined via energy-dispersive X-ray spectroscopy (EDS) on a JEOL system 840A scanning electron microscope (SEM) with an IXRF X-ray analyzer system and a Kevex Quantum light element detector. A beam of approximately 20kV and 0.3 nA was used to gain count rates of about 2500 s^{-1}. Data were taken on several crystals from each system to further establish the approximate 5:3 atomic ratios of the Sc:(B + B') components. The compounds Sc_5Ga_3, Sc_9Te_2, Sc_2Al, Sc_5Sn_3, and Sc_5Sb_3 were used as standards in relating peak areas to atomic percentages, which gave more accurate composition determinations.

Properties. Powdered samples of ~50 mg of a range of $Sc_5B_{3-x}B'_x$ phases were each loaded inside a He-filled glovebox into a susceptibility apparatus where ~50mg was sandwiched between two glass rods inside a 3 mm i.d. fused silica tube. Magnetizations for the samples were measured from 6 to 300 K in a field of 3 T with a Quantum Design MPMS SQUID magnetometer. The data were corrected for diamagnetism of both the sample holders and the atomic cores. Resistivities of powdered, sized samples of ~50 mg of each sample were diluted with Al_2O_3 and were measured with a "Q" apparatus between 100 and 300 K.[26]

Results and Discussion

Synthetic Results. For each of the six $Sc_5B_{3-x}B'_x$ systems (B = Al or Ga; B' = Sn, Sb, or Te) a series of reactions over a range of $0 \leq x \leq 3$ was performed. The appearance of

Sc_2Al, Sc_5Sb_3 (Yb_5Bi_3 type), or ScTe in the powder patterns of the products was an indication that the phase-width boundaries had been exceeded in each of the systems. This was also used as a rough boundary for the refined X-ray compositions of samples and also of the approximate 5:3 atomic ratios of Sc:(B + B'). Typically, the threshold for the observance of a minor phase in an X-ray powder pattern is 5 - 10%, and so it must be present in a good proportion. Table 3 lists for comparison the EDS and single crystal results for the phase width determinations. The onset of Sc_xB components for each of the systems was found to occur for reactions loaded $Sc_5Al_{2.5}Te_{0.5}$, $Sc_5Al_{2.5}Sb_{0.5}$, $Sc_5Al_{1.95}Sn_{1.1}$ (below the minimum x) and usually for $x = 0.25$ intervals. All of the gallium systems extend to Sc_5Ga_3 ($x = 0$). However, Sc_5Ga_3 could not be synthesized in pure form, and powder patterns typically contained a few extra lines. The occurrence of Sc_xB' products (above maximum x) first appeared in reactions loaded as $Sc_5Al_{1.75}Te_{1.25}$, $Sc_5Al_{0.75}Sb_{2.25}$, $Sc_5Ga_{1.5}Te_{1.5}$, $Sc_5Ga_{0.75}Sb_{2.25}$, again for $x = 0.25$ intervals. The tin systems extend to Sc_5Sn_3 ($x = 3$), meaning $Sc_5Ga_{3-x}Sn_x$ is homogeneous across the entire system, $0 \le x \le 3$. Comparisons of these boundary extremes with the refined X-ray compositions for single crystals isolated from beyond the phase boundaries, Table 3, shows that the composition extremes so estimated from powder samples do, within error, all correctly exceed the X-ray refinement results at the B and B' limits. EDS data were obtained only for 5:3 crystals in samples that exceeded the phase boundaries. The EDS results in Table 3 also roughly correspond, within 3σ, with the single crystal and powder X-ray results of the phase boundary determinations, with no new features of note.

A complication arose in the study of product formation in two systems, $Sc_5Ga_{3-x}Sb_x$ and $Sc_5Ga_{3-x}Te_x$. Approximately 10 - 25% of an unidentified phase sporadically appeared in the powder patterns throughout their listed homogeneity ranges. These samples were not used in any subsequent analyses since either another phase evidently lies outside these pseudobinary systems or the loaded stoichiometries were in error. As stated earlier, the binary Sc_5Ga_3 does not synthesize in high yield either.

A better delineation of the trends and phase boundaries may be found when the unit cell volumes, c/a ratios, a axis and c axis parameters in Table 1 are plotted as a function of x, in Figures 1 - 4. As figure 1 shows, the cell volume remains nearly constant beyond the phase boundary limits, which are marked by the vertical lines according to the methods discussed above. In all cases, the cell volume increases nearly linearly with increasing amounts of Sn, Sb or Te substitution for Al or Ga, as expected from size effects. The slopes are also found to increase from Sn to Sb to Te, corresponding to the increasing size differences between them and the triel. For the Al-Te and some parts of the Ga-Te system, the slope is almost entirely zero. Regarding the triels, the cell volume and $\partial V/\partial x$ for an aluminum system is greater than that for the respective gallium system, and becomes increasingly so at higher triel concentrations, i.e. compare Al - (Sb or Sn) with Ga - (Sb or Sn) where the data is more complete. The reason behind these trends may again be entirely attributed due to size, as gallium is smaller than aluminum, but this may also be assisted by the lower energy of the gallium p-orbitals depleting the metal-framework of electrons.

The *c/a* ratios plotted in Figure 2 reveal more sharply the reapportioning of the lattice dimensions brought about by the changing atomic sizes and electron concentrations. Increasing *c/a* ratios result from relative shortening of the metal bonds along the *a* axis versus the *c* axis, and vice versa. The *c/a* ratios for the Ga-Te and Ga-Sn systems increase for $0.25 < x < 0.5$ and then decrease for higher Te or Sn concentrations. This corresponds to a relative shortening of the metal bonds along *a* versus *c* at high triel concentrations, and then the reverse at low triel concentrations. This latter is the general trend among all 6 systems with the exception of Al-Sn, which displays the former tendency. Definite conclusions here are problematic, as the gallium systems contained small amounts of composition-altering unknowns.

Changes in the individual *a* and *c* axis parameters for increasing substitutions of Sn, Sb, and Te for Al and Ga are shown in Figures 3 and 4, respectively. A comparison of these figures for the Ga-Sn sytem (excluding the problematic Sc_5Ga_3) reveals that the changes in *a* lattice parameters are more than 3× greater than the changes in *c* lattice parameters. This pattern will be related to structural features described later. The *a* axis parameters increase for all 6 systems, and more so for the gallium systems versus the aluminum systems. The reason behind this trend is again most likely due to the size differences. The *c* axis parameters follow unidentified patterns, and for the gallium systems, contain many suspicious data points.

$Sc_5Al_{3-x}Sn_x$ was the only system in which the Al-richest phase boundary was not established by single crystal methods, and the $x = 1.2$ end point as determined by lattice constant variations is marked with a solid bar on Figures 1 - 4. This result is not dissimilar with that from the use of the product formation as a guide to the end point, which gave $1.1 \leq x \leq 1.25$.

Structure. Compounds with this structure type have been described previously and frequently.[1] A near-[001] view of the structure is shown in Figure 5 with the Sc and B/B' atoms shaded and open, respectively. The Sc2 atoms form the common triangular faces of trigonal antiprisms down the *c* axis. The common basal edges are all bridged by the B/B' atoms. The resulting confacial chains of $Sc_{6/2}(B)_{6/2}$ units are globally packed into a hexagonal configuration. The Sc1 atoms form a closely spaced string that repeats along the *c* axis, in which each atom resides in a distorted octahedral coordination formed by the B components. Figure 6 shows how the Sc1 atoms fall at the midpoints of the $Sc_{6/2}(B)_{6/2}$ antiprisms along *c*.

Selected atomic distances determined by single-crystal data refinements are given in Table 4. The atomic distances will be discussed in two parts, considering a) the Sc - Sc and b) the Sc - B/B' distances. The size of and matrix effects from B and B' mixed on a single site are not completely separable, and it is expected that a stable mixed B element product reaches some dimensional compromise with the electronic structure.

The Sc2 atoms that form the confacial edges of trigonal antiprisms are spaced at 3.37 - 3.46 Å. This distance generally naturally increases for larger B, compare $Sc_5Al_{1.616}Sb_{1.384(7)}$ and $Sc_5Al_{0.74}Sb_{2.26(2)}$. On the other hand, distances along the Sc2 chain (twice as frequent) change much less at 3.56 - 3.58Å, as does *c*. This distance is a fairly long scandium bond (see Sc_8Te_3),[22] and is drawn as dashed in Figure 5. The Sc1 separations in the closely spaced linear string repeats at $c/2$ and has distances ranging only from 2.97 - 2.98 Å, and generally changes only slightly with ascending x. The larger Sc2 - Sc2 distance changes on the confacial edges of the trigonal antiprisms result in a more significant adjustment of the a axis parameters compared to c.

The shortest metal - non-metal distance is Sc2 - B/B', located on the triangular edges of the antiprismatic chain, from 2.80 - 2.85Å (Figure 5), and increases with substitution of Sb for Te and with increasing x (~0.03Å). The Sc1 - B/B' distances, from the non-metals to the Sc1 positions of the string, are slightly longer at 2.92 - 2.97Å. Longer distances, for Sc2 - B/B', are between atoms in adjacent layers (3.23 - 3.26Å) or on adjacent metal chains (3.00 - 3.08Å).

Properties. Q-method conductivity results for the samples within their respective phase widths are given in Table 5. All of the phases have resistivities on the order of 14 - 50 μΩ·cm, and their temperature dependencies range from -0.17(2) to 0.15(1) % K^{-1}. Within the extended $Sc_5Ga_{3-x}Sn_x$ series, the resistivity peaks at 46 μΩ·cm at $x = 1$, and decreases on either side to 31 μΩ·cm for Sc_5Ga_3 and 14 μΩ·cm for Sc_5Sn_3, each with a larger positive temperature dependence. Fairly small temperature dependencies are observed for Sc_5Ga_2Sb, $Sb_5Ga_{1.5}Sb_{1.5}$, $Sb_5Ga_{2.75}Te_{0.25}$, and $Sb_5Ga_2Te_1$. The $Sc_5Al_{3-x}B'_x$ systems all show positive temperature dependencies except Sc_5Al_2Te, which occurs within the small phase width for this system. It is difficult to draw conclusions about correlations of the resistivity with the atomic structures and valence electron counts, not just because the latter are difficult to define, but the absolute values of the resistivities are rough estimations to within a factor of three (although internal consistency for related samples is probably better).[26]

Magnetic susceptibility measurements taken for the $Sc_5B_{3-x}B'_x$ series of compounds are listed in Table 6. The magnetic susceptibilities are listed for 6K and 298K to give some measure of magnitude of their temperature dependencies. About half of the compounds show a temperature independent Pauli-paramagnetic signal of $5 - 8 \times 10^{-4}$ emu·mol^{-1}. However, there seems to be no relationship between the magnetic results and the resistivity characteristics. The substitution of Sn, Sb or Te for Ga in $Sc_5Ga_{2.75}B'_{0.25}$ lowers the room temperature paramagnetic susceptibility (χ_{298}) with the first and raises it for Sb and Te. For the $Sc_5Ga_{3-x}(Sn\ or\ Sb)_x$ compounds, there is a crossover from temperature independent to dependent behavior at $x > 1.00$ and 1.50 respectively. Magnetic data are plotted for the Ga-Sn system in Figure 7 to give an idea of the non-linear nature of the temperature dependencies, which cannot be fitted to a sum of Pauli-paramagnetic and Curie-Weiss contributions. Instead, this situation may be understood as a number of delocalized electrons (itinerant) that change with temperature as electrons gain small orbital contributions at particular cores,[27] as described for Sc_8Te_3.[28] The $Sc_5Ga_{3-x}Sn_x$ ($1 \le x \le 3$) series shows an increase in the magnetic signal from $x = 1.00$ to 2.00 and then a decrease in the magnetic signal from $x = 2.00$ to 3.00. The *c* axis dimension (Table 1) also peaks in this series of compounds for $x = 2.00$. The large flexibility of the $Sc_5B_{3-x}B'_x$ series of compounds shows a range of physical properties that could possibly be correlated with substitutions levels or electronic structure. Investigations into more mixed B-site chemistry may lead to better predictability and tunability of structure and property changes.

Conclusions. Compounds of the compositions $Sc_5B_{3-x}B'_x$ (B = Al or Ga; B' = Sn, Sb, or Te) may be synthesized using high-temperature solid-state techniques. A substitutional chemistry is revealed for the B-atomic position within the Mn_5Si_3 (A_5B_3) structure type. The phase width boundaries were explored for each system, and the interatomic distances and lattice dimensions were discussed in correlation with the substitution of Sn, Sb or Te for Al or Ga within these compounds. Cell volumes change as expected with size effects and the *c/a* ratios show a reapportioning of the metal framework dimensions. Physical property measurements indicate metallic behavior for many of these compounds. Investigations into more mixed B-site chemistry may lead to better predictability and tunability of structure and property changes.

Acknowledgements

The authors thank W. Straszheim for help with EDS measurements, J. Ostenson for the magnetic susceptibility measurements, and R. Jacobson for provision of diffractometer time.

Supporting Information Available

Tables of additional data collection and refinement information and the anisotropic displacement parameters for six $Sc_5B_{3-x}B'_x$ samples are given.

References

(1) Corbett, J. D.; Garcia, E.; Guloy, A. M.; Hurng, W.-M.; Kwon, Y.-U.; Leon-Escamilla, E. A. *Chem. Mater.* **1998**, *10*, 2824.

(2) Franceschi, E. A.; Ricaldone, F. *Rev. Chim. Min.* **1984**, *21*, 202.

(3) Villars, P.; Calvert, L. D. *Pearson's Handbook of Crystallographic Data for Intermetallic Phases*, 2nd ed.; American Society for Metals International: Metals Park, OH, **1991**.

(4) Garcia, E.; Corbett, J. D. *Inorg. Chem.* **1988**, *27*, 2353.

(5) Kwon, Y.-U.; Corbett, J. D. *Chem. Mater.* **1992**, *4*, 1348.

(6) Kwon, Y.-U.; Corbett, J. D. *J. Alloys Compd.* **1993**, *190*, 219.

(7) Guloy, A. M.; Corbett, J. D. *J. Solid State Chem.* **1994**, *109*, 352.

(8) a) Guloy, A. M.; Corbett, J. D. *Inorg. Chem.* **1993**, *32*, 3532; b) Guloy, A.M..; Corbett, J.D. *Inorg. Chem.* **1996**, *35*, 4669.

(9) Kwon, Y.-U.; Rzeznik, M. A.; Guloy, A. M.; Corbett, J. D. *Chem. Mater.* **1990**, *2*, 546.

(10) Leon-Escamilla, E. A.; Corbett, J. D. *J. Alloys Compd.* **1994**, *206*, L15.

(11) Leon-Escamilla, E. A.; Corbett, J. D. *J. Alloys Compd.* **1998**, *265*, 104.

(12) Jensen, E. A.; Hoistad, L. M.; Corbett, J. D. *J. Solid State Chem.* **1999**, *144*, 175.

(13) a) Schubert, K.; Meissner, H. G.; Pötzschke, M.; Rossteutscher, W.; Stolz, E. *Naturwissenschaften* **1962**, 49, 57; b) Pötzschke, M.; Schubert, K. *Z. Metallkd.* **1962**, 53, 474.

(14) Kwon, Y.-U.; Corbett, J. D. *Chem. Mater.* **1990**, *2*, 27.

(15) Kematick, R. J.; Franzen, H. F. *J. Solid State Chem.* **1984**, *54*, 226.

(16) Kwon, Y.-U.; Sevov, S. C.; Corbett, J. D. *Chem. Mater.* **1990**, *2*, 550.

(17) Narasimhan, K. S. V. L.; Steinfink, H.; Ganapathy, E. V. *J. Appl. Phys.* **1969**, *40*, 51.

(18) Kappel, G.; Fischer, G.; Jaègle A. *Phys. St. Sol. Sec. A* **1976**, *34A*, 691.

(19) Holleck, H.; Benesovsky, F.; Nowotny, H. *Monat. Chem.* **1965**, *96*, 570.

(20) Boller, H.; Parthè E. *Acta Cryst.* **1963**, *16*, 830.

(21) Waterstrat, R. M.; Kuentzler, R.; Muller, J. *J. Less-Common Met.* **1990**, *167*, 169.

(22) Maggard, P. A.; Corbett, J. D. *Inorg. Chem.* **1999**, *38*, 1945.

(23) Sheldrick, M. SHELXS-86. Universität Göttingen, Germany, 1986.

(24) TEXSAN, Version 6.0, Molecular Structure Corp., The Woodlands, Texas, 1990.

(25) Walker, N.; Stuart, D. *Acta Crystallogr.* **1983**, *A39*, 158.

(26) a. Shinar, J.; Dehner, B.; Beaudry, B. J.; Peterson, D. T. *Phys. Rev. B* **1988**, *37*, 2066.

b. Tai,-J.; Corbett, J.D. *Inorg. Chem.* **1995**, *34*, 378.

(27) Jiles, D. *Introduction of Magnetism and Magnetic Materials*, 2nd ed.; Chapman & Hall: London, 1998; p. 316.

(28) Maggard, P. A.; Corbett, J. D. *Inorg. Chem.* **1998**, *37*, 814.

Table 1. Lattice Constants (Å) and Cell Volumes (Å^3) for the A_5B_3 phases in $Sc_5B_{3-x}B'_x$ (B = Al or Ga; B' = Sn, Sb or Te) samples.

		Lattice Parameters			
Composition	loaded *x*	*a*	*c*	*V*	*c*/*a* ratio
$Sc_5Al_{3-x}Te_x$	0.5 (0.83)[a]	8.2676(7)	5.9516(8)	352.30(7)	0.720
	0.8	8.2689(9)	5.9524(8)	352.45(9)	0.720
	1.0	8.274(1)	5.947(2)	352.6(1)	0.719
	1.25 (0.960)	8.2735(8)	5.9464(9)	352.50(9)	0.719
$Sc_5Al_{3-x}Sb_x$	0.5 (1.384)	8.2722 (7)	5.9668(8)	353.59(8)	0.721
	1.0	8.2742(4)	5.9643(6)	353.61(5)	0.721
	1.5	8.2856(6)	5.9704(7)	354.96(7)	0.721
	2	8.3156(2)	5.9591(3)	356.86(2)	0.717
	2.15	8.3326(2)	5.9541(3)	358.02(3)	0.715
	2.25 (2.26)	8.3350(4)	5.9516(4)	358.08(4)	0.714
	2.75	8.3318(6)	5.9508(5)	357.76(6)	0.714
$Sc_5Al_{3-x}Sn_x$	0.5	8.316(2)	6.001(3)	359.4(2)	0.722
	1.0	8.320(1)	6.006(1)	360.1(1)	0.722
	1.25	8.3218(4)	6.0010(9)	359.91(6)	0.721
	1.5	8.331(1)	6.018(2)	361.7(1)	0.722
	2	8.344(2)	6.043(2)	364.3(2)	0.724
	2.5	8.3818(4)	6.0590(4)	368.64(4)	0.723
	2.75	8.3830(4)	6.0599(5)	368.80(5)	0.723
	3.0	8.3956(2)	6.0622(3)	370.05(5)	0.722
$Sc_5Ga_{3-x}Te_x$	0.0	8.086(2)	5.949(4)	336.8(3)	0.736
	0.25	8.0772(2)	6.0387(4)	341.20(3)	0.748
	0.5	8.0889(6)	6.0431(8)	342.43(7)	0.747

Table 1. (continued)

	1.0	8.1201(3)	5.9765(4)	341.27(3)	0.736
	1.5	8.148(2)	5.976(1)	343.6(2)	0.733
	1.75 (1.25)	8.1478(8)	5.967(1)	343.0(1)	0.732
$Sc_5Ga_{3-x}Sb_x$	0.0	8.086(2)	5.949(4)	336.8(3)	0.736
	0.25	8.100(2)	5.954(2)	338.3(2)	0.735
	1.0	8.1403(4)	5.9969(4)	344.14(4)	0.737
	1.5	8.1960(8)	5.9840(9)	348.12(8)	0.730
	1.8	8.2440(3)	5.9698(3)	351.37(3)	0.724
	2.25	8.277(1)	5.960(1)	353.6(1)	0.720
	2.35 (2.24)	8.2771(6)	5.9618(8)	353.72(7)	0.720
$Sc_5Ga_{3-x}Sn_x$	0.0	8.086(2)	5.949(4)	336.8(3)	0.736
	0.25	8.0923(3)	6.1035(4)	346.14(3)	0.754
	1.0	8.172(4)	6.053(4)	350.1(4)	0.741
	1.5	8.220(2)	6.064(2)	354.9(2)	0.738
	2.0	8.297(2)	6.079(2)	362.5(2)	0.733
	2.75	8.3975(4)	6.0696(6)	370.67(5)	0.723
	3.0	8.3956(2)	6.0622(3)	370.05(5)	0.722

---

[a] The numbers in parentheses indicate the compositions determined by structural refinements (below) of crystals from the mixed-phase products.

Table 2. Summary of Single Crystal X-ray Data Collection, Refinement and Positional Parameters for Six $Sc_5B_{3-x}B'_x$ Limits.

B-B'	Al-Te[a] (x ~ 0.83)	Al-Te[b] (x ~ 0.96)	Al-Sb[c] (x ~ 1.38)	Al-Sb[d] (x ~ 2.26)	Ga-Te[e] (x ~ 1.25)	Ga-Sb[f] (x ~ 2.24)
formula weight	389.3	402.3	436.9	520.0	506.3	551.0
space group, Z			$P6_3/mcm$ (No. 193), 2			
d_{calc} (g/cm^3)	3.69	3.81	4.10	4.81	4.90	5.17
μ, Mo K_α (cm^{-1})	81.64	86.80	98.60	128.66	165.35	157.22
R, R_w,[g] %	3.2, 4.3	3.1, 3.5	1.3, 1.2	3.2, 2.8	2.8, 2.2	4.6, 4.3
			Refined Parameters[h, i]			
Sc1, U_{iso}	0.93(4)	1.06(6)	0.81(2)	0.59(6)	0.86(6)	0.76(8)
Sc2, y	0.2354(2)	0.2364(1)	0.23642(2)	0.2397(2)	0.2380(3)	0.2395(2)
U_{iso}	1.0(1)	1.01(3)	0.80(4)	0.7(1)	0.8(2)	0.8(1)
B + B', x	0.3935(2)	0.3927(1)	0.39410(5)	0.3912(1)	0.3940(1)	0.39205(8)
U_{iso}	1.04(6)	1.05(3)	0.80(2)	0.59(4)	0.79(6)	0.68(4)
B' atom, %	27.67(3)	32.000(3)	46.133(2)	75.200(7)	41.67(1)	74.80(2)

[a] $Sc_5Al_{2.17}Te_{0.83(1)}$, [b] $Sc_5Al_{2.040}Te_{0.960(8)}$, [c] $Sc_5Al_{1.616}Sb_{1.384(7)}$, [d] $Sc_5Al_{0.74}Sb_{2.26(2)}$, [e] $Sc_5Ga_{1.75}Te_{1.25(4)}$, [f] $Sc_5Ga_{0.76}Sb_{2.24(7)}$

[g] $R = \Sigma||F_o| - |F_c||/\Sigma|F_o|$; $R_w = [\Sigma w(|F_o| - |F_c|)^2/\Sigma w(F_o)^2]^{1/2}$; $w = \sigma_F^{-2}$.

[h] The atomic types are Sc1 $(0,y,1/4)$, Sc2 $(2/3,1/3,0)$, B/B' $(x,0,3/4)$.

[i] The respective lattice constants may be found in Table 1.

Table 3. Comparison of the EDS and Single Crystal X-ray results for the $Sc_5B_{3-x}B'_x$ System Phase Limits.[a]

Compound	EDS Data (Excess ScB or ScB')	Single Crystal Data
	Maximal x (B' richest)	
$Sc_5Al_{3-x}Te_x$	$Sc_{5.0(1)}Al_{1.9(1)}Te_{1.1(1)}$	$Sc_5Al_{2.040}Te_{0.960(8)}$
$Sc_5Al_{3-x}Sb_x$	$Sc_{5.0(1)}Al_{0.6(1)}Sb_{2.3(1)}$	$Sc_5Al_{0.74}Sb_{2.26(2)}$
$Sc_5Ga_{3-x}Te_x$	$Sc_{4.9(1)}Ga_{2.4(1)}Te_{0.7(1)}$	$Sc_5Ga_{1.75}Te_{1.25(4)}$
$Sc_5Ga_{3-x}Sb_x$	$Sc_{5.0(1)}Ga_{0.8(1)}Sb_{2.2(1)}$	$Sc_5Ga_{0.76}Sb_{2.24(7)}$
	Minimal x (B richest)	
$Sc_5Al_{3-x}Te_x$	$Sc_{5.0(1)}Al_{2.2(1)}Te_{0.8(1)}$	$Sc_5Al_{2.17}Te_{0.83(1)}$
$Sc_5Al_{3-x}Sb_x$		$Sc_5Al_{1.616}Sb_{1.384(7)}$
$Sc_5Al_{3-x}Sn_x$	$Sc_{5.2(1)}Al_{1.1(1)}Sn_{1.6(1)}$[b]	

[a] Phase widths in gallium and tin systems extend to Sc_5Ga_3 and Sc_5Sn_3.

[b] For on a polycrystalline sample with excess Sc_2Al.

Table 4. Selected Distances in $Sc_5B_{3-x}B'_x$ Compounds from Single Crystal X-ray Data.

			$Sc_5Al_{3-x}B'_x$ Phases				$Sc_5Ga_{3-x}B'_x$ Phases	
Site 1	Site 2	x	Te[a] (x~0.83)	Te[b] (x~0.96)	Sb[c] (x~1.38)	Sb[d] (x~2.26)	Te[e] (x~1.25)	Sb[f] (x~2.24)
Sc1	Sc1	2x	2.9758(4)	2.9732(4)	2.9834(4)	2.9758(2)	2.9835(5)	2.9809(4)
	B	6x	2.9470(4)	2.9500(2)	2.9484(2)	2.9707(3)	2.9161(4)	2.9545(3)
Sc2	Sc2[g]	2x	3.371(2)	3.387(2)	3.387(1)	3.460(3)	3.359(4)	3.433(3)
	Sc2[h]	4x	3.556(1)	3.559(1)	3.5672(5)	3.584(1)	3.558(1)	3.580(1)
	B	2x	2.835(1)	2.8328(6)	2.8417(4)	2.8477(7)	2.800(1)	2.8332(6)
	B		3.068(2)	3.069(1)	3.0560(9)	3.077(2)	2.998(3)	3.050(2)
	B	2x	3.2501(8)	3.2422(6)	3.2560(5)	3.2327(8)	3.243(1)	3.2375(9)
B	B	2x	3.458(1)	3.4634(8)	3.4597(6)	3.4848(9)	3.448(1)	3.4755(8)
	Sc1	4x	2.9470(4)	2.9500(2)	2.9484(2)	2.9707(3)	2.9161(4)	2.9545(3)
	Sc2	2x	2.835(1)	2.8328(6)	2.8417(4)	2.8477(7)	2.800(1)	2.8332(6)
	Sc2		3.068(2)	3.069(1)	3.0560(9)	3.077(2)	2.998(3)	3.050(2)
	Sc2	2x	3.2501(8)	3.2422(6)	3.2560(5)	3.2327(8)	3.243(1)	3.2375(9)

[a] $Sc_5Al_{2.17}Te_{0.83(1)}$, [b] $Sc_5Al_{2.040}Te_{0.960(8)}$, [c] $Sc_5Al_{1.616}Sb_{1.384(7)}$, [d] $Sc_5Al_{0.74}Sb_{2.26(2)}$,

[e] $Sc_5Ga_{1.75}Te_{1.25(4)}$, [f] $Sc_5Ga_{0.76}Sb_{2.24(7)}$

[g] Intratriangle/intraplane distance.

[h] Intertriangle/interplane distance.

Table 5. Room Temperature Resistivities (μΩ·cm) and Temperature Dependencies ((∂ρ/∂T)/ρ, %/K) for the $Sc_5B_{3-x}B'_x$ Systems.

B =	Ga	Al	Ga	Al	Ga	Al
B' =		Sn	Sb	Sb	Te	Te
x = 0.0	30, 0.134(7)		30, 0.134(7)		30, 0.134(7)	
0.25	41, -0.17(2)		28, 0.063(2)		36, -0.05(1)	
1.00	46, 0.04(1)		22, -		24, 0.028(7)	21, 0.014(6)
1.50	39, 0.15(1)	21, 0.112(3)	34, -0.06(1)	22, 0.071(4)		
2.00	24, 0.069(4)	19, 0.138(2)		17, 0.086(2)		
2.75	22, 0.075(3)	15, 0.108(2)				
3.00	14, 0.069(3)	14, 0.069(3)				

Table 6. Magnetic Susceptibilities (emu·mol^{-1} × 10^{3}) and Temperature Dependencies for the Sc$_5$B$_{3-x}$B'$_x$ Systems (1st line for 6K, 2nd line for 298K).

B =	Ga	Al	Ga	Al	Ga	Al
B' =	Sn	Sn	Sb	Sb	Te	Te
x = 0.0	0.630		0.630		0.630	
	0.632		0.632		0.632	
0.25	0.485		0.835		2.59	
	0.448		0.821		0.710	
1.00	2.59		0.484		0.865	0.774
	0.852		0.488		0.667	0.597
1.50	2.53	2.08	2.11	2.35		
	0.803	0.650	0.591	0.684		
2.00	4.25	0.643		0.559		
	2.37	0.623		0.553		
2.75	3.34	0.681				
	1.52	[a]0.560				
3.00	3.60	3.60				
	1.12	1.12				

[a] Compound undergoes a sharp transition between 46 - 56K from 6.7×10^{-4} emu·mol^{-1} to 5.7×10^{-4} emu·mol^{-1} between two temperature independent paramagnetic signals.

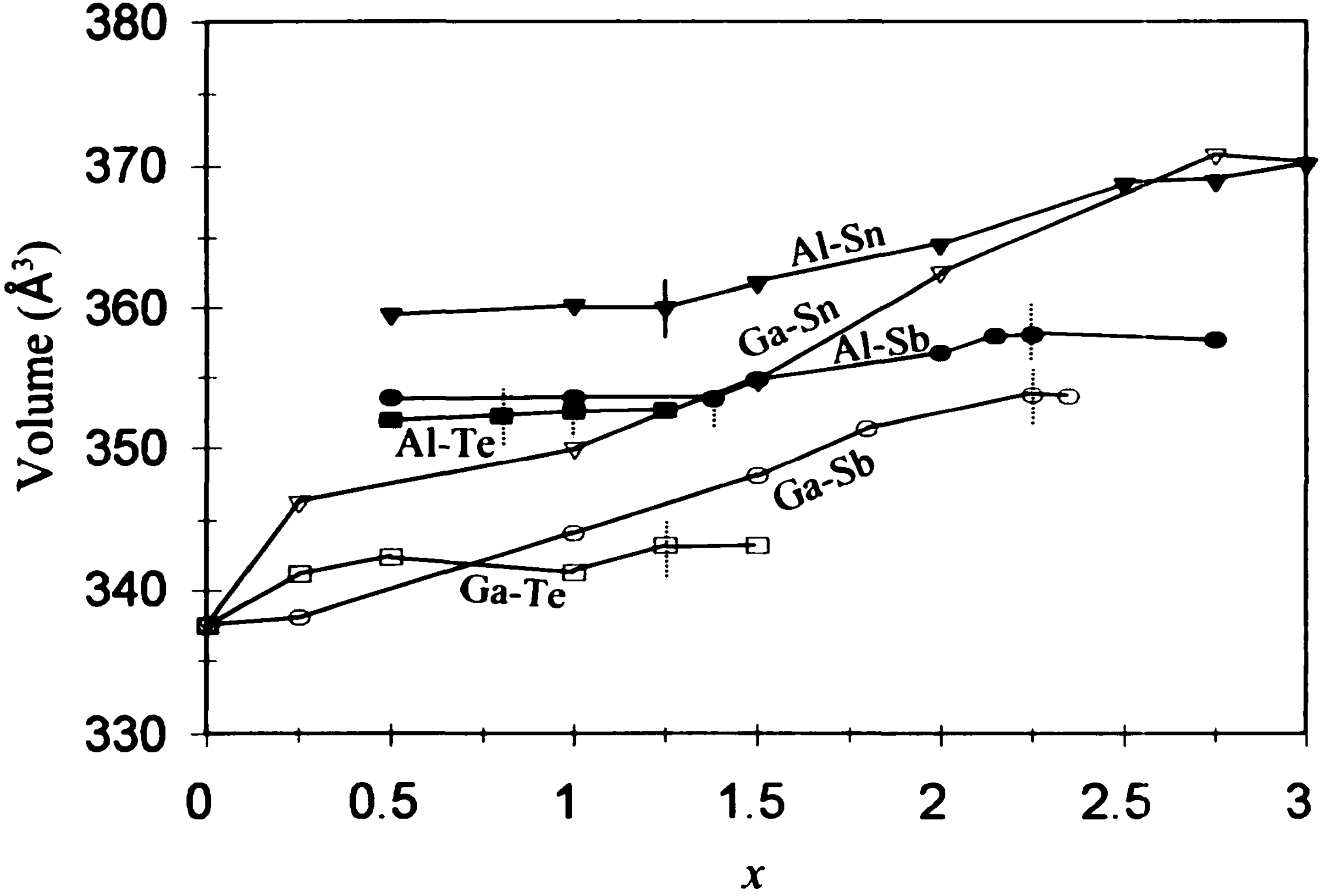

Figure 1. Cell volume (Å^3) versus x for $Sc_5B_{3-x}B'_x$. Shaded and open symbols represent Al and Ga systems, respectively. Vertical dashed lines indicate single-crystal composition endpoints and the solid line for Al-Sn shows the end point determined from powder pattern date.

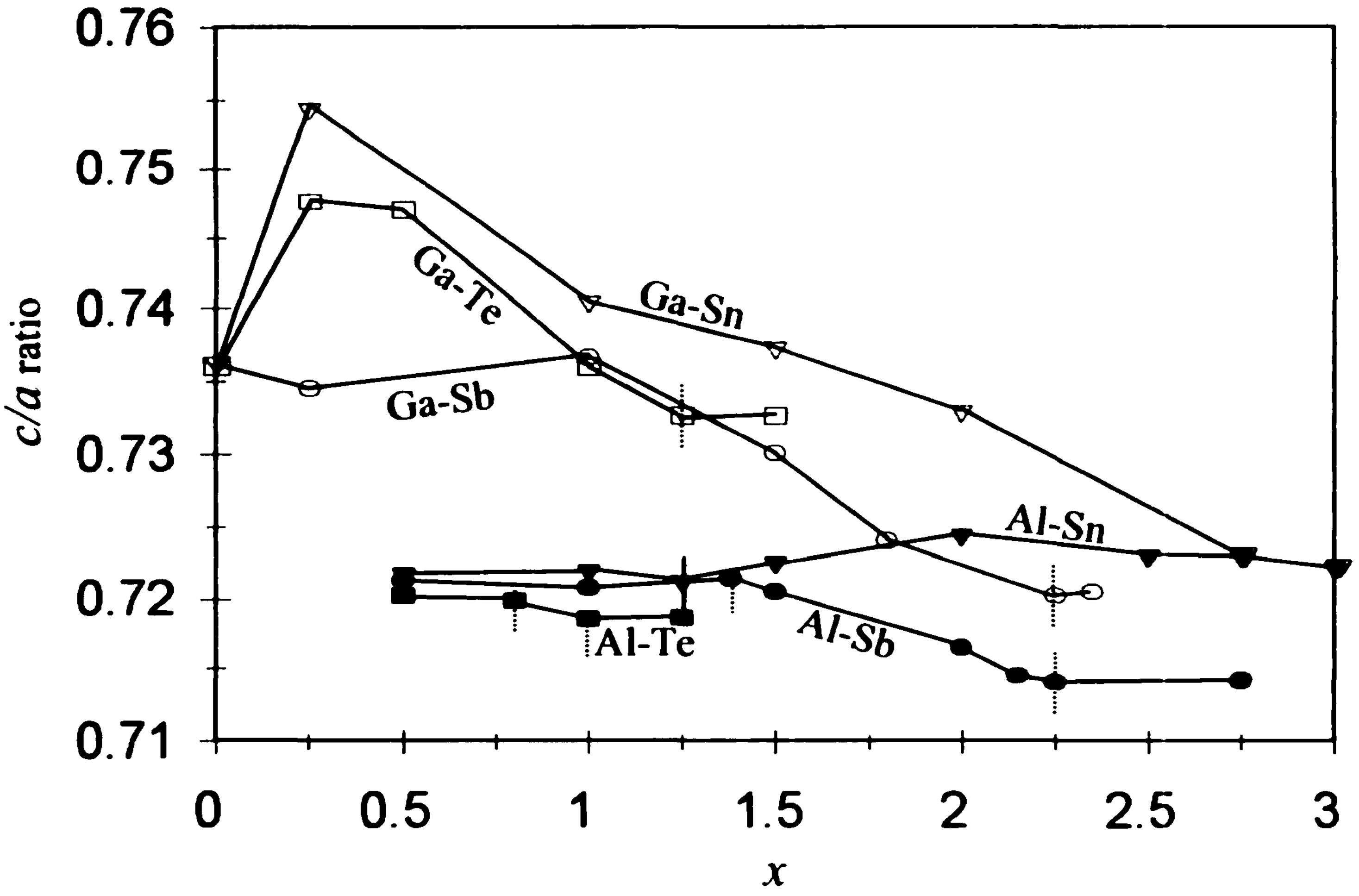

Figure 2. c/a ratio versus x for $Sc_5B_{3-x}B'_x$. Shaded and open symbols represent Al and Ga systems, respectively. Vertical line indications are identical to Figure 1.

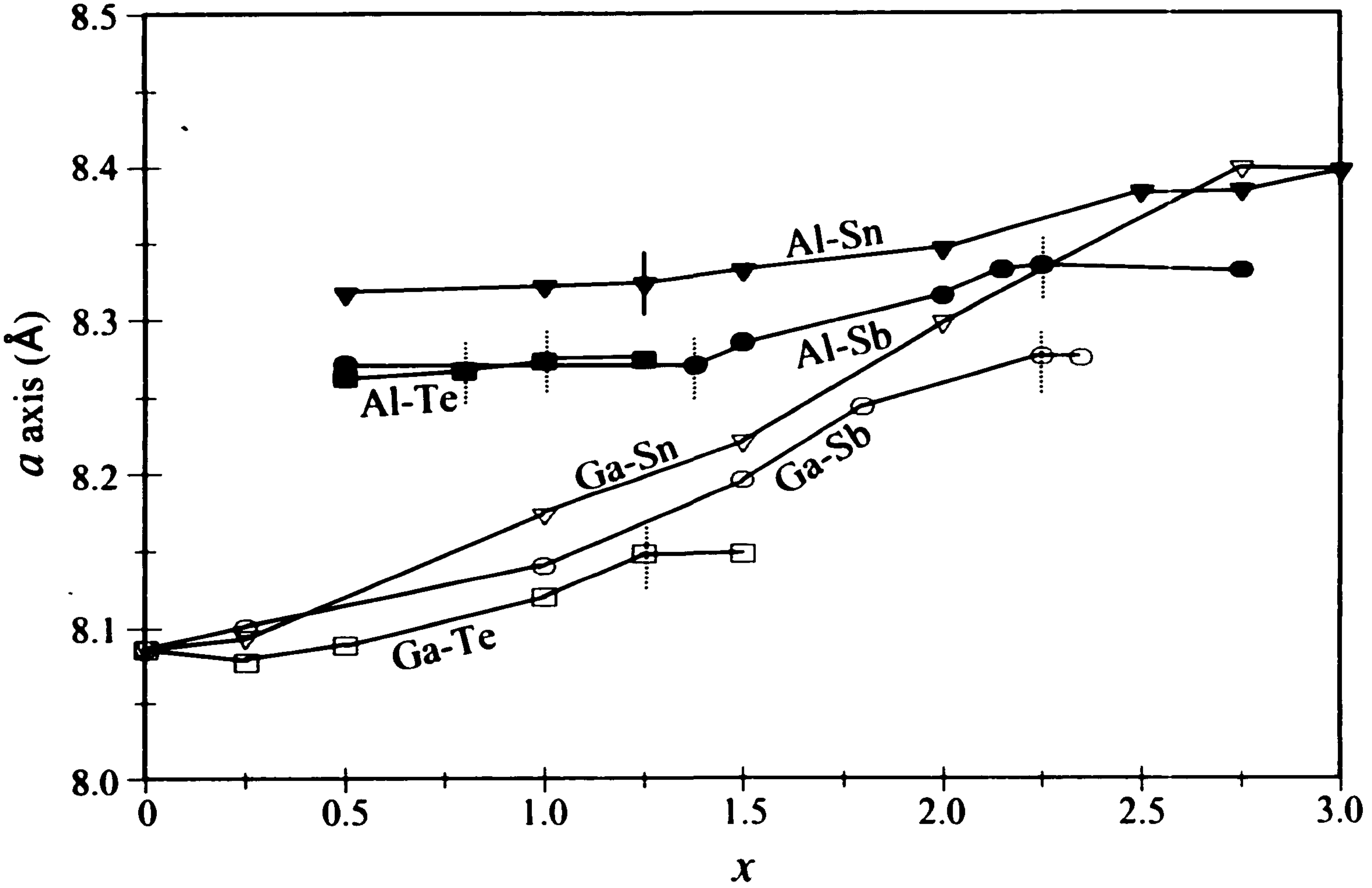

Figure 3. *a* axis versus *x* for $Sc_5B_{3-x}B'_x$. Shaded and open symbols represent Al and Ga systems, respectively. Vertical line indications are identical to Figure 1.

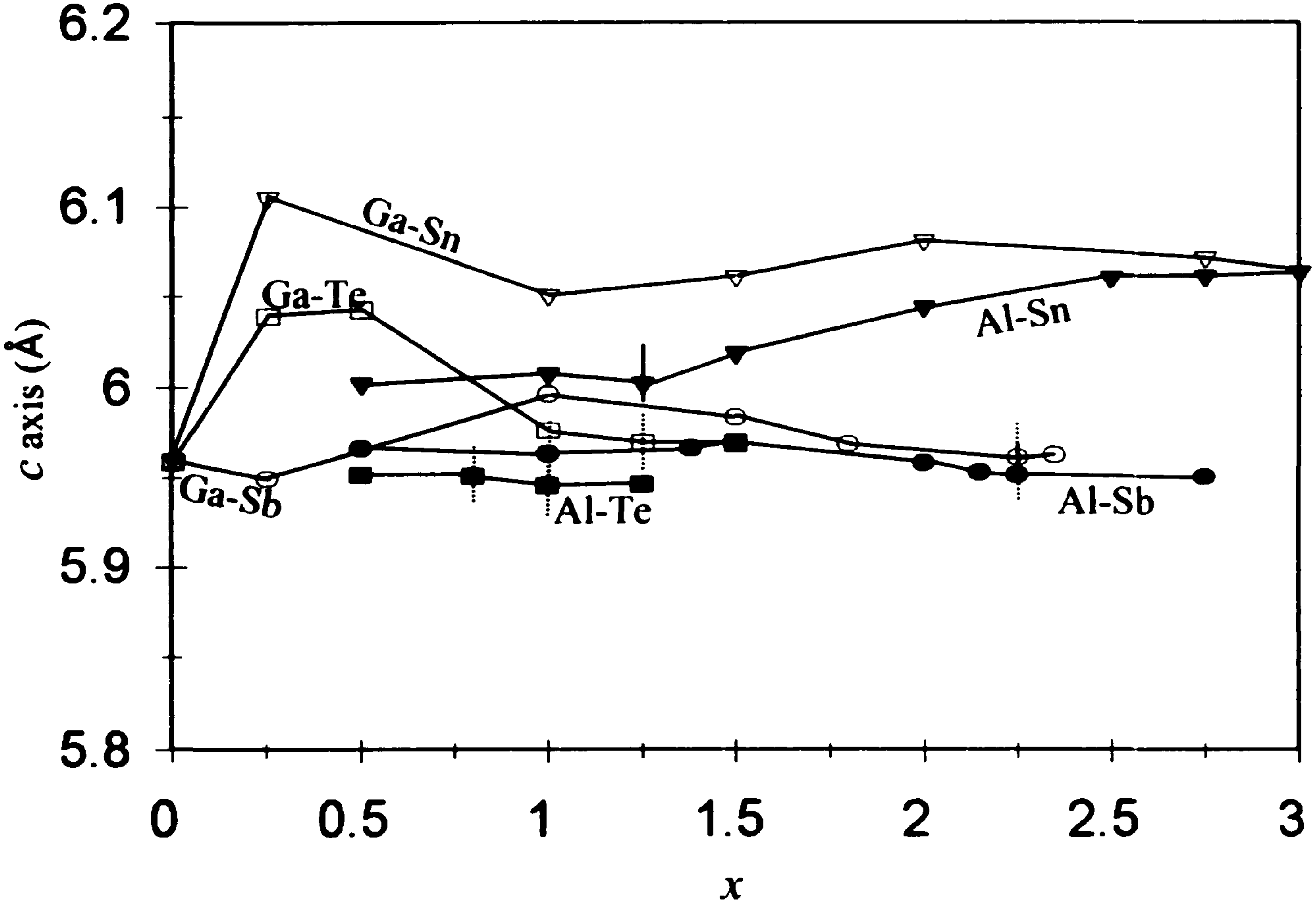

Figure 4. c axis versus x for $Sc_5B_{3-x}B'_x$. Shaded and open symbols represent Al and Ga systems, respectively. Vertical line indications are identical to Figure 1.

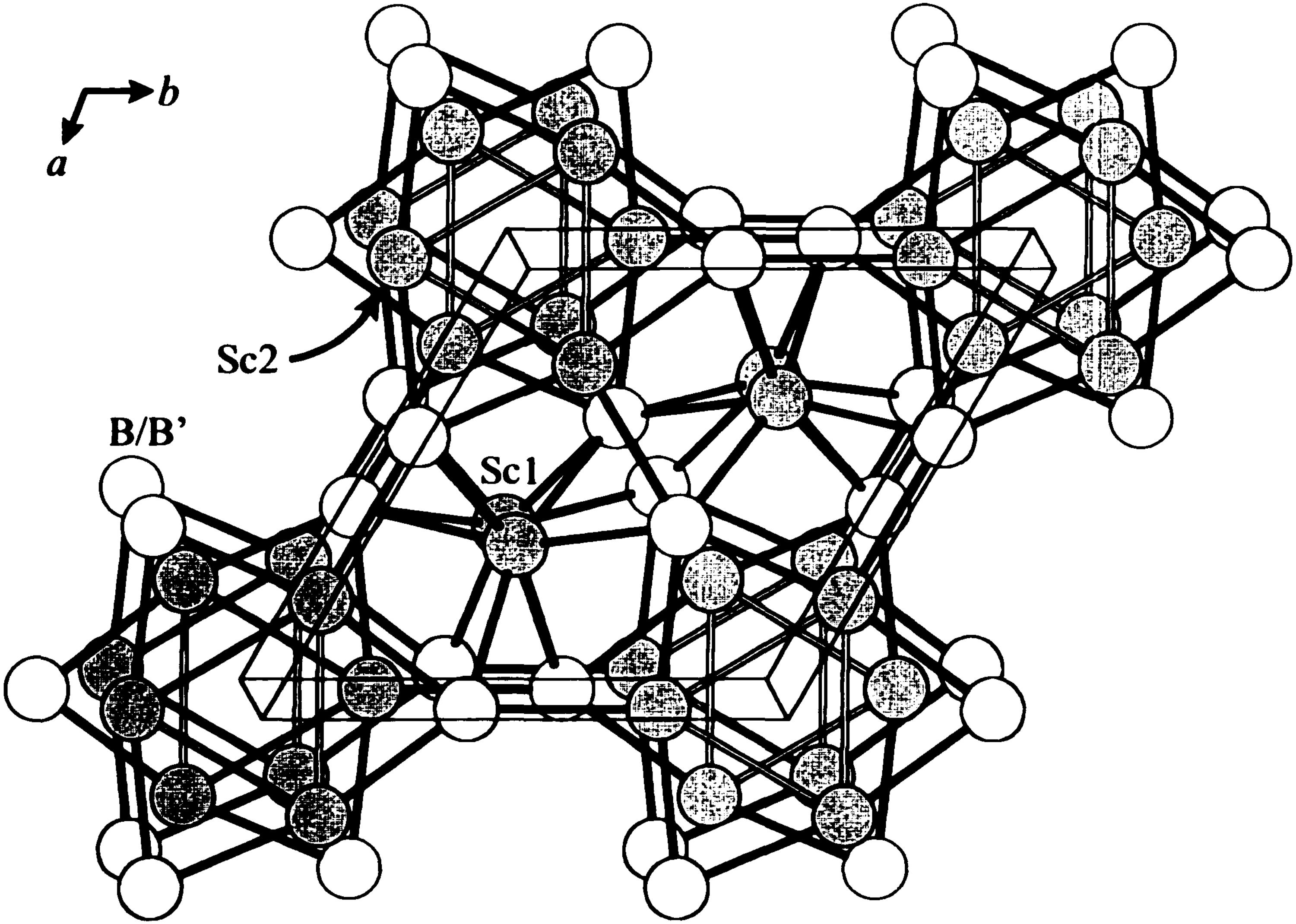

Figure 5. The unit cell of $Sc_5B_{3-x}B'_x$ (B = Al or Ga; B' = Sn, Sb or Te) viewed down [001].

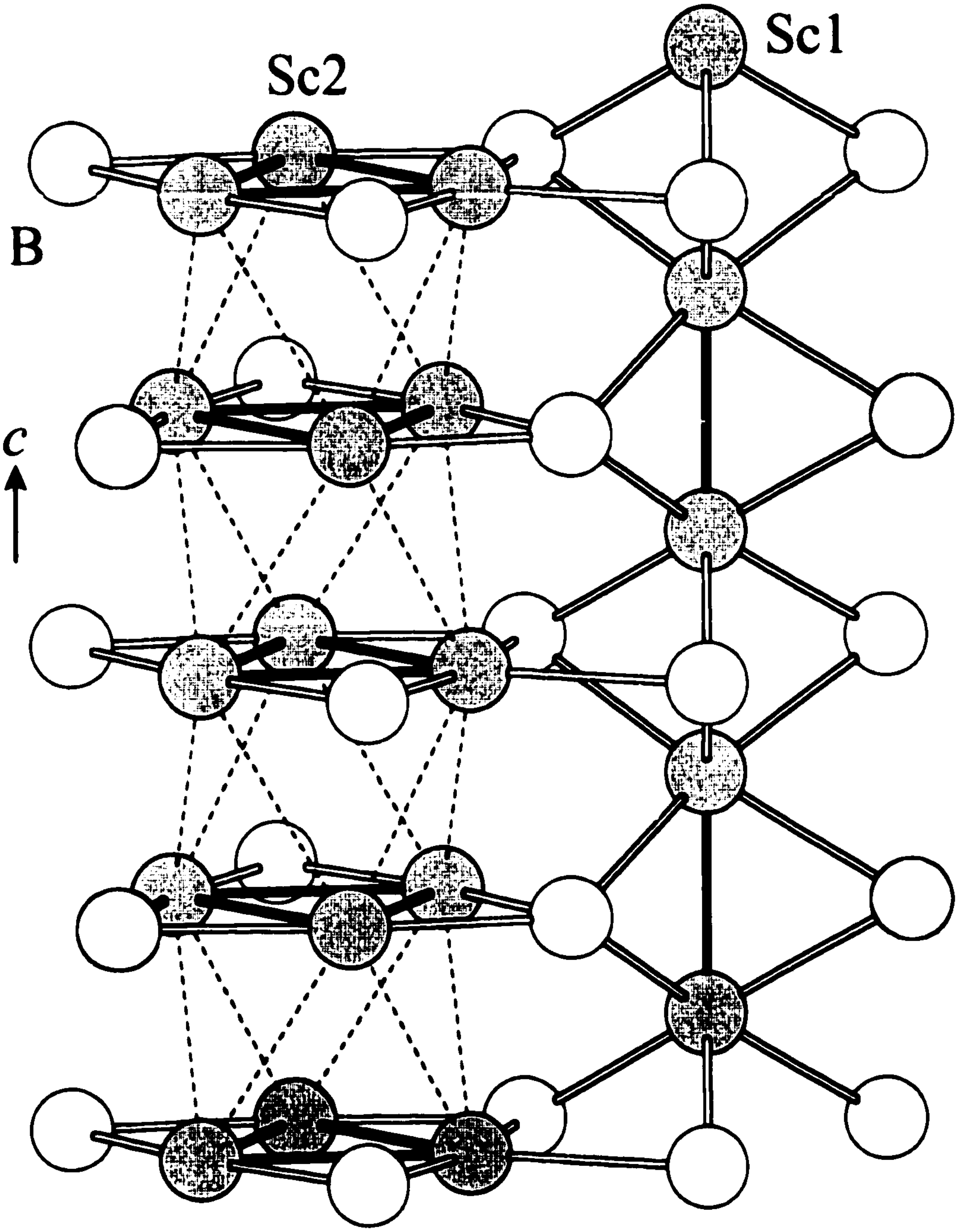

Figure 6. A view of $Sc_5B_{3-x}B'_x$ (Mn_5Si_3-type) along (110).

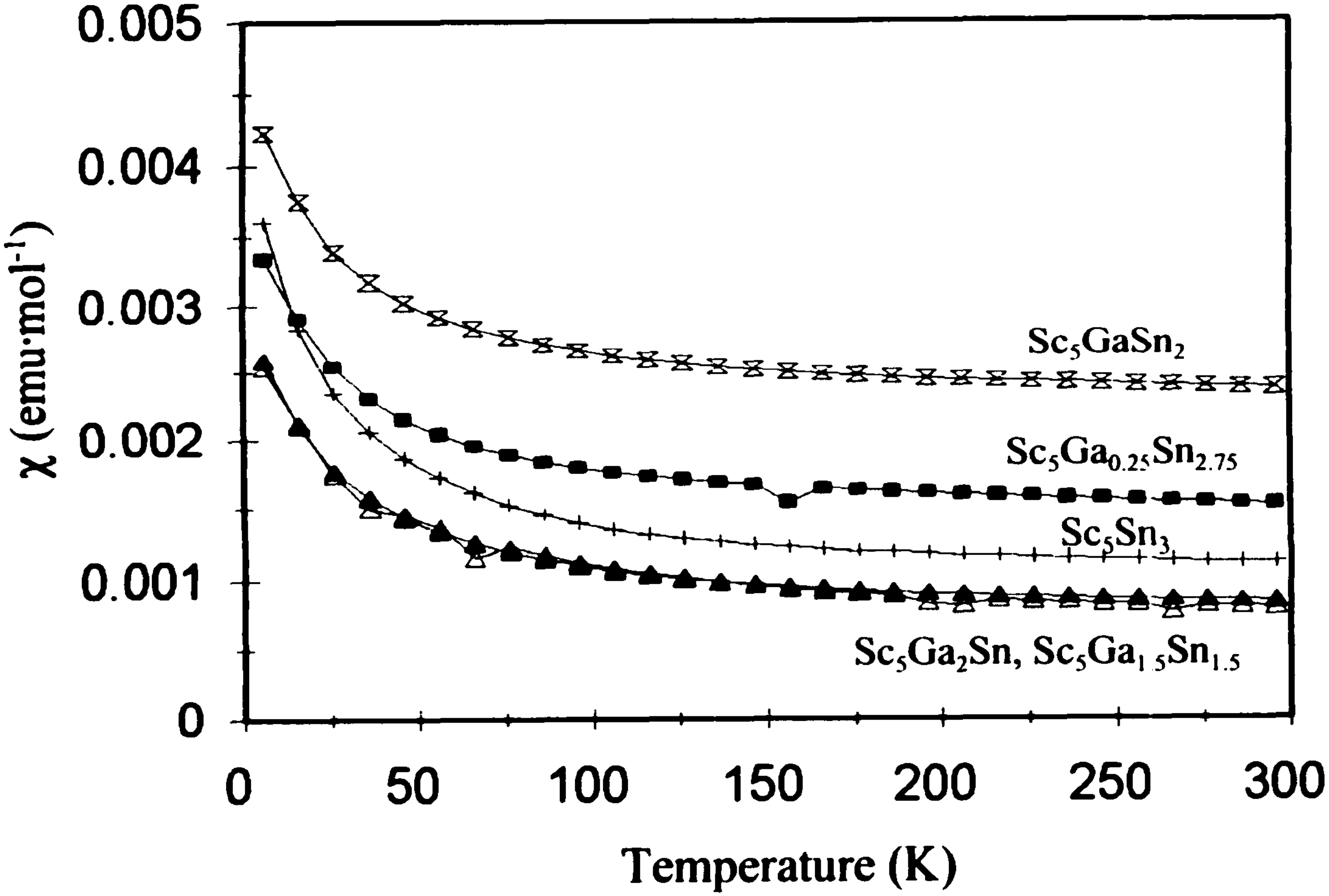

Figure 7. Magnetic susceptibility ((χ) versus Temperature (K) for the Sc$_5$Ga$_{3-x}$Sn$_x$ (1 ≤ x ≤ 3) Series of Compounds

CHAPTER 9. CONCLUSIONS

The chemistry of metal-rich compounds has evolved predominantly in one of two areas, the early transition metals (Sc, Y, Zr, Nb...) in combination with halides (I, Br, Cl) or the electron-richer transition metals (Ti, Nb, Zr...) in combination with chalcogenides (S, Se, Te). Compounds in the former category nearly always contain transition-metal chains or clusters, while those in the later usually comprise transition-metal layers or 3D-networks. These two solid state chemistry areas, the halides and chalcogenides, have usually been regarded as unrelated or at least treated separately in the literature, implying the absence of structural interrelationships or similar bonding principles. Furthermore, most of the earliest transition metals (Sc, Y, La) in combination with a halide require a main group or late-transition metal interstitial (C, O, N; Fe, Co, Ni) to stabilize the metal-metal bonding. From this, it might have been incorrectly concluded that the chalcogenides of the earliest transition-metals, compounds even electron poorer than the halides, could not exist, at least as binaries.

The work reported in this thesis has shown that metal-rich compounds containing the earliest transition metals, scandium and yttrium, in combination with a particular chalcogenide, tellurium, exist, and that they share many structural and bonding features relating to both electron-richer transition metal chalcogenides and halides. Sc_2Te was found to have double edge-sharing octahedral chains, similar to that found in Sc_7Cl_{10},[1] that could be also looked upon as a dissociation product of electron-richer frameworks. Then two of these double octahedral chains were found condensed together in a so-called Z-type unit in the 2D Sc_8Te_3 structure, which revealed more direct relationships to the electron-richer and more 3D metal-bonded $Ti_8(S,Se)_3$[2,3] compounds. Cooperative matrix effects and bonding effects, or the interplay of anion size, valence electron concentration, and stoichiometry were found to influence metal-framework dimensionality. The metal-richest compound reported here, Sc_9Te_2, shows a rare example of what is the widely predicted normal predisposition for low-dimensionally bonded structures, i.e. a metal-lattice modulation arising from the differentiation of internal and external metal-metal bond orders. Similar metal displacements in Y_8Te_3 have not been identified with an ordered arrangement.

Beyond this binary chemistry are the interesting ternary compounds containing manganese, iron, cobalt, nickel or aluminum (and even some hydrogen). One need but scratch the surface of ternary systems and come up with a handful of new compounds. These third elements stabilized two new metal-bonded isomers, $Sc_5Ni_2Te_2$ and $Y_5(Fe,Co,Ni)_2Te_2$, with a 1D Sc_5Ni_2 double chain and 2D Y_5Ni_2 layer, respectively. They both may be derived from the condensation of 1D metal-units in Gd_3MnI_3,[4] while the scandium example is also isostructural to the 3D metal-bonded structure of $Hf_5Co_{1-x}P_{3-x}$.[5] Only the $Y_5Ni_2Te_2$ example was (accidentally) found to take up hydrogen, which showed the way to a new compound containing buckled Y-Ni layers. The $Sc_5B_{3-x}B'_x$ (B = Al or Ga; B" = Sn, Sb or Te) phases passed beyond imagination at the time. Despite the fact that neither Sc_5Al_3 or Sc_5Te_3 was known, trial substitutions of aluminum for scandium in the metal-rich phases found $Sc_5Al_{3-x}Te_x$ with a narrow composition range. Slipping through this small crack, a new mixed B-site substitution chemistry was found for the Mn_5Si_3 structure type, in an area that currently defies boundaries and chemical sensibility. All the examples above show that what is possible chemically is sometimes beyond prediction or imagination, and the only way to find to new chemistry is to make it.

Attempted reactions, unresolved problems, and future work. In the search for new metal-metal bonding motifs in this emerging area, a few additional systems were tested for unknown or isostructural metal-rich phases. A few metal-rich compositions in the Sc-Se and La-S binary systems were reacted by arc-melting but produced only simple binaries and metal. Also, the Y-Te system was explored through arc-melting reactions, producing only Y_8Te_3, but more phases may be possible here via reactions at lower temperatures. The (Sc or Y)-C-Te systems were tested through arc-melting, producing a few unidentified phases but no large single crystals for X-ray diffraction. Lastly, preliminary lattice constant evidence suggests that aluminum substitution for tellurium in Sc_2Te, Sc_8Te_3 and Sc_9Te_2 is possible to a large extent.

Two unresolved problems included in the appendices are the disordered crystal structure solution for Y_8Te_3, and a few new ScTe polytypes for which ED may be more appropriate for full characterization. Beyond these unresolved problems however, new synthetic chemistry is very wide open among the earliest transition-metal chalcogenide systems. Even now, research colleagues have shown that similar metal-rich chemistry is possible for probably most of the lanthanides as well.[6] The best and easiest immediate prospects would probably include a) the *completely* unexplored R-M-Te ® = Rare earth; M = late-transition metal) ternary realms, which is most assuredly full of undiscovered treasures, b) new metal-rich compounds through the substitution of Al or Ga for Te (or vice versa), c) hydrogen absorption studies in the ternary compounds with late transition metals, d) extension of similar binary chemistry to the rare-earth metal selenides or calcium chalcogenides (much more difficult tasks), and e) mixed early-transition-metal quasi-binaries. A fuller and detailed map of the new chemistry possible is like charting the ocean from shorelines, new chemistry waits to be uncovered for anyone who cares to cast in their line or to dive deep.

References

(1) Poeppelmeier, K.R.; Corbett, J.D. *Inorg. Chem.* **1977**, *16*, 1107.

(2) Owens, J.P.; Franzen, H.F. *Acta Crystallogr.* **1974**, *B30*, 427.

(3) Weirich, T.E.; Pöttgen, R.; Simon, A. *Z. Kristallogr.* **1996**, *211*, 929.

(4) Kleinke, H.; Franzen, H.F. *J. Alloys Compd.* **1996**, *238*, 68; Kleinke, H.; Franzen, H.F. *J. Alloys Compd.* **1997**, *255*, 110.

(5) Ebihara, M.; Martin, J.D.; Corbett, J.D. *Inorg. Chem.* **1994**, *33*, 2078.

(6) Herle, S.; Corbett, J.D. Unpublished results.

APPENDIX A. THE X-RAY STRUCTURE SOLUTION OF Y_8Te_3

A paper prepared for submission to Inorganic Chemistry

Paul A. Maggard and John D. Corbett

Department of Chemistry, Iowa State University, Ames, IA 50011

Abstract

Y_8Te_3 was synthesized by high-temperature solid-state techniques and characterized at 23 °C by single crystal X-ray diffraction to be monoclinic *C2/m* (No. 12, Z = 4) with *a* = 31.173(5) Å, *b* = 4.0697(6) Å, *c* = 24.394(4) Å, and *β* = 122.749(3)°. Y_8Te_3 is nominally isotypic with Sc_8Te_3, consisting of corrugated sheets of early-transition metal comprising a complex network of trans-edge-sharing metal octahedral and square pyramidal chains separated by well-spaced tellurium neighbors. Within one yttrium chain, three metal positions show exaggerated thermal displacement parameters. No superstructure or lower-symmetry solution could be found, which prompted an additional data set collection at - 100 °C with *a* = 31.131(5) Å, *b* = 4.0689(7) Å, *c* = 24.351(4) Å, and *β* = 122.728(3)°. The X-ray structure solutions suggest disorder inside one of the yttrium cluster chains, similar to that for Sc_9Te_2, which is known to have similar distended ellipsoids (in the subcell) arising from a metal-lattice modulation.

Introduction

As has been known and described for scandium-rich compounds of the tellurides,[1-3] are unique differences compared to their later-transition metal progenitors. Reduction in dimensionality, greater matrix effects, and new metal clusters and chains represent a few changing features of this chemistry found in the binary and ternary scandium tellurides. A recent discovery for these low-dimensional metallic compounds, revealed in Sc_9Te_2,[3] has been symmetry-lowering via metal-lattice modulations and a more prominent delineation of internal and external metal overlap populations, as compared to undistorted models in the Ti_9Se_2 type. The detection of this supercell and ordered solution was elicited by apparent extreme displacement parameters in Sc_9Te_2. Y_8Te_3 parallels Sc_9Te_2 among these metal-rich compounds, showing extreme displacement parameters on similar internal metal positions. The synthesis and property measurements for Y_8Te_3 have been reported,[2] but with no fine structural details. The results of two x-ray single crystal refinements and the search for an ordered solution of Y_8Te_3 is discussed and juxtaposed with Sc_9Te_2.

Experimental

Synthesis. Synthesis of Y_8Te_3 began with the preparation of Y_2Te_3 (NaCl-type with disordered cation vacancies) from reaction of the elements (Y sheet, 99.8%, Alfa; Te powder, 99.99%, Aldrich) inside fused-silica tubing. Arc-melting and annealing a pressed-pellet containing Y and Y_2Te_3, with the composition Y_8Te_3, resulted in ≥95% yield of product according to X-ray powder diffraction. The arc-melted button was annealed inside tantalum and fused-silica containers at 1150°C for 3 - 4 days, and single crystals obtained therefrom. Higher annealing temperatures or longer reaction times resulted in complete decomposition of the product.

Single-Crystal Diffraction. Several black and irregularly shaped crystals were obtained from reactions loaded Y_8Te_3. Crystal qualities were checked with Laue photographs, and the best crystal was taken for a data set collection on a Bruker CCD diffractometer operating at room temperature with Mo Kα_1 radiation. A set of ninety reflection frames with 30-s exposures were collected and analyzed to determine provisional lattice constants and crystal orientation. The indexing gave a monoclinic unit cell with a = 31.173(5) Å, b = 4.0697(6) Å, c = 24.394(4) and β = 122.749(3)°. One full sphere of reflections was collected to $2\theta \sim 56°$, using a total of 1,818 CCD frames. After data collection, several hundred of the reflection frames were examined visually as well as integrated to search for unindexed reflections, but none were found. Integration and filtering of the CCD frames was performed by SAINTPLUS.[4] Out of 6399 possible reflections, 2292 were observed ($I \geq 2\sigma$) and unique. An absorption correction was applied using SADABS.[5] Extinction conditions suggested the possible space groups *C2/m*, *C2*, and *Cm*. Intensity distribution statistics favored the centric space group, and the structure was refined in *C2/m*. Single crystal X-ray data collection and refinement parameters are shown in Table 1. The refinement converged at $R1/wR2$ = 0.059/0.149 against F^2 ($I \geq 2\sigma$). The final positional, isotropic and anisotropic thermal parameters are located in Tables 2 and 3. A few exaggerated thermal ellipsoids are apparent for Y9, Y13 and Y15. Structure solutions attempted in *C2*, *Cm*, *P2/m*, *P2*, *Pm*, *P-1*, and *P1* in the centered and primitive unit cell settings did not result in less exaggerated atomic displacement parameters.

To help determine if the elongated displacement ellipsoids were temperature-dependent, a second data set was taken on the Bruker CCD diffractometer operating at -100°C. Data collection and analysis procedures are identical to those given above, Table 1. Indexing found a monoclinic unit cell with a = 31.131(5) Å, b = 4.0689(7) Å, c = 24.351(4) and β = 122.728(3)°. Several hundred of the CCD frames were examined visually as well as integrated to search for extra reflections. A few reflections found indicated a possible doubling for h, k, and l. Integration of all the CCD frames (1,818) found less than 1% of these reflections were observed, indicating either no real superstructure or an extremely weak one. The solution was refined in *C2/m*, and the final positional and thermal parameters are given in Tables 2 and 3 (the second line). For this second data collection, the extended ellipsoids for Y9, Y13 and Y15 are still apparent with little change in magnitude or direction. Again, solutions attempted in *C2*, *Cm*, *P2/m*, *P2*, *Pm*, *P-1*, and *P1* in the centered and primitive unit cell settings did not result in less exaggerated atomic displacement parameters. Also, modeling the disorder as split positions for Y9, Y13 and Y15 did not attenuate the thermal ellipsoid problems.

The solutions to the data sets given in tables 2 and 3 are taken as currently the most accurate representation of the structure. A complete listing of interatomic distances out to 4.0 Å is given in Table 4 (296K) and Table 5 (173K).

Results and Discussion

Structural Description. Y_8Te_3 (and also Sc_8Te_3) has the Ti_8S_3[6] structure type. Sc_8Te_3 has been described in some detail, which contained general comments about Y_8Te_3 having 0.25-0.40Å (10%) longer metal-metal distances and expanded lattice constants, with comparable bonding trends and features. These general observations are confirmed by this x-ray structure solution.

A near-[010] projection of the Y_8Te_3 structure (99.9% thermal ellipsoids) is shown in Figure 1, with the Y-Y bond distance limit set at 3.85 Å. All atoms repeat down the short *b* axis, 4.07 Å, in projection and the metal atoms are condensed along *a* into two partially separated and corrugated metal sheets. The corrugated metal sheets stack ABAB down *c*, demarcated by tellurium atoms. The two shortest intersheet distances are labeled at 3.75 Å and 3.79 Å for Y3-Y4 and Y10-Y14, but these are known to be typically weak metal-metal interactions because of tellurium near neighbors.[2]

The two corrugated yttrium sheets are given in Figure 2 (A and B) separately. The structural units and metal distances follow the same basic trends as in Sc_8Te_3, and are given a briefer description here. The corrugated sheet in Figure 2A shows two main yttrium units, an infinite trans-edge-sharing chain of single octahedra (Y5 and Y6) and four infinite trans-edge-sharing chains of octahedra condensed through the sharing of six edges (Y3, Y9, Y11, Y13, and Y15), called the Z unit. The single edge-sharing octahedral chain has the shortest distance on the shared edge for Y5-Y5 at 3.43 Å and longer apex distances for the nonshared edges, Y5-Y6 at 3.53 Å and 3.62 Å. The vertex-vertex distance, Y6-Y6, is significantly larger at > 4.0 Å. Similarly, the Z unit has the shortest distances on the shared edges of different octahedral chains, Y15–Y15 at 3.19 Å and Y15–Y13 at 3.48 Å, and longer distances among the external (peripheral) and inside trans-edges of the chains, 3.47-3.81 Å. The Z unit and the single octahedral chain are connected via a trans-edge-sharing chain of square pyramids, Y5–Y14 at 3.63 Å and Y9–Y14 at 3.58 Å.

The other, more condensed, corrugated sheet is shown in figure 2B. An analogous Z unit can be identified in the middle of the sheet (Y1, Y2, Y7, Y8 and Y10). As before, the shortest Y-Y distances occur on the shared edges of different octahedral chains, Y8-Y8 at 3.32 Å and Y8-Y10 at 3.41 Å, and longer yttrium distances along the periphery, 3.56–3.65 Å. The Z unit is then condensed on both ends via Y1-Y7 at 3.44 Å to strings of three infinite trans-edge-sharing octahedral chains sharing vertices. This string of three octahedral chains comprises two unique yttrium chains (Y1, Y7, Y12, Y16 and Y4, Y4, Y16, Y16). The central octahedral chain exclusively shares vertices with the neighboring octahedra, while the two end octahedral chains share a vertice and two edges. While the octahedral chains have similar metal distances on the shared edges down the short axis, Y16–Y16 at 3.55 Å and Y1-Y12 at 3.59 Å, they have dissimilar metal-distances on the periphery, Y4–Y16 at 3.45Å and 3.56Å compared to Y1-Y16 at 3.51 Å, Y12-Y16 at 3.73 Å, and Y7-Y12, 3.82 Å. Compared to Sc_8Te_3, Y_8Te_3 has a longer short axis but otherwise structurally similar octahedral chains along it.

Tellurium atoms within the structure are coordinated by a trigonal prism of yttrium, capped 1-3 times on their rectangular faces. Compared to Y-Y, the Y-Te distances are narrower in range at 3.1-3.3 Å. All Te-Te distances are ≥ 4.07Å, and Te-Te bonding is not evident.

Fine X-ray Structure Details. The structural description is not complete without mention of the problematic thermal displacement parameters for three yttrium positions, Y9, Y13 and Y15. These positions comprise most of the Z unit highlighted in the unit cell in Figure 3A, and shown projected horizontally, with 98% thermal ellipsoids. The internal Y15 position has electron density spread vertically, while the Y9 and Y13 positions have electron density exaggerated horizontally. This is similar in appearance to the apparent disorder first detected in Sc_9Te_2, shown in Figure 3B, for which an ordered atomic displacement pattern was found. The ordered version of Sc_9Te_2 has internal body-centered cube positions of scandium that alternate up and down along the short axis, while the scandium nearest neighbors alternated left and right down the short axis (indicated with arrows). A similar metal-lattice modulation down the short axis of the yttrium phase is suggested by the thermal displacement parameters, but no sign of order has been found. However, the metal features of both chains and the packings in their respective structures are different, and it is difficult to quantify how these effects would influence a metal-lattice modulation.

Conclusions. Y_8Te_3 is nominally isotypic with the Ti_8S_3 family of compounds, containing a complex network of trans-edge-sharing metal octahedral and square pyramidal chains condensed into 2D layers. The X-ray structure solutions suggest that the octahedral chains in one Z unit contain a disordered metal-lattice modulation on three internal yttrium positions. In Sc_9Te_2, an ordered solution was found, while for Y_8Te_3, no ordered solution could be.

Acknowledgements

We thank Ilia Guzei for help with the CCD diffractometer. This work was supported by the National Science Foundation, Solid State Chemistry, via Grants DMR-9510278 and DMR-9809850 and was carried out in the facilities of Ames Laboratory, U.S. Department of Energy.

References

(1) Maggard, P.A.; Corbett, J.D. *Angew. Chem., Int. Ed. Engl.* **1997**, *36*, 1974.

(2) Maggard, P.A.; Corbett, J.D. *Inorg. Chem.* **1998**, *37*, 814.

(3) Maggard, P.A.; Corbett, J.D. *J. Am. Chem. Soc.* **2000**, *122*, 838.

(4) *SAINTPLUS*; Bruker AXS, Inc.: Madison, WI, 1996.

(5) Sheldrick, G.M. *SHELXS-86*; Universität Göttingen: Germany, 1986.

(6) Owens, J.P.; Franzen, H.F. *Acta Crystallogr.* **1974**, *B30*, 427.

Table 1. Single Crystal X-ray Data Collection and Refinement Parameters for Y_8Te_3 (296K, 173K).

Formula weight, g mol^{-1}	1094.08
Space group, Z	$C2/m$ (No. 12), 4
Lattice parameters and cell volume	
a (Å)	31.173(5), 31.131(5)
b (Å)	4.0697(6), 4.0689(7)
c (Å)	24.394(4), 24.351(4)
β (deg.)	122.749(3), 122.728(2)
V (Å^3)	2602.8(7), 2594.9(8)
d_{calc} (g cm^{-3})	2.792, 2.801
μ (Mo K_α) (cm^{-1})	20.882, 20.946
Diffractometer	CCD-equipped Bruker AXS
Octants collected	±h, ±k, ±l
2θ-maximum (deg.)	56, 52
Independent Parameters	134
Processed Reflections	6399, 9682
Unique reflections	3330, 2917
Observed unique reflections (> 2σ)	2292, 2209
Residuals $R1$, $wR2$,[a] %	0.059, 0.149; 0.069, 0.179
Extinction coefficient	0.0013(1), 0.00010(5)

[a] $R1 = \Sigma||F_o| - |F_c||/\sum|F_o|$; $wR2 = [\sum w(F_o^2 - F_c^2)^2/\sum w(F_o^2)^2]^{1/2}$, $w = 1/(\sigma_F^2)^2$.

Table 2. Positional and Isotropic Thermal Parameters for Y_8Te_3 (1st line - 296K, 2nd line - 173K).

atom	x	z	B_{eq}(Å^2)
Te1	0.26055(5)	0.22026(7)	0.0080(3)
	0.26057(6)	0.22047(7)	0.0078(4)
Te2	0.89533(5)	0.81367(7)	0.0073(3)
	0.89539(6)	0.81359(7)	0.0070(4)
Te3	0.94314(5)	0.67628(7)	0.0080(3)
	0.94301(6)	0.67593(7)	0.0082(4)
Te4	0.57173(5)	0.69222(7)	0.0078(3)
	0.57188(6)	0.69192(8)	0.0081(4)
Te5	0.87118(5)	0.46947(8)	0.0148(4)
	0.87109(6)	0.46894(9)	0.0165(4)
Te6	0.13036(5)	0.02597(6)	0.0070(3)
	0.13035(6)	0.02587(7)	0.0075(4)
Y1	0.59000(8)	0.9102(1)	0.0083(4)
	0.58995(9)	0.9101(1)	0.0086(5)
Y2	0.71999(7)	0.1044(1)	0.0078(4)
	0.71997(9)	0.1044(1)	0.0081(5)
Y3	0.69698(8)	0.2479(1)	0.0101(5)
	0.69683(9)	0.2478(1)	0.0113(5)
Y4	0.58361(8)	0.0758(1)	0.0097(4)
	0.58364(9)	0.0760(1)	0.0096(5)
Y5	0.56454(8)	0.5553(1)	0.0091(4)
	0.56461(9)	0.5553(1)	0.0093(5)
Y6	0.98968(7)	0.5903(1)	0.0083(4)
	0.98983(9)	0.5902(1)	0.0087(5)
Y7	0.05893(8)	0.7800(1)	0.0082(4)
	0.05909(9)	0.7799(1)	0.0079(5)

Table 2. (continued)

Y8	0.20015(9)	0.9682(1)	0.0192(5)
	0.2002(1)	0.9683(1)	0.0177(6)
Y9	0.29219(8)	0.3669(1)	0.0158(5)
	0.2918(1)	0.3669(1)	0.0176(6)
Y10	0.32972(8)	0.1600(1)	0.0127(5)
	0.32990(9)	0.1602(1)	0.0129(6)
Y11	0.37051(8)	0.5663(1)	0.0114(5)
	0.37034(9)	0.5657(1)	0.0126(6)
Y12	0.45677(7)	0.7834(1)	0.0082(4)
	0.45679(9)	0.7834(1)	0.0081(5)
Y13	0.83391(8)	0.6577(1)	0.0209(6)
	0.8337(1)	0.6575(1)	0.0221(7)
Y14	0.84987(8)	0.3032(1)	0.0108(5)
	0.84971(9)	0.3035(1)	0.0116(6)
Y15	0.7611(1)	0.4589(2)	0.053(1)
	0.7611(1)	0.4591(3)	0.066(2)
Y16	0.01009(8)	0.9350(1)	0.0106(5)
	0.01019(9)	0.9353(1)	0.0110(5)

Table 3. Anisotropic Thermal Parameters for Y_8Te_3 (1st line - 296K, 2nd line - 173K).

atom	U11[a]	U22	U33	U13
Te1	0.0084(6)	0.0066(7)	0.0107(7)	0.0063(5)
	0.0086(8)	0.0056(8)	0.0159(8)	0.0111(7)
Te2	0.0068(6)	0.0066(7)	0.0094(6)	0.0050(5)
	0.0073(8)	0.0050(8)	0.0144(8)	0.0096(7)
Te3	0.0067(6)	0.0092(7)	0.0097(6)	0.0056(5)
	0.0079(8)	0.0082(8)	0.0148(8)	0.0103(7)
Te4	0.0073(6)	0.0073(7)	0.0098(6)	0.0052(5)
	0.0078(8)	0.0061(8)	0.0154(8)	0.0095(7)
Te5	0.0074(7)	0.0064(7)	0.0301(9)	0.0097(6)
	0.0098(9)	0.0065(9)	0.0381(1)	0.0163(8)
Te6	0.0069(6)	0.0071(7)	0.0083(6)	0.0050(5)
	0.0071(8)	0.0061(8)	0.0153(8)	0.0100(7)
Y1	0.0089(9)	0.009(1)	0.0092(9)	0.0065(8)
	0.010(1)	0.009(1)	0.013(1)	0.010(1)
Y2	0.0059(9)	0.007(1)	0.0093(9)	0.0032(7)
	0.008(1)	0.008(1)	0.014(1)	0.009(1)
Y3	0.0059(9)	0.006(1)	0.017(1)	0.0057(8)
	0.008(1)	0.008(1)	0.022(1)	0.011(1)
Y4	0.015(1)	0.007(1)	0.012(1)	0.0095(8)
	0.013(1)	0.008(1)	0.016(1)	0.014(1)
Y5	0.0078(9)	0.013(1)	0.0086(9)	0.0056(7)
	0.008(1)	0.013(1)	0.015(1)	0.011(1)
Y6	0.0065(9)	0.009(1)	0.009(1)	0.0042(8)
	0.009(1)	0.006(1)	0.0018(1)	0.012(1)
Y7	0.0092(9)	0.009(1)	0.0084(9)	0.0062(8)
	0.009(1)	0.007(1)	0.015(1)	0.011(1)

Table 3. (continued)

Y8	0.024(1)	0.019(1)	0.027(1)	0.022(1)
	0.021(1)	0.016(1)	0.032(2)	0.025(1)
Y9	0.0058(9)	0.034(2)	0.008(1)	0.0042(8)
	0.007(1)	0.038(2)	0.012(1)	0.008(1)
Y10	0.008(1)	0.018(1)	0.013(1)	0.0066(8)
	0.009(1)	0.017(1)	0.019(1)	0.012(1)
Y11	0.011(1)	0.010(1)	0.016(1)	0.0088(8)
	0.012(1)	0.008(1)	0.026(1)	0.016(1)
Y12	0.0078(9)	0.008(1)	0.011(1)	0.0060(8)
	0.007(1)	0.007(1)	0.017(1)	0.010(1)
Y13	0.008(1)	0.047(2)	0.010(1)	0.0062(8)
	0.006(1)	0.049(2)	0.017(1)	0.010(1)
Y14	0.0074(9)	0.006(1)	0.019(1)	0.0076(8)
	0.010(1)	0.005(1)	0.026(1)	0.014(1)
Y15	0.016(1)	0.034(2)	0.109(3)	0.035(2)
	0.022(2)	0.034(2)	0.152(5)	0.054(3)
Y16	0.0064(9)	0.019(1)	0.008(1)	0.0050(8)
	0.006(1)	0.019(1)	0.014(1)	0.009(1)

[a] U23 = U12 = 0.

Table 4. Interatomic Distances (< 4.0 Å) for Y_8Te_3 (296K).

Atom 1	Atom 2	Mult.	Distance
Te1	Y2	2x	3.140(2)
	Y3	2x	3.157(2)
	Y9		3.153(3)
	Y10		3.199(3)
	Y14	2x	3.145(2)
Te2	Y3	2x	3.162(2)
	Y4	2x	3.150(2)
	Y12	2x	3.144(2)
	Y13		3.203(3)
	Y16		3.178(2)
Te3	Y6		3.130(3)
	Y7		3.090(2)
	Y11	2x	3.146(2)
	Y12	2x	3.155(2)
	Y13		3.126(2)
Te4	Y5		3.223(3)
	Y6	2x	3.160(2)
	Y7	2x	3.132(2)
	Y10		3.232(3)
	Y14	2x	3.136(2)
Te5	Y5	2x	3.136(2)
	Y6		3.249(2)
Te5	Y9	2x	3.131(2)
	Y11	2x	3.126(2)
	Y15		3.298(3)
Te6	Y1	2x	3.139(2)
	Y2	2x	3.135(2)
	Y4	2x	3.108(2)
	Y8		3.167(3)
	Y16		3.159(2)
Y1	Te6	2x	3.139(2)
	Y7	2x	3.441(2)
	Y8	2x	3.560(3)
	Y10		3.720(3)
	Y12		3.594(3)
	Y16	2x	3.512(3)
Y2	Te1	2x	3.140(2)
	Te6	2x	3.135(2)
	Y3		3.935(3)
	Y4		3.918(3)
	Y8	2x	3.651(3)
	Y8		3.756(3)
	Y10	2x	3.558(2)

Table 4. (continued)

Y3	Te1	2x	3.157(2)
	Te2	2x	3.162(2)
	Y4		3.750(3)
	Y9	2x	3.471(2)
	Y13	2x	3.574(3)
Y4	Te2	2x	3.150(2)
	Te6	2x	3.108(2)
	Y2		3.918(3)
	Y3		3.750(3)
	Y16	2x	3.451(2)
	Y16	2x	3.561(2)
Y5	Te4		3.223(2)
	Te5	2x	3.136(2)
	Y5		3.425(4)
	Y6	2x	3.531(2)
	Y6	2x	3.623(2)
	Y9		3.792(3)
	Y14	2x	3.634(2)
Y6	Te3		3.130(3)
	Te4	2x	3.160(2)
	Te5		3.249(2)
	Y5	2x	3.531(2)
	Y5	2x	3.623(2)
Y6	Y7		3.908(3)
	Y11	2x	3.991(3)
Y7	Te3		3.090(2)
	Te4	2x	3.132(2)
	Y1	2x	3.441(2)
	Y6		3.908(3)
	Y10	2x	3.583(2)
	Y12	2x	3.818(3)
Y8	Te6		3.167(3)
	Y1	2x	3.560(3)
	Y2	2x	3.651(3)
	Y2		3.756(3)
	Y8	2x	3.315(4)
	Y10	2x	3.413(3)
Y9	Te1		3.153(3)
	Te5	2x	3.131(2)
	Y3	2x	3.471(2)
	Y5		3.792(3)
	Y13		3.642(3)
	Y14	2x	3.578(3)
	Y15	2x	3.532(4)

Table 4. (continued)

Y10	Te1		3.199(3)	Y13	Y11	2x	3.629(3)
	Te4		3.232(3)		Y12	2x	3.938(3)
	Y1		3.720(3)		Y15	2x	3.448(4)
	Y2	2x	3.558(2)				
	Y7	2x	3.583(2)	Y14	Te1	2x	3.145(2)
	Y8	2x	3.413(3)		Te4	2x	3.136(2)
	Y14	2x	3.790(3)		Y5	2x	3.634(2)
					Y9	2x	3.578(3)
Y11	Te3	2x	3.146(2)		Y10	2x	3.790(3)
	Te5	2x	3.126(2)				
	Y6	2x	3.991(3)	Y15	Te5		3.298(3)
	Y13	2x	3.629(3)		Y9	2x	3.532(4)
	Y15	2x	3.601(3)		Y11	2x	3.601(3)
	Y15		3.806(4)		Y11		3.806(4)
					Y13	2x	3.448(4)
Y12	Te2	2x	3.144(2)		Y15	2x	3.185(7)
	Te3	2x	3.155(2)				
	Y1		3.594(3)	Y16	Te2		3.178(2)
	Y7	2x	3.818(3)		Te6		3.159(2)
	Y13	2x	3.938(3)		Y1	2x	3.512(2)
	Y16	2x	3.731(3)		Y4	2x	3.451(2)
					Y4	2x	3.561(2)
Y13	Te2		3.203(3)		Y12	2x	3.731(3)
	Te3		3.126(2)		Y16		3.553(4)
	Y3	2x	3.574(3)				
	Y9		3.642(3)				

Table 5. Interatomic Distances (< 4.0 Å) for Y_8Te_3 (173K).

Atom 1	Atom 2	Mult.	Distance	Atom 1	Atom 2	Mult.	Distance
Te1	Y2	2x	3.138(2)	Te5	Y5	2x	3.126(2)
	Y3	2x	3.154(2)		Y6		3.253(3)
	Y9		3.149(3)		Y9	2x	3.125(2)
	Y10		3.200(3)		Y11	2x	3.122(2)
	Y14	2x	3.140(2)		Y15		3.300(4)
Te2	Y3	2x	3.158(2)	Te6	Y1	2x	3.137(2)
	Y4	2x	3.145(2)		Y2	2x	3.134(2)
	Y12	2x	3.139(2)		Y4	2x	3.108(2)
	Y13		3.202(3)		Y8		3.161(3)
	Y16		3.178(3)		Y16		3.152(3)
Te3	Y6		3.127(3)	Y1	Te6	2x	3.137(2)
	Y7		3.094(3)		Y7	2x	3.437(3)
	Y11	2x	3.146(2)		Y8	2x	3.558(3)
	Y12	2x	3.156(2)		Y10		3.710(3)
	Y13		3.181(3)		Y12		3.587(3)
					Y16	2x	3.512(3)
Te4	Y5		3.211(3)				
	Y6	2x	3.156(2)	Y2	Te1	2x	3.138(2)
	Y7	2x	3.132(2)		Te6	2x	3.134(2)
	Y10		3.227(3)		Y3		3.926(3)
	Y14	2x	3.133(2)		Y4		3.914(3)
					Y8	2x	3.650(3)

Table 5. (continued)

Y2	Y8		3.752(3)
	Y10	2x	3.559(3)
Y3	Te1	2x	3.154(2)
	Te2	2x	3.158(2)
	Y4		3.750(3)
	Y9	2x	3.468(3)
	Y13	2x	3.570(3)
Y4	Te2	2x	3.145(2)
	Te6	2x	3.108(2)
	Y2		3.914(3)
	Y3		3.750(3)
	Y16	2x	3.446(3)
	Y16	2x	3.555(3)
Y5	Te4		3.211(3)
	Te5	2x	3.126(2)
	Y5		3.425(5)
	Y6	2x	3.524(3)
	Y6	2x	3.615(3)
	Y9		3.794(4)
	Y14	2x	3.628(3)
Y6	Te3		3.127(3)
	Te4	2x	3.156(2)
	Te5		3.253(3)
Y6	Y5	2x	3.524(3)
	Y5	2x	3.615(3)
	Y7		3.902(3)
	Y11	2x	3.990(3)
Y7	Te3		3.094(3)
	Te4	2x	3.132(2)
	Y1	2x	3.437(3)
	Y6		3.902(3)
	Y10	2x	3.572(3)
	Y12	2x	3.818(3)
Y8	Te6		3.161(3)
	Y1	2x	3.558(3)
	Y2	2x	3.650(3)
	Y2		3.752(3)
	Y8	2x	3.313(4)
	Y10	2x	3.410(3)
Y9	Te1		3.149(3)
	Te5	2x	3.125(2)
	Y3	2x	3.468(3)
	Y5		3.794(4)
	Y13		3.624(4)
	Y14	2x	3.575(3)
	Y15	2x	3.522(5)

Table 5. (continued)

Y10	Te1		3.200(3)
	Te4		3.227(3)
	Y1		3.710(3)
	Y2	2x	3.559(3)
	Y7	2x	3.572(3)
	Y8	2x	3.410(3)
	Y14	2x	3.791(3)
Y11	Te3	2x	3.146(2)
	Te5	2x	3.122(2)
	Y6	2x	3.990(3)
	Y13	2x	3.632(3)
	Y15	2x	3.592(4)
	Y15		3.801(4)
Y12	Te2	2x	3.139(2)
	Te3	2x	3.156(2)
	Y1		3.587(3)
	Y7	2x	3.818(3)
	Y13	2x	3.939(3)
	Y16	2x	3.733(3)
Y13	Te2		3.202(3)
	Te3		3.181(3)
	Y3	2x	3.570(3)
	Y9		3.624(3)
Y13	Y11	2x	3.632(3)
	Y12	2x	3.939(3)
	Y15	2x	3.441(4)
Y14	Te1	2x	3.140(2)
	Te4	2x	3.133(2)
	Y5	2x	3.628(2)
	Y9	2x	3.575(3)
	Y10	2x	3.791(3)
Y15	Te5		3.300(4)
	Y9	2x	3.522(5)
	Y11	2x	3.592(4)
	Y11		3.801(4)
	Y13	2x	3.441(4)
	Y15	2x	3.177(8)
Y16	Te2		3.178(3)
	Te6		3.152(3)
	Y1	2x	3.512(3)
	Y4	2x	3.446(3)
	Y4	2x	3.555(3)
	Y12	2x	3.733(3)
	Y16		3.534(5)

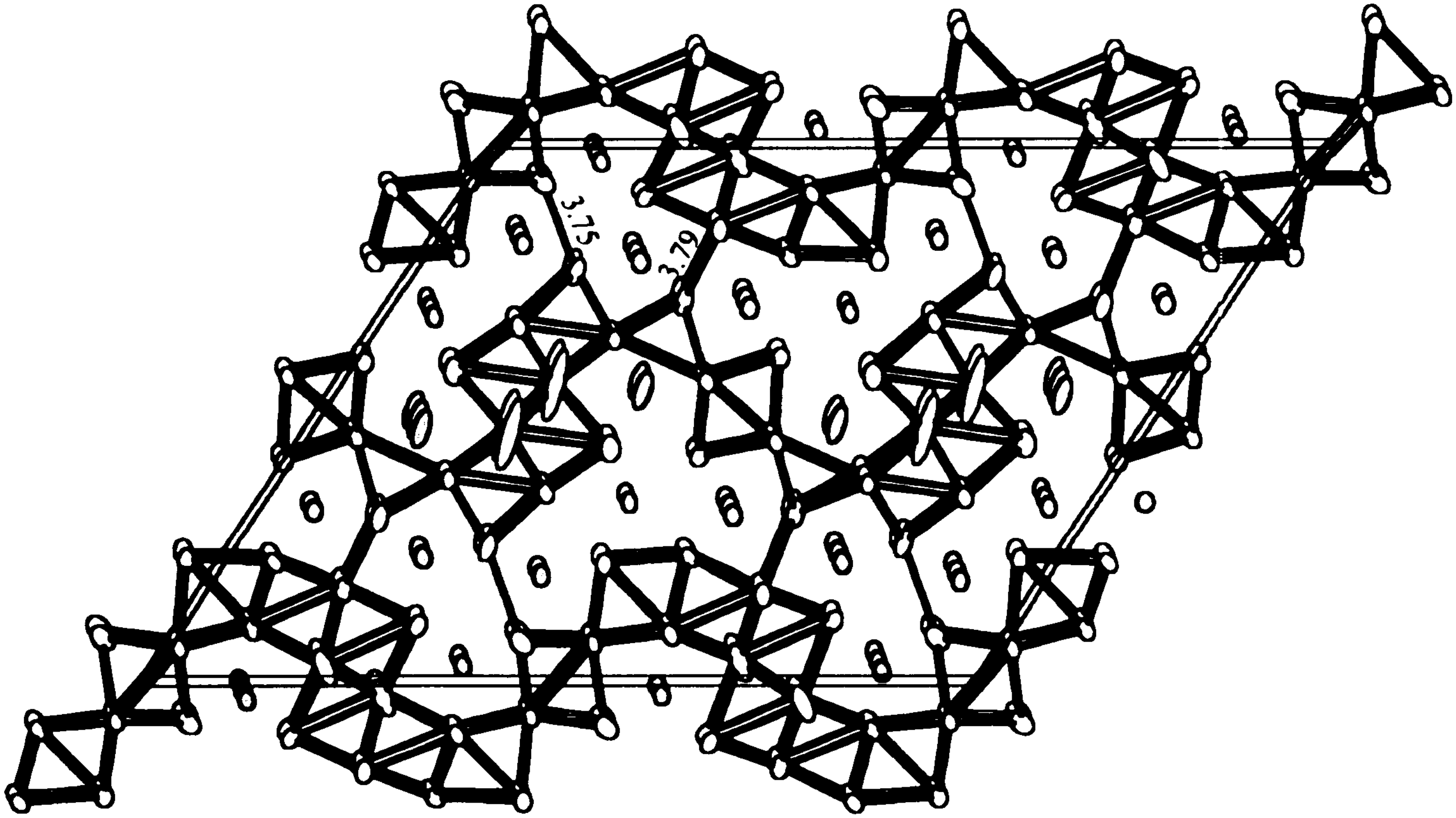

Figure 1. Near-[010] projection of the Y_8Te_3 unit cell (99.9% probability thermal ellipsoids) with bonds drawn for $d(Y-Y) \leq 3.85$Å. Intersheet distances marked in Å. Dark atoms are tellurium; light atoms, yttrium.

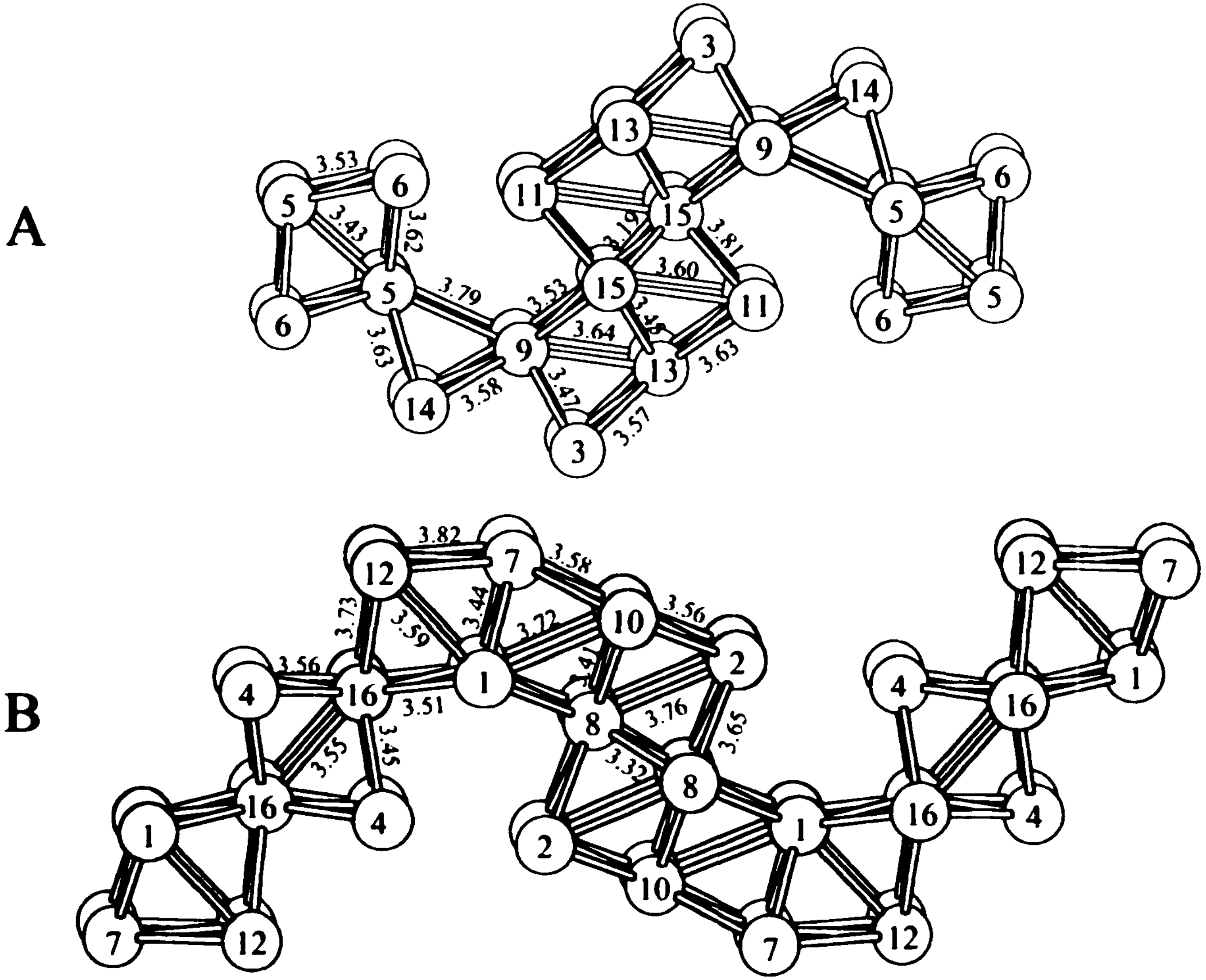

Figure 2. (A) Less-condensed corrugated sheet and (B) more condensed corrugated sheet in Y_8Te_3 with bond distances marked in Å. Two-fold rotation axes pass through the middle of bonds for Y5–Y5, Y8–Y8, Y15–Y15, and Y16–Y16.

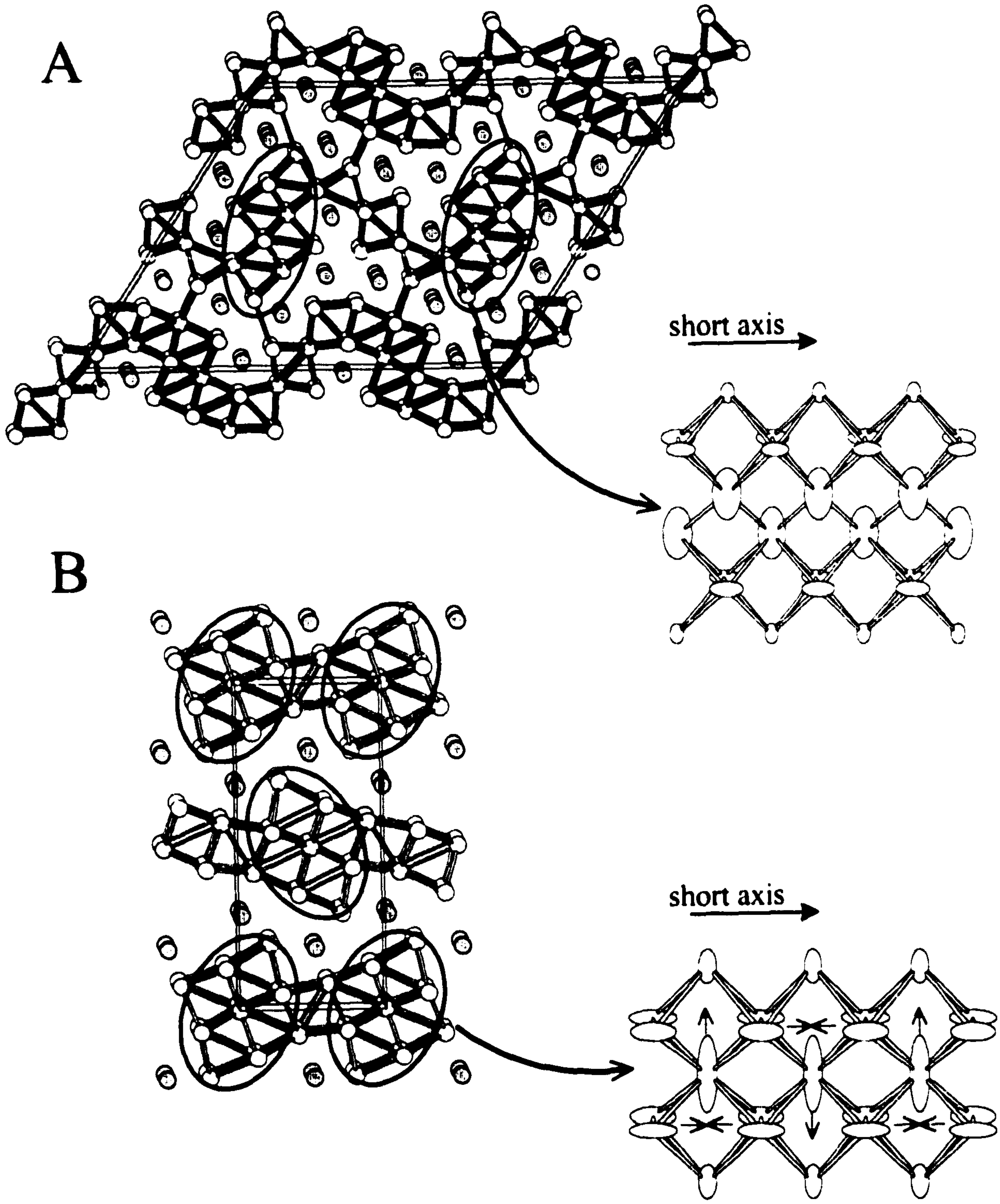

Figure 3. Comparison of the locations and directions of exaggerated thermal parameters found in (A) Y_8Te_3 and (B) the subcell of Sc_9Te_2. Circled are regions of disorder and in (B) the arrows mark the actual atomic displacement pattern.

APPENDIX B. SYNTHESIS AND STRUCTURE OF THE $Sc_{0.847(7)}Te$ AND $Sc_{0.69(3)-0.94(1)}Te$ COMPOUNDS

A paper prepared for submission to an Inorganic Chemistry

Paul A. Maggard and John D. Corbett

Department of Chemistry, Iowa State University, Ames, IA 50011

Abstract

$Sc_{0.847(7)}Te$ and $Sc_{0.69(3)-0.94(1)}Te$ were synthesized by high-temperature solid-state techniques and characterized at 23 °C by single crystal X-ray diffraction. $Sc_{0.847(7)}Te$ is rhombohedral *R-3m* (No. 166, $Z = 6$) with $a = 4.115(1)$ Å, $c = 30.300(6)$ Å and $V = 444.3(1)$ Å^3, while Sc_xTe is hexagonal *P-62m* (No. 187, $Z = 2$) with $a = 4.1121(4) - 4.1255(3)$ Å, $c = 6.752(1) - 6.7283(7)$ Å and $V = 98.87(2) - 99.17(1)$ for $0.69(3) \leq x \leq 0.94(1)$ respectively. $Sc_{0.847(7)}Te$ and $Sc_{0.69-0.94}Te$ are intermediate in composition between the known Sc_2Te_3 (defect NaCl-type) and ScTe (NiAs-type) compounds. The new $Sc_{0.847(7)}Te$ has tellurium layers that stack ABABCBCAC (or chh)$_3$, with scandium in all the octahedral interstices, except every third layer which is 54(2)% vacant. Crystals of this compound obtained only after arc-melting are obverse/reverse twinned, and upon annealing at ~ 900°C transform to $Sc_{0.69-0.94}Te$. Sc_xTe has hcp tellurium layers with scandium occupying a range of 69(3) - 94(1)% of all of the octahedral sites. The result is an unusual nonstoichiometric NiAs-related structure, which can also be synthesized by

a low-temperature reaction (500 -900°C) of scandium with Sc_2Te_3. The $Sc_{0.69-0.94}Te$ composition spans almost the entire range between the known Sc_2Te_3 and ScTe compounds.

Introduction

The search for new metal rich compounds in the Sc-Te system included the discovery of new binary compounds close to the 1:1 compositions. There are three scandium-telluride compounds reported with a Sc:Te ratio near 1: Sc_2Te_3,[1] ccp tellurium with scandium randomly occupying 2/3 of the octahedral sites (NaCl-type), ScTe,[2] hcp tellurium with scandium fully occupying the octahedral voids (NiAs-type), and $Sc_{2.3}Te_3$,[3] an intermediate containing both hcp and ccp tellurium regions, stacking as ABCACABCBCAB or $(cchh)_3$ with scandium occupying all octahedral sites, except that every other gallery is 1/3 empty. The structures Sc_2Te_3 and ScTe were determined from X-ray powder diffraction data on film, while the larger superstructure, $Sc_{2.3}Te_3$, was determined from X-ray single crystal data on film. The samples were prepared from reactions at 1000°C and 1050°C respectively, and their phase widths were not investigated. In this 2:3 to 1:1 composition region, different tellurium stackings evidently result from the small energy differences between the hcp and ccp alternatives. For comparison, the $Ti_{1-x}S$ system has approximately 15 polytypes which also differ in the sulfur stacking and titanium occupancies, and with repeating patterns of sometimes more than 100 layers.[4] Two new compounds were identified in the 2:3 to 1:1 Sc:Te composition region, $Sc_{0.847(7)}Te$ and $Sc_{0.69(3)-0.94(1)}Te$, and their single-crystal structure and synthesis are described herein that shows only the beginning details into the probably complex non-equilibrium chemistry of this area.

Experimental

Synthesis of $Sc_{0.847(7)}Te$. This began with the preparation of Sc_2Te_3 from elemental scandium and tellurium with purities as described before.[5] Appropriate amounts of Sc and Sc_2Te_3 to give the compositions $Sc_{2.0,\ 2.45,\ 2.7,\ 3.0}Te_3$ were pelletized inside a He-filled glovebox with the aid of a hydraulic press. The resulting pellets were then arc-melted for 20 s per side with a current of 60 amps. Guinier patterns of the products at this point revealed quantitative yields (> 95%) of $Sc_{0.847(7)}Te$ in the first three reactions, and a mixture containing mostly ScTe (NiAs) and a smaller amount of $Sc_{0.847(7)}Te$ in the last one. These and identically prepared samples were annealed in sealed tantalum tubing at 900 - 1100 °C for 24 - 72 hrs, and allowed to radiatively cool. After annealing, Guinier powder diffraction film data again revealed quantitative yield of the $Sc_{0.847(7)}Te$ phase in the first three reactions, and ScTe (NiAs) in the last.

Synthesis of Sc_xTe. This began with the preparation of Sc_2Te_3 from elemental scandium and tellurium with purities as described before.[5] Appropriate amounts of Sc and Sc_2Te_3 to give the compositions $Sc_{0.7,\ 0.8,\ 0.9,\ 1.0}Te$ were pelletized inside a He-filled glovebox with the aid of a hydraulic press. Pellets of these compositions were sealed inside tantalum and fused-silica tubing and heated to 1100 - 1300 °C for 2 - 14 days. Guiner patterns of the products at this point revealed a mixture of Sc_xTe and an unknown

(1 - 2 strong lines, in the same intensity proportions as Sc_xTe lines). ScTe (NiAs-type) was prepared by arc-melting a reaction loaded $Sc_{1.1}Te$ and annealing at 1000°C for 2 days. No samples simultaneously contained both the new Sc_xTe phase and either Sc_2Te_3 or ScTe. Reactions under non-equilibrium conditions, at lower temperatures of 500 - 800 °C and varied time durations, showed that the crystals grew as dendritic plates from the surface of the scandium metal. These same plates were scraped from the scandium metal surface, and Guinier powder diffractions revealed a similar mixture of Sc_xTe and the same unknown. Although light/dark areas from EDS probing suggested more than one phase was present, the lighter areas could never be synthesized as a separate phase.

Powder X-ray Diffraction. The powder diffraction patterns of $Sc_{0.847(7)}Te$ and $Sc_{0.69(3)-0.94(1)}Te$ were obtained with the aid of an Enraf-Nonius Guinier powder camera and monochromatic Cu $K\alpha_1$ radiation. The samples were crushed into powder form, mixed with standard silicon (NIST), and placed between two strips of Scotch-brand tape on a frame for mounting on the camera rotation motor. Lattice parameters were obtained by least squares from the measured and indexed lines in each sample. The lattice parameters for $Sc_{0.847(7)}Te$ and $Sc_{0.69(3)-0.94(1)}Te$ are given in Table 1 along with those for the other reported ~1:1 Sc:Te compounds.

Single Crystal Diffraction of $Sc_{0.847(7)}Te$. Several black, irregularly shaped crystals were obtained from a reaction loaded $Sc_{2.7}Te_3$ and mounted inside 0.3mm i.d. glass capillaries sealed off and attached to metal pins. Their crystal quality was checked by means of Laue photographs, and the best crystal from the group was selected for a data set collection on a Rigaku AFC6R (Mo Kα_1 radiation) diffractometer equipped with a rotating anode and operating at room temperature. Twenty five centered reflections gathered from a random search were used to determine provisional lattice constants and the crystal system. One-quarter of a sphere of data was collected (h, ±k, l), and these were subsequently corrected for Lorentz and polarization effects. The data were further corrected for absorption with the aid of three ψ-scans. Of 2226 measured reflections ($2\theta \leq 54°$), 779 had $I > 3\sigma(I)$, and 510 of these were unique. Observation conditions showed two classes of reflections, -h + k + l = 3n and h - k + l = 3n, characteristic of obverse/reverse twinning for a rhombohedral system. There were several possible space groups, of which only *R-6m* (No. 166) was found to result in a reasonable crystal structure solution. The structure was solved by direct methods and refined with obverse/reverse twinning using the SHELXTL^6 program. After anisotropic refinement, large displacement parameters suggested a reduced occupancy of the Sc3 site. The final refinement converged at $R1/wR2$ = 3.6/2.8 % for the composition $Sc_{0.847(7)}Te$, and a minor twin proportion of 0.30(9). Selected crystallographic data, atomic positions, temperature factors and interatomic distances are given in Tables 2 – 5.

Single Crystal Diffraction of $Sc_{0.69(3)-0.94(1)}Te$. Several plate-like crystals obtained from reactions loaded $Sc_{0.7-0.9}Te$ were mounted inside 0.3mm i.d. glass capillaries and attached to metal pins. Their crystal quality was checked by means of Laue photographs, and the best crystal of each group selected for a data set collection on a Rigaku AFC6R diffractometer equipped with a rotating anode and operating at room temperature.

Twenty-five centered reflections gathered from a random search were used to determine provisional lattice constants and crystal system. A search for additional reflections corresponding to the unknown powder diffraction lines, as noted in the synthesis section, was performed by scanning reciprocal axis directions for extra reflections, but none were found. One-quarter of a sphere of data was collected (h, ±k, l), and these were subsequently corrected for Lorentz and polarization effects. The data were further corrected for absorption with the aid of three averaged ψ scans. In the single crystal structure solution of $Sc_{0.89}Te$, there were 260 measured reflections ($2\theta \leq 56°$), 200 had $I > 3\sigma(I)$, and 199 of these were unique. Most single-crystal data sets showed $00l$ classes of reflections, usually 5 – 10 strong reflections, that reduced the symmetry from $P6_3/mmc$ (No. 194, NiAs-type) to $P\text{-}6m2$ (No. 187). However, ignoring these violations (incorrectly) would still allow refinements with agreeable R indices and thermal ellipsoids in the higher-symmetry $P6_3/mmc$ space group in the NiAs structure type. The structure was solved by direct methods (SHELXS[6]) and refined with the TEXSAN[7] package in $P\text{-}6m2$. Subsequent trial refinements in additional hexagonal space groups were unsuccessful. After anisotropic refinement, large displacement parameters suggested an occupancy refinement on the Sc site. The final refinement converged at $R/R_w = 2.2/2.6$ for the $Sc_{0.89(3)}Te$ composition. Additional data set collections on different crystals gave the compositions $Sc_{0.94(1),0.72(3),0.69(3)}Te$. Selected crystallographic data, atomic positions, temperature factors and interatomic distances are given in Tables 6 – 9.

Results and Discussion

Lattice Constants. Lattice constants of all known phases in the Sc_xTe ($2/3 \leq x \leq 1$) range are given in Table 1. Altogether, there are now five reported (equilibrium?) phases existing within this narrow composition. $Sc_{0.847(7)}Te$ has not shown a measurable phase width, and is known to be a metastable phase that converts to Sc_xTe upon annealing. Sc_xTe has a large phase width extending from $x = 2.1 - 2.8$. The lattice constant and phase width ranges are taken from products of reactions loaded $Sc_{0.7,0.8,0.9,1.0}Te$, but the end-points have been difficult to determine, as the composition spans almost the entire range from Sc_2Te_3 to ScTe, and there is always the presence of a suspicious impurity. The original study of ScTe (postulated NiAs-type) reported lattice constants and synthesis conditions more consistent with the Sc_xTe compounds here, and are within the same listed range in the Table. Experiments performed here give more accurately the lattice constants of stoichiometric ScTe (NiAs) with a larger *c* parameter.

An interesting trend in the last column of Table 1 is the average separation of the closest-packed tellurium layers, and the effect of increasing scandium concentration. The smallest tellurium spacing is for ccp Sc_2Te_3[1] at 3.121. Intermediate phases containing both hcp and ccp tellurium layers are $Sc_{2.3}Te_3$ ($Sc_{0.766}Te$), $Sc_{0.847(7)}Te$, and $Sc_{0.69(3)-0.94(1)}Te$ (Sc_xTe) at 3.383, 3.367, and 3.364 - 3.376 respectively. Lastly, the ScTe phase has the largest tellurium layer separation at 3.440. This trend of increasing tellurium layer separation is expected as scandium fills the octahedral sites, and is also accompanied by the transition from ccp to hcp tellurium. This trend from ccp to hcp tellurium packing is discussed below.

Structural Descriptions. A [001] and near-[010] view of $Sc_{0.847(7)}Te$ are given as A and B in Figure 1. The tellurium atoms stack ABABCBCAC, or $(chh)_3$, containing regions both cubic-close packed and hexagonal-close packed. Scandium atoms occupy all the octahedral sites between the layers, except for every third layer, which 54(2) % full. This scandium vacancy in every third layer occurs between the chh triple repeat units, on the Sc3 sites.

Nearest neighbor distances around each atom are given in Table 5. Te1 and Te3 are surrounded by a scandium octahedron, at 2.86 - 2.92 Å, while Te2 is coordinated in a scandium trigonal prism at 2.93 - 2.96 Å. Contrastingly, all three scandium positions are located in tellurium octahedra at 2.88 - 2.96 Å. This packing generates short scandium distances for Sc1 - Sc2 at 3.39(4)Å and Sc1 - Sc3 at 3.48(5) Å. The marginally shorter scandium distance occurs across regions of hcp tellurium (ABA or BCB), while the longer distance occurs within the region of ccp tellurium (ABC or BCA). This structure represents an intermediate between the ccp NaCl structure-type and the hcp NiAs structure-type, where the only difference is the coordination of scandium around tellurium. It is known in many metal and electron rich structures that tellurium prefers a scandium trigonal prismatic environment,[5,8-9] and it is not surprising to see this transition from ccp to hcp, or tellurium octahedral to trigonal prismatic scandium coordination.

A near-[010] view of the Sc_xTe ($0.69 \leq x \leq 0.94$) unit cell is shown in Figure 2. Tellurium is hcp as in the NiAs structure type. Scandium atoms occupy all the octahedral voids between the tellurium layers and are distorted towards one another into dimeric units. Each scandium site is from 69(3) - 94(1) % filled. This structure type converts to the NiAs structure by fixing the scandium z parameter at 1/4.

The interatomic distances for Sc_xTe are given in Table 9 for $x = 0.89$. Te1 and Te2 are surrounded by a scandium trigonal prism at 2.86 - 2.98 Å, while scandium has a tellurium octahedral environment also at 2.86 - 2.98 Å. The scandium displacement has resulted in short and long Sc - Sc distances at 3.17(1) and 3.58(1) Å. The stoichiometric ScTe (NiAs-type) structure has a uniform Sc - Sc distance of 3.44 Å down the *c* axis.

Conclusions. Two new binary compounds, $Sc_{0.847(7)}Te$ and $Sc_{0.69(3)-0.94(1)}Te$, have been synthesized. $Sc_{0.847(7)}Te$ contains hcp and ccp tellurium regions, with scandium occupying the octahedral sites, which are 54(2) % absent every third layer. Sc_xTe has hcp tellurium packing, with scandium occupying the octahedral sites from 69(3) - 94(1) %, or almost the entire range between the known Sc_2Te_3 and ScTe compounds. Both compounds are intermediate in composition between the 2:3 and 1:1 Sc:Te phases. Also, the lattice parameters for the previously reported ScTe (NiAs-type) are more consistent with the Sc_xTe phases than with the ScTe compound reported here.

Acknowledgements

The authors would like to thank R. Jacobson for provision of diffractometer time. This research was supported by the National Science Foundation, Solid State Chemistry, via grants DMR-9510278 and DMR-9809850, and was carried out in the facilities of Ames Laboratory, U.S. Department of Energy.

References

(1) Menkov, A.A.; Komissarova, L.N.; Simanov, Yu.P.; Spitsyn, V.I. *Proc. Acad. Sci. USSR, Chem. Sect.*, **1959**, *128*, 693.

(2) Menkov, A.A.; Komissarova, L.N.; Simanov, Yu.P.; Spitsyn, V.I. *Proc. Acad. Sci. USSR, Chem. Sect.*, **1961**, *141*, 1137.

(3) White, J.G.; Dismukes, J.P. *Inorg. Chem.* **1965**, *4*, 1760.

(4) Krishna, P. *Crystal Growth and Characterization of Polytype Structures*. Pergamon Press: Oxford, v. 7, 1982.

(5) Maggard, P.A.; Corbett, J.D. *Inorg. Chem.* **1998**, *37*, 814.

(6) Sheldrick, M. *SHELXS-86*; Universität Göttingen: Germany, 1986.

(7) *TEXSAN*, version 6.0; Molecular Structure Corp.: The Woodlands, TX, 1990.

(8) Maggard, P.A.; Corbett, J.D. *Angew. Chem., Int. Ed. Engl.* **1997**, *18*, 336.

(9) Maggard, P.A.; Corbett, J.D. *J. Am. Chem. Soc.* **2000**, *122*, 838.

Table 1. Lattice constants of Sc_xTe ($2/3 \le x \le 1$) reported binary phases.

Compound	a	c	V	Å / Te layer	Ref.
Sc_2Te_3 (NaCl)	5.405(5)	-	157.9(3)	3.121	1
$Sc_{2.3}Te_3$	4.109(4)	40.59(5)	593(1)	3.383	2
$Sc_{0.847}Te$	4.115(1)	30.300(6)	444(1)	3.367	
$Sc_{0.69\text{-}0.94}Te_3$[a]	4.1121(4) - 4.1255(3)	6.752(1) - 6.7283(7)	98.87(2) - 99.17(1)	3.364 - 3.376	
ScTe (NiAs)[b]	4.112(1)	6.879(3)	100.73(6)	3.440	

[a] The previously reported ScTe (NiAs) phase shows lattice parameters in the same range and synthesis more consistent with the Sc_xTe phases reported here: $a = 4.112(5)$, $c = 6.735(5)$.

[b] Lattice constants from Guiner powder diffraction refinements from experiments perfomed herein.

Table 2. Single Crystal X-ray Data Collection and Refinement Parameters for $Sc_{0.847(7)}Te$.

Formula weight, g mol^{-1}	496.99
Space group, Z	*R-3m* (No. 166), 6
d_{calc} (g cm^{-3})	5.160
μ (Mo K_{α}) (cm^{-1})	157.02
Diffractometer	Rigaku AFC6R
Octants collected	±h, k, ±l
2θ-maximum (deg.)	54
Independent Parameters	22
Processed Reflections	2226
Observed reflections (> 3σ)	779
Unique reflections	510
Residuals $R1$, w$R2$,[a] %	3.6; 2.8
Minor twin proportion (BASF parameter)	0.30(9)

[a] $R1 = \Sigma||F_o| - |F_c||/\sum|F_o|$; $wR2 = [\sum w(F_o^2 - F_c^2)^2/\sum w(F_o^2)^2]^{1/2}$, $w = 1/(\sigma_F^2)^2$.

Table 3. Positional and Isotropic Thermal Parameters for $Sc_{0.847(7)}Te$.

atom	x	y	z	$B_{eq}(Å^2)$
Te1	0	0	0.15296(3)	0.007(1)
Te2	2/3	1/3	0.2632(2)	0.0126(3)
Te3	1/3	2/3	0.37405(7)	0.013(1)
Sc1	0	0	0.4320(7)	0.015(1)
Sc2	1/3	2/3	0.2080(8)	0.008(2)
Sc3[a]	0	0	0.313(2)	0.012(6)

[a] Position occupancy: 0.54(2)%.

Table 4. Anisotropic Thermal Parameters for $Sc_{0.847(7)}Te$.

atom	U11[a]	U22	U33	U13
Te1	0.008(2)	0.008	0.007(3)	0.0038
Te2	0.0124(4)	0.0124	0.0132(5)	0.0062
Te3	0.012(2)	0.012	0.014(3)	0.0061
Sc1	0.0172(8)	0.0172	0.010(3)	0.0086
Sc2	0.009(2)	0.009	0.007(7)	0.004
Sc3	0.018(5)	0.018	0.01(1)	0.009

[a] U23 = U12 = 0

Table 5. Interatomic Distances (< 4.0 Å) for $Sc_{0.847(7)}Te$.

Atom 1	Atom 2	Mult.	Distance	Atom 1	Atom 2	Mult.	Distance
Te1	Sc1	3x	2.92(1)	Sc1	Te1	3x	2.92(1)
	Sc2	3x	2.92(1)		Te3	3x	2.96(2)
					Sc2		3.39(4)
Te2	Sc2	3x	2.88(2)		Sc3		3.48(5)
	Sc3	3x	2.86(2)				
				Sc2	Te1	3x	2.92(1)
Te3	Sc1	3x	2.93(2)		Te2	3x	2.88(2)
	Sc3	3x	2.96(2)		Sc1		3.39(4)
				Sc3	Te2	3x	2.86(2)
					Te3	3x	2.96(2)
					Sc1		3.48(5)

Table 6. Single Crystal X-ray Data Collection and Refinement Parameters for Sc_xTe phases, $x = 0.89$.

Formula weight, g mol^{-1}	169.86
Space group, Z	$P\text{-}62m$ (No. 187), $Z = 2$
d_{calc} (g cm^{-3})	5.687
μ (Mo K_α) (cm^{-1})	87.914
Diffractometer	Rigaku AFC6R
Octants collected	h, ±k, l
2θ-maximum (deg.)	56
Independent Parameters	9
Processed Reflections	260
Observed reflections (> 3σ)	200
Unique reflections	199
Residuals R, R_w,[a] %	2.2, 2.6

[a] $R = \Sigma||F_o| - |F_c||/\sum|F_o|$; $R_w = [\sum w(F_o^2 - F_c^2)^2/\sum w(F_o^2)^2]^{1/2}$, $w = 1/(\sigma_F^2)^2$.

Table 7. Positional and Isotropic Thermal Parameters for Sc_xTe, x = 0.94, 0.89, 0.72, 0.69.

atom	x	y	z	B_{eq}(Å^2)
Te1	0	0	0	0.67(2)
Te2	1/3	2/3	1/2	0.86(3)
Sc[a]	2/3	1/3	0.260(3) [b]0.257(1) 0.259(2) 0.271(2)	0.92(1)

[a] Position occupancy %: 0.94(1), 0.89(3), 0.72(3), 0.69(3), respectively.

[b] z parameters from additional single crystal data collections, as before.

Table 8. Anisotropic Thermal Parameters for Sc_xTe for x = 0.89.

atom	U11[a]	U22	U33	U12
Te1	0.0082(3)	0.0082	0.092(5)	0.0041
Te2	0.0113(4)	0.0114	0.0100(5)	0.0057
Sc	0.0138(1)	0.0138	0.0111(4)	0.0069

[a] U13 = U23 = 0

Table 9. Interatomic Distances (< 4.0 Å) for $\mathrm{Sc}_x\mathrm{Te}$ for $x = 0.89$.

Atom 1	Atom 2	Mult.	Distance	Atom 1	Atom 2	Mult.	Distance
Te1	Sc1	6x	2.983(6)	Sc	Te1	3x	2.983(6)
					Te2	3x	2.863(7)
Te2	Sc1	6x	2.860(7)		Sc		3.17(1)
					Sc		3.58(1)

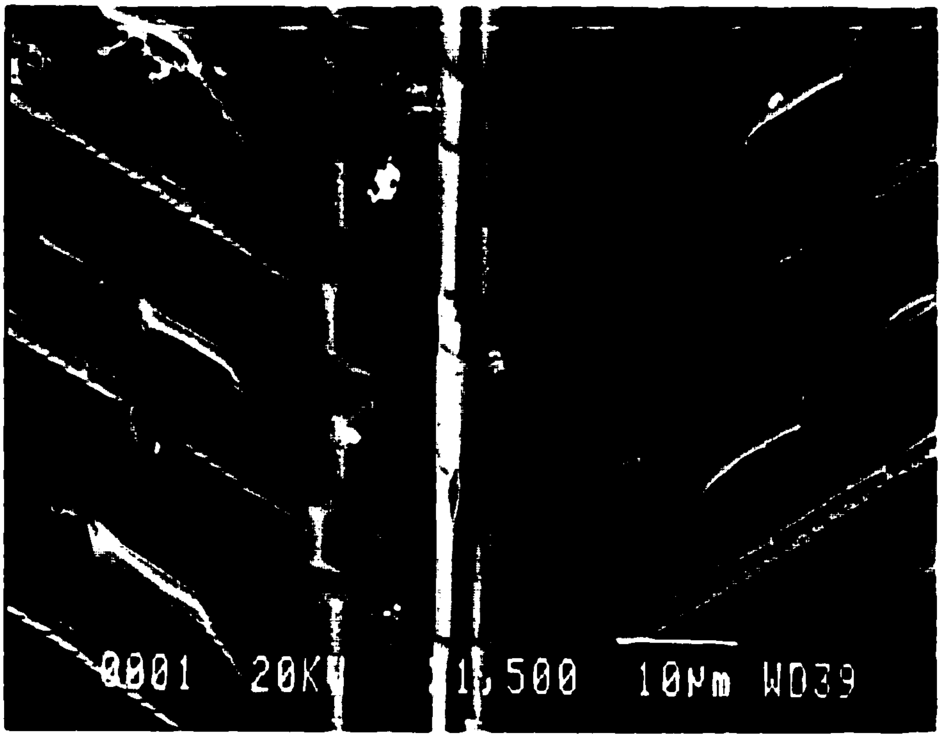

Figure 1. EDS picture of Sc$_x$Te.

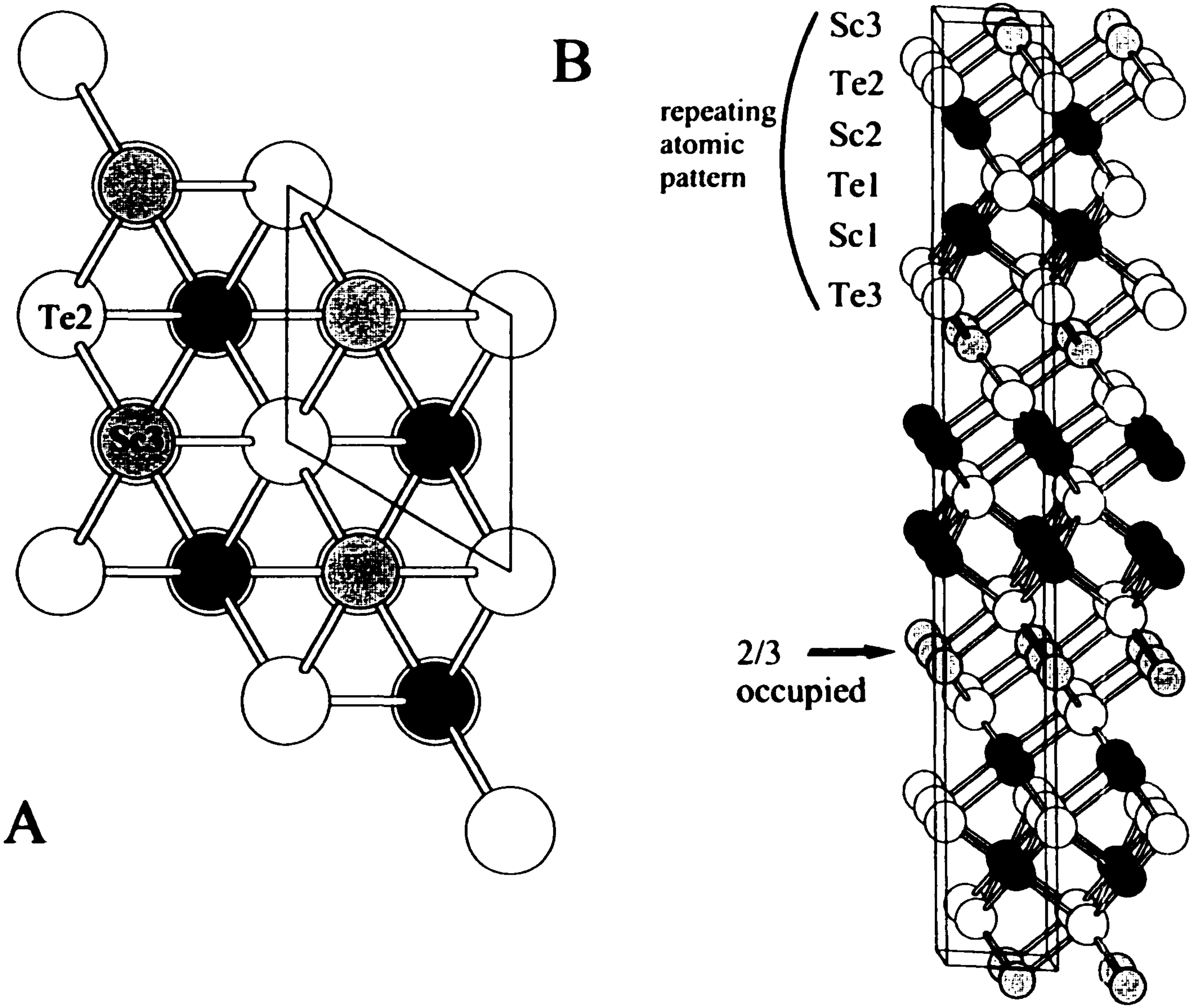

Figure 2. A [001] (A) and a near-[010](B) view of $Sc_{0.847(7)}Te$.

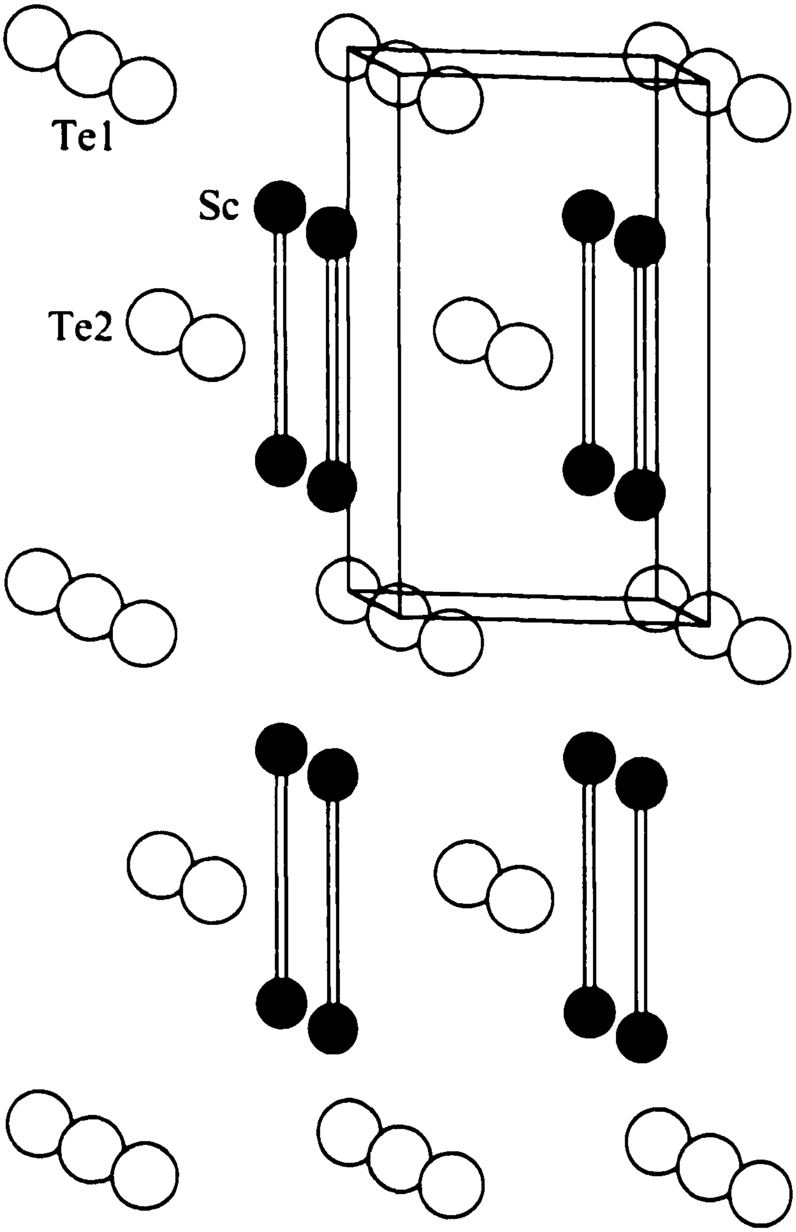

Figure 3. A near-[010] view of the Sc_xTe ($0.69 < x < 0.94$) unit cell.

ACKNOWLEDGEMENTS

The names of people helpful in particular projects have been included at the end of the respective thesis chapters. I particularly thank Dr. John D. Corbett, from whom I have received a great fundamental training in solid-state chemistry, one that stresses synthesis and understanding, and a good use of the English language. I would also like to thank the rest of the inorganic chemistry department at Iowa State University for admitting me to the program, and for their patience and open-mindedness during seminars and classes.

I am happy to have spent 5 years with the graduate, undergraduate and postdoctoral students in the research group. In particular, I thank Dr. Michael Lulei for guiding my first summer of research, and Mr. Douglas Knight who I attempted to guide in new chemistry as well. I also thank Shirley Standley, our research group secretary who helped edit all the published manuscripts.

During this time, there were also many things I learned about the strength and support of family. They provided the solid foundation from which I could concentrate on my research and studies. We will continue to grow together.